

Armed Services Technical Information Agency

Because of our limited supply, you are requested to return this copy WHEN IT HAS SERVED YOUR PURPOSE so that it may be made available to other requesters. Your cooperation will be appreciated.

AD

28499

NOTICE: WHEN GOVERNMENT OR OTHER DRAWINGS, SPECIFICATIONS OR OTHER DATA ARE USED FOR ANY PURPOSE OTHER THAN IN CONNECTION WITH A DEFINITELY RELATED GOVERNMENT PROCUREMENT OPERATION, THE U. S. GOVERNMENT THEREBY INCURS NO RESPONSIBILITY, NOR ANY OBLIGATION WHATSOEVER; AND THE FACT THAT THE GOVERNMENT MAY HAVE FORMULATED, FURNISHED, OR IN ANY WAY SUPPLIED THE SAID DRAWINGS, SPECIFICATIONS, OR OTHER DATA IS NOT TO BE REGARDED BY IMPLICATION OR OTHERWISE AS IN ANY MANNER LICENSING THE HOLDER OR ANY OTHER PERSON OR CORPORATION, OR CONVEYING ANY RIGHTS OR PERMISSION TO MANUFACTURE, USE OR SELL ANY PATENTED INVENTION THAT MAY IN ANY WAY BE RELATED THERETO.

Reproduced by
DOCUMENT SERVICE CENTER
KNOTT BUILDING, DAYTON, 2, OHIO

UNCLASSIFIED

INSTITUTE OF AEROPHYSICS

UNIVERSITY OF TORONTO

A THEORETICAL AND EXPERIMENTAL STUDY OF THE SHOCK TUBE

BY

I. I. GLASS, W. MARTIN
and
G. N. PATTERSON



NOVEMBER 1953

UTIA REPORT NO. 2

A THEORETICAL AND EXPERIMENTAL STUDY
OF THE SHOCK TUBE

BY

I. I. GLASS, W. MARTIN
and
G. N. PATTERSON

NOVEMBER, 1953

UTIA REPORT NO. 2

ACKNOWLEDGEMENT

The authors would like to express their sincerest appreciation to Mr. I. J. Billington for his very valuable assistance in proof-reading the manuscript and in the preparation of the graphs and figures.

Thanks are due to Mr. A. Ford and Mr. R. Martino for their help in conducting some of the experiments and for computing some of the data.

The discussions with Professor B. Etkin, Mr. J. Steketee, Mr. G. Hall and Mr. L. R. Fowell have been useful and stimulating.

The financial assistance received from the Defence Research Board is gratefully acknowledged.

TABLE OF CONTENTS

	<u>Page</u>
SUMMARY	iii
NOTATION	v
INTRODUCTION	vii
I. RELEVANT WAVE THEORY	
1.01 Basic Equations for Rarefaction Waves.	2
1.02 Basic Equations for Shock Waves.	10
1.03 Wave System in a Shock Tube.	13
1.04 Basic Equations for the Wave System in a Shock Tube.	18
1.05 Determination of Physical Quantities and Wave Speeds in a Shock Tube.	24
1.06 Deviations from Thermal Equilibrium in a Shock Tube.	53
II. WAVE INTERACTIONS	
2.01 Normal Reflection of a Shock Wave.	82
2.02 Normal Reflection of a Rarefaction Wave.	89
2.03 Interaction of a Shock Wave and a Contact Surface.	91
2.04 Interaction of a Rarefaction Wave and a Contact Surface.	99
2.05 Theoretical Requirements for Chamber and Channel Length of a Shock Tube.	100
III. PRODUCTION OF STRONG SHOCK WAVES	111

	<u>Page</u>
IV. DESIGN AND CONSTRUCTION CRITERIA FOR SHOCK TUBES	
4.01 Shock Tubes in General.	119
4.02 3 inch x 3 inch Wave Interaction Tube	121
V. COMPARISON OF THEORY AND EXPERIMENT	
5.01 Experimental Procedure.	133
5.02 The Wave System at the Origin in a Real Shock Tube.	136
5.03 Some Experimental and Theoretical Aspects of Shock Wave Attenuation.	170
5.04 Contact Front Velocity Measurements.	204
5.05 Flow in the Uniform State Bounded by the Shock Wave and the Contact Surface.	211
5.06 Flow in the Uniform State Bounded by the Contact Surface and Rarefaction Wave.	212
5.07 Rarefaction Wave Velocity Measurements.	215
5.08 Real Flows at an Open or Closed Chamber and Channel.	222
5.09 Experiments on One-dimensional Wave Interactions.	228
VI. CONCLUSIONS.	248
REFERENCES.	251
APPENDIX A.	257
APPENDIX B.	275

SUMMARY

The theory of the shock tube is developed from basic considerations. Relations and comprehensive graphs are presented for the determination of wave speeds and the physical quantities of the uniform states. The effects of variable specific heat on the rarefaction wave and the shock wave are also considered.

A discussion is given of normal reflection of shock and rarefaction waves, the refraction of shock and rarefaction waves at a contact surface, the requirements for the production of strong shock waves and some essential criteria for the design and operation of shock tubes.

In all cases the theoretical considerations are compared with actual one-dimensional (x, t) -plane schlieren photographs of real flows in a 3 inch x 3 inch wave interaction tube. This tube has been designed and constructed with the utmost care, in order to obtain a tube alignment and uniformity of high accuracy as appraised by present-day machine shop standards. Despite these precautions, it has been found that the shock speed attenuates, and simultaneously the contact surface speed increases, with increasing diaphragm pressure ratio and distance from the diaphragm station.

It is shown that a train of transverse shock waves accompanies the primary shock wave regardless of its position from the diaphragm (0 to 142 inches or 0 to 50 tube widths). As these waves criss-cross the tube, they undergo regular and Mach reflection. After a long time, the waves which are shed far behind the primary shock wave, become sound waves. During this process these weak shock waves act as a dissipative mechanism and contribute to the total shock wave attenuation. The transverse waves also alter the physical properties of the uniform states behind the primary shock wave.

An empirical relation is given for the total shock wave attenuation, for this tube only, as a function of the shock wave position from the diaphragm. The total attenuation in shock wave velocity consists of a formation decrement plus a distance attenuation. For weak or strong shock waves there exists a formation distance, where the shock wave accelerates and reaches a uniform optimum speed. For weak waves the optimum speed is the one predicted theoretically. (There was no measurable distance attenuation over the 142 inches investigated during the present experiments.) For strong shock waves the optimum speed is less than the theoretical value (the formation decrement) and beyond the formation distance the shock speed decreases monotonically with distance (the distance attenuation).

A Rayleigh type incompressible ("pipe") flow analysis overestimates the experimental total attenuation results about threefold. By assuming that the real flow consists of a thin boundary layer and an inviscid core, and defining a displacement thickness (δ^*) at the contact front, it is possible to show that (δ^*) varies linearly with (x) , and its rate of growth

($\frac{d\delta^*}{dx}$) is about one-tenth the value encountered in stationary flow for an equivalent Mach number range. The value of (δ^*) was not measured directly, but was derived from the actual total attenuation results. It is noted that a satisfactory theory which would explain the observed shock wave attenuation results from various investigations has not been developed to-date. Such a theory, to be valid, should explain the shock attenuation and the contact front speed up simultaneously, since they are two concurrent phenomena in the shock tube.

Although numerous investigations have been conducted in shock tubes, there is no evidence available of direct measurements of pressure, density or temperature, over a wide range of diaphragm pressure ratios, in the uniform regions separated by the contact front. Hence, the questions whether these states are really uniform and whether it is valid to use the shock velocity to calculate the magnitude of the physical quantities in the flow regions separated by the contact surface can not be answered. Until this problem is settled, the researcher can not accept, without reservations, the assumption that the physical properties of the flows behind a shock wave may be calculated from its speed.

One-dimensional records are presented of the flow at the origin and beyond, over a range of diaphragm pressure ratios. The deviations from the ideal flow solution are analysed and discussed.

Schlieren photographs of the flow from an open channel and chamber are also given, and the departures from the inviscid flow solutions are discussed.

It is noted that experiments on the head-on collisions of shock waves and shock and rarefaction waves as well as shock wave refraction at a contact surface are all in good agreement with the simple wave element solutions, when the deviation from thermal equilibrium is negligible. This has also been confirmed recently for the preliminary work on the overtaking of two similarly facing shock waves.

Several schlieren photographs of the interaction of a shock wave with wire screens of different mesh size are also included to show their possible use in compressible flow studies.

It is noted that to-date the shock tube has not achieved its once expected prominence as an intermittent type of supersonic wind tunnel. This has been due mainly to the difficulties involved in measuring transient physical quantities and trying to extrapolate the results for steady supersonic flow. Nevertheless, the data that shock tubes have yielded on wave interactions, shock structure, thermal equilibrium and magneto-hydrodynamics have established that it is a unique instrument for the investigation of numerous fundamental problems in fluid mechanics.

(v)
NOTATION

The notation He/Air is used to designate a combination of helium and air separated by a diaphragm in a shock tube, the helium being at a higher pressure (in the chamber) than the air (in the channel). The notation Air//He signifies an air to helium contact surface where both gases have the same pressure and velocity.

The wave system involves regions of constant state denoted by (4) and (1) at $t = 0$ and by (3) and (2) at a subsequent time t . These symbols are applied as subscripts to a flow quantity in a particular state. For example, p_2 is the pressure in state (2).

The following symbols are used to denote physical quantities.

a	velocity of sound
C_p	coefficient of specific heat at constant pressure
C_v	coefficient of specific heat at constant volume
e	internal energy per unit mass
m	mass flow
p	pressure
t	time
t_1	specific time following $t = 0$
u	particle velocity
v	velocity relative to the shock front
w	speed of the shock wave
x	position along the shock tube measured from the diaphragm
x_1	a specific position along the tube
L	chamber length
ρ	density
μ	viscosity
ν	kinematic viscosity (μ/ρ)
M	Flow Mach Number (u/a)

T temperature

η entropy

$\left(\frac{Re}{l}\right)$ Reynolds number/ft.

The following symbols are used to denote dimensionless quantities as indicated :

$$A_{ij} = \frac{a_i}{a_j} \quad \left(\text{i.e. } A_{14} = \frac{a_1}{a_4} \right)$$

$$E_{ij} = \frac{(C_p T)_i}{(C_p T)_j} = \frac{e_i}{e_j} = K T_{ij}$$

$$M_i = \frac{u_i}{a_i}$$

$$\gamma_i = \left(\frac{C_p}{C_v} \right)_i$$

$$P_{ij} = \frac{p_i}{p_j}$$

$$\alpha_i = \frac{\gamma_i + 1}{\gamma_i - 1}$$

$$T_{ij} = \frac{T_i}{T_j}$$

$$\beta_i = \frac{\gamma_i - 1}{2\gamma_i}$$

$$\Gamma_{ij} = \frac{\rho_i}{\rho_j}$$

$$n = \frac{x}{a_4 t}$$

$$C_{ij} = \frac{c_i}{a_j}$$

$$c = \frac{x}{t}$$

$$U_{ij} = \frac{u_i}{a_j}$$

$$X = \frac{x}{L}$$

$$W_{ij} = \frac{w_i}{a_j}$$

$$\tau = \frac{a_4 t}{L}$$

NOTE : In section 1.06, α and β are used to designate thermodynamic parameters which are currently in use in the literature.

INTRODUCTION

During the past ten years the shock tube has attained singular recognition as the basic instrument for the study of nonstationary problems in fluid mechanics. At the same time the literature on the subject has become quite extensive. Therefore, a report of this nature would not be justified unless the presentation and the new experimental material contributed toward the understanding of this recent field of research. The authors sincerely hope that this goal has been achieved in some measure.

The use of the shock tube as an instrument for the investigation of problems in fluid mechanics was started by Vieille in 1899 (ref. 1). A significant contribution to the experimental knowledge of flows in a shock tube was made by Payman and Shepherd about forty years later (ref. 2). Since 1940 the work in this field has become extensive in scope and varied in application. The shock tube has now been successfully applied to the study of transition through shock fronts; wave interactions; subsonic, transonic and supersonic flows; wave diffraction and refraction; shock loading of structures; the measurement of the speed of sound in gases; relaxation phenomena in gases; condensation; flame propagation; chemical reaction kinetics; the atomic physics of the states behind strong shock waves and magneto-hydrodynamics (refs. 3 to 29).

The fundamental theory concerning the wave elements produced in a shock tube is due to Stokes, Riemann, Rankine and others (ref. 30). The basic theory of the shock tube was developed later by a number of investigators (refs. 31 to 34). Although the importance of the pressure ratio across the diaphragm was recognized early as a fundamental parameter in the study of flows in a shock tube, another parameter, the internal energy ratio across the diaphragm, is shown in the present analysis to be of equal importance.

The shock tube, in its simplest form, consists of a straight tube of uniform cross-section containing a diaphragm which separates two compartments. One compartment is filled with a gas at high pressure and is designated as the high pressure chamber (or simply the chamber), the other contains a gas at a lower pressure and is called the low pressure

chamber (or the channel). The dividing diaphragm may be cellophane, paper, metallic foil or any other material. Before the diaphragm is ruptured the gases in the two sections are in thermal equilibrium. When the diaphragm is broken, it is observed experimentally that a shock wave races in one direction along the channel at supersonic speeds while a rarefaction or expansion wave moves into the chamber at the local sonic speed, as shown on plate 1. This wave system, which can be deduced just as well from theoretical consideration, is shown in figure 1. In this case the theory assumes that the diaphragm is completely and instantaneously removed and as a result a plane shock wave is instantly propagated into the channel and a centred rarefaction wave into the chamber.

The gas in the channel, which is compressed adiabatically* by the shock wave, is assumed to have a uniform state with constant thermodynamic quantities of pressure, density, temperature, entropy and flow velocity. At the same time the gas from the chamber is expanded isentropically** through the rarefaction wave to the same pressure and flow velocity attained by the gas in the channel. Although a uniform state is also theoretically achieved behind the rarefaction wave, the temperature, density and entropy will be different from the gas state behind the shock wave.

In order for these two regions to coexist side by side, it is assumed that they are separated by a contact surface. In the initial analysis an additional assumption is made that the specific heats of the gases remain constant during the process.

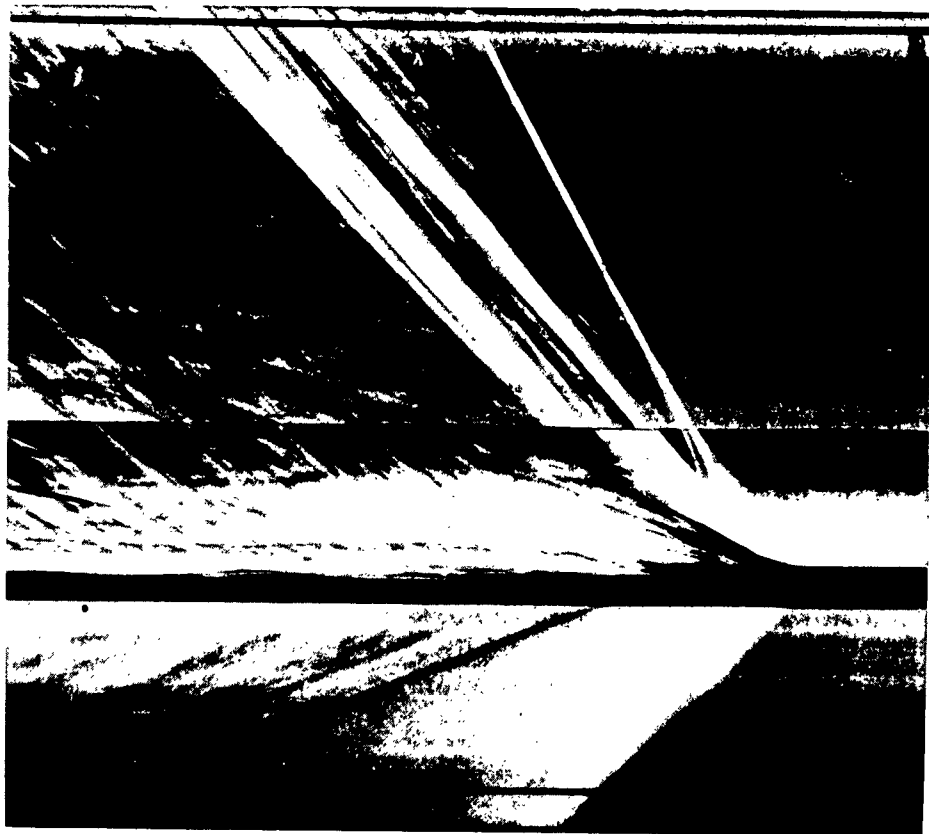
In reality this ideal wave system is not quite achieved as may be seen from plate 1, which shows a schlieren (x, t) -plane photograph of a real flow in a shock tube from the instant the diaphragm is ruptured.

With the above assumptions it is possible to develop a theoretical relationship between the pressure ratio and the specific heat ratios across the diaphragm and the pressure ratio across the shock wave. Once the shock wave pressure ratio is known the wave speeds and the thermodynamic properties of the uniform states are readily determined.

Theoretical relationships for other flows and wave interactions in a shock tube are also developed and analysed in this report and a comparison is made with recent experimental work conducted at the Institute of Aerophysics. The results were obtained with the 3 inch x 3 inch wave interaction tube in conjunction with a schlieren system and wave speed camera, which yielded actual (x, t) -plane photographs of the various flows.

* irreversible process

** adiabatic reversible process



WAVE SYSTEM IN A SHOCK TUBE FROM THE INSTANT THE DIAPHRAGM RUPTURES.

PLATE 1.

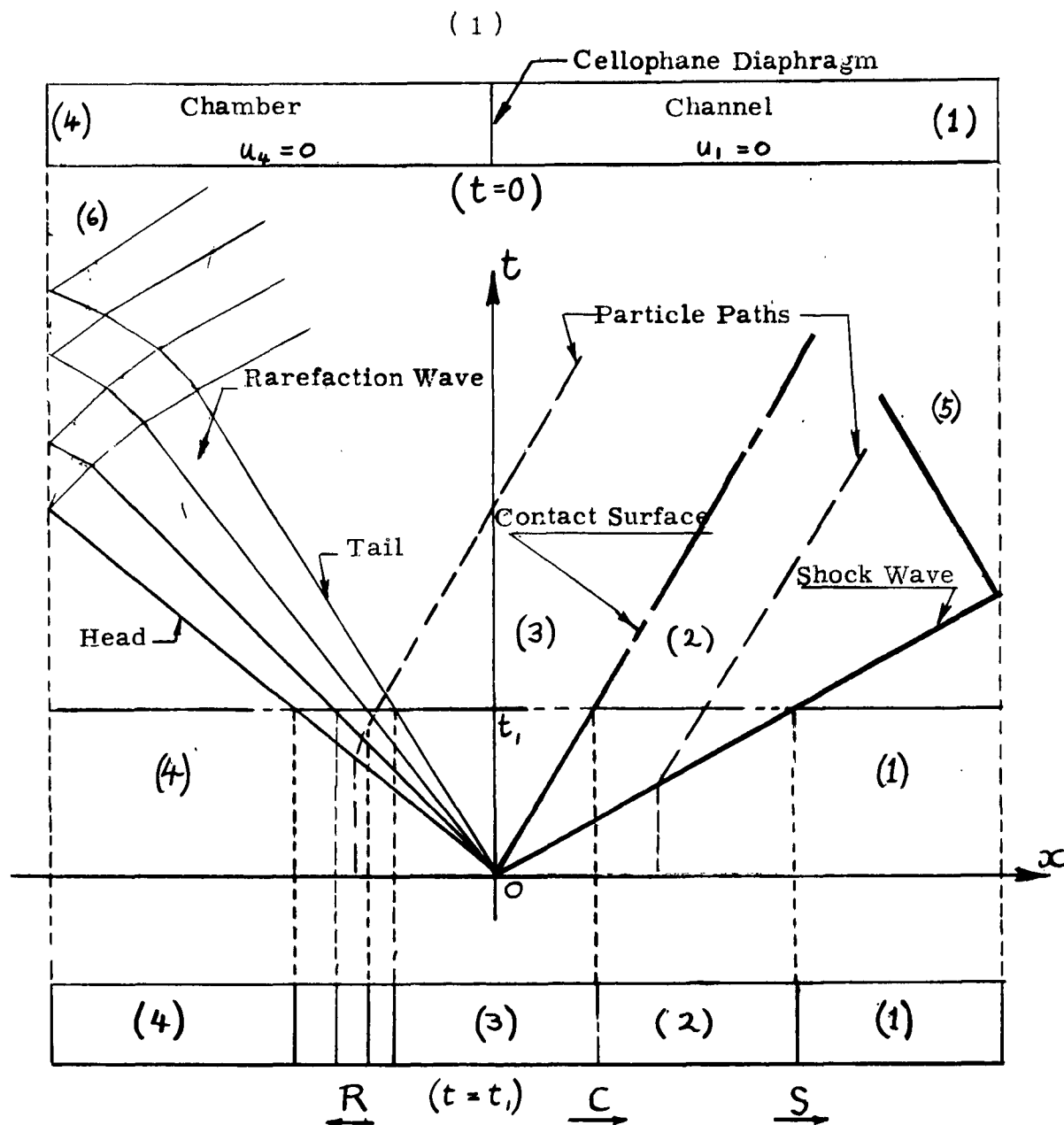


FIGURE 1.

THEORETICAL DIAGRAM OF THE (x, t) -PLANE SHOWING THE WAVES AND STATES IN THE CHAMBER AND CHANNEL FROM THE INSTANT THE DIAPHRAGM RUPTURES.

I. RELEVANT WAVE THEORY

1.01 Basic Equations for Rarefaction Waves

In one-dimensional, unsteady and isentropic flow (compression or rarefaction wave), the propagation of a disturbance of finite amplitude can be considered as one composed of an infinite number of small disturbances (Mach waves or characteristic lines) propagated at the speed of sound with respect to the gas at the point under consideration.

Rarefaction waves are disturbances which are propagated so that they spread and become less steep with time, while compression waves become more steep with time and finally converge to form a shock front. These waves are aperiodic and are really transition fronts which separate two constant states. Classical theory (reference 30) assumes that when a piston in a cylinder accelerates, a compression wave is formed and moves ahead of the piston, and the fluid particles behind the wave follow at the piston speed, whereas, behind the piston a rarefaction wave is generated which moves in a direction opposite to the piston, but the gas particles go through this wave and follow the piston at piston speed (figure 2).

In the theory of the shock tube it is assumed that when the diaphragm, which separates the high and low pressure chambers filled with a gas at rest, is suddenly ruptured, a contact surface C is formed which behaves like a piston that has attained constant velocity through instantaneous infinite acceleration. As a result a centred rarefaction wave R , is propagated into the chamber and a plane shock wave S , moves ahead of the contact surface at supersonic velocity into the channel. The shock wave compresses the gas in the channel to an intermediate pressure and accelerates the flow in its direction. The rarefaction wave reduces the pressure in the high pressure chamber to the same intermediate pressure and accelerates the fluid particles in a direction opposite to the advance of the rarefaction wave (figure 1), so that they follow the contact surface.

The centred rarefaction wave R , is represented by a pencil of straight lines (Mach waves or characteristic lines) radiating from the origin. It will be shown that along such a characteristic line, the flow speed, density or any other thermodynamic quantity is constant. The origin of the centred wave represents an initial discontinuity which is smoothed out immediately and is one of the properties of non-linear

flow (reference 30). In practice the wave model is as shown on plate 1, and it approximates the conditions given on figure 2, that is, the rarefaction wave is not centred; the shock wave is formed by the converging characteristic lines; the contact surface is in fact a region or front which rapidly accelerates at the origin and later achieves a nearly uniform velocity. The actual flow at the origin will be discussed in section 5.03.

In the analysis of the rarefaction wave in one-dimensional, unsteady and inviscid flow the following relations are applied.

Equation of continuity:

$$\frac{\partial \rho}{\partial t} + u \frac{\partial \rho}{\partial x} + \rho \frac{\partial u}{\partial x} = 0 \quad (1.1)$$

Equation of motion:

$$\frac{\partial u}{\partial t} + u \frac{\partial u}{\partial x} + \frac{1}{\rho} \frac{\partial p}{\partial x} = 0 \quad (1.2)$$

Equation of state for an ideal gas:

$$p = \rho R T \quad (1.3)$$

Isentropic expansion through the wave:

$$p = A \rho^\gamma \quad (1.4)$$

In general the pressure is a function of density and entropy,

$$p = p(\rho, \eta) \quad \text{and} \quad dp = \left(\frac{\partial p}{\partial \rho} \right)_\eta d\rho + \left(\frac{\partial p}{\partial \eta} \right)_\rho d\eta \quad (1.5)$$

Let $\left(\frac{\partial p}{\partial \rho} \right)_\eta = a^2$, then for an isentropic flow:

$$\frac{dp}{d\rho} = a^2 = \gamma A \rho^{\gamma-1} \quad (1.6)$$

(4)

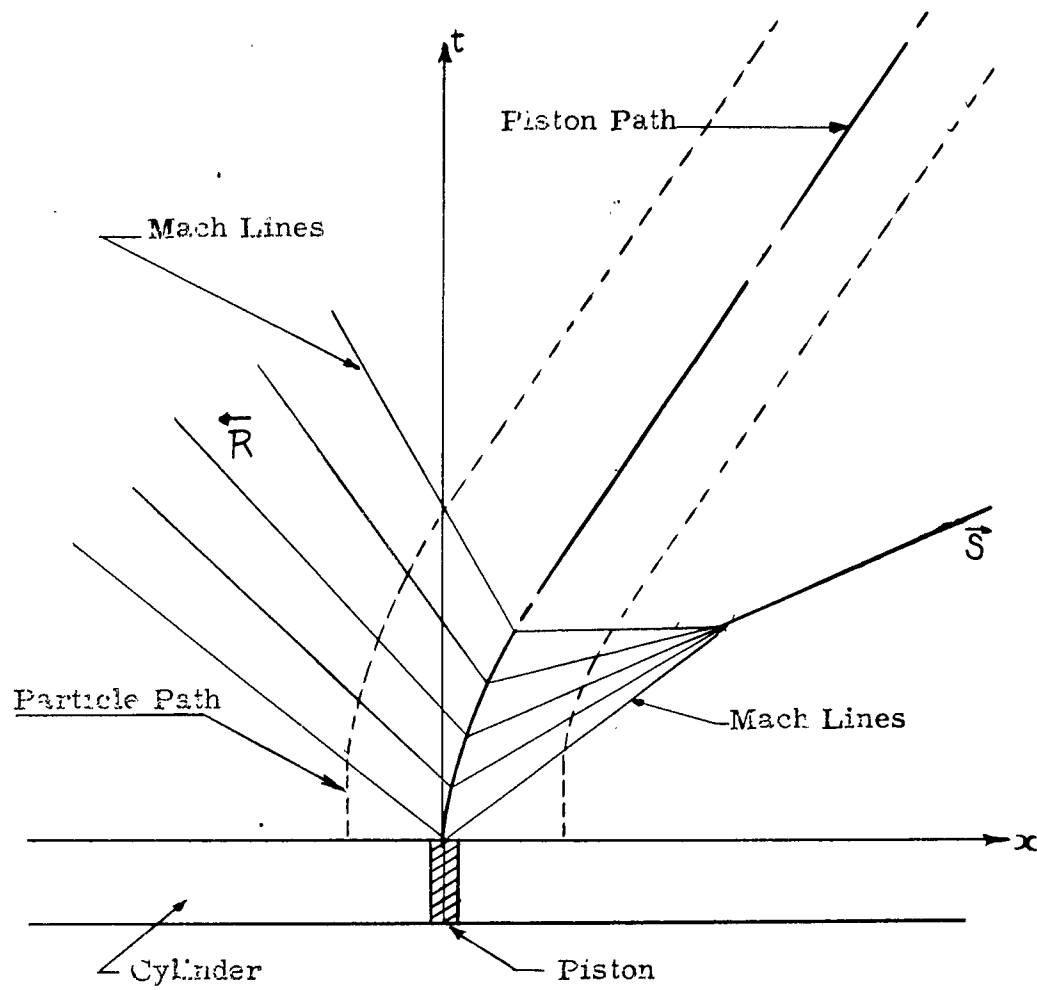


FIGURE 2.

THE WAVE SYSTEM PRODUCED BY
A MOVING PISTON IN A CYLINDER

$$\frac{\partial p}{\partial t} = \frac{2}{\gamma-1} \frac{p}{a} \frac{\partial a}{\partial t} \quad (1.7)$$

$$\frac{1}{p} \frac{\partial p}{\partial x} = \frac{2a}{\gamma-1} \frac{\partial a}{\partial x} \quad (1.8)$$

The above relations transform equations (1.1) and (1.2) into

$$\frac{2}{\gamma-1} \left(\frac{\partial a}{\partial t} + u \frac{\partial a}{\partial x} \right) + a \frac{\partial u}{\partial x} = 0 \quad (1.9)$$

$$\frac{\partial u}{\partial t} + u \frac{\partial u}{\partial x} + \frac{2a}{\gamma-1} \frac{\partial a}{\partial x} = 0 \quad (1.10)$$

Adding and subtracting (1.9) and (1.10) gives :

$$\left[\frac{\partial}{\partial t} + (u+a) \frac{\partial}{\partial x} \right] \left(u + \frac{2a}{\gamma-1} \right) = 0 \quad (1.11)$$

$$\left[\frac{\partial}{\partial t} + (u-a) \frac{\partial}{\partial x} \right] \left(u - \frac{2a}{\gamma-1} \right) = 0 \quad (1.12)$$

Equations (1.11) and (1.12) define two sets of special curves which are called the characteristics of the equations. If a curve exists that has the special slope

$$\frac{dx}{dt} = u + a \quad (1.13)$$

then (1.11) becomes an exact differential and

$$u + \frac{2a}{\gamma-1} = \phi = \text{constant}, \quad (1.14)$$

along this curve. Similarly for a curve that has a slope

$$\frac{dx}{dt} = u - a \quad (1.15)$$

then from (1.12)

$$u - \frac{2a}{\gamma-1} = \psi = \text{constant}, \quad (1.16)$$

along this curve.

Equations (1.14) and (1.16) define the ϕ and ψ families of characteristics. In general a characteristic of one family intersects all the characteristics of the other family.

In the physical (x,t) -plane (figure 1 or plate 1), the curves with the characteristic slopes $\frac{dx}{dt} = u + a$ and $\frac{dx}{dt} = u - a$, represent the motion of an infinite number of small disturbance fronts of the finite disturbance (compression or rarefaction) wave. The rate of advance of these is given by $(u + a)$ and $(u - a)$ respectively. This rate of propagation when referred to flow speed u at each point under consideration is given by $\pm a$. Therefore, the front of such a characteristic line travels with the sound speed relative to the gas, and the quantity " a ", may now justifiably be called the speed of sound. These characteristic fronts are therefore called sound waves, Mach waves or characteristic lines, and the first characteristic line (head of rarefaction wave) travelling into the gas at rest ($u_0 = 0$) when the diaphragm is ruptured, advances into the chamber with a speed,

$$\frac{dx}{dt} = -a_0$$

the speed of sound of the rest state. The negative sign is consistent with figure 1, where the rarefaction wave advances in the negative x -direction.

From previous considerations it can be seen that this sound wave is a ψ -characteristic and since it intersects all the ϕ -characteristics where $u_0 = 0$ and $a = a_0$, therefore

$$\phi = \frac{2a_0}{\gamma-1} \quad (1.17)$$

This value of ϕ applies to the entire family of ϕ -characteristics intersected by the sound wave and is a constant for the entire region covered by these characteristics.

Since along a ψ - characteristic $u - \frac{2a}{\gamma-1}$ is a constant, and $u + \frac{2a}{\gamma-1} = \frac{2a_0}{\gamma-1}$ throughout the entire region, therefore along a ψ - characteristic u is constant and "a" is constant. Consequently along a ψ - characteristic line $\frac{dy}{dx} = u - a$ is a constant, and the lines are straight as shown in figure 1. This result is a basic property of a compression or rarefaction wave (reference 30).

For a centred rarefaction wave a new variable c is introduced such that,

$$c = \frac{x}{t}$$

$$\frac{\partial}{\partial x} = \frac{1}{t} \frac{d}{dc} \quad (1.18)$$

$$\frac{\partial}{\partial t} = -\frac{c}{t} \frac{d}{dc}$$

Substituting (1.18) in the basic equations (1.1) and (1.2) yields :

$$\frac{\rho'}{t} (u - c) = -\frac{\rho}{t} u' \quad (1.19)$$

$$\frac{u'}{t} (u - c) = -\frac{a^2 \rho'}{\rho t} \quad (1.20)$$

where $u' = \frac{du}{dc}$ and $\rho' = \frac{d\rho}{dc}$

A multiplication and division of these equations results in :

$$(c - u)^2 = a^2 \quad (1.21)$$

$$\left(\frac{u'}{\rho'}\right)^2 = \left(\frac{a}{\rho}\right)^2 \quad (1.22)$$

Therefore

$$c - u = \pm a \quad (1.23)$$

$$u' = \pm \frac{a}{\rho} \rho' \quad (1.24)$$

Since from (1.6) $\frac{2da}{a} = (\gamma-1) \frac{d\rho}{\rho}$, therefore from (1.24) :

$$u = \pm \frac{2a}{\gamma-1} + \text{constant} \quad (1.25)$$

The correct signs must be chosen for (1.23) and (1.25). In the present case the speed u is positive. For increasing u the density ρ and the speed of sound a decrease, hence $c - u = -a$ and $u = -\frac{2a}{\gamma-1} + \text{constant}$ apply. Therefore the equations for a centred rarefaction wave moving to the left (figure 1) are :

$$\frac{x}{t} = u - a \quad (1.26)$$

$$u + \frac{2a}{\gamma-1} = \text{constant}$$

For the head of the wave $u = u_4 = 0$ and $a = a_4$, and the constant is therefore $\frac{2a_4}{\gamma_4-1}$. For the tail of the wave $\frac{x}{t} = u_3 - a_3$ and $u_3 = \frac{2}{\gamma_4-1}(a_4 - a_3)$. Solving for u and a from (1.26) yields :

$$a = -\frac{\gamma_4-1}{\gamma_4+1} \left(\frac{x}{t} \right) + \frac{2a_4}{\gamma_4+1} \quad (1.27)$$

$$u = \frac{2}{\gamma_4+1} \left(\frac{x}{t} \right) + \frac{2a_4}{\gamma_4+1} \quad (1.28)$$

From these equations it is possible, theoretically, to find u and a at any ψ - characteristic of the rarefaction wave from its slope $\left(\frac{x}{t} \right)$, the speed of sound in the rest state (a_4) and the specific

heat ratio of the gas in the chamber (γ_4). In reality, this may be practical for the two bordering characteristics of the rarefaction wave, that is, the head and the tail of the wave, where it will be shown that the density derivative ($\frac{\partial \rho}{\partial x}$) is discontinuous and thus they may lend themselves to schlieren photography.

$$\text{Since } u + \frac{2a}{\gamma_4 - 1} = u_4 + \frac{2a_4}{\gamma_4 - 1} \quad (u_4 = 0)$$

$$\text{therefore } \frac{a}{a_4} = 1 - \frac{\gamma_4 - 1}{2} \frac{u}{a_4} \quad (1.29)$$

$$\text{and } \frac{a}{a_4} = \left(\frac{T}{T_4} \right)^{1/2} = \left(\frac{\rho}{\rho_4} \right)^{\frac{\gamma_4 - 1}{2}} = \left(\frac{P}{P_4} \right)^{\frac{\gamma_4 - 1}{2\gamma_4}} \quad (1.30)$$

$$\begin{aligned} \text{or } \frac{T}{T_4} &= \left(1 - \frac{\gamma_4 - 1}{2} \frac{u}{a_4} \right)^2 \\ \frac{\rho}{\rho_4} &= \left(1 - \frac{\gamma_4 - 1}{2} \frac{u}{a_4} \right)^{\frac{2}{\gamma_4 - 1}} \\ \frac{P}{P_4} &= \left(1 - \frac{\gamma_4 - 1}{2} \frac{u}{a_4} \right)^{\frac{2\gamma_4}{\gamma_4 - 1}} \end{aligned} \quad (1.31)$$

Substituting the value of u from (1.28)

$$\begin{aligned} \frac{a}{a_4} &= 1 - \frac{\gamma_4 - 1}{\gamma_4 + 1} \left(\frac{x}{a_4 t} + 1 \right) \\ \frac{T}{T_4} &= \left[1 - \frac{\gamma_4 - 1}{\gamma_4 + 1} \left(\frac{x}{a_4 t} + 1 \right) \right]^2 \\ \frac{\rho}{\rho_4} &= \left[1 - \frac{\gamma_4 - 1}{\gamma_4 + 1} \left(\frac{x}{a_4 t} + 1 \right) \right]^{\frac{2}{\gamma_4 - 1}} \\ \frac{P}{P_4} &= \left[1 - \frac{\gamma_4 - 1}{\gamma_4 + 1} \left(\frac{x}{a_4 t} + 1 \right) \right]^{\frac{2\gamma_4}{\gamma_4 + 1}} \\ M &= \left| \frac{u}{a} \right| = \frac{\frac{x}{a_4 t} + 1}{1 - \frac{\gamma_4 - 1}{2} \frac{x}{a_4 t}} \end{aligned} \quad (1.32)$$

The above equations give the physical flow quantities through the rarefaction wave in terms of the slope of the characteristic and the initial values of the rest state (4).

1.02 Basic Equations for the Shock Wave

In section 1.01 it was indicated how a shock wave is formed from the convergent characteristic lines of a compression wave due to the motion of a piston (figure 2 and reference 10) or by rupturing a diaphragm in a shock tube (plate 1).

In its simplest form the shock wave is regarded as a thin front (of the order of a few mean free paths) in which very rapid transitions of velocity, pressure density and temperature take place.

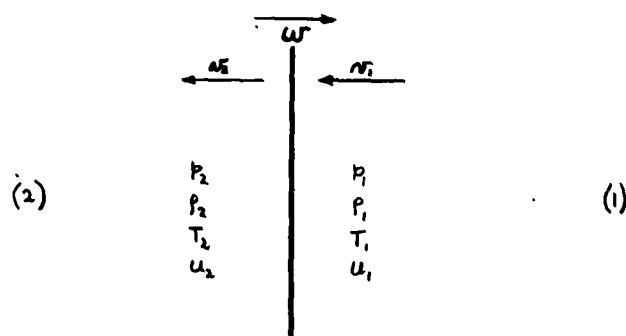


FIGURE 3

TRANSITION ACROSS A SHOCK FRONT

The shock front separates the two states (1) and (2) in which $\frac{dT}{dx} = 0$ and $\frac{dn}{dx} = 0$. For convenience, the shock front which is travelling at a constant velocity w in the shock tube may be considered at rest by a change of reference axes with respect to the shock wave, that is, by superposing an equal velocity w in the opposite direction on the entire flow field (figure 3) so that

$$\begin{aligned} n_1 &= u_1 - w \\ n_2 &= u_2 - w \end{aligned} \quad (1.33)$$

The shock front is assumed to lie in a plane perpendicular to the flow direction so that the problem can be considered as one-dimensional steady flow for an ideal gas.

For one-dimensional flow the equations of motion are as follows :

Continuity equation :

$$\frac{d}{dx}(\rho v) = 0 \quad (1.34)$$

Momentum equation :

$$\frac{d}{dx} \left[\rho v^2 + p - \frac{4}{3} \mu \frac{dv}{dx} \right] = 0 \quad (1.35)$$

Energy equation :

$$\frac{d}{dx} \left[\rho v \left(C_p T + \frac{1}{2} v^2 \right) - \frac{4}{3} \mu v \frac{dv}{dx} - k \frac{dT}{dx} \right] = 0 \quad (1.36)$$

Equation of state :

$$p = \rho (C_p - C_v) T \quad (1.37)$$

For all values of x ,

$$\rho v = \text{constant} \quad (1.38)$$

$$p + \rho v^2 - \frac{4}{3} \mu \frac{dv}{dx} = \text{constant} \quad (1.39)$$

$$\rho v \left(C_p T + \frac{1}{2} v^2 \right) - \frac{4}{3} \mu v \frac{dv}{dx} - k \frac{dT}{dx} = \text{constant} \quad (1.40)$$

(12)

If state (1) is known and $\left(\frac{dv}{dx}\right)_1, \left(\frac{dT}{dx}\right)_1 = 0$, then the constants may be determined.

$$pN = p_1 N_1 \quad (1.41)$$

$$p + pN^2 - \frac{4}{3}\mu \frac{dv}{dx} = p_1 + p_1 N_1^2 \quad (1.42)$$

$$pN \left(C_p T + \frac{1}{2} N^2 \right) - \frac{4}{3}\mu \frac{dv}{dx} - k \frac{dT}{dx} = p_1 N_1 \left(C_p T_1 + \frac{N_1^2}{2} \right) \quad (1.43)$$

By combining the above equations along with the relation that μ and k are functions of temperature, in a dimensionless form, it has been possible to give a general solution to the transition problem through weak shock fronts with varying Prandtl numbers (reference 39) and to determine theoretically the shock thickness and the distribution of the physical flow quantities.

If the conditions that $\frac{dv}{dx} = 0$ and $\frac{dT}{dx} = 0$ are applied to the initial state (1) and the final state (2), then the above equations reduce to algebraic forms and the Rankine-Hugoniot relations for the pressure and density across a normal shock wave are obtained.

$$p_2 N_2 = p_1 N_1 \quad (1.44)$$

$$p_2 + p_2 N_2^2 = p_1 + p_1 N_1^2 \quad (1.45)$$

$$C_p T_2 + \frac{1}{2} N_2^2 = C_p T_1 + \frac{1}{2} N_1^2 \quad (1.46)$$

$$\frac{p_2}{p_1} = \frac{\left(1 - \frac{\gamma-1}{\gamma+1} \frac{p_1}{p_2}\right)}{\left(\frac{p_1}{p_2} - \frac{\gamma-1}{\gamma+1}\right)} \quad (1.47)$$

$$\frac{p_2}{p_1} = \frac{\left(\frac{\gamma-1}{\gamma+1} + \frac{p_2}{p_1}\right)}{\left(\frac{\gamma-1}{\gamma+1} \frac{p_2}{p_1} + 1\right)} = \frac{N_1}{N_2} \quad (1.48)$$

$$\eta_2 - \eta_1 = C_v \ln \left[\frac{p_2}{p_1} \left(\frac{p_1}{p_2} \right)^\gamma \right] \quad (1.49)$$

According to the second law of thermodynamics $\eta_2 \geq \eta_1$, and it may be shown that this occurs when $\frac{N_1}{a_1} = M_1 > 1$. These relations may be compared with the isentropic equations (1.31) and it will be noted that by expanding the pressure ratios in a series form they become equivalent only for very weak shocks (Mach waves).

It should be pointed out that the above relations were derived by assuming that the specific heat ratio (γ) is a constant. In reality, γ is a function of temperature and pressure, and their effects on the specific heat will be discussed in section 1.06.

1.03 Wave System in a Shock Tube

The wave system in a shock tube from the instant the diaphragm ruptures as shown in figure 1 may be deduced from a discussion of the transition relations for shock fronts and rarefaction waves by utilizing the (p, u)-plane for their graphical representation (reference 30).

Consider the shock front separating the two constant states (1) and (2) in figure 3, and apply the mechanical shock relations.

$$p_2 N_2 = p_1 N_1 = m \quad (1.44)$$

$$p_2 + p_2 N_2^2 = p_1 + p_1 N_1^2 \quad (1.45)$$

$$\begin{aligned} \text{where} \quad N_1 &= u_1 - w \\ N_2 &= u_2 - w \end{aligned} \quad (1.33)$$

(14)

By combining (1.45) and (1.33),

$$\frac{P_2 - P_1}{u_2 - u_1} = -m \quad (1.50)$$

and from (1.44) and (1.33),

$$m^2 = \frac{P_2 - P_1}{\frac{1}{P_1} - \frac{1}{P_2}} \quad (1.51)$$

From (1.50), (1.51) and (1.48),

$$u_2 = u_1 \pm \varphi_1(P_2) \quad (1.52)$$

where

$$\varphi_1(P_2) = (P_2 - P_1) \sqrt{\frac{2}{P_1[(\gamma-1)P_1 + (\gamma+1)P_2]}} \quad (1.53)$$

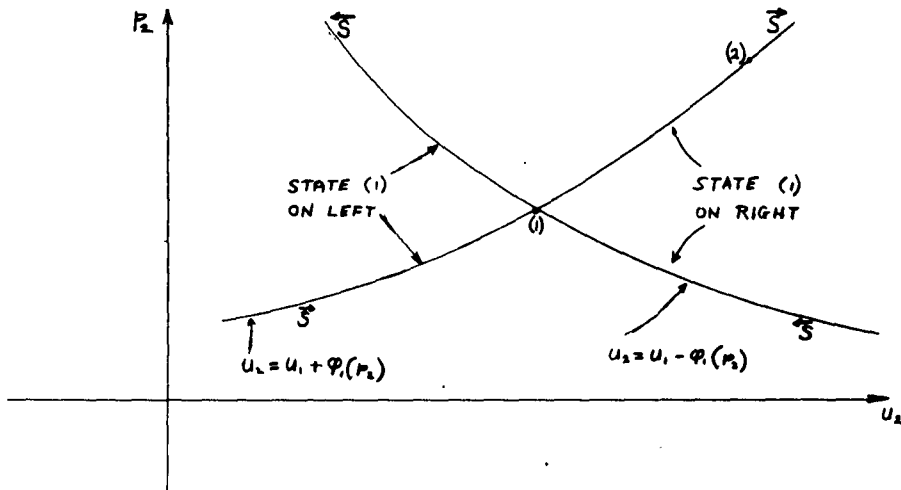


FIGURE 4

LOCUS OF ALL STATES (2) THAT MAY BE CONNECTED
WITH A GIVEN STATE (1) BY A FORWARD OR BACKWARD
FACING SHOCK WAVE

These waves are plotted on figure 4. The positive sign applies to shock waves facing in the positive x-direction (\bar{S}) (forward facing wave). A forward facing wave is one in which the particles enter it from right to left. The opposite is true for a backward facing wave (\bar{S}). For example, by considering the particular state (2) in figure 4, it is seen that the unknown state (2) is connected to the known state (1) on its right, by a forward facing shock wave (\bar{S}).

In a similar manner for a rarefaction wave

$$u_2 \pm \frac{2a_2}{\gamma-1} = u_1 \pm \frac{2a_1}{\gamma-1} \quad (1.25)$$

$$u_2 = u_1 \pm \psi_1(p_2) \quad (1.54)$$

where
$$\psi_1(p_2) = \frac{2a_1}{\gamma-1} \left[\left(\frac{p_2}{p_1} \right)^{\frac{\gamma-1}{2\gamma}} - 1 \right] \quad (1.55)$$

These curves are plotted in figure 5.

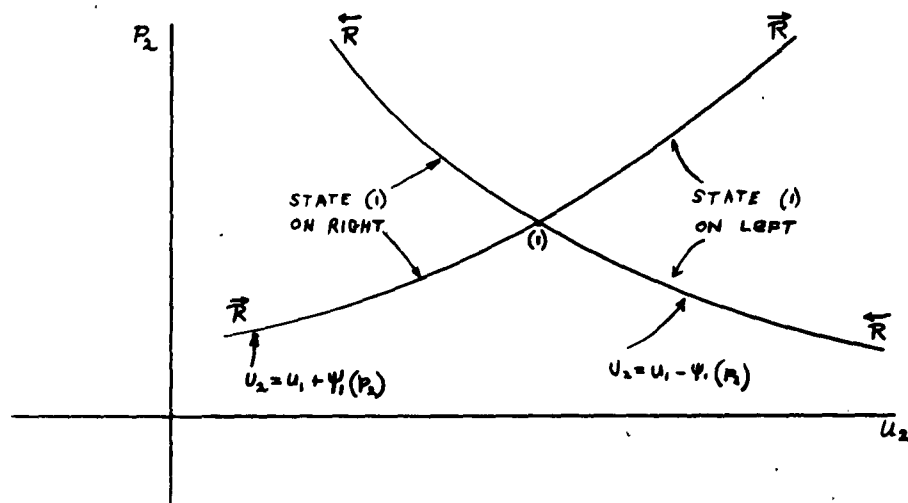


FIGURE 5

LOCUS OF ALL STATES (2) THAT MAY BE CONNECTED WITH A KNOWN STATE (1) BY A FORWARD OR BACKWARD FACING RAREFACTION WAVE

By combining figures 4 and 5, the following two diagrams are obtained :

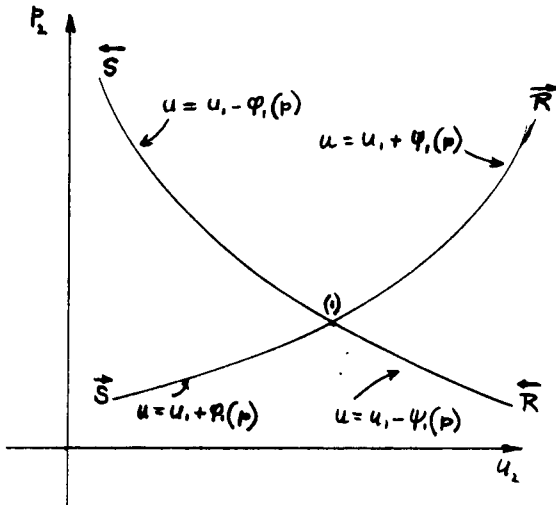


FIGURE 6

Locus of all the States (2) that may be reached from a given state (1) on the left by forward or backward facing waves.

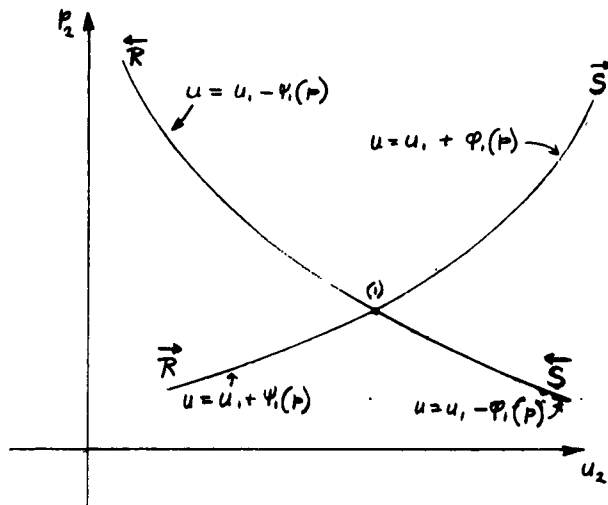


FIGURE 7

Locus of all the States (2) that may be reached from a given state (1) on the right by forward or backward facing waves.

This combination is justified since at the point of intersection (1), $\varphi_1'(p_1) = \psi_1'(p_1) = \sqrt{\frac{1}{\gamma p_1 \rho_1}}$ and $\varphi_1''(p_1) = \psi_1''(p_1)$

$$= -\frac{\gamma+1}{2} \frac{1}{(\gamma p_1)^{3/2} \rho_1^{1/2}} \quad \text{and the curves join at (1) in a smooth manner.}$$

Although $\varphi_1'''(p_1) \neq \psi_1'''(p_1)$ this has little effect on a physical flow.

These diagrams may now be applied to the shock tube problem in the following manner. Given a shock tube as shown in figure 8, which has two gaseous states (4) and (1) separated by a diaphragm, such that $p_4 > p_1$ and $u_4 = u_1 = 0$ at $t = 0$, plot the two states in the (p, u) -plane and draw the waves for the left state (4) and the right state (1) as shown in figure 9.

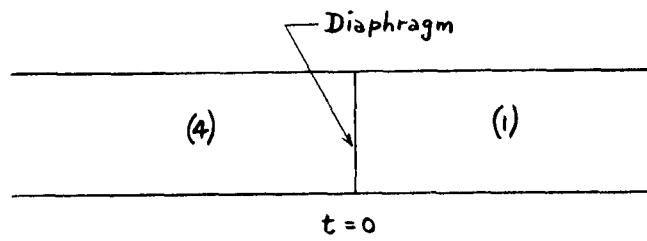


FIGURE 8

INITIAL CONDITIONS IN A SHOCK TUBE

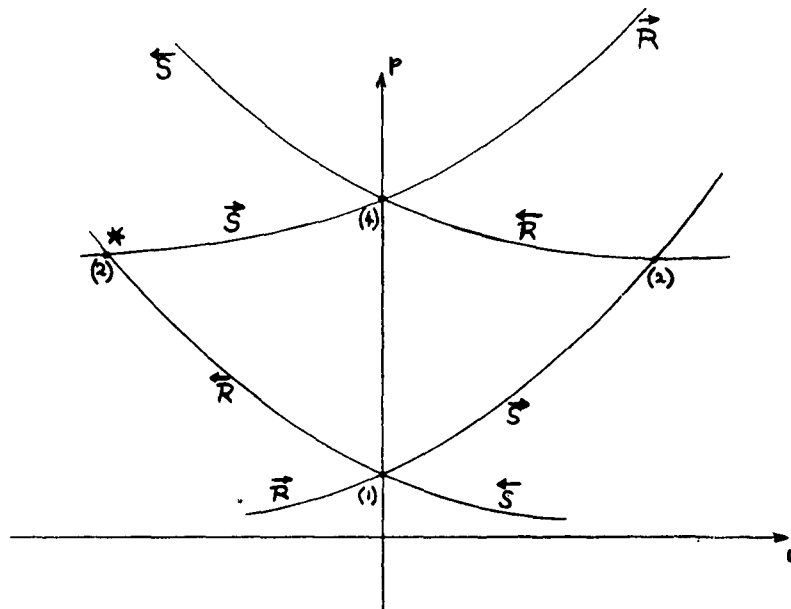


FIGURE 9

THE SHOCK TUBE PROBLEM IN THE (p, u) -PLANE

From figure 9, it is seen that when the diaphragm is ruptured one of two new states (2) and (2*) may be formed (figure 10).

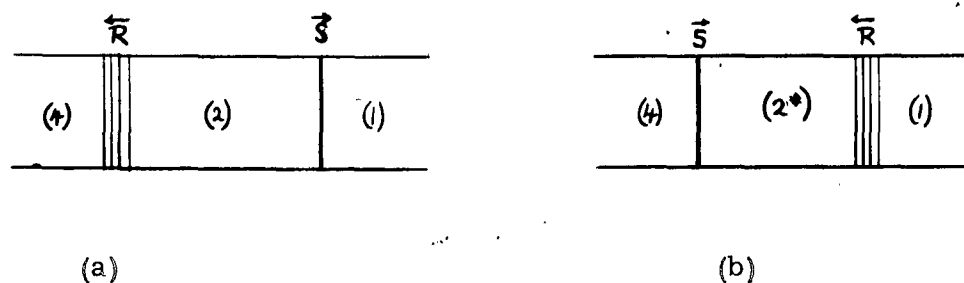


FIGURE 10

POSSIBLE WAVE SYSTEMS IN A SHOCK TUBE FOLLOWING THE RUPTURING OF THE DIAPHRAGM

States of the type (2*) are impossible because the two waves are approaching. This implies the existence of a pressure discontinuity at infinity at $t = 0$, which is contrary to the initial boundary condition that at $t = 0$ the pressure discontinuity is at the origin. The only physically possible solution is that given by state (2), that is, when the diaphragm is ruptured a shock moves into the low pressure state (1) and a rarefaction wave into the high pressure state (4) and a new state (2) is formed such that $P_4 > P_2 > P_1$ and $u_2 > u_4 = u_1 = 0$. It will be noted that nothing is learned about the possibility of the existence of a contact surface from the (p, u) -plane because across the contact surface p and u were assumed equal. Its existence was deduced above from entropy considerations of the shock tube problem. Thus, so far as the (p, u) -plane is concerned states (2) and (3) are equivalent.

The (p, u) -plane may be applied successfully to the analysis of complex wave interactions in one-dimensional flow (references 12, 16, 17 and 40) and its validity has been established by the excellent agreement obtained between theory and experiment where this method of analysis was utilized.

1.04 Basic Equations for the Wave System in a Shock Tube

In section 1.03 it was established that the wave system for a shock tube is as shown in figure 1. At $t = 0$ the diaphragm is at $x = 0$ and separates two infinite tubes of different thermodynamic states (4) and (1), in which the gases are at rest and in thermal equilibrium. The

diaphragm is ruptured at $t = 0$, and the position of the waves at any subsequent time $t = t_1$ is obtained from the (x, t) -plane as illustrated in figure 1. The states (3) and (2) as predicted from the (p, u) -plane analysis in the previous section have equal pressure and particle velocity. The (p, u) -plane analysis can not predict the existence of a contact surface since across it p , and u are continuous. A contact surface must be assumed for the coexistence of the two states (3) and (2) which were formed by different processes and have different densities, temperatures and entropies. This assumption has been confirmed by experimental results for weak shock waves (reference 20). On plate 1, the contact surface appears as a finite layer rather than a surface, due to the imperfect rupture of the diaphragm.

Physically a surface of this type can not exist for very long without spreading due to heat conduction and diffusion. The transition across a contact surface becomes analogous to the problem of transition through a shock front and requires a solution of a set of non-linear differential equations in heat conduction (see ref. 68).

The states (3) and (2) are assumed uniformly constant since changes of state occur only through the waves. In practice (see plate 1) this is not achieved because flow disturbances are propagated from the jagged remains of the diaphragm along the entire x -direction. The train of regular and Mach reflected waves behind the main shock wave also affects the flow behind it. This train of waves is the basic mechanism through which the initially curved primary shock wave finally becomes a plane shock wave.

The basic shock tube problem is to find the unknown flow parameters in states (3) and (2) in terms of the known quantities in the initial states (4) and (1). This may be accomplished as follows, assuming the specific heats of the gases remain constant.

Across the contact surface the velocities and pressures are the same, therefore

$$u_3 = u_2 \quad (1.56)$$

$$p_3 = p_2 \quad (1.57)$$

For a backward facing rarefaction wave from equation (1.31),

$$\frac{u_3}{a_4} = \frac{2}{\gamma_4 - 1} \left[1 - \left(\frac{p_3}{p_4} \right)^{\frac{\gamma_4 - 1}{2\gamma_4}} \right] \quad (1.58)$$

For a forward facing shock wave from equations (1.52) and (1.53) :

$$\frac{u_2}{a_1} = \left(\frac{P_2}{P_1} - 1 \right) \sqrt{\frac{2}{\gamma_1 \left[(\gamma_1 + 1) \frac{P_2}{P_1} + (\gamma_1 - 1) \right]}} \quad (1.59)$$

Consequently there are four equations for the four unknowns, u_3 , u_2 , P_3 and P_2 . It should be noted that in general $\gamma_4 \neq \gamma_1$, as the gas in the chamber may be different from the gas in the channel.

Equations (1.56) to (1.59) have the following dimensionless forms :

$$U_{34} = A_{14} U_{21} \quad (1.60)$$

$$P_{34} = P_{14} P_{21} \quad (1.61)$$

$$U_{34} = \frac{1}{\gamma_4 \beta_4} \left[1 - P_{34}^{\beta_4} \right] \quad (1.62)$$

$$U_{21} = \frac{P_{21} - 1}{\gamma_1 \sqrt{\beta_1 (\alpha_1 P_{21} + 1)}} \quad (1.63)$$

and they may be combined to form a relation between the shock pressure ratio P_{21} and the known parameters P_{14} , A_{14} , γ_4 and γ_1 which may be written as,

$$\left(P_{14} P_{21} \right)^{\beta_4} + \frac{\gamma_4}{\gamma_1} \beta_4 A_{14} (P_{21} - 1) \sqrt{\frac{1}{\beta_1 (\alpha_1 P_{21} + 1)}} - 1 = 0 \quad (1.64)$$

Since $A_{14} = \frac{\gamma_1}{\gamma_4} \sqrt{\frac{\beta_1}{\beta_4} E_{14}}$, it combines the basic gas parameters E_{14} , γ_4 and γ_1 , and equation (1.64) can be reduced to a simpler form,

$$(P_{21} - 1) \sqrt{\frac{\beta_4 E_{14}}{\alpha_1 P_{21} + 1}} + (P_{14} P_{21})^{\beta_4} - 1 = 0 \quad (1.65)$$

This equation has a complex algebraic form and an explicit solution $P_{21} = P_{21}(P_{14}, E_{14}, \gamma_4, \gamma_1)$ has not been obtained. The following form is convenient for plotting curves of equation (1.65):

$$P_{14} = \frac{1}{P_{21}} \left[1 - (P_{21} - 1) \sqrt{\frac{\beta_4 E_{14}}{\alpha_1 P_{21} + 1}} \right]^{\frac{1}{\beta_4}} \quad (1.66)$$

which gives the relation between the strength of the shock wave (P_{21}) produced in a shock tube as a function of the pressure ratio across the diaphragm (P_{14}), the specific heat ratios (γ_4, γ_1), and the internal energy ratio (E_{14}) of the gases used in the channel and the chamber.

Some interesting mathematical limits may be derived from equation (1.66). When $P_{14} = 0$ (i.e. $P_1 \rightarrow 0$ or $P_4 \rightarrow \infty$, conditions which are not realistic physically),

$$[P_{21}]_{P_{14}=0} = 1 + \frac{\alpha_1}{2\beta_4 E_{14}} + \sqrt{\frac{1}{\beta_4 \beta_1 E_{14}} + \left(\frac{\alpha_1}{2\beta_4 E_{14}}\right)^2} \quad (1.67)$$

This gives the relation for the strongest possible shock wave that may be produced in a shock tube with an infinite pressure ratio (P_{41}) across the diaphragm. It is seen that the strongest waves are produced for small values of $E_{14} = \frac{(C_v T)_1}{(C_v T)_4} = K T_{14}$, and immediately suggests the use of a combination such as H_2/A , H_2/N_2 or He/Air for the production of strong shock waves even at room temperature (E_{14} is 0.0309, 0.0735 and 0.231 for the three combinations respectively, see table 1).

For example, using the combination Air/Air at room temperature $E_{14} = 1$ and $[P_{21}]_{P_{41}=0} = 44$; for He/Air at room temperature $E_{14} = 0.231$ and $[P_{21}]_{P_{41}=0} = 132$; for H_2/N_2 at room temperature $E_{14} = 0.0735$ and $[P_{21}]_{P_{41}=0} = 574$. The advantage in using such gas combinations for the production of strong shock waves is quite evident. It is much more efficient to ignite combustible mixtures such as $.86 H_2 + .14 O_2$ (reference 29) or $.7 He + .2 H_2 + .1 O_2$ (mole fraction) in the chamber in order to produce very strong shock waves. A very large gain is obtained from the high value of T_4 . This topic will be considered in section 4.

It may be worth noting that when $E_{14} \leq 1$, a good approximation to equation (1.67) is :

$$[P_{21}]_{P_{41}=0} \approx \frac{\alpha_1}{\beta_4 E_{14}} + 1 \quad (1.68)$$

It will be noted that from equation (1.67), when $E_{14} \rightarrow 0$, $[P_{21}]_{P_{41}=0} \rightarrow \infty$, and when $E_{14} \rightarrow \infty$, $[P_{21}]_{P_{41}=0} \rightarrow 1$. The mathematical limits of $E_{14} = 0$ or $E_{14} = \infty$ are physically impossible since they imply that either the temperature $T_1 = 0$ or $T_4 = \infty$.

The criteria for strong shock waves are therefore,

- (1) A very large diaphragm pressure ratio, $P_{41} \rightarrow \infty$
- (2) A gas combination which will give a small energy ratio across the diaphragm, $E_{14} \rightarrow 0$

A graphical solution for equation (1.66) is shown on figure 11 for the case of Air/Air. It is seen that the curves occupy the region between two straight lines which pass through the point (1, 1). These lines correspond to the theoretical limiting values of E_{14} , that is, when $E_{14} = 0$, $P_{21} = P_{41}$ and when $E_{14} = \infty$, $P_{21} = 1$ regardless of the value of P_{41} , and illustrates the previous discussion on the production of strong shock waves. A similar plot is shown on figure 12 for different gas combinations at the same temperature, ($T_{14} = 1$).

GAS	Molecular Weight	γ 1 atmos. 0 - 25°C	$\alpha = \frac{\gamma+1}{\gamma-1}$	$\beta = \frac{\gamma-1}{2\gamma}$	C_v cal/gm/°c	μ Viscosity (micropoise)	n Index of Refraction	Boiling Point °C	Toxic Properties
Air	28.8	1.404	5.95	0.144	0.172	185	1.00029		
Argon	39.94	1.667	4.00	0.200	0.075	222	1.00028	-185.7	
CO ₂	44.01	1.300	7.67	0.115	0.151	150	1.00045	-78.5	Toxic
CCl ₄	153.84	1.130	16.38	0.058	0.1167	100	1.00018	76.8	
-chloride									
C ₃ H ₈	72.15	1.086	24.3	0.039	0.416	67	1.00017	28	
Isopentane									
C ₂ H ₆	30.05	1.22	10.09	0.090	0.316	95	1.00008	-88.3	
Ethane									
C ₂ H ₄	28.03	1.255	8.84	0.102	0.2862	100	1.00072	-103.9	Toxic
Ethylene									
CCl ₂ F ₂	120.9	1.139	15.35	0.061	0.1297	123		-28	
Freon 12									
He	4.003	1.667	4.00	0.200	0.746	95	1.000035	-268.9	
Helium									
H ₂	2.016	1.407	5.91	0.145	0.173	88	1.00014	-252.8	
Hydrogen									
Kr	82.9	1.689	3.90	0.234	0.036*	246	1.00043	-152.9	
Krypton									
CH ₄	16.03	1.313	7.39	0.119	0.402	109	1.00045	-161.5	
Methane									
Ne	20.18	1.342	4.12	0.196	0.149*	312	1.00067	-245.9	
Neon									
N ₂	28.02	1.404	5.95	0.144	0.177	176	1.00030	-195.8	
Nitrogen									
Sulfur Hexafluoride	146.04	1.093	21.9	0.044	0.227	150	1.00078	-63.8	
ST ₆									
Xenon	131.3	1.667	4.00	0.200	0.023*	226	1.00070	-107.1	

* Calculated

Sources: Handbook of Physics and Chemistry
International Critical Tables
Smithsonian Tables

Duff, R.E., University of Michigan, Ann Arbor, Engineering Research Institute,
Report 51-3 (1951).

TABLE I.
PHYSICAL PROPERTIES OF GASES

1.05 Determination of Physical Quantities and Wave Speeds in a Shock Tube

Once the shock pressure ratio (P_{21}) has been determined from the given initial conditions in the tube (equation 1.66), all other quantities of the flow may be calculated.

1. Density Ratios

From equations (1.30) and (1.48),

$$\rho_{34} = \frac{\rho_2}{\rho_4} = P_{34}^{1/4} = [P_{14} P_{21}]^{1/4} \quad (1.69)$$

$$\rho_{21} = \frac{\rho_2}{\rho_1} = \frac{1 + \alpha_1 P_{21}}{\alpha_1 + P_{21}} \quad (1.70)$$

2. Speed of Sound and Temperature Ratios

$$A_{34} = \frac{a_3}{a_4} = \left[\frac{T_3}{T_4} \right]^{1/2} = T_{34}^{1/2} = P_{34}^{1/4} = [P_{14} P_{21}]^{1/4} \quad (1.71)$$

$$A_{21} = \frac{a_2}{a_1} = \left[\frac{T_2}{T_1} \right]^{1/2} = T_{21}^{1/2} = \left[\frac{P_{21} (\alpha_1 + P_{21})}{1 + \alpha_1 P_{21}} \right]^{1/2} \quad (1.72)$$

3. Velocity of the Shock Wave

By definition, for stationary flow

$$M_1 = \frac{|u_1|}{a_1} = \frac{|u_1 - w_1|}{a_1} = \frac{w_1}{a_1} = W_{11}$$

since
$$P_{21} = \frac{1 + \alpha_1 P_{21}}{\alpha_1 + P_{21}} = \frac{\alpha_1}{1 + \frac{\alpha_1 - 1}{M_1^2}}$$

therefore
$$W_{11} = [\beta_1 (1 + \alpha_1 P_{21})]^{1/2} \quad (1.73)$$

4. Particle Velocity or Contact Surface Velocity

$$U_{21} = \frac{u_2}{a_1} = \frac{(P_{21} - 1)}{\gamma_1 [\beta_1 (\alpha_1 P_{21} + 1)]^{1/2}} \quad (1.63)$$

$$U_{34} = \frac{u_3}{a_4} = \frac{1}{\gamma_4 \beta_4} [1 - (P_{14} P_{21})^{\beta_4}] = A_{14} U_{21} \quad (1.62)$$

5. Speed of Head and Tail of Rarefaction Waves

For a backward facing rarefaction wave the head and tail of the wave have the following characteristic speeds,

$$C_{44} = \frac{c_4}{a_4} = \frac{u_4 - a_4}{a_4} = -1 \quad (1.74)$$

$$C_{34} = \frac{c_3}{a_4} = \frac{u_3 - a_3}{a_4} = U_{34} - A_{34}$$

$$C_{34} = -\frac{1}{\beta_4 \gamma_4} [1 - (P_{14} P_{21})^{\beta_4}] - [P_{14} P_{21}]^{\beta_4} \quad (1.75)$$

6. Local Mach Numbers

$$M_3 = \frac{u_3}{a_3} = \frac{U_{34}}{A_{34}} = \frac{1}{\beta_4 \gamma_4} [(P_{14} P_{21})^{\beta_4} - 1] \quad (1.76)$$

$$M_2 = \frac{u_2}{a_2} = \frac{U_{21}}{A_{21}} = \frac{(P_{21} - 1)}{\gamma_1 [\beta_1 P_{21} (\alpha_1 + P_{21})]^{1/2}} \quad (1.77)$$

It is of interest to examine the mathematical limits of the above relations for very strong shock waves. The values appear in table 2 for three gas combinations in the shock tube. In all cases considered in table 2, the diaphragm pressure ratio $P_{41} = p_4/p_1$ is taken as infinity, that is, p_1 is of order zero by comparison with the magnitude of p_4 . For Air/Air, when $E_{14} = 1$, the limiting shock strength $P_{21} = 44$, the pressure ratio across the rarefaction wave $P_{34} = 0$ and the speeds of the tail of the rarefaction wave, the particle velocity in state (3) and (2) are respectively $C_{34} = U_{34} = U_{21} = 5$, the escape speed. In other words, the tail of the rarefaction wave coincides with the contact surface and state (3) is non-existent. At a first glance it appears as if the conditions in the shock tube are violated at the contact surface, since on the one hand a complete centred rarefaction wave results from the assumption of $P_{41} = \infty$, and on the other hand the results show that a shock wave pressure ratio $P_{21} = 44$ exists. It is recalled that the shock tube equation was developed on the conditions that $p_3 = p_2$ and $u_3 = u_2$, exist at the contact surface. By assuming that $P_{41} = p_4/p_1 = \infty$, then $P_{34} = P_{14}P_{21}$ or $p_3/p_4 = p_1/p_4$ has in it an assumption with regard to the order of magnitude, that is, p_2, p_3 and p_1 are zero by comparison with p_4 , and this tends to violate the initial conditions that $p_3 = p_2 \neq 0$. Therefore, the results from the basic shock tube equation will apply except for the error in the order of magnitude introduced by $p_1/p_4 = \infty$. Thus, even if $p_4/p_1 = 44$,

$P_{34} = P_{14}P_{21}$ still applies because p_1/p_4 is also of order zero.

Physically the condition that $P_{41} = \infty$ is impossible. It could be achieved by having $p_1 = 0$ and p_4 finite, in which case a complete expansion wave only would result; or else $p_4 = \infty$ and p_1 finite, in which case the above discussion applies, that is, a shock is produced such that $p_2 = 44 p_1$, but whose order of magnitude by comparison to p_4 is zero. A centred rarefaction wave is also formed such that p_3 is of order zero by comparison to p_4 , and therefore the complete centred rarefaction wave solution is approached and yields the escape speed as the particle velocity as noted in table 2.

TABLE 2

Flow Quantities for Very Strong Shock Waves

(a) Case Air/Air

 $P_{14} = 0, \quad \alpha = 6, \quad \beta = \frac{1}{7}, \quad * = \text{indeterminate}$

E ₁₄	P ₂₁	Γ_{34}	A ₃₄	T ₃₄	Γ_{21}	A ₂₁	T ₂₁	W ₁₁	U ₃₄	U ₂₁	M ₃	M ₂	C ₃₄
0	∞	*	*	*	6	∞	∞	∞	*	∞	*	1.89	*
0.1	422	0	0	0	5.92	8.45	71.4	19.0	5	15.8	∞	1.87	5
1.0	44	0	0	0	5.30	2.88	8.30	6.16	5	5.0	∞	1.73	5

(b) Case He/Air

 $P_{14} = 0, \quad \alpha_1 = 6, \quad \beta_1 = \frac{1}{7}, \quad \alpha_4 = 4, \quad \beta_4 = \frac{1}{5}, \quad T_4 = T_1$

E ₁₄	P ₂₁	Γ_{34}	A ₃₄	T ₃₄	Γ_{21}	A ₂₁	T ₂₁	W ₁₁	U ₃₄	U ₂₁	M ₃	M ₂	C ₃₄
.231	132	0	0	0	5.75	4.79	23.0	10.6	3.00	8.83	∞	1.84	3

(c) Case H₂/N₂
 $P_{14} = 0, \quad \alpha = 6, \quad \beta = \frac{1}{7}, \quad T_4 = T_1$

E ₁₄	P ₂₁	Γ_{34}	A ₃₄	T ₃₄	Γ_{21}	A ₂₁	T ₂₁	W ₁₁	U ₃₄	U ₂₁	M ₃	M ₂	C ₃₄
.0735	574	0	0	0	5.94	9.82	96.5	22.2	5	18.5	∞	1.88	5

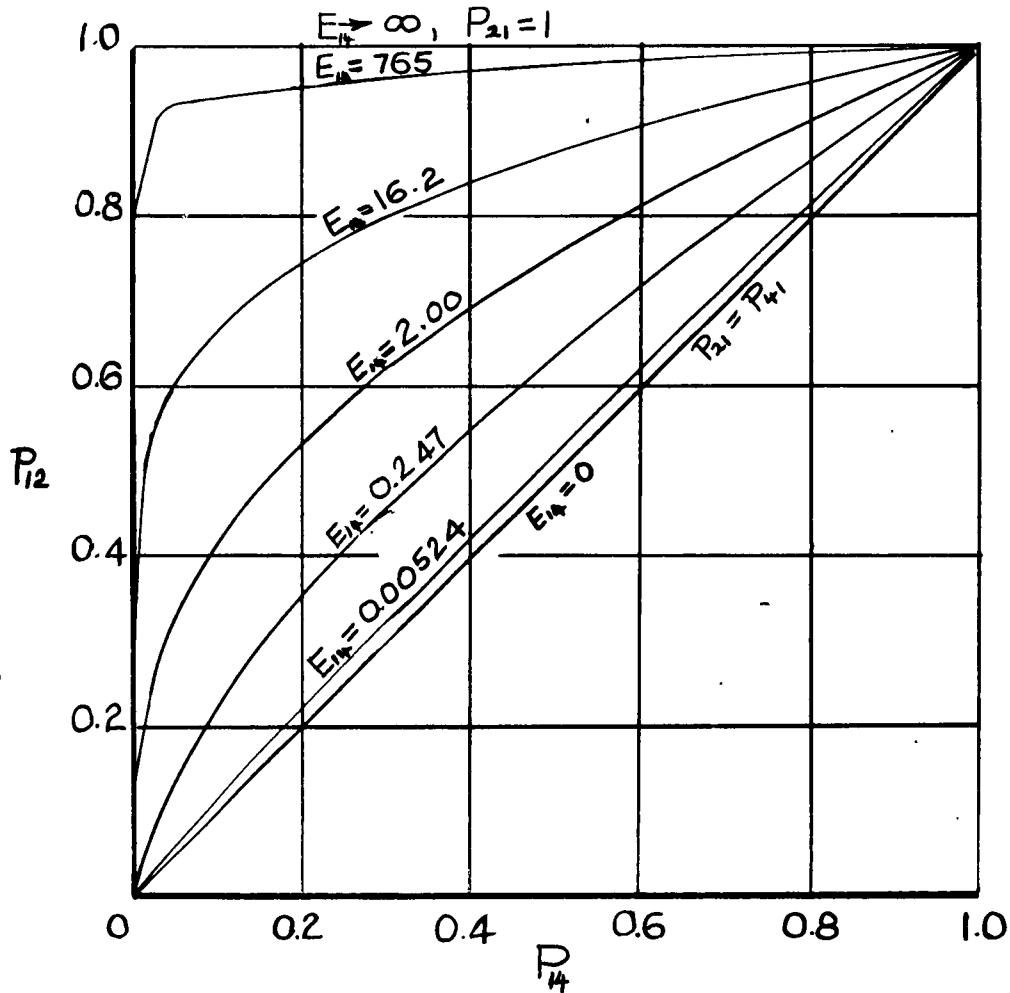


FIGURE 11.

VARIATION OF THE SHOCK PRESSURE RATIO (P_{21})
WITH THE DIAPHRAGM PRESSURE RATIO (P_{14}) AND
THE INTERNAL ENERGY RATIO (E_{14}) ACROSS THE
DIAPHRAGM. CASE Air/Air.

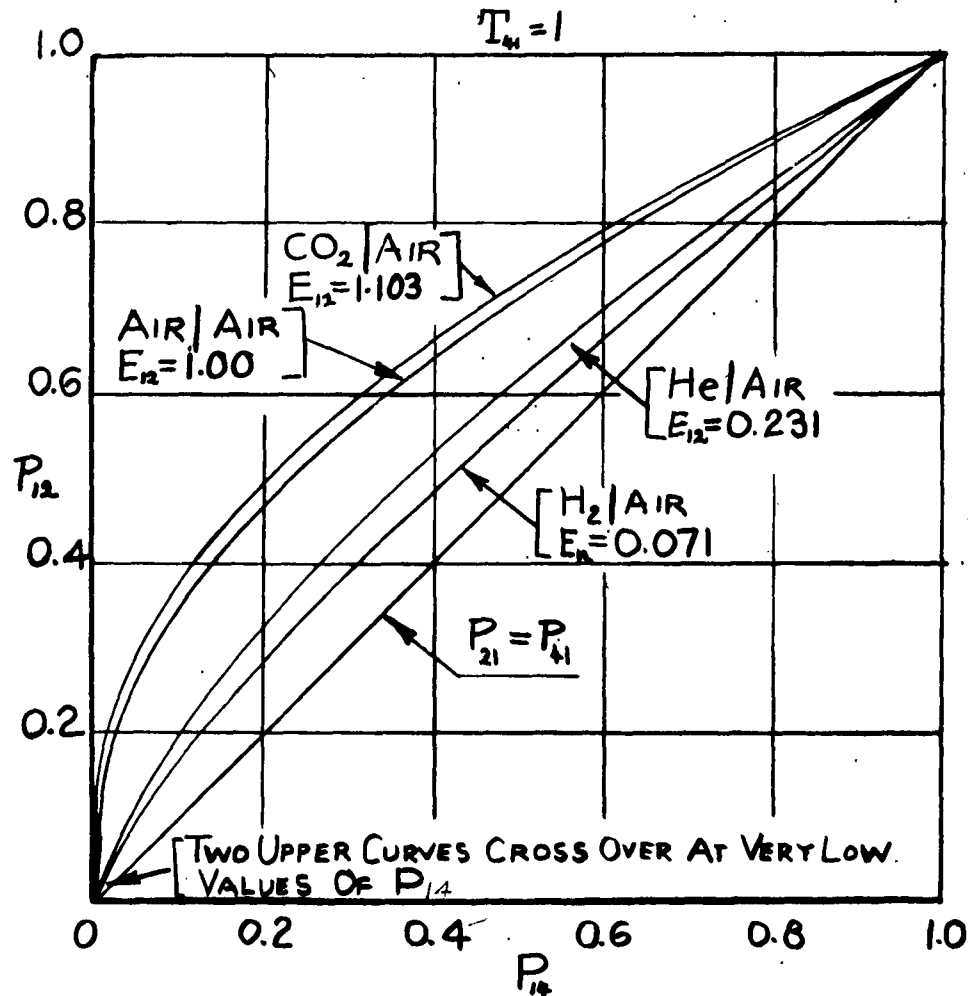


FIGURE 12.

VARIATION OF THE SHOCK PRESSURE RATIO (P_{12})
 WITH THE DIAPHRAGM PRESSURE RATIO (P_{14})
 FOR DIFFERENT GAS COMBINATIONS AT THE
 SAME TEMPERATURE ($T_{41} = 1$).

If, in addition to $P_{41} = \infty$, $E_{14} = 0$, i.e. $T_1 = 0$ or $T_4 = \infty$, then the flow quantities are as shown, for the case Air/Air. The interesting limits are for $\Gamma_2 = \rho_2/\rho_1 = 6$ and $M_2 = u_2/a_2 = 1.89$ when $P_{21} = \infty$. Again, these conditions are not attainable physically. For the case Air/Air, $E_{14} = 0.1$ could be obtained by having $T_1 = 300^\circ\text{K}$ and $T_4 = 3000^\circ\text{K}$. Assuming γ constant, then $P_{21} = 422$, $U_{34} = A_{14}U_{21} = 15.8/\sqrt{10} = 5 = C_{34}$. In this case as well, the tail of the rarefaction wave coincides with the contact surface and they move with the escape speed $(2Q_4/(\gamma_4 - 1))$ of the gas in the chamber. At room temperature (or equal temperatures in the chamber and channel) $E_{14} = 1$ for Air/Air, $E_{14} = .231$ for He/Air and $E_{14} = .0735$ for H_2/N_2 . The great advantage in using the latter two combinations for the production of strong shock waves and high values of the other flow quantities is illustrated in table 2.

If aerodynamic testing is required in the constant state regions (3) and (2) then the best type of gas to be used for the production of high Mach numbers may be obtained by differentiating equations (1.66), (1.76) and (1.77) with respect to the diaphragm pressure ratio (P_{41}), and obtaining the maximum limits when $P_{41} = 1$, that is, when very weak shock waves are produced.

$$\left. \begin{aligned} \left(\frac{\partial P_{21}}{\partial P_{41}} \right)_{P_{41}=1} &= \frac{1}{1 + \sqrt{\frac{\beta_1 E_{14}}{\beta_4}}} = \frac{1}{1 + \sqrt{B_{14} E_{14}}} \\ \left(\frac{\partial M_3}{\partial P_{41}} \right)_{P_{41}=1} &= \frac{1}{\gamma_4 \left(1 + \sqrt{\frac{\beta_4}{\beta_1 E_{14}}} \right)} = \frac{1}{\gamma_4 \left(1 + \sqrt{\frac{1}{B_{14} E_{14}}} \right)} \\ \left(\frac{\partial M_2}{\partial P_{41}} \right)_{P_{41}=1} &= \frac{1}{\gamma_1 \left(1 + \sqrt{\frac{\beta_1 E_{14}}{\beta_4}} \right)} = \frac{1}{\gamma_1 \left(1 + \sqrt{B_{14} E_{14}} \right)} \end{aligned} \right\} \quad (1.78)$$

where $B_{14} = \beta_1/\beta_4$

A comparison of the above derivatives when $P_{41} = 1$ gives a good indication, over most of the range, of the important parameters required for the production of strong shock waves and high Mach number flows. The derivative $\left(\frac{\partial P_{21}}{\partial P_{41}}\right)_{P_{41}=1}$ shows that the greatest increase in shock strength with an increase in the diaphragm pressure ratio occurs when $E_{14} \rightarrow 0$ (i.e. $P_{21} = P_{41}$, see figure 11). For strong shocks the product $(BE)_{14}$ must be made small by an appropriate choice of a gas combination, say H_2/SF_6 or H_2/A .

On the other hand the derivative $\left(\frac{\partial M_3}{\partial P_{41}}\right)_{P_{41}=1}$, shows that for the production of a high Mach number flow in state (3), E_{14} should be very large. Thus there is an opposing demand in this case for a gas combination, say A/H_2 or SF_6/H_2 , which will give weak shocks. The reason for this may be seen from a plot of M_3 vs $P_{34} = P_{14}P_{21}$ (figure 13). For the production of a shock wave of reasonable strength (P_{21})

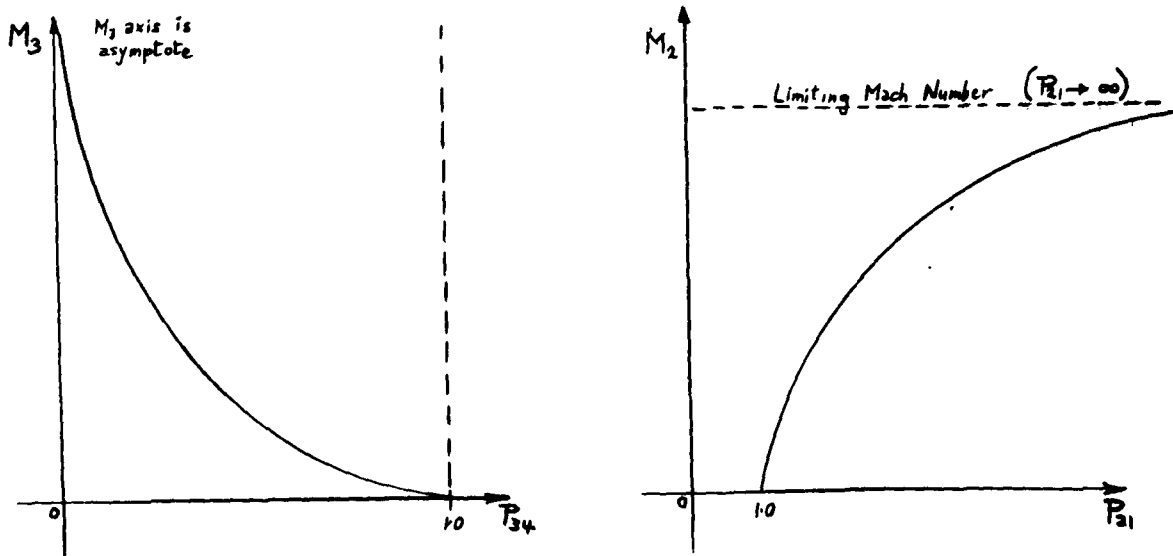


FIGURE 13.

VARIATION OF MACH NUMBER WITH PRESSURE RATIO.

it will require a very much larger diaphragm pressure ratio (P_{41}), when a gas combination is used which has a large value of E_{14} . Hence $P_{34} = P_{14}P_{21}$ is very small, and as a result M_3 is very large. Although the values of γ for real gases do not differ very radically (γ ranges from about 1.1 to 1.66), nevertheless the best result for a high Mach number flow (M_3) is obtained by using a gas combination with a large value of E_{14} and a low value of γ_4 , which also implies a large value of $(BE)_{14}$. For example $\left(\frac{\partial M_3}{\partial P_{41}}\right)_{P_{21}=1}$ is much greater for the combination SF_6/H_2 than for A/H_2 (.804 and .497 respectively). In this case the low value of γ and β for SF_6 has a telling effect. Furthermore the index of refraction of SF_6 is considerably greater than that of A and is a useful asset for optical studies of the flow, (see figure 15 and 16).

The derivative $\left(\frac{\partial M_2}{\partial P_{41}}\right)_{P_{21}=1}$ shows that for high Mach number flows in state (M_2) it is important to use a gas combination with a low value of BE_{14} and a low value of γ_1 . Combinations such as H_2/A and H_2/SF_6 are very useful for the production of strong shocks and high Mach number flow behind the shock wave. The combination H_2/SF_6 is much better than H_2/A since it has a higher $\left(\frac{\partial M_2}{\partial P_{41}}\right)_{P_{21}=1}$ value (.804 and .497 respectively). Also for SF_6 $M_2 \text{ max.} = 4.36$ as compared to $M_2 \text{ max.} = 1.34$ for argon. However, the combination H_2/A is useful for the production of strong shock waves in a monatomic gas (A), since it is not affected by dissociation at tens of thousands of degrees Kelvin and ionization phenomena may be studied much more readily.

The variation of M_2 with P_{14} and E_{14} is shown for Air/Air on figure 14, and for M_3 on figure 15. The effect of different gas combinations on M_3 appears on figure 16.

Although the above curves are useful for illustrating the range of the parameters involved in the shock tube problem they cannot be utilized too readily for experimental comparisons. As a result the curves are replotted so that they may be applied to actual problems. Figure 17 shows the variation of P_{41} vs P_{21} for the case Air/Air, $T_{14} = 1$. Figure 18 shows the variation of P_{41} vs P_{21} for He/Air, $T_{14} = 1$. The relations for the wave speeds in Air/Air as a function of shock pressure ratio (P_{21}) and diaphragm pressure ratio (P_{41}) appear

in figures 19 and 20. The variation of the flow parameters in regions (3) and (2) as a function of shock strength (P_{21}) are shown on figures 21 and 22. The above graphs make it possible to determine quickly the flow parameters in a shock tube as a function of shock strength (P_{21}) diaphragm pressure ratio (P_{41}) or shock wave Mach number (W_{11}). Similar curves for the case He/Air are shown on figures 23 and 24.

It will be noted that the curves which give the variation of the physical quantities with shock pressure ratio (P_{21}), for air, are not extended beyond $P_{21} = 33$. The reason for this is that specific heat ratio (γ) can no longer be assumed constant, and variable specific heat must be considered. This problem is discussed in detail in Section 1.06.

In order to compare some of the experimental results obtained in various shock tubes on shock wave attenuation, boundary layer growth, shock-boundary-layer interactions and model tests in the uniform state regions, it is necessary to maintain dynamic similarity, and the Reynolds number becomes one of the important non-dimensional parameters. Strictly speaking, this implies that for two flows the Reynolds number for corresponding points in the flow must be identical, in order to achieve dynamic similarity. Since the flow in a shock tube is assumed as one-dimensional, a typical length dimension is not readily available, unless the shock thickness or the mean free path is used. (A cross-sectional dimension, boundary layer thickness or a model dimension could also be used for real flows.) However, for any point in the flow the mean free path may readily be utilized as a fundamental length parameter and the Reynolds number is given then by the relation:

$$R_\lambda = \frac{\rho u \lambda}{\mu}$$

where ρ = gas density

u = mass motion of the gas or the free stream velocity

λ = equilibrium molecular mean free path of the gas

μ = gas viscosity

From the kinetic theory of gases

$$\mu = 0.499 \rho \bar{c} \lambda$$

where \bar{c} = the mean molecular velocity

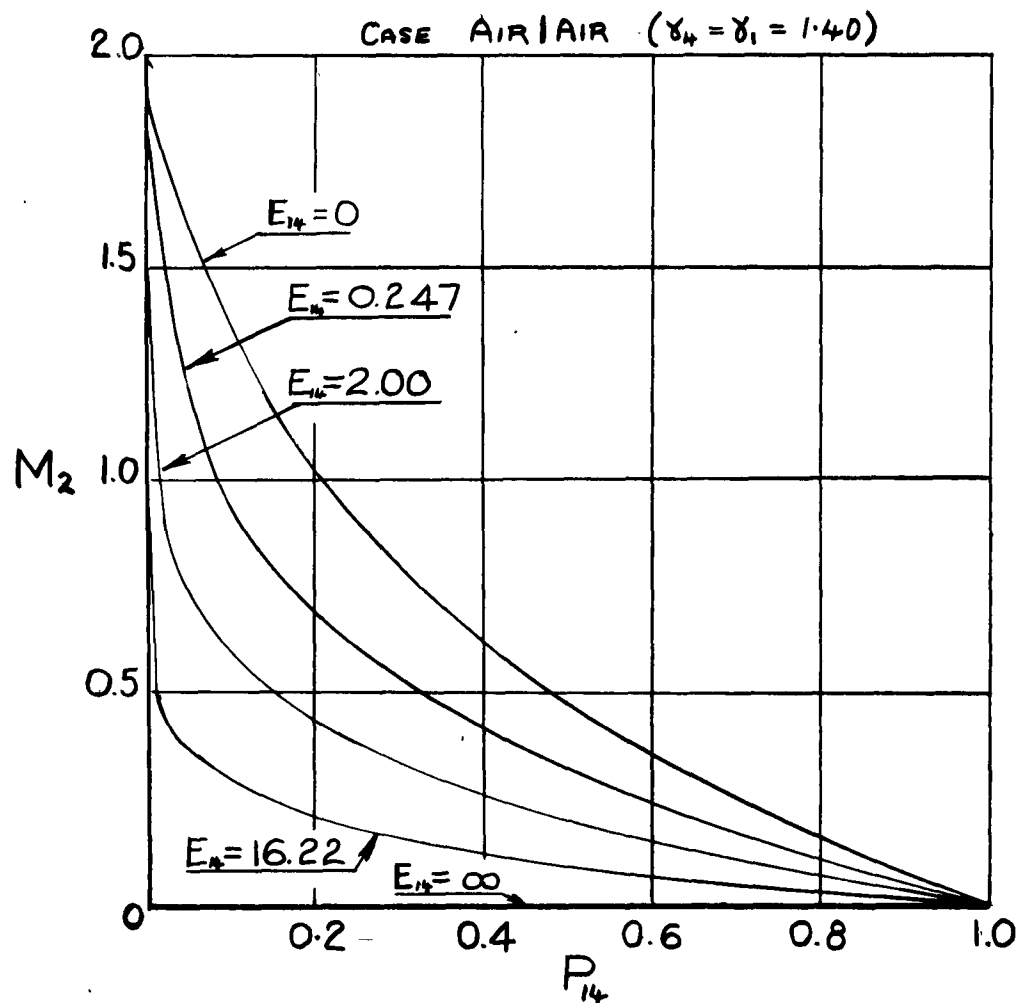


FIGURE 14.

VARIATION OF MACH NUMBER IN STATE (2) WITH
THE DIAPHRAGM PRESSURE RATIO (P_{14}) FOR
DIFFERENT INTERNAL ENERGY RATIOS (E_{14})
ACROSS THE DIAPHRAGM.

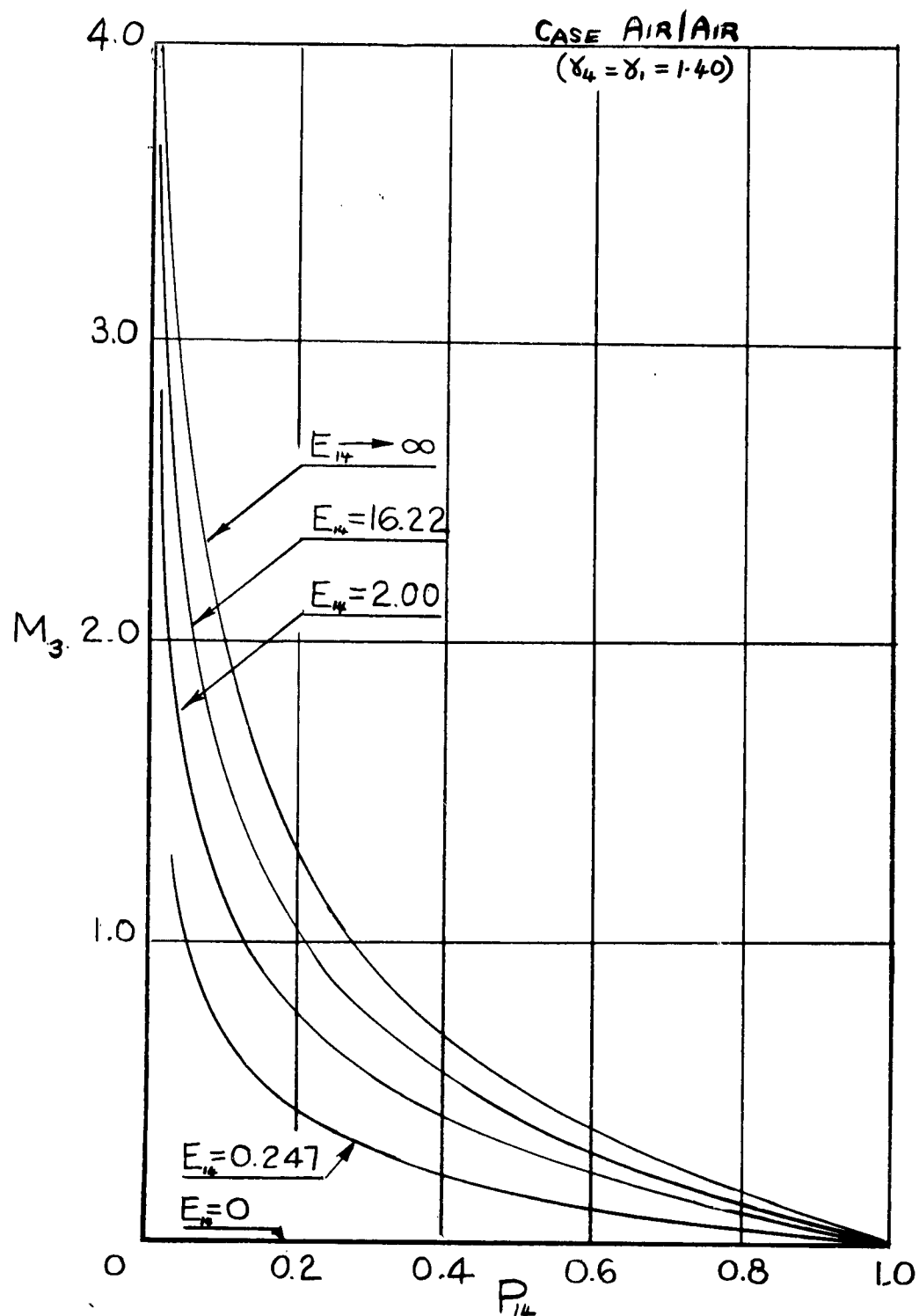


FIGURE 15.

VARIATION OF MACH NUMBER IN STATE (3)
WITH THE DIAPHRAGM PRESSURE RATIO (P_{14})
FOR DIFFERENT ENERGY RATIOS (E_{14})
ACROSS THE DIAPHRAGM

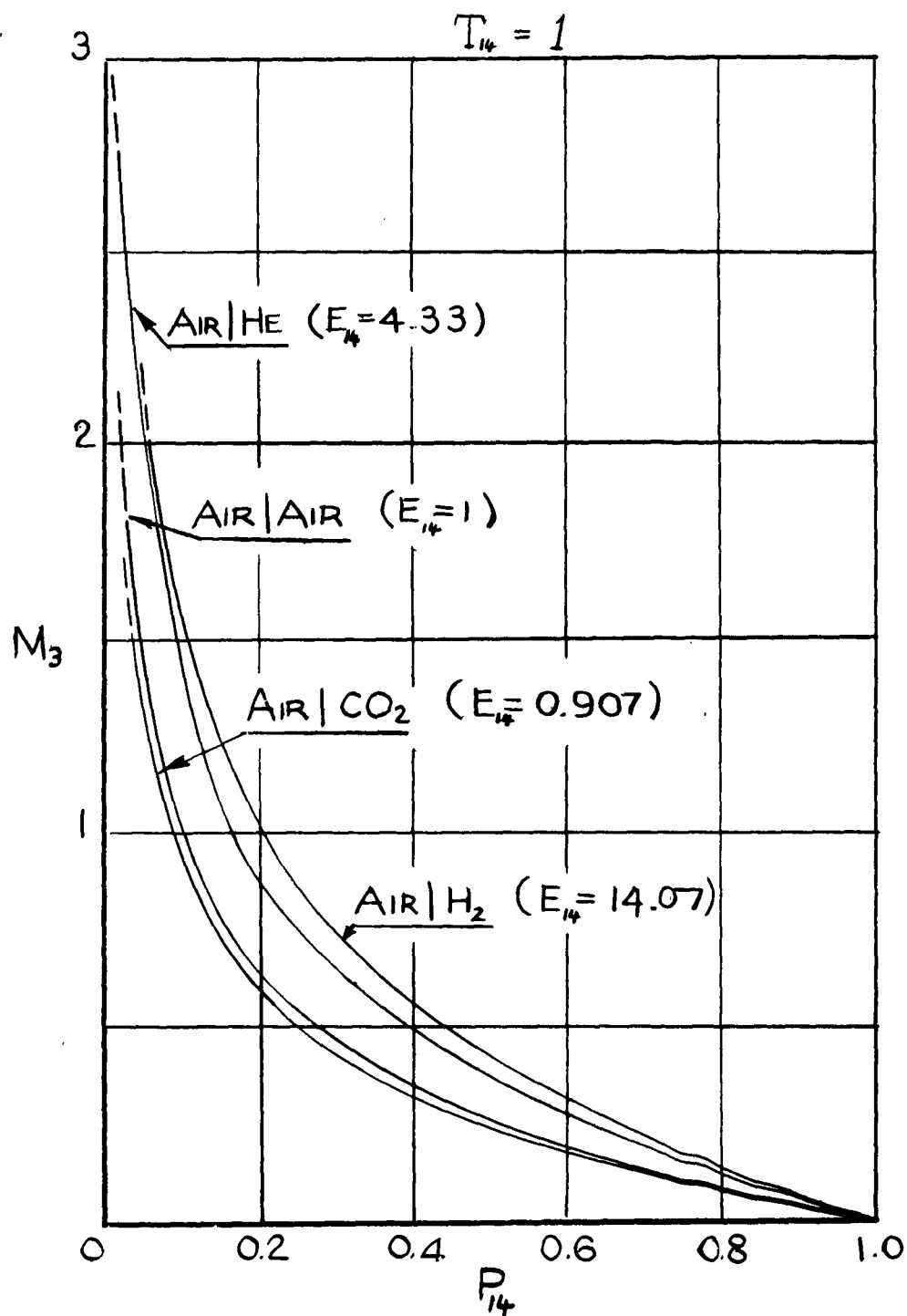
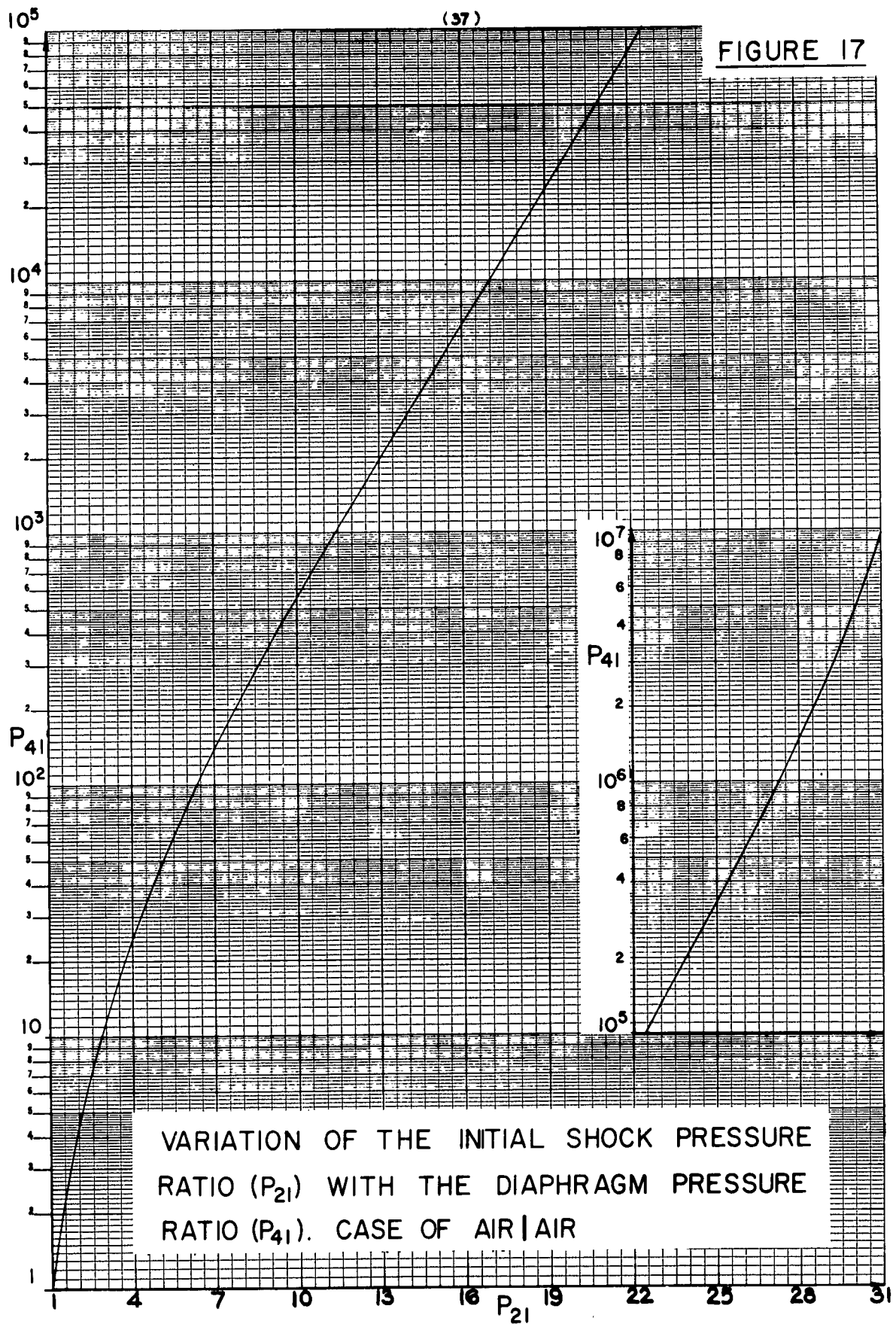
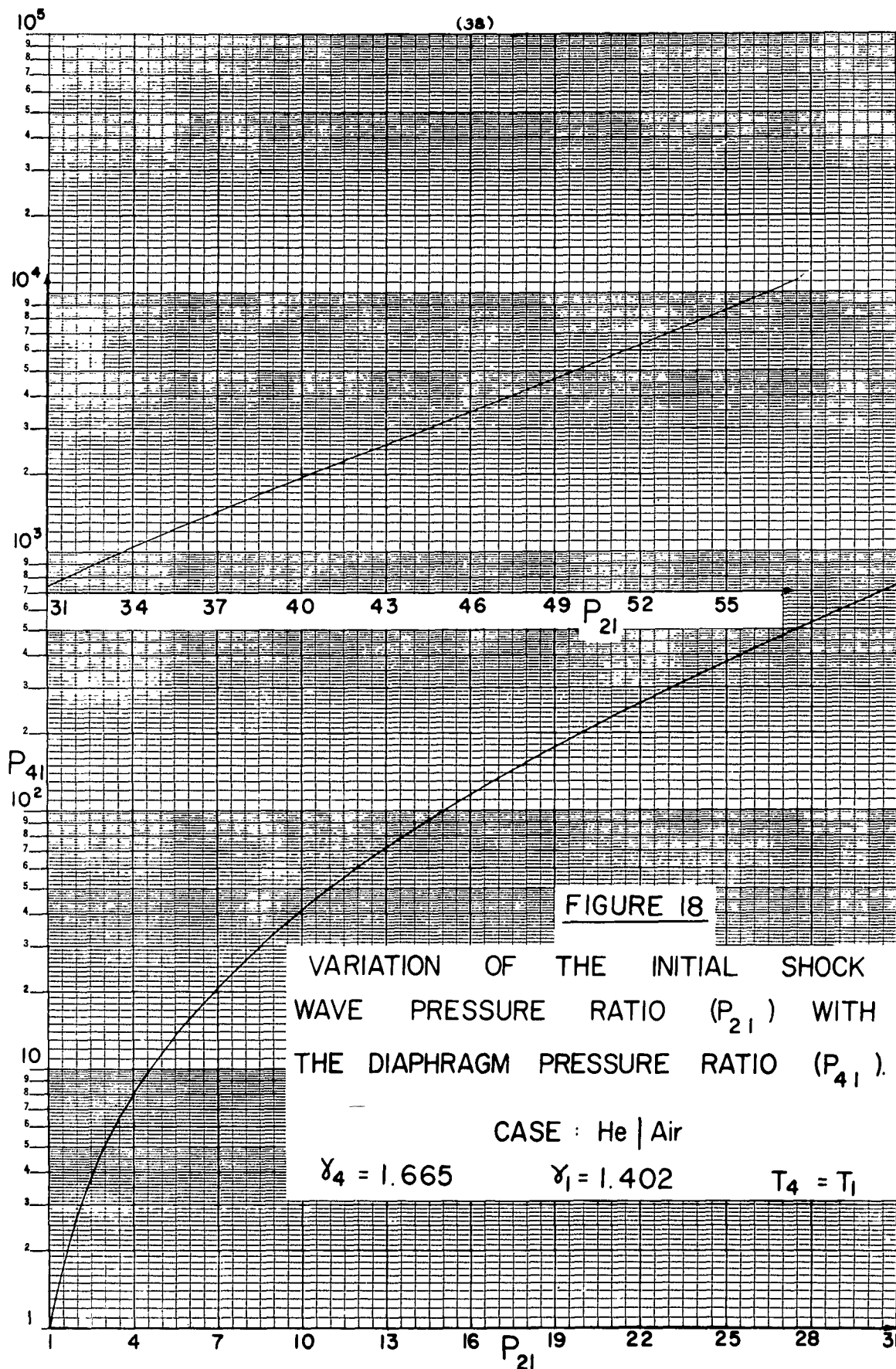


FIGURE 16.

VARIATION OF MACH NUMBER IN STATE (3)
WITH DIAPHRAGM PRESSURE RATIO (P_{14})
AND INTERNAL ENERGY RATIO (E_{14})
ACROSS THE DIAPHRAGM AT $T_{14} = 1$.



(38)



VARIATION OF INITIAL SHOCK WAVE VELOCITY
 (W_{11}), PARTICLE VELOCITY (U_{21}), & RAREFACTION
 FRONT VELOCITIES (C_{34} & C_{44}) WITH THE
 INITIAL SHOCK PRESSURE RATIO (P_{21}).

CASE: Air | Air

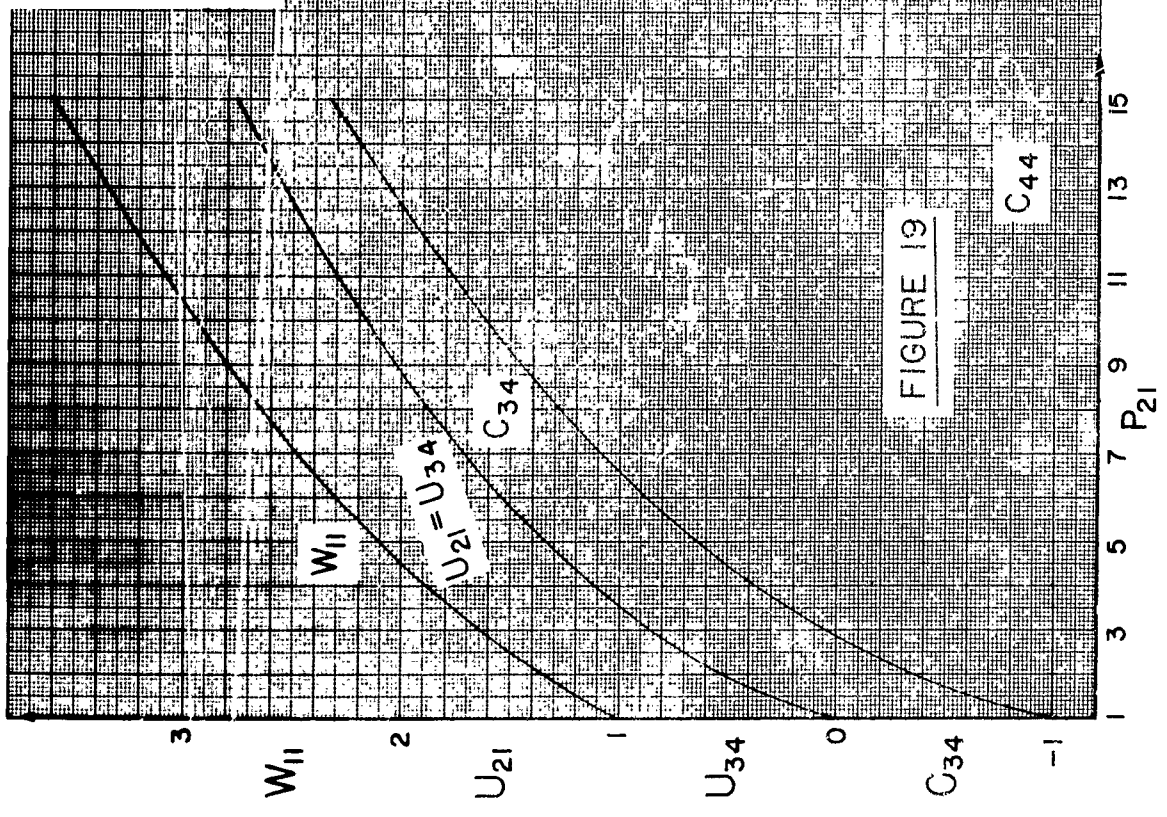
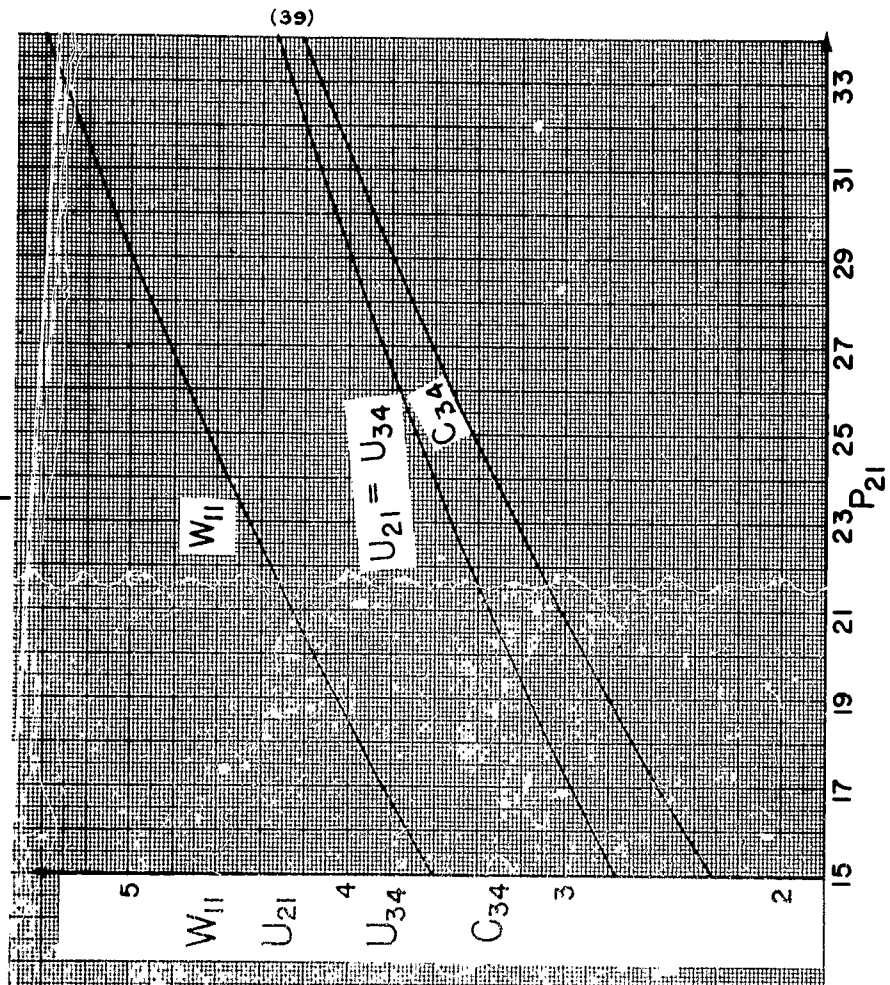


FIGURE 19



10⁵

(40)

FIGURE 20

10⁴

10³

P₄₁

10²

10

-1.2

-0.6

0

0.6

W₁₁

1.2

U₂₁

1.8

C₃₄

2.4

C₄₄

3.0

3.6

4.2

4.8

VARIATION OF INITIAL SHOCK
WAVE VELOCITY (W_{11}), PARTICLE
VELOCITY (U_{21}), & RAREFACTION
FRONT VELOCITIES (C_{44} & C_{34})
WITH THE PRESSURE RATIO
(P_{41}) ACROSS THE DIAPHRAGM.

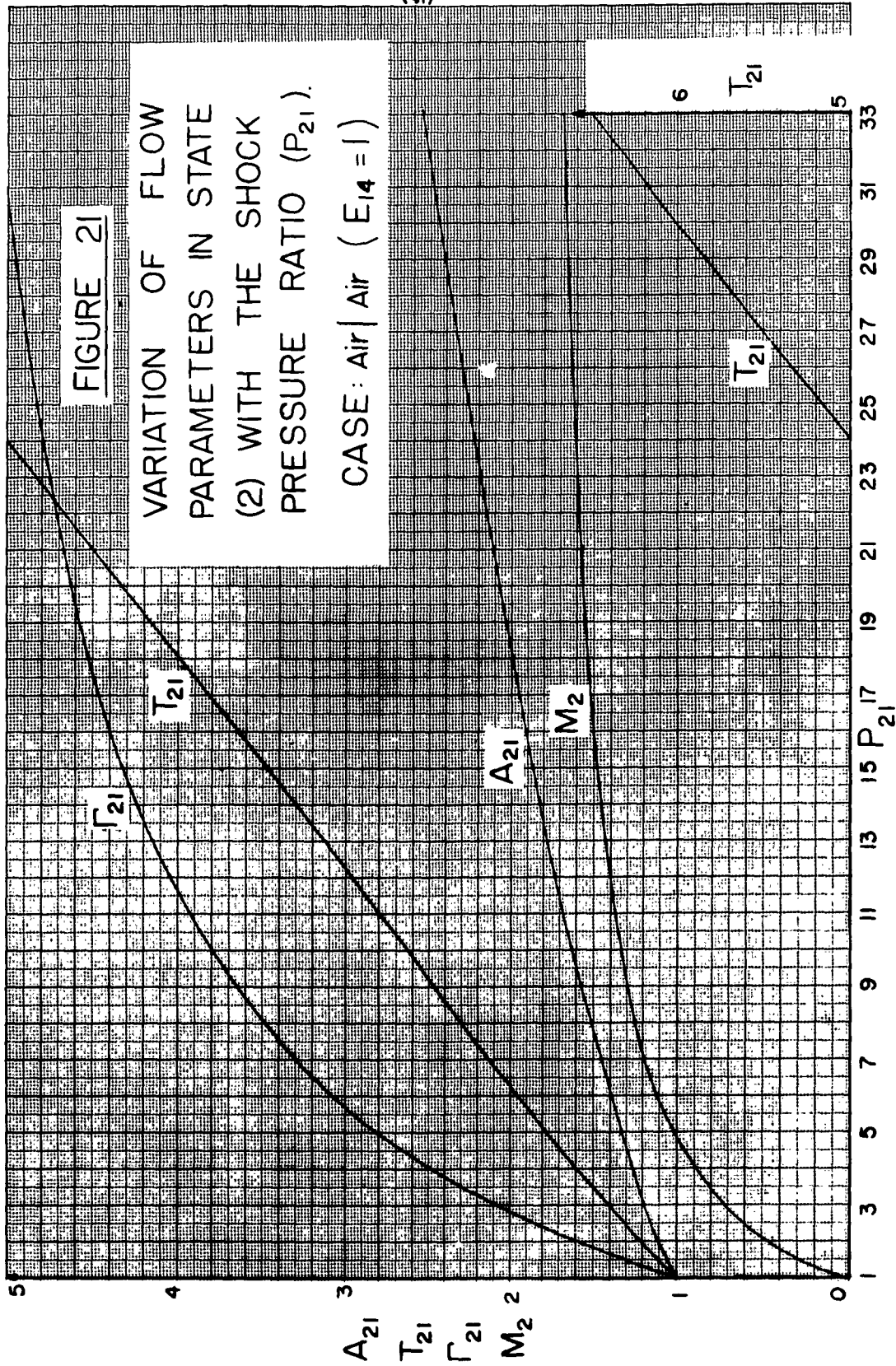
CASE: Air|Air

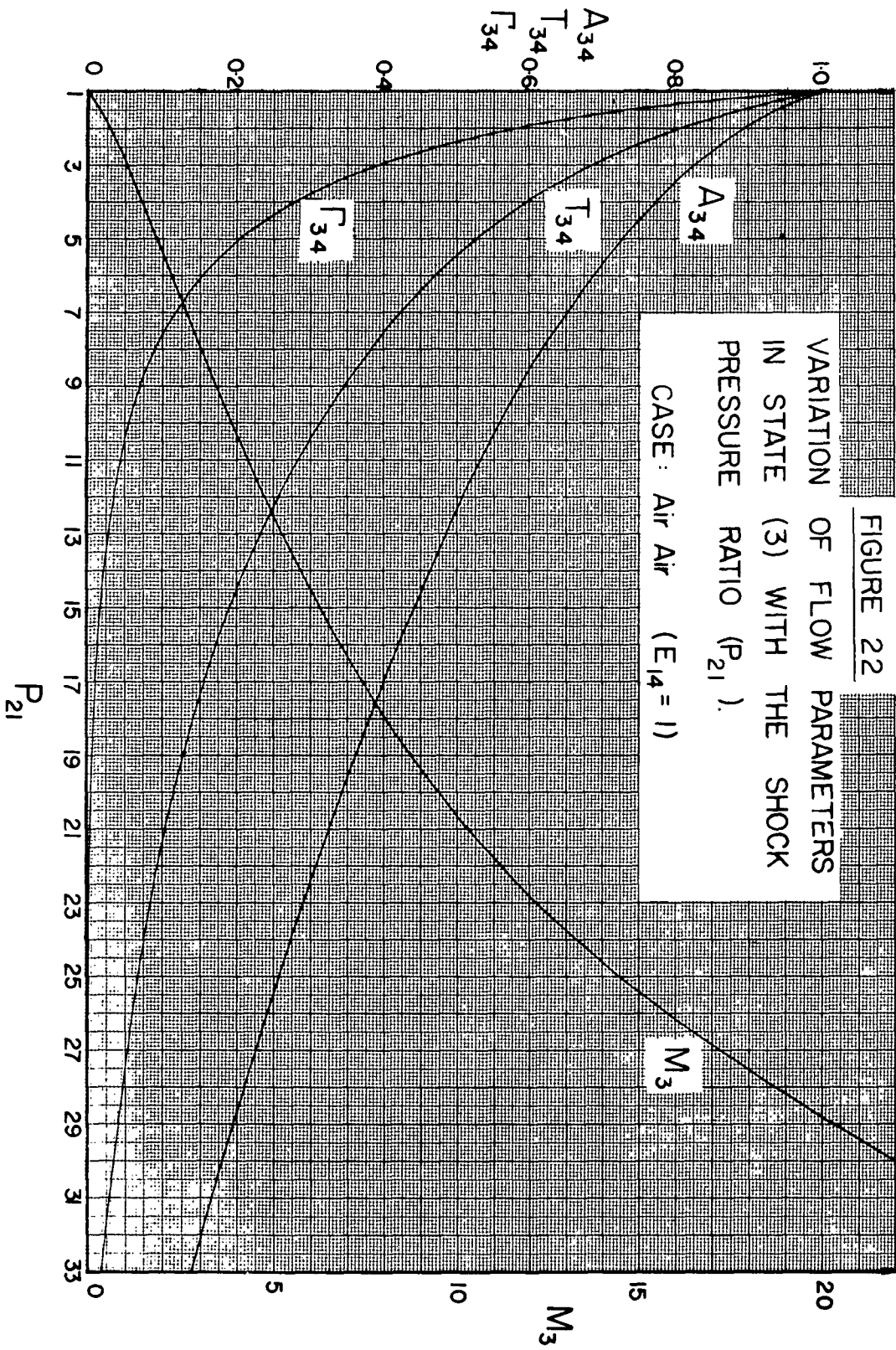
C₄₄

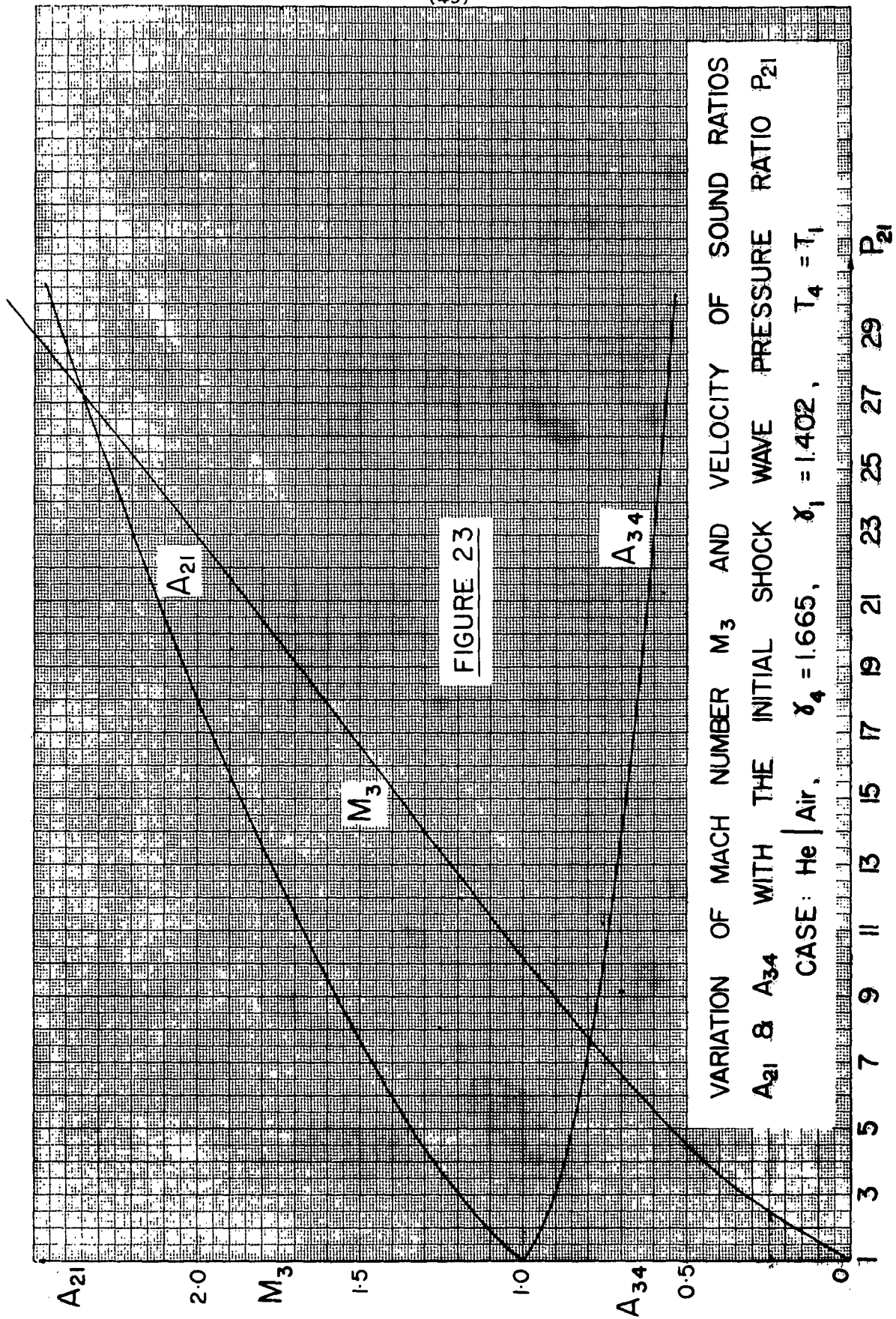
C₃₄

U₂₁

W₁₁





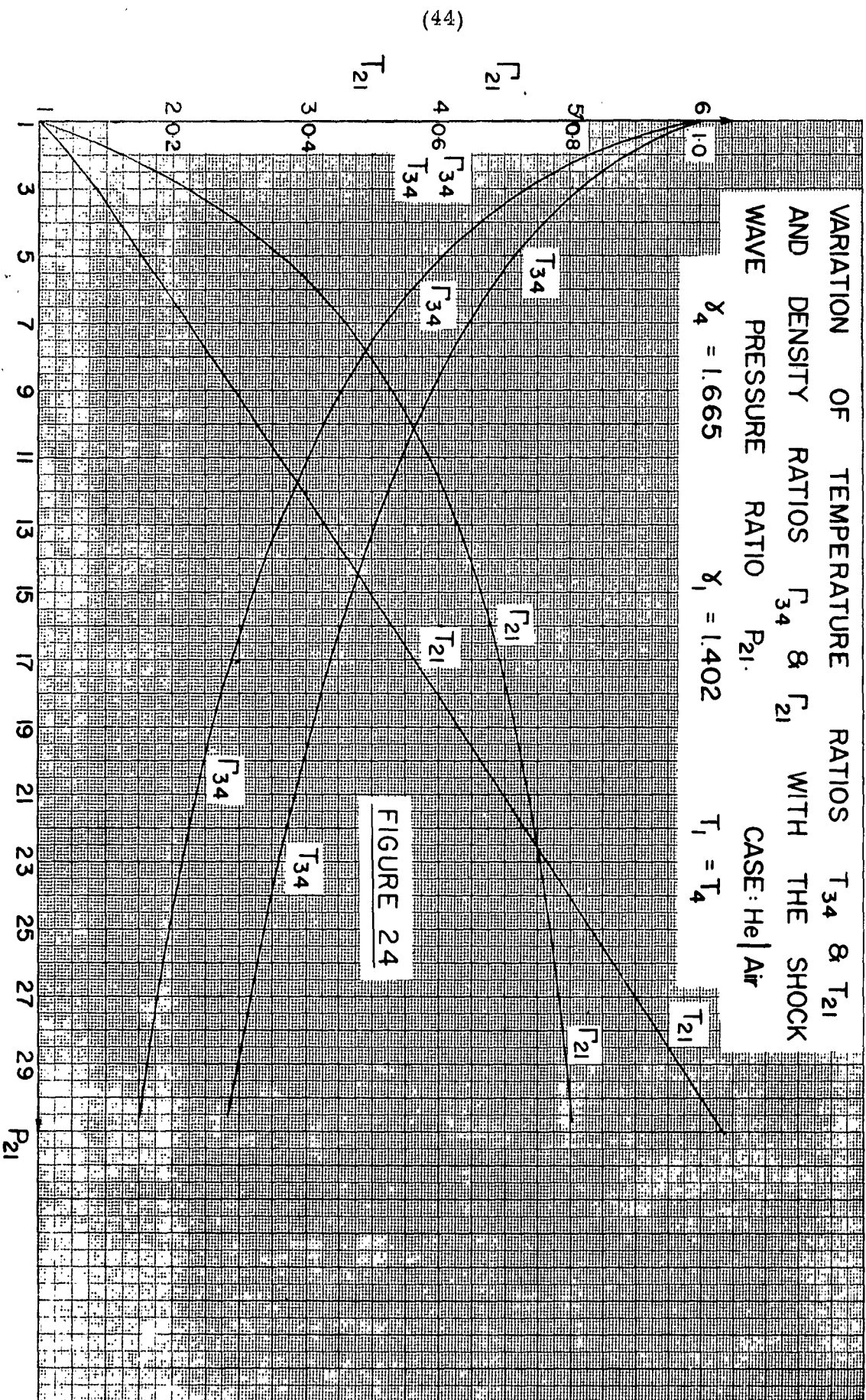


VARIATION OF TEMPERATURE RATIOS T_{34} & T_{21}
 AND DENSITY RATIOS Γ_{34} & Γ_{21} WITH THE SHOCK
 WAVE PRESSURE RATIO P_{21} .
 CASE: He | Air

$$\gamma_4 = 1.665$$

$$\gamma_1 = 1.402$$

$$T_1 = T_4$$



$$\text{or } \bar{c} = \sqrt{\frac{8}{\pi \gamma}} a$$

where a = speed of sound of the gas

γ = specific heat ratio C_p/C_v

Hence $R_\lambda = 1.486 M$, and for isentropic flow, the Reynolds number at a point depends only on Mach number. The form that the Reynolds number usually takes is,

$$Re = \frac{R_\lambda}{\lambda/l} = 1.486 \left(\frac{M}{K} \right)$$

where $K = \lambda/l$, Knudsen number.

l = an arbitrary linear dimension which fixes the scale.

For most shock tube work the Knudsen number is very small, and in order to compare the Reynolds numbers in the uniform state regions (2) and (3), the Reynolds number per foot is arbitrarily used and is given by, $\frac{Re}{l} = \frac{\rho u}{\mu}$. Thus, for state (3),

$$\left(\frac{Re}{l} \right)_3 = \frac{\rho_3 u_3}{\mu_3} \quad (1.79)$$

$$\text{or } \left(\frac{Re}{l} \right)_3 = \frac{\gamma_4}{\mu_4 a_4} P_4 P_1 \frac{\Gamma_{34} U_{34}}{T_{34}^{.76}} \quad (1.80)$$

where the viscosity as a function of temperature is assumed as

$$\frac{\mu_3}{\mu_4} = T_{34}^{.76} \quad (1.81)$$

$$\text{Similarly } \left(\frac{Re}{l} \right)_2 = \frac{\gamma_1 P_1}{\rho_1 \mu_1} \frac{\Gamma_{21} U_{21}}{T_{21}^{.76}} \quad (1.82)$$

TABLE 3

Reynolds Number Per Foot in States (2) and (3), $T_1 = T_4 = 288^\circ\text{K}$ $p_1 = 1 \text{ mm. Hg.}$

P_{41}	P_{21}	f_{21}	f_{34}	T_{21}	T_{34}	U_{21}	$\left(\frac{Re}{L}\right)_2$	$\frac{(Re)_3}{(Re)_2}$
1	1.0	1.000	1.00	1.00	1.00	0	0	1.00
10	2.80	2.013	.420	1.387	.700	.81	11950	3.52
100	6.35	3.15	.142	2.025	.455	1.62	28300	14.0
1,000	11.4	3.96	.040	2.875	.225	2.35	39200	62.1
10,000	17.0	4.45	.010	3.825	.159	2.96	44700	255

For the case Air/Air, the Reynolds number ratio is

$$\frac{(Re)_3}{(Re)_2} = P_{41} \frac{\Gamma_{34}}{\Gamma_{21}} \left(\frac{T_{21}}{T_{34}} \right)^{0.76} \quad (1.83)$$

Assuming an initial temperature in the shock tube of 15° C, and a pressure in the channel $p_1 = 1$ mm. Hg., then,

$$T_1 = T_4 = 288^\circ \text{ K}$$

$$a_1 = a_4 = 1117 \text{ f.p.s.}$$

$$\mu_1 = \mu_4 = 3.7194 \times 10^{-7} \text{ slugs per ft. sec.}$$

$$\rho_1 = 3.13 \times 10^{-6} \text{ slugs per cu. ft.}$$

$$p_1 = 1 \text{ mm. Hg.}$$

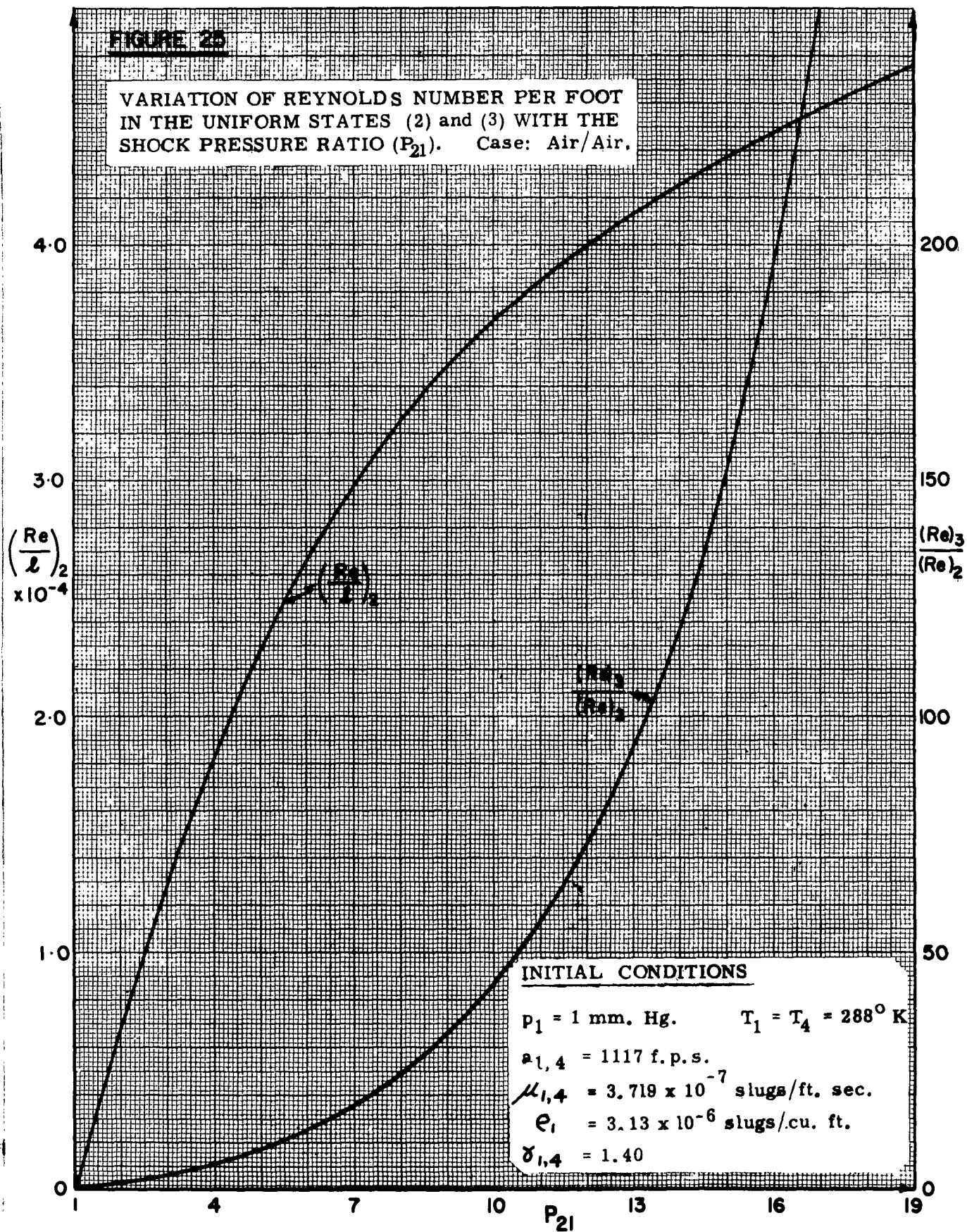
and the variation of the Reynolds number per foot in state (2) and the Reynolds number ratio with diaphragm pressure ratio (P_{41}), is as shown in table 3 and plotted in figure 25.

It is seen that even at a low channel pressure ($p_1 = 1$ mm. Hg.) the Reynolds number per foot is sizeable. The Reynolds number per foot in state (3) is considerably greater than in state (2), and the ratio $\frac{(Re)_3}{(Re)_2}$ increases with increasing diaphragm pressure ratio. Thus by varying the channel pressure (p_1) and the diaphragm pressure ratio (P_{41}), it is possible to get a large range of Reynolds and Mach numbers in a shock tube for aerodynamic testing in the uniform state regions. Although theoretically region (3) has the larger Mach and Reynolds number range, in practice this region passes over the jagged remains of the diaphragm and is found to be quite turbulent, and perhaps may not be as useful for testing purposes as state (2). However, preliminary work conducted in state (3) (reference 27) indicates that high Mach numbers and uniform flow can be achieved.

In order to illustrate the variation of the physical and thermodynamic quantities of the flow in a shock tube as derived from the previous equations, figure 26 is included for a specific case. The flow properties along the tube are shown for an initial tube temperature

FIGURE 25

VARIATION OF REYNOLDS NUMBER PER FOOT
IN THE UNIFORM STATES (2) and (3) WITH THE
SHOCK PRESSURE RATIO (P_{21}). Case: Air/Air.



of 288°K, a channel pressure $p_1 = 100$ mm. Hg., a diaphragm pressure ratio $P_{41} = 20$, case Air/Air, for $t_1 = 1000 \mu$ sec. after rupturing the diaphragm. The pressure (p), density (ρ), temperature (T), particle velocity (u), Mach number (M) Reynolds number (Re), entropy ($\frac{A}{C_p}$), and the conserved flow parameters $C_p T_0$ and $\frac{2}{\gamma_4 - 1} a_4$ are shown along the tube length (x). The actual values of the quantities are also given and were obtained from the previous graphs.

The transition values through the rarefaction wave may be determined as follows :

By introducing a dimensionless parameter

$$n = \frac{x}{a_4 t} = U_{34} - A_{34} \quad (1.84)$$

equations (1.32) take the following form

$$\left. \begin{aligned} \frac{a}{a_4} &= \left[1 - \frac{\gamma_4 - 1}{\gamma_4 + 1} (n + 1) \right] \\ \frac{T}{T_4} &= \left[1 - \frac{\gamma_4 - 1}{\gamma_4 + 1} (n + 1) \right]^2 \\ \frac{p}{p_4} &= \left[1 - \frac{\gamma_4 - 1}{\gamma_4 + 1} (n + 1) \right]^{\frac{2}{\gamma_4 - 1}} \\ \frac{\rho}{\rho_4} &= \left[1 - \frac{\gamma_4 - 1}{\gamma_4 + 1} (n + 1) \right]^{\frac{2\gamma_4}{\gamma_4 - 1}} \\ M &= \left[\frac{n + 1}{1 - \frac{\gamma_4 - 1}{2} n} \right] \end{aligned} \right\} \quad (1.85)$$

Differentiating the above relations with respect to n , or perpendicular to the characteristic lines,

$$\left. \begin{aligned} \frac{da}{dn} &= - \frac{\gamma_4 - 1}{\gamma_4 + 1} a_4 \\ \frac{du}{dn} &= \frac{2}{\gamma_4 + 1} a_4 \end{aligned} \right\} \quad (1.86)$$

$$\left. \begin{aligned}
 \frac{dT}{dn} &= -\frac{2(\gamma_4-1)}{\gamma_4+1} T_4 \left[1 - \frac{\gamma_4-1}{\gamma_4+1} (n+1) \right] \\
 \frac{d\rho}{dn} &= -\frac{2}{\gamma_4+1} \rho_4 \left[1 - \frac{\gamma_4-1}{\gamma_4+1} (n+1) \right]^{\frac{2-\gamma_4}{\gamma_4-1}} \\
 \frac{dp}{dn} &= -\frac{2\gamma_4}{\gamma_4+1} p_4 \left[1 - \frac{\gamma_4-1}{\gamma_4+1} (n+1) \right]^{\frac{\gamma_4+1}{\gamma_4-1}} \\
 \frac{dM}{dn} &= \frac{\gamma_4+1}{2 \left(1 - \frac{\gamma_4-1}{2} n \right)^2}
 \end{aligned} \right\} (1.86)$$

The derivatives may be evaluated quite readily at three points of interest, namely, at the head of the rarefaction wave ($n = -1$), at the point where the flow reaches a Mach number of unity ($n = 0$, $u = a$) and the tail of the rarefaction wave (i.e., where $n = U_{34} - A_{34}$).

TABLE 4a

Transition Through a Rarefaction Wave for Air/Air

n	$\frac{1}{a_4} \frac{da}{dn}$	$\frac{1}{a_4} \frac{du}{dn}$	$\frac{1}{T_4} \frac{dT}{dn}$	$\frac{1}{p_4} \frac{dp}{dn}$	$\frac{1}{p_4} \frac{dp}{dn}$	$\frac{dM}{dn}$
-1	-.166	.833	-.333	-.833	-1.166	.833
0	-.166	.833	-.278	-.402	-.390	1.200

From Tables 4a and 4b the following may be deduced :

- The profile of a given transition curve through the characteristics of the rarefaction wave is fixed by the set of initial conditions in the chamber.
- The amount that the transition curve extends toward the limiting case of a complete centred rarefaction wave depends on the initial diaphragm pressure ratio.

TABLE 4b

Transition Through a Rarefaction Wave for Air/Air

P_{41}	P_{21}	$n = \frac{u_4}{u_{34}} - A_{34}$	$\frac{1}{a_4} \frac{da}{dn}$	$\frac{1}{a_4} \frac{du}{dn}$	$\frac{1}{T_4} \frac{dT}{dn}$	$\frac{1}{P_4} \frac{dP}{dn}$	$\frac{1}{P_4} \frac{dp}{dn}$	$\frac{dM}{dn}$
4.34	2.0	-.372	-.166	.833	-.298	-.535	-.600	1.14
10.5	2.9	0	-.166	.833	-.278	-.402	-.390	1.20
46.1	5.0	.629	-.166	.833	-.242	-.233	-.174	1.57
554.	10.0	1.609	-.166	.833	-.188	-.085	-.0379	2.61
34550	20.0	2.916	-.166	.833	-.116	-.0121	-.00204	6.90
∞	44	5	-.166	.833	0	0	0	∞

(c) When an infinite diaphragm pressure ratio is used then a complete centred wave results and the transition curve is complete; that is, the density, temperature, pressure and speed of sound are zero; the particle velocity is $5a_4$ and the Mach number is infinite at the tail of the wave.

(d) For an incomplete centred rarefaction wave all the derivatives are discontinuous at the head and at the tail of the wave.

(e) For a complete centred rarefaction wave all the derivatives are discontinuous at the head of the wave. The density, temperature and pressure derivatives are zero at the tail and the curves are tangent to the n -axis. The values of the speed of sound and particle velocity derivatives are finite at the tail; and that of the Mach number is infinite (see table 4b). The transition profiles are illustrated in figure 27.

Since

$$\left(\frac{\partial}{\partial x}\right)_t = \left(\frac{\partial n}{\partial x}\right)_t \left(\frac{d}{dn}\right) \quad (1.87)$$

the above derivatives may be transformed to the (x, t) -plane by multiplying by $1/a_+ t$, that is,

$$\frac{\partial p}{\partial x} = \frac{1}{a_+ t} \frac{\partial p}{\partial n} \quad (1.88)$$

It will be noted that when $t \rightarrow 0$, the above derivatives become infinite at the origin and typifies the discontinuity of a centred rarefaction wave. When $t \rightarrow \infty$ all become zero except the Mach number derivative which is infinite. Thus there is a discontinuity at the origin which is assumed to be smoothed out at once. If the initial values in the chamber are not infinite then at an infinite time from the breaking of the diaphragm the disturbance is dissipated. The above are mathematical concepts which are not realised in actual shock tube flows because the tube is of finite length and the ruptured diaphragm does not give rise to a centred expansion wave as can be deduced from plate 1. The interesting result from table 4, is obtained from the density derivative column. It is seen that $\frac{dp}{dn}$ is of comparable order of magnitude for the head and tail of weak rarefaction waves. Therefore it might be expected that both border Mach lines of the expansion wave would appear in a schlieren photograph, since it records $\frac{\partial p}{\partial x}$. In actual flows only the head of the rarefaction wave appears in a (x, t) -plane schlieren photograph and this will be discussed in section 5.07.

Referring to figure 26, it is of interest to note that at the contact surface only the particle velocity and the pressure are continuous and all other parameters are discontinuous. Since the temperature and the density are discontinuous at the contact surface there exists a molecular transfer of heat between region (3) and (2). The transition through the contact front will consist of a solution analogous to the transition through a shock front.

It should be noted that the greatest change in entropy exists at the contact front and not at the shock front, and arises from the fact that state (4) being a region of high pressure but at the same temperature as state (1), has a very much lower entropy.

In order to solve the shock tube problem the particle velocities $u_3 = u_2$ and the pressures $p_3 = p_2$ were matched. The process for the rarefaction wave was shown to be unsteady and isentropic. The differential equations of continuity (1.1) and motion (1.2) defining this flow were not solved directly, instead, the equations of the characteristics (1.13) to (1.16)

were found. Whereas, the shock wave process was shown to be equivalent to an adiabatic steady process. The differential equations of continuity, momentum and energy were solved directly for this case. As a result of the matching of these two different flows, two conserved flow parameters appear on figure 26 at the contact surface, i.e. $C_p T_0$ and $\frac{2}{\gamma_4 - 1} a_4$. Due to the steady state process $C_p T_0 = \frac{1}{2} \omega^2 + C_p T_1$, the stagnation enthalpy, remains constant for regions (1) and (2), but due to the unsteady state process $u + \frac{2a}{\gamma_4 - 1} = \frac{2a_4}{\gamma_4 - 1}$, the constant of the ϕ family of characteristics, applies to regions (4) and (3).

It is interesting to note that the constant per unit mass for (1) and (2) is an energy constant, and for (4) and (3) a momentum constant. This anomaly along with the "escape speed" for one-dimensional unsteady ($\hat{u} = \frac{2}{\gamma - 1} a_0$) and for one-dimensional steady ($\hat{u} = \sqrt{\frac{2}{\gamma - 1}} a_0$) flows, has to date not been explained satisfactorily.

1.06 Deviations from Thermal Equilibrium in a Shock Tube

The basic equation for flows in a shock tube (1.65), was derived in section 1.05 under the assumption that the specific heat ratio (γ) remained constant. It was shown in table 2, that for very large diaphragm pressure ratios very high temperatures can be achieved in state (2) and very low temperatures in state (3). Under these extreme temperature conditions the assumption of constant specific heat is no longer valid and these deviations are considered in the present section.

(a) Flow Through a Centred Rarefaction Wave with Variable Specific Heat

It was shown in section 1.01 that the basic equations to be solved for a centred rarefaction wave were

$$(c-u) = \pm \sqrt{\frac{dp}{d\rho}} \quad (1.21)$$

$$du = \pm \sqrt{\frac{dp}{d\rho}} \frac{d\rho}{\rho} \quad (1.22)$$

Applying the first law of thermodynamics to an isentropic process, then

$$\frac{C_v dT}{T} - \frac{R d\rho}{\rho} = 0 \quad (1.89)$$

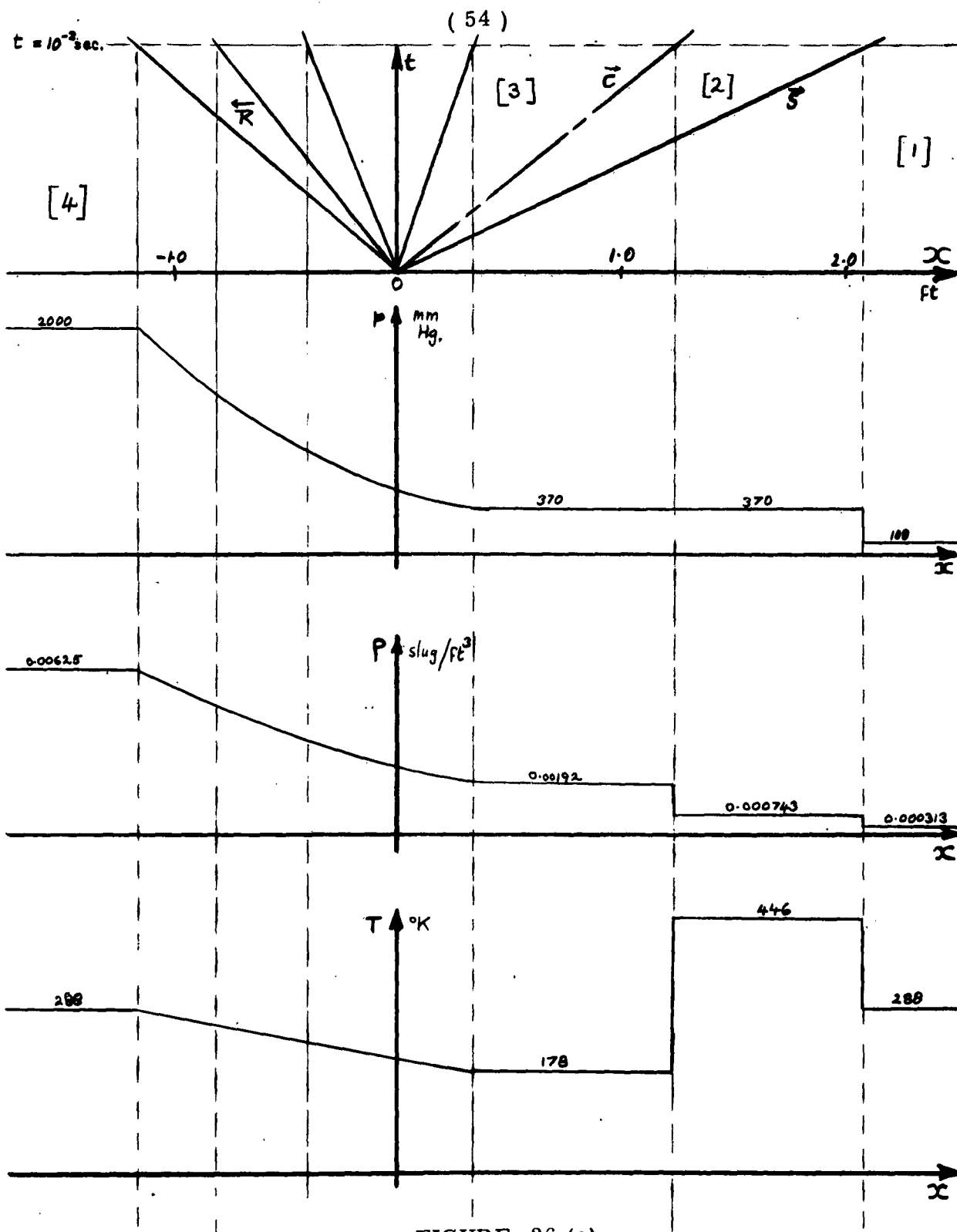


FIGURE 26 (a)

VARIATION OF FLOW PROPERTIES p , ρ , T ALONG A SHOCK TUBE
AT TIME $t = 10^{-3} \text{ sec.}$ INITIAL CONDITIONS:

$T = 288^\circ \text{ K}$, $p_1 = 100 \text{ mm. Hg.}$, $P_{41} = 20$. CASE: Air/Air.

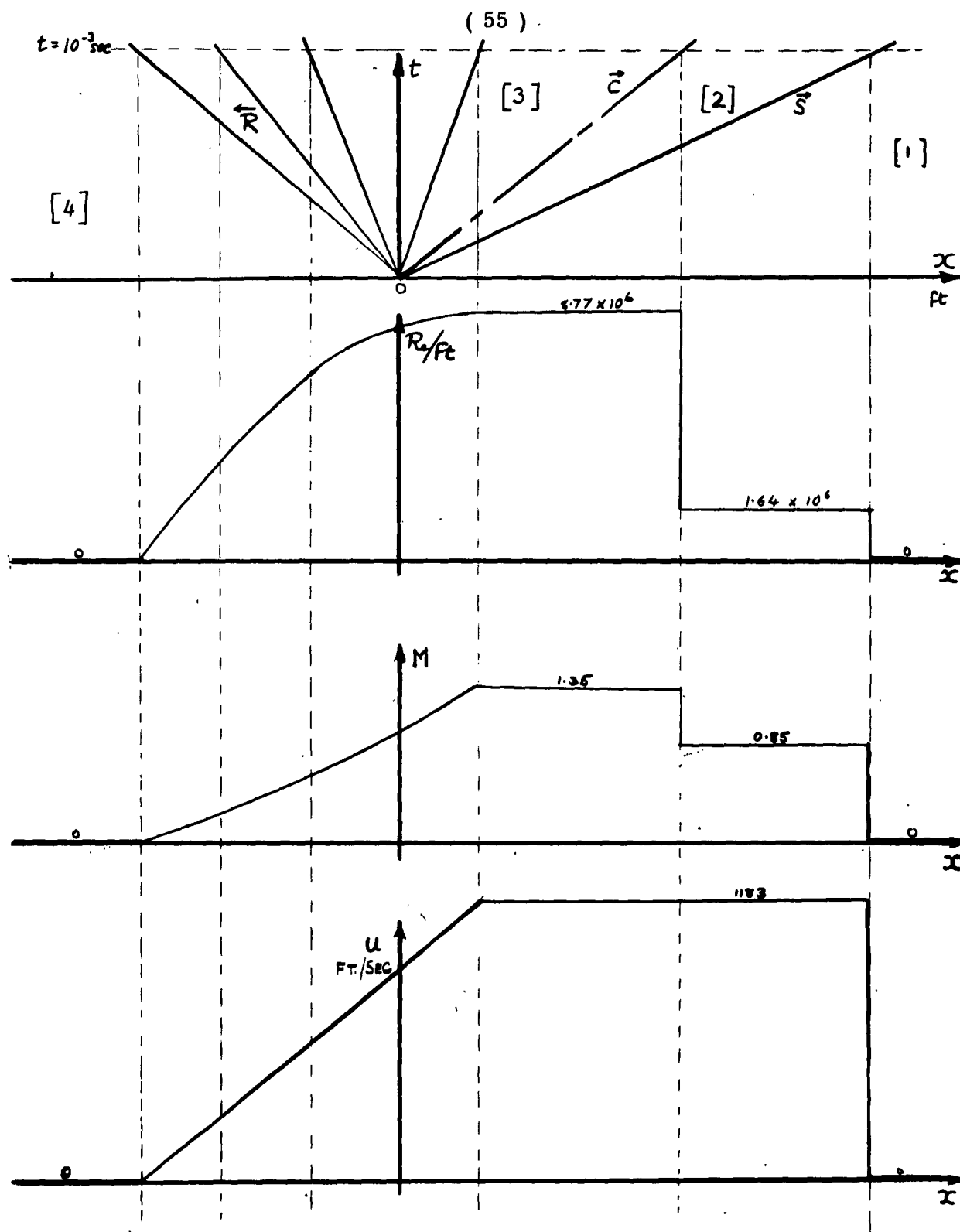


FIGURE 26 (b).

VARIATION OF FLOW PROPERTIES $Re/ft.$, M , u ,
ALONG A SHOCK TUBE UNDER CONDITIONS
GIVEN FOR FIGURE 26 (a).

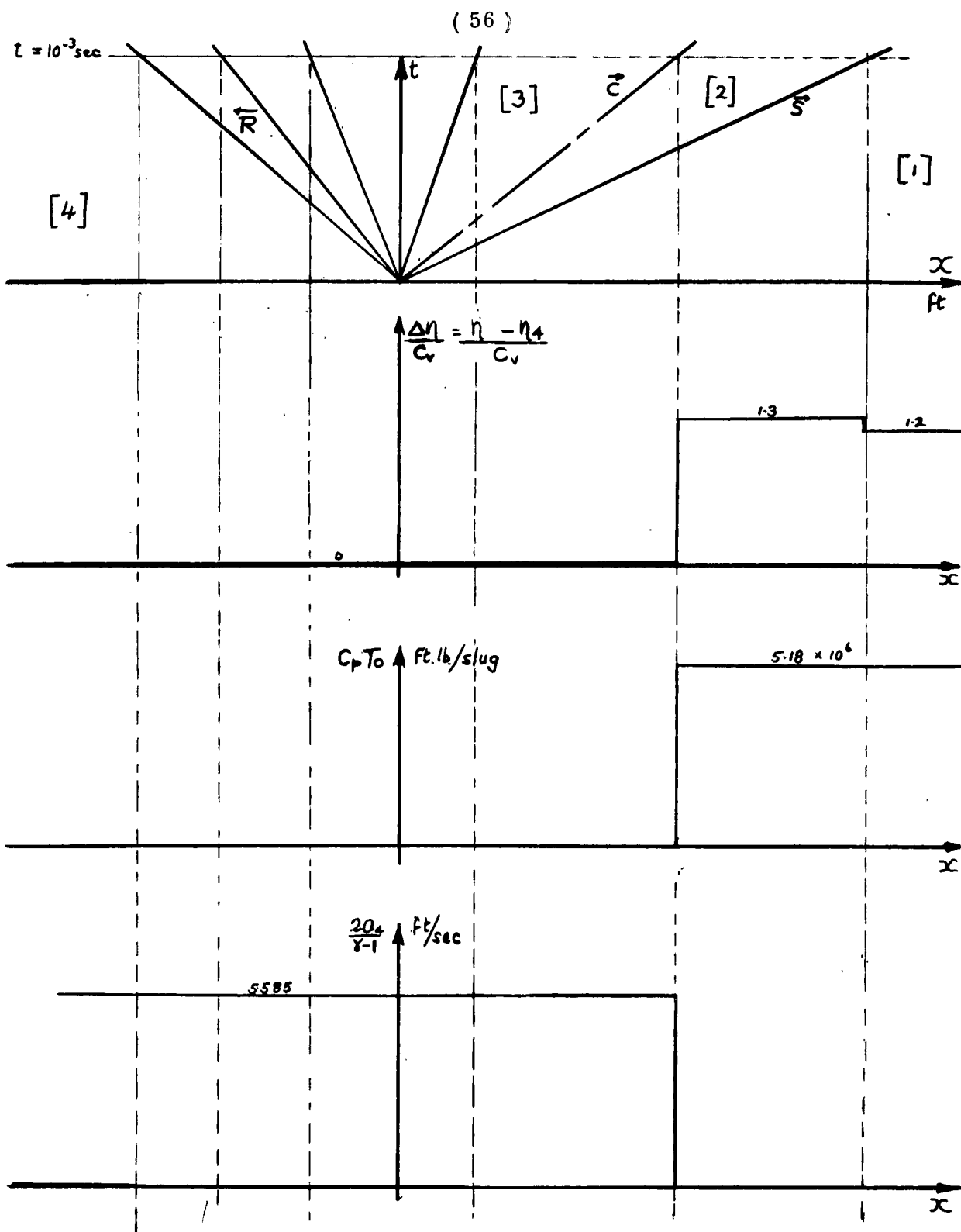


FIGURE 26 (c)

VARIATION OF FLOW PROPERTIES $\frac{\Delta h}{C_v}$, $C_p T_0$, $\frac{2a_4}{\gamma-1}$

ALONG A SHOCK TUBE UNDER CONDITIONS GIVEN

FOR FIGURE 26 (a).

(57)

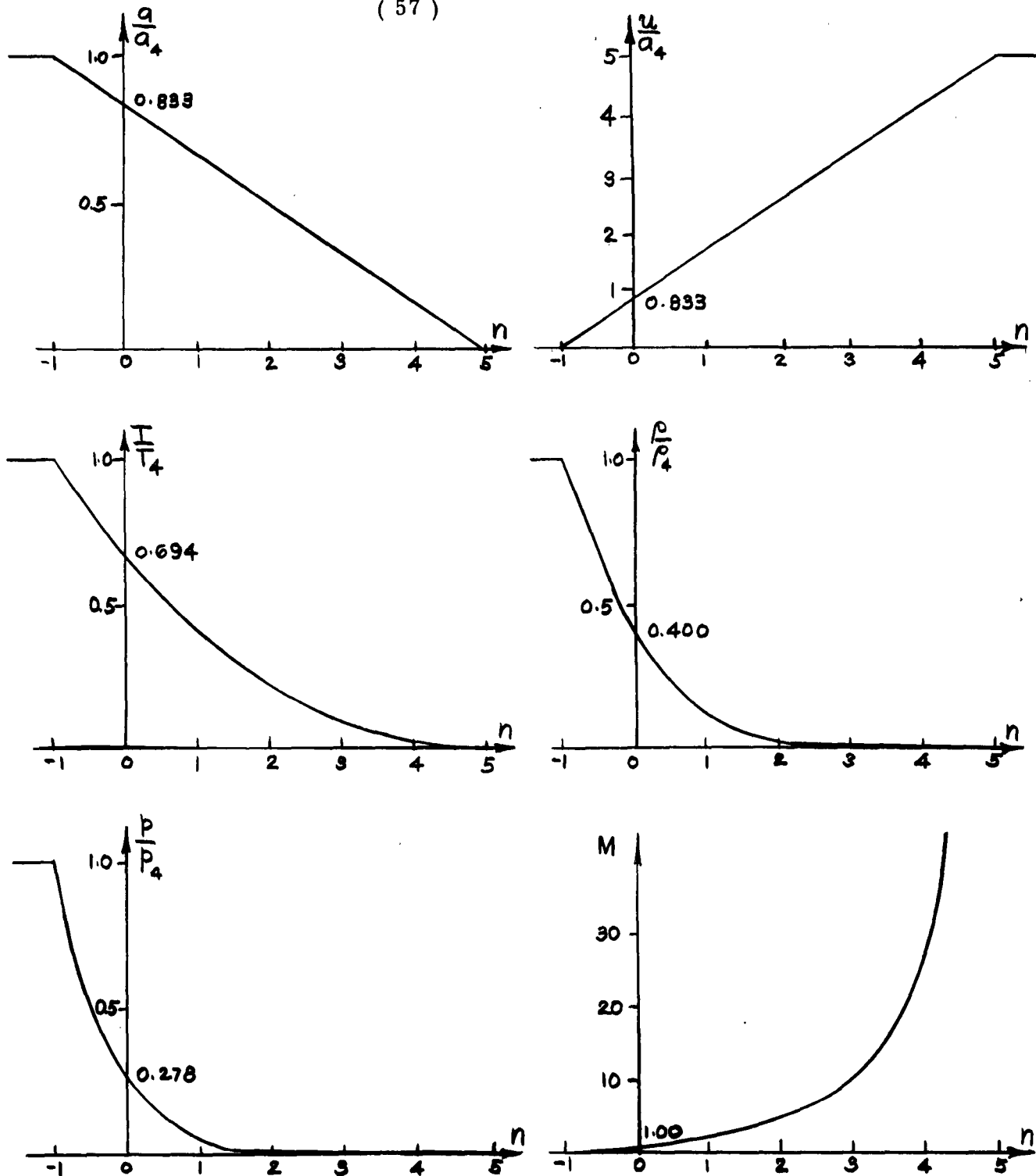


FIGURE 27

TRANSITION FRONT PROFILES THROUGH A COMPLETE CENTRED RAREFACTION WAVE SHOWING THE VARIOUS FLOW PARAMETERS.

NOTE: The incomplete centred rarefaction wave profiles are identical in shape up to the tail of the wave.

Since the equation of state may be assumed to apply,

$$\frac{dp}{p} - \frac{dP}{P} = \frac{dT}{T} \quad (1.90)$$

and

$$\frac{C_v dp}{p} - \frac{C_p dP}{P} = 0 \quad (1.91)$$

Let

$$\left. \begin{aligned} C_p &= C_{p_0} + C'_p \\ C_v &= C_{v_0} + C'_v \end{aligned} \right\} \quad (1.92)$$

Where $C'_p = C'_v$ is the decrease in the specific heat due to the de-excitation of the rotational (or vibrational) degree of freedom of the molecules as the temperature drops. C_{p_0} and C_{v_0} are the initial values of the specific heats at constant pressure and volume respectively.

Hence

$$R = C_p - C_v = C_{p_0} - C_{v_0}$$

$$\gamma_0 = \frac{C_{p_0}}{C_{v_0}}$$

Substituting in (1.91) then,

$$\frac{dp}{p} - \gamma_0 \frac{dP}{P} + \frac{C'_v}{C_{v_0}} \frac{dT}{T} = 0 \quad (1.93)$$

$$\ln A = \ln p - \gamma_0 \ln P + \frac{1}{C_{v_0}} \int C'_v \frac{dT}{T}$$

Let

$$\ln \chi(T) = -\frac{1}{C_{v_0}} \int C'_v \frac{dT}{T} \quad (1.94)$$

and then

$$p = A p^{\gamma_0} \chi(T) \quad (1.95)$$

This is the modified isentropic relation and reduces to the standard form of

$p = A p^{\gamma}$ when $C'_v = 0$ or $\chi(T) = 1$. From equation (1.95)

$$\frac{dp}{dp} = A \gamma_0 p^{\gamma_0-1} \chi + A p^{\gamma_0} \frac{d\chi}{dp} \quad (1.96)$$

$$\frac{d\chi}{d\rho} = \frac{d\chi}{dT} \frac{dT}{d\rho} = \frac{d\chi}{dT} \left(\frac{1}{R\rho} \frac{d\rho}{dT} - \frac{P}{R\rho^2} \right) \quad (1.97)$$

$$\text{or} \quad \frac{d\chi}{d\rho} = \frac{d\chi}{dT} \left(\frac{1}{R\rho} \frac{d\rho}{dT} - \frac{T}{\rho} \right)$$

Substituting from equation (1.94) $\frac{1}{\chi} \frac{d\chi}{dT} = -\frac{C_v'}{TC_{v_0}}$, then

$$\frac{d\chi}{d\rho} = -\frac{\chi}{C_{v_0}} \left(\frac{C_v'}{P} \frac{d\rho}{dT} - \frac{C_v'}{\rho} \right) \quad (1.98)$$

$$\text{Therefore,} \quad \frac{d\rho}{d\rho} \left(1 + \frac{A\rho^{\gamma_0}\chi}{P} \frac{C_v'}{C_{v_0}} \right) = A\chi_0 \rho^{\gamma_0-1} \chi + A\rho^{\gamma_0-1} \chi \frac{C_v'}{C_{v_0}}$$

$$\text{or} \quad \frac{d\rho}{d\rho} \left(1 + \frac{C_v'}{C_{v_0}} \right) = A\chi_0 \rho^{\gamma_0-1} \chi \left(1 + \frac{1}{\gamma_0} \frac{C_v'}{C_{v_0}} \right)$$

$$\text{or} \quad \frac{d\rho}{d\rho} = A\chi_0 \rho^{\gamma_0-1} \chi \frac{1 + \frac{1}{\gamma_0} \frac{C_v'}{C_{v_0}}}{1 + \frac{C_v'}{C_{v_0}}} \quad (1.99)$$

$$\text{or} \quad \frac{d\rho}{d\rho} = A\chi_0 \rho^{\gamma_0-1} \delta^2$$

$$\text{where} \quad \delta^2 = \chi \frac{1 + \frac{1}{\gamma_0} \frac{C_v'}{C_{v_0}}}{1 + \frac{C_v'}{C_{v_0}}}$$

Integrating equation (1.22).

$$u = \pm \int \sqrt{A\chi_0} \rho^{\frac{\gamma_0-1}{2}} \delta d\rho \quad (1.100)$$

$$\text{or} \quad u = \pm \frac{2}{\gamma_0-1} \sqrt{A\chi_0} \int \delta d(\rho^{\frac{\gamma_0-1}{2}})$$

$$\text{and let } u = \pm \frac{2}{\gamma_0-1} \sqrt{A\chi_0} \rho^{\frac{\gamma_0-1}{2}} \bar{\delta} + \text{constant} \quad (1.101)$$

It is necessary at this stage to investigate the value of $\bar{\delta}$. This can be done for a simple example if

$$C'_v = C'_p = \epsilon T C_{v_0} \quad (1.102)$$

where ϵ is a small order quantity.

Hence from equation (1.94)

$$\ln \chi(T) = -\int \epsilon dT = -\epsilon T + c \quad (1.103)$$

when $\epsilon = 0$, $\ln \chi(T) = 0$ and $c = 0$

$$\chi = e^{-\epsilon T} \quad (1.104)$$

and the modified adiabatic relation is

$$P = A P^{y_0} e^{-\epsilon T} \quad (1.105)$$

Also

$$\delta^2 = e^{-\epsilon T} \left(\frac{1 + \frac{\epsilon T}{y_0}}{1 + \epsilon T} \right) \quad (1.106)$$

Since ϵ is small,

$$\delta^2 \approx (1 - \epsilon T) \left(1 + \frac{\epsilon T}{y_0} \right) (1 - \epsilon T)$$

$$\delta^2 \approx 1 - \epsilon T \left(\frac{2y_0 - 1}{y_0} \right)$$

or

$$\delta \approx 1 - \epsilon T \left(\frac{2y_0 - 1}{2y_0} \right) \quad (1.107)$$

From equation (1.105),

$$P R T = A P^{y_0} (1 - \epsilon T)$$

therefore

$$\delta = 1 - \left(\frac{2y_0 - 1}{2y_0} \right) \frac{A \epsilon P^{y_0}}{P R + A \epsilon P^{y_0}}$$

$$\delta \approx 1 - \left(\frac{2\gamma_0 - 1}{2\gamma_0} \right) \left(\frac{A\epsilon \rho^{\gamma_0}}{R\rho} \right) \left(1 - \frac{\epsilon}{R} A \rho^{\gamma_0 - 1} \right)$$

$$\delta \approx 1 - \varphi_1 \rho^{\gamma_0 - 1} + \varphi_2 \rho^{2(\gamma_0 - 1)}$$

where $\varphi_1 = \frac{2\gamma_0 - 1}{2\gamma_0} \frac{A\epsilon}{R}$

$$\varphi_2 = \frac{2\gamma_0 - 1}{2\gamma_0} \left(\frac{A\epsilon}{R} \right)^2$$

Neglecting second order quantities, then

$$\delta = 1 - \varphi_1 \rho^{\gamma_0 - 1} < 1 \quad (1.108)$$

Equation (1.100) may now be written as

$$u = \pm \sqrt{A\gamma_0} \int \rho^{\frac{\gamma_0 - 3}{2}} (1 - \varphi_1 \rho^{\gamma_0 - 1}) d\rho$$

$$u = \pm \sqrt{A\gamma_0} \left[\frac{2}{\gamma_0 - 1} \rho^{\frac{\gamma_0 - 1}{2}} - \frac{2}{3} \frac{\varphi_1}{(\gamma_0 - 1)} \rho^{\frac{3(\gamma_0 - 1)}{2}} \right] + C$$

$$u = \pm \sqrt{A\gamma_0} \frac{2}{\gamma_0 - 1} \rho^{\frac{\gamma_0 - 1}{2}} \left[1 - \frac{\varphi_1}{3} \rho^{\gamma_0 - 1} \right] + C \quad (1.109)$$

Therefore $\bar{\delta} = 1 - \frac{\varphi_1}{3} \rho^{\gamma_0 - 1} \leq 1 \quad (1.110)$

For constant specific heat $\epsilon = 0$ and $\bar{\delta} = \delta = 1$. The boundary conditions for equation (1.109) are that when $u = u_0$, $\rho = \rho_0$, $\bar{\delta} = \bar{\delta}_0 = 1$ and

$$u = u_0 + \frac{2}{\gamma_0 - 1} \sqrt{A\gamma_0} \left(\rho_0^{\frac{\gamma_0 - 1}{2}} - \rho^{\frac{\gamma_0 - 1}{2}} \bar{\delta} \right) \quad (1.111)$$

for a backward facing rarefaction wave. This relation may also be transformed in terms of the pressures.

Since $p = A \rho^{\gamma_0} \chi(\tau)$, then the case of $\bar{\delta}_0 = 1$ corresponds with $\chi = 1$ and

$$p_0 = A \rho_0^{\gamma_0}$$

or

$$\rho_0^{\frac{\gamma_0-1}{2}} = \left(\frac{p_0}{A} \right)^{\frac{\gamma_0-1}{2\gamma_0}}$$

while

$$\rho^{\frac{\gamma_0-1}{2}} = \left(\frac{p}{A\chi} \right)^{\frac{\gamma_0-1}{2\gamma_0}}$$

Hence

$$u = u_0 + \left(\frac{2}{\gamma_0-1} \right) \frac{\sqrt{A\gamma_0}}{A^{\frac{\gamma_0-1}{2\gamma_0}}} \left[p_0^{\frac{\gamma_0-1}{2\gamma_0}} - \bar{\delta} \left(\frac{p}{\chi} \right)^{\frac{\gamma_0-1}{2\gamma_0}} \right]$$

$$u = u_0 + \left(\frac{2}{\gamma_0-1} \right) \sqrt{A^{\frac{1}{\gamma_0}} \gamma_0} \left[p_0^{\frac{\gamma_0-1}{2\gamma_0}} - \bar{\delta} \left(\frac{p}{\chi} \right)^{\frac{\gamma_0-1}{2\gamma_0}} \right]$$

Since

$$\chi = e^{-\epsilon\tau} \approx 1 - \epsilon\tau$$

$$\left(\frac{1}{\chi} \right)^{\frac{\gamma_0-1}{2\gamma_0}} = 1 + \frac{\gamma_0-1}{2\gamma_0} \epsilon\tau$$

$$\text{but } \tau = \frac{A \rho^{\gamma_0}}{R \rho + A \rho^{\gamma_0} \epsilon} = \frac{A \rho^{\gamma_0-1}}{R} \left(1 - \frac{A}{R} \rho^{\gamma_0-1} \epsilon \right)$$

$$\text{hence } \left(\frac{1}{\chi} \right)^{\frac{\gamma_0-1}{2\gamma_0}} = 1 + \frac{\gamma_0-1}{2\gamma_0} \left[\frac{A \rho^{\gamma_0-1} \epsilon}{R} - \left(\frac{A \rho^{\gamma_0-1} \epsilon}{R} \right)^2 \right]$$

and neglecting second order quantities

$$\left(\frac{1}{\chi} \right)^{\frac{\gamma_0-1}{2\gamma_0}} \approx 1 + \frac{\gamma_0-1}{2\gamma_0-1} \varphi_1 \rho^{\gamma_0-1} \quad (1.112)$$

Also
$$\bar{\delta} = 1 - \frac{\varphi_1 p^{\gamma_0-1}}{3}$$

and
$$\bar{\delta} \left(\frac{1}{\chi} \right)^{\frac{\gamma_0-1}{2\gamma_0}} \approx 1 + \varphi_1 p^{\gamma_0-1} \left[\frac{\gamma_0-1}{2\gamma_0-1} - \frac{1}{3} \right]$$

$$\bar{\delta} \left(\frac{1}{\chi} \right)^{\frac{\gamma_0-1}{2\gamma_0}} = 1 + \varphi_1 p^{\gamma_0-1} \left[\frac{\gamma_0-2}{3(2\gamma_0-1)} \right] \quad (1.113)$$

Let
$$\Phi = 1 - \varphi_1 p^{\gamma_0-1} \left[\frac{2-\gamma_0}{3(2\gamma_0-1)} \right] \leq 1 \quad (1.114)$$

Therefore
$$u = u_0 + \frac{2}{\gamma_0-1} \sqrt{A^{\frac{1}{\gamma_0}} \gamma_0} \left[p_0^{\frac{\gamma_0-1}{2\gamma_0}} - p^{\frac{\gamma_0-1}{2\gamma_0}} \Phi \right]$$

or
$$u = u_0 + \frac{2a_0}{\gamma_0-1} \left[1 - \left(\frac{p}{p_0} \right)^{\frac{\gamma_0-1}{2\gamma_0}} \Phi \right] \quad (1.115)$$

This relation may be compared with equation (1.29) for the case of constant specific heat, that is

$$u = u_0 + \frac{2a_0}{\gamma_0-1} \left[1 - \left(\frac{p}{p_0} \right)^{\frac{\gamma_0-1}{2\gamma_0}} \right]$$

It is seen from equation (1.115) that the particle velocity (u_3) in state (3) would be increased as a result of the de-excitation of the rotational degrees of freedom due to the decrease in temperature.

In reference (9) it is shown that C_v for hydrogen, between 190°K and 300°K, may be represented empirically by

$$C_v = C_{v_0} \left[1 - \alpha (T_0 - T)^2 \right] \quad (1.116)$$

where $C_{v_0} = 10.1 \text{ ergs/gm}$

$\alpha = 9.31 \times 10^{-6} \text{ degree}^{-2}$

$T_0 = 300^\circ\text{K}$

C_v is of the form used in equations (1.92) and (1.102). It is shown that in this temperature range the variation in u_3 and $P_{34} = p_3/p_4$ is quite small. For example, at $T_3 = 190^\circ\text{K}$, $u_3 = 1.315 \text{ mm}/\mu \text{ sec}$, $p_3/p_4 = .2077$ (constant C_v); $P_3/p_4 = .2177$ (variable C_v). Thus for equal pressure ratios across the rarefaction wave the particle velocity with variable specific heat is greater, as predicted by equation (1.115).

It should be noted that a value of $P_{34} = .2$ for the case Air/Air is achieved with a low diaphragm pressure ratio (about 17) and the variation due to specific heat will be small. However, for shock tube work a diaphragm pressure ratio (P_{41}) of 10,000 can easily be attained. In this case $P_{34} = .0017$, $P_{21} = 17$ and $T_3 = .16 \times 300^\circ\text{K} = 48^\circ\text{K}$ which is below the boiling point of nitrogen and oxygen. This will lead to the condensation of these constituents of air (reference 27), and the error in assuming constant specific heat for large expansion waves can no longer be neglected.

(b) Flow Through a Shock Front with Variable Specific Heat

In section 1.02 it was shown that the following relations apply across a shock front.

$$\rho v = m \quad (1.117)$$

$$p + m v = m V \quad (1.118)$$

$$e + \frac{p}{\rho} + \frac{1}{2} v^2 = \frac{1}{2} c^2 \quad (1.119)$$

where
$$c = \sqrt{\frac{2}{\gamma-1}} a_0 \quad (1.120)$$

The first two are the mechanical or dynamic shock equations and the last one is the energy or thermodynamic equation, which may be written in the following alternative form.

$$\beta \frac{p}{\rho} + \frac{v^2}{2} = \frac{c^2}{2} \quad (1.121)$$

where

$$e = (\beta - 1) \frac{p}{\rho}$$

$$\beta = \beta_t + \beta_r + \beta_v + \beta_e + \beta_d + \beta_i + 1$$

The subscripts denote the main components of the internal energy content of a gas per gram, that is

- 1) the kinetic energy of translation of a molecule (t)
- 2) the energy of molecular rotation (r)
- 3) the energy of molecular vibration (v)
- 4) the energy of electronic excitation (e)
- 5) the energy of molecular dissociation into atomic groups (d)
- 6) the energy of ionization (i).

The inclusion of the term 1 in β simplifies the energy equation (1.119) due to the appearance of the pressure energy term p/ρ , and equation (1.121) follows as a consequence.

The above equations may be combined and the following solution results

$$\mathcal{N} = \frac{\beta V \pm \sqrt{\beta^2 V^2 - (2\beta - 1)c^2}}{2\beta - 1} \quad (1.122)$$

If V and C are real and positive then $\mathcal{N}_+ > a_1$ (that is the flow is supersonic on the low pressure side of the shock) and $\mathcal{N}_- < a_1$ (subsonic on the high pressure side of the shock).

If $\beta_2 = \beta_1 = \beta$, then $\mathcal{N}_+ = \mathcal{N}_1$ and $\mathcal{N}_- = \mathcal{N}_2$

$$\text{or} \quad \mathcal{N}_2 = \frac{1}{2\beta - 1} \left[\mathcal{N}_1 + 2(\beta - 1) \frac{a_1^2}{\mathcal{N}_1} \right] \quad (1.123)$$

This is obtained by substitution for V and C , and it follows that

$$\mathcal{N}_1 \mathcal{N}_2 = a_*^2 = \frac{1}{2\beta_1 - 1} \left[\mathcal{N}_1^2 + 2(\beta - 1) a_1^2 \right] \quad (1.124)$$

which is the Prandtl form of the energy equation for constant specific heat.

The difficulty arises from the fact that for a real gas β is not constant but a monotonically increasing function of the temperature. Thus equation (1.122) must be solved for β at the given temperature.

This problem is analysed in detail in reference 36. The contributions to the internal energy ($\beta - 1$) term may be described briefly as follows.

The translational energy $e_t = \frac{3P}{2\rho} = \frac{3}{2}RT$, if no dissociation is present (otherwise $P/\rho = RT(1+\alpha)$ where α is the degree of dissociation). This is true for any gas.

The rotational energy e_r is zero for monatomic gases, $2\left(\frac{1}{2}RT\right)$ for all diatomic gases (except hydrogen), $2\left(\frac{1}{2}RT\right)$ for all linear polyatomic molecules (e.g. CO_2), and $3\left(\frac{1}{2}RT\right)$ for all other polyatomic molecules.

The vibrational energy may be approximated (when the temperatures are not excessive) by resolving the vibration into normal modes and treating each mode as an harmonic oscillator. Diatomic gases have one normal mode. Linear polyatomic gases have $3n - 5$ modes (where n = number of atoms on a straight line, e.g. CO_2 has 4 normal modes). Other polyatomic gases have $3n - 6$ normal modes. The vibrational energy per gram per mode is

$$e_v = RT \frac{z}{e^z - 1}$$

where $z = \frac{h\nu}{kT} = 1.438 \frac{\nu}{T}$

ν = vibrational frequency in waves per cm. (wave numbers)

T = temperature $^{\circ}\text{K}$

h = Planck's constant

k = Boltzmann's constant

The frequencies are obtained from spectrographic analysis of band spectra (e.g. $\nu_{\text{N}_2} = 2345$, $\nu_{\text{O}_2} = 1570$, $\nu_{\text{CO}_2} = 667, 667, 1336, 2350$). It is seen that for low temperature z is large and $e_v \rightarrow 0$. At high temperatures $e_v \rightarrow RT$ per mode, a value which is attained very slowly. At high temperatures the vibrations cannot be regarded as harmonic, and an interaction occurs between the rotational and the vibrational modes. These effects increase the vibrational energy (e.g. N_2 at 5000°K has an $e_v = .753 RT$ whereas the harmonic oscillator gives an $e_v = .669 RT$). For air e_v is about 3% effective at 800°K and about 50% effective at 5000°K .

The electronic excitation becomes of significance beyond 5000°K , and is usually small by comparison with vibration and dissociation energies.

The dissociation energy becomes important above $2000\text{--}3000^{\circ}\text{K}$ when $kT \ll D/R$ per molecule, where D is the dissociation energy in calories per mole. For a dissociated gas, the equation of state has the form $P/P = RT(1 + \alpha)$ where α = degree of dissociation, which varies as the temperature and inversely as the pressure.

The ionization energy becomes important at temperatures above 5000°K when $kT \ll I/R$ per molecule, where I is the ionization energy in calories per mole. The equation of state then has the form $P/P = (1 + \alpha + \delta)RT$ where α = degree of dissociation, and δ = degree of ionization. Since ionization takes place at extremely high temperatures it may be neglected by comparison with the other energies considered in the present case.

The values of α , β and e/RT as a function of temperature for air are given in table 5 (see reference 36) and plotted on figure 28. They were calculated by using the following composition of air by volume.

N_2	=	78.05 %
O_2	=	21.00 %
Rare gases	=	0.92 %
CO_2	=	0.03 %

According to reference 36 the energy constant β of nitrogen and oxygen at temperatures from 300° down to the liquefaction temperature remains almost unchanged. Hence the flow through a rarefaction wave in air will only be slightly affected up to the condensation temperature.

Qualitatively, the transition through a strong shock front may be discussed as follows. Immediately at the shock front, the temperature jumps suddenly to a high value. This is due to the fact that the active degrees of freedom, translation and rotation are excited almost instantaneously in the distance of a few mean free paths

(λ) (λ_e and $\lambda_r \approx 10^{-5}$ cm at N.T.P., they are independent of the temperature to a first approximation and vary inversely as the pressure). It may therefore be assumed that this initial jump will be given by the Rankine-Hugoniot relations which are based on the active degrees of freedom. Equation (1.121) then becomes

$$\frac{v_2^2}{2} + \frac{\gamma}{\gamma-1} \frac{P_2}{\rho_2} = \frac{v_1^2}{2} + \frac{\gamma}{\gamma-1} \frac{P_1}{\rho_1}$$

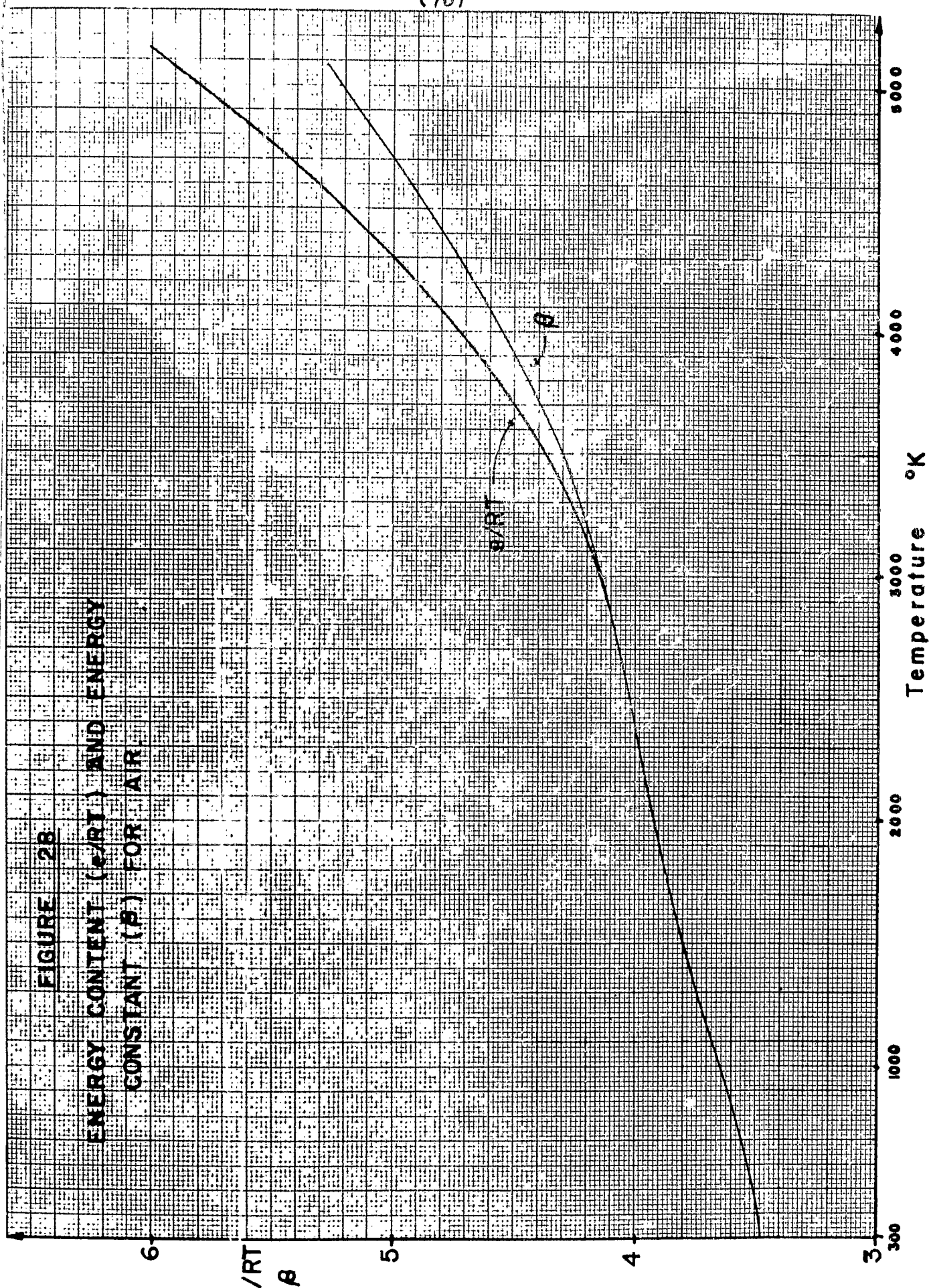
and $\beta = \frac{\gamma}{\gamma-1} = \frac{7}{2}$ for diatomic and polyatomic linear molecules. In case of carbon dioxide $\gamma = 1.3$ at room temperature and the vibrational energy is already partially excited. Thus the initial jump across the shock is predicted by the Rankine-Hugoniot conditions for diatomic and polyatomic linear molecules by using $\gamma = 1.4$ or $\beta = 7/2$. After this initial jump thermal equilibrium will be reached in an exponential form during the relaxation period when energy is transferred from the active to the inert degrees of freedom, (vibration, dissociation, electronic excitation, ionization) which are then excited. This stage is marked by a decrease in the temperature and it takes place in longer times and at a greater distance (λ_v for oxygen ≈ 1 cm at N.T.P. or 10^{-3} cm at 5000°K at an eightfold increase in density, λ_d for oxygen $\approx 10^2$ cm at 2500°K and 10^{-1} cm at 5000°K). At a given temperature these mean free paths vary inversely as the pressure. The relaxation times for vibrational equilibrium for oxygen is about $100 \mu\text{sec}$ at N.T.P. and $10^{-1} \mu\text{sec}$ at 5000°K ; for dissociation it is about $100 \mu\text{sec}$ at 5000°K). At the temperatures reached in normal shock tube work the vibrational degree is the most important one to consider. The value of β for air when thermal equilibrium is reached at a given temperature is found from table 5. These values will now be called β_2^* , as distinct from β_2 employed only for the active degrees.

Equations (1.117) to (1.121) may be reconsidered now in the following way. The equations of continuity and motion (1.117 and 1.118) are unaffected by changes in the thermodynamic states. The energy equation (1.121) is assumed to be valid behind the shock front where β_2^* has reached its equilibrium value corresponding to a given temperature. This assumption is valid in the absence of dissociation when the equation of state is still given by $p = \rho RT$, that is only the vibrational degree is excited. For most of the experiments conducted in a shock tube this is a reasonable assumption due to the very short duration of the steady state flows and the long relaxation times for dissociation at low density. The energy equation becomes then

$$\frac{v_2^{*2}}{2} + \beta_2^* \frac{P_2^*}{\rho_2^*} = \frac{v_1^2}{2} + \beta_1 \frac{P_1}{\rho_1} \quad (1.125)$$

TABLE 5Energy Content and Dissociation of Air

T (°K)	β	α	$\beta(1+\alpha)$ $= \frac{e}{RT}$
300	3.483		3.483
400	3.494		3.494
500	3.507		3.507
600	3.527		3.527
700	3.552		3.552
800	3.580		3.580
900	3.613		3.613
1,000	3.647		3.647
1,250	3.727		3.727
1,500	3.805		3.805
1,750	3.869		3.869
2,000	3.924	0.0000	3.924
2,500	4.023	0.0004	4.024
3,000	4.133	0.0030	4.145
3,500	4.307	0.0121	4.359
4,000	4.562	0.0331	4.713
4,500	4.875	0.0687	5.211
5,000	5.227	0.1058	5.780



The continuity and momentum equations remain unchanged as

$$\rho_2^* \nu_2^* = \rho_1 \nu_1 \quad (1.126)$$

$$p_2^* + \rho_2^* \nu_2^{*2} = p_1 + \rho_1 \nu_1^2 \quad (1.127)$$

From table 5 it may be seen that the equilibrium value of the energy constant β is completely determined by the temperature or that $T_e = T(\beta)$. However by combining equations (1.125), (1.126) and (1.127) equation (1.122) results, which shows that ν_2^* may be uniquely determined as a function of β_2^* since V and C are determined by the initial conditions p_1 , ρ_1 , ν_1^2 , and β_1 (also ν_2^* is subsonic on the high pressure side of the shock front). By combining equations (1.126) and (1.127)

$$\frac{p_2^*}{\rho_2^*} = RT_2^* = \left(\frac{p_1}{\rho_1 \nu_1} + \nu_1 - \nu_2^* \right) \nu_2^* \quad (1.128)$$

Therefore T_2^* can be determined from ν_2^* . Thus the shock wave theory shows that T_2^* is a given function of β which is denoted by $T_s(\beta)$. It is possible to determine the temperature T_2^* and the energy constant β_2^* by solving the equation

$$T_e(\beta) = T_s(\beta) \quad (1.129)$$

This equation has only one solution for ν_2^* on the high pressure side of the shock wave for which ν_2^* is less than the speed of sound. This follows from the fact that $T_s(\beta)$ decreases with increasing β over almost the entire range of β , whereas $T_e(\beta)$ increases monotonically with β (see table 5), or $\frac{dT_s}{d\beta} < \frac{dT_e}{d\beta}$. Therefore

β_2^* , T_2^* and the other flow quantities p_2^* , ρ_2^* , ν_2^* are uniquely determined from the initial conditions on the low pressure side of the shock front. Thus the physical flow quantities on the high pressure side at a sufficient distance from the shock front, are independent of the intervening processes which establish the equilibrium between the active and inert degree of freedom and give rise to the energy constant β_2^* .

For convenience in the calculation of the flow quantities in the high pressure state (2*) behind the shock flow from the initial conditions in the state (1) in front of the shock front, T_1 and T_2^* are assumed as given and v_1 and v_2^* are calculated. The values of β at the given temperatures are taken from table 5. Equations (1.125, 1.126 and 1.127) are rearranged for ease in calculating V_1 and V_2^* from the following two equations

$$v_1(v_2^{*2} + RT_2^*) = v_1^*(v_1^2 + RT_1) \quad (1.130)$$

$$2\beta_2^*RT_2^* + v_2^{*2} = 2\beta_1RT_1 + v_1^2 \quad (1.131)$$

Let $v_1 = \frac{v_1}{v_2^*} v_2^* = g v_2^*$ where $g = \frac{v_1}{v_2^*}$

From (1.13) $v_2^{*2} = \frac{2R(\beta_2^*T_2^* - \beta_1T_1)}{g^2 - 1} \quad (1.132)$

From (1.130) $v_2^{*2} = \frac{R(T_1 - gT_2^*)}{(-g)(g-1)} \quad (1.133)$

Therefore $g = \frac{v_1}{v_2^*} = b + \sqrt{b^2 + \frac{T_1}{T_2^*}} \quad (1.134)$

where $b = \left(\beta_2^* - \frac{1}{2}\right) - \frac{T_1}{T_2^*} \left(\beta_1 - \frac{1}{2}\right) \quad (1.135)$

and from (1.132) $v_2^{*2} = RT_2^* \frac{2b + 1 - \frac{T_1}{T_2^*}}{\left(\frac{v_1}{v_2^*}\right)^2 - 1} \quad (1.136)$

It should be noted that the above relations have been developed by assuming that the degree of dissociation α is small enough to be neglected or the temperature is not sufficiently high to cause dissociation; that is, the equation of state $p = \rho RT$ applies.

The flow quantities on the high pressure side of the shock wave as given in table 6 are listed in reference 36 and plotted on figures 29 to 32. The values of ν_2^* and ν_1 are determined from equations (1.134) to (1.136) by using different T_2^* and the corresponding β_2^* from table 5. T_1 is taken as 300°K and β_1 as 3.483. The values of p_2^* and ρ_2^* are obtained from equations (1.126) and (1.127). The above quantities apply at a sufficient distance from the shock front when vibrational equilibrium is attained. Immediately at the wave front the Rankine-Hugoniot conditions are valid and the flow quantities are calculated on the basis that $\beta_2 = \beta_1 = 3.483$, from equations (1.122, 1.126 and 1.127). These values are identical with those plotted on figures 19 and 21.

An examination of the flow quantities with constant and variable specific heats shows that there is reasonable agreement for shock wave Mach numbers up to 3. Beyond this value the divergence becomes more pronounced as the wave Mach number increases, that is $\rho_2^* > \rho_2$, $\nu_2^* < \nu_2$, or $u_2^* > u_2$, $p_2^* > p_2$ and $T_2^* < T_2$. Thus the shock wave consists of an almost discontinuous short front where the flow quantities jump to the values determined from the active degrees of freedom, followed by a longer region where the inert degrees of freedom reach their equilibrium, and the values denoted by (*) are then reached exponentially (see reference 36). The greatest changes are encountered in ρ_2^* , T_2^* and ν_2^* ; and the least in p_2^* . Even at a shock pressure ratio of 100, which could be obtained in a shock tube by using H₂/Air or He/Air, the difference from the Rankine-Hugoniot value is only about 6 percent. The profiles of the physical quantities at the shock front are shown qualitatively in figure 33.

For convenience in shock tube work it is better to change the frame of reference to one in which the air in front of the shock is at rest. With this change (ν/a_1) becomes the Mach number of the shock wave referred to the air at rest as it progresses down the tube, and $U_{21}^* = \frac{\nu_1 - \nu_2^*}{a_1}$ or $U_{21} = \frac{\nu_1 - \nu_2}{a_1}$ is the particle velocity, with variable or constant specific heat respectively, behind the shock wave referred to the speed of sound of the rest state.

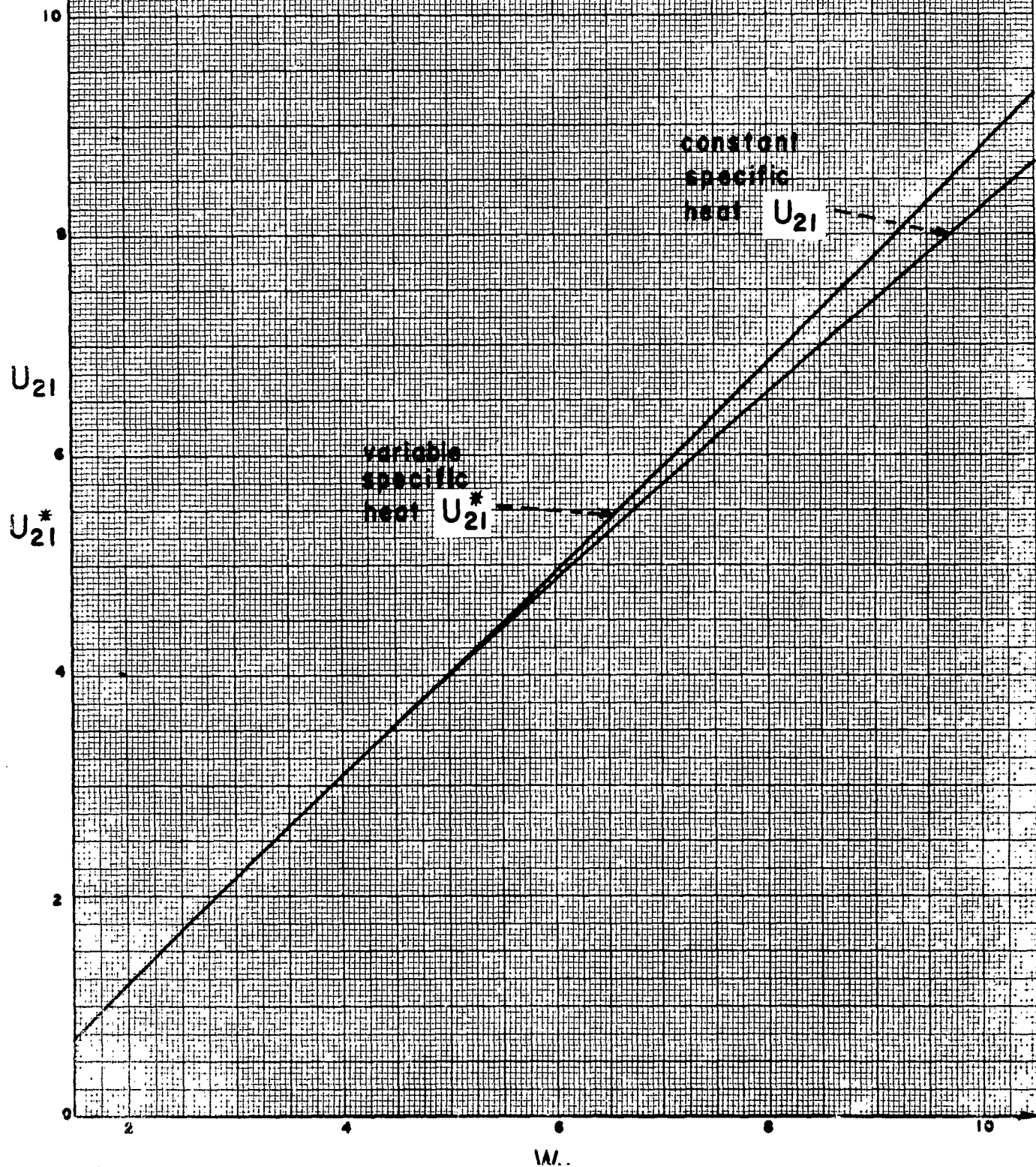
TABLE 6

Flow Quantities on the High Pressure Side of Shock Waves in Air with
Constant Specific Heat (2) and Temperature Dependent Specific Heat (2*).

W_{11}	U_{21}	U_{21}^*	Γ_{21}	Γ_{21}^*	T_2 °K	T_2^* °K	P_{21}	P_{21}^*
1.523	0.723	0.725	1.904	1.907	400	400	2.53	2.54
1.984	1.235	1.238	2.647	2.659	501	500	4.42	4.43
2.377	1.630	1.640	3.189	3.225	604	600	6.41	6.45
2.725	1.966	1.981	3.591	3.663	709	700	8.49	8.55
3.041	2.262	2.284	3.904	4.015	816	800	10.62	10.71
3.331	2.528	2.559	4.146	4.314	925	900	12.77	12.94
3.611	2.780	2.816	4.346	4.540	1036	1000	15.01	15.23
4.235	3.335	3.400	4.706	5.069	1320	1250	20.72	21.12
4.797	3.827	3.917	4.945	5.454	1616	1500	26.66	27.27
5.307	4.266	4.384	5.098	5.746	1925	1750	32.70	33.52
5.778	4.675	4.812	5.236	5.978	2222	2000	38.75	39.85
6.643	5.415	5.598	5.409	6.359	2848	2500	51.4	53.0
7.453	6.103	6.338	5.521	6.685	3510	3000	64.6	67.0
8.315	6.834	7.148	5.615	7.122	4300	3500	80.5	84.1
9.297	7.664	8.089	5.691	7.697	5300	4000	100.6	106.0
10.410	8.601	9.169	5.754	8.385	6570	4500	126.2	134.4
11.595	9.598	10.326	5.804	9.136	8030	5000	155.6	168.4

FIGURE 29

VARIATION OF THE FLOW VELOCITY
RATIOS BEHIND A SHOCK WAVE
WITH THE WAVE MACH NUMBER (M_1)



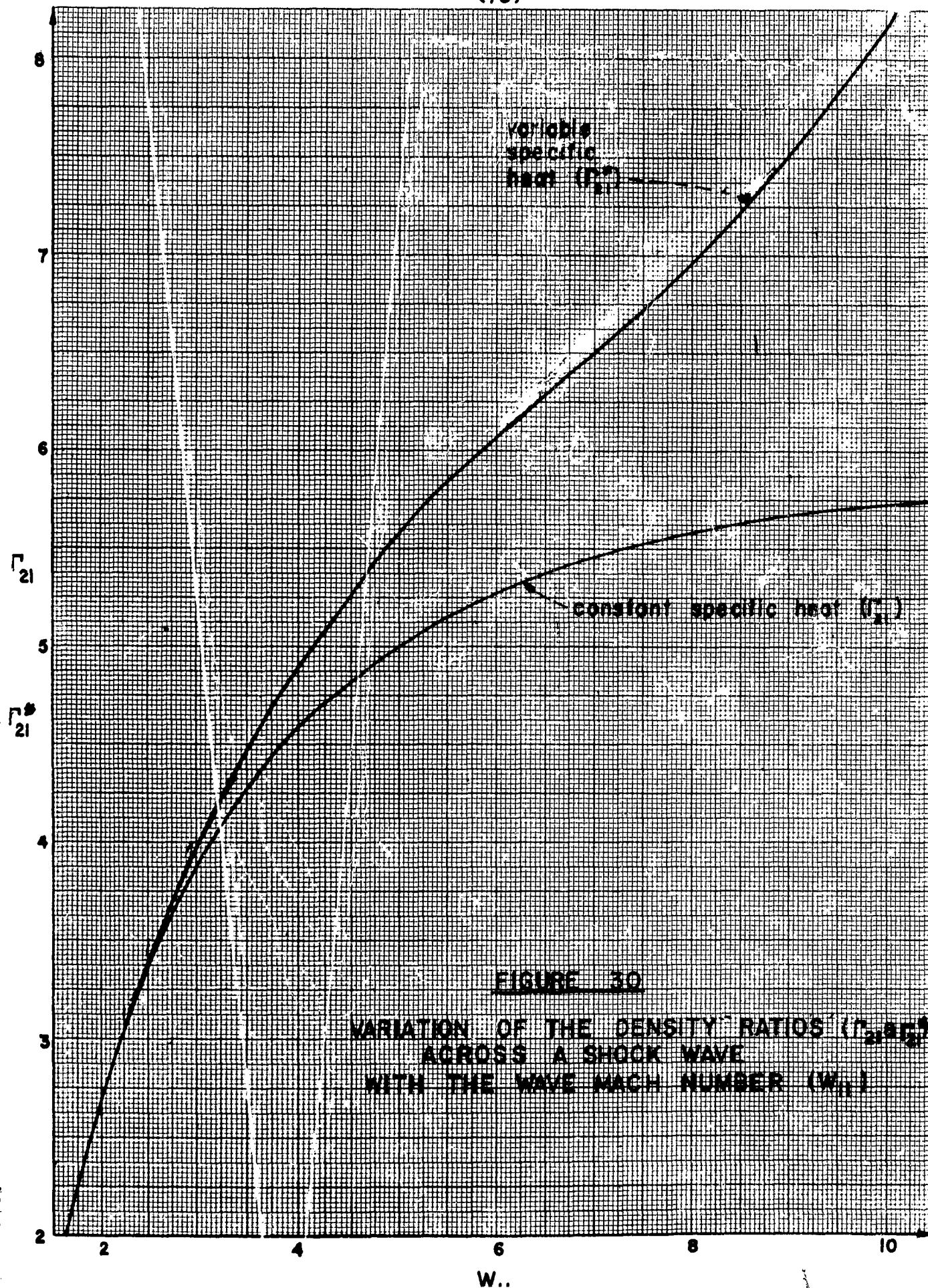


FIGURE 31

VARIATION OF THE TEMPERATURES (T_2 & T_2^*)
BEHIND A SHOCK WAVE
WITH THE WAVE MACH NUMBER (W_{11})

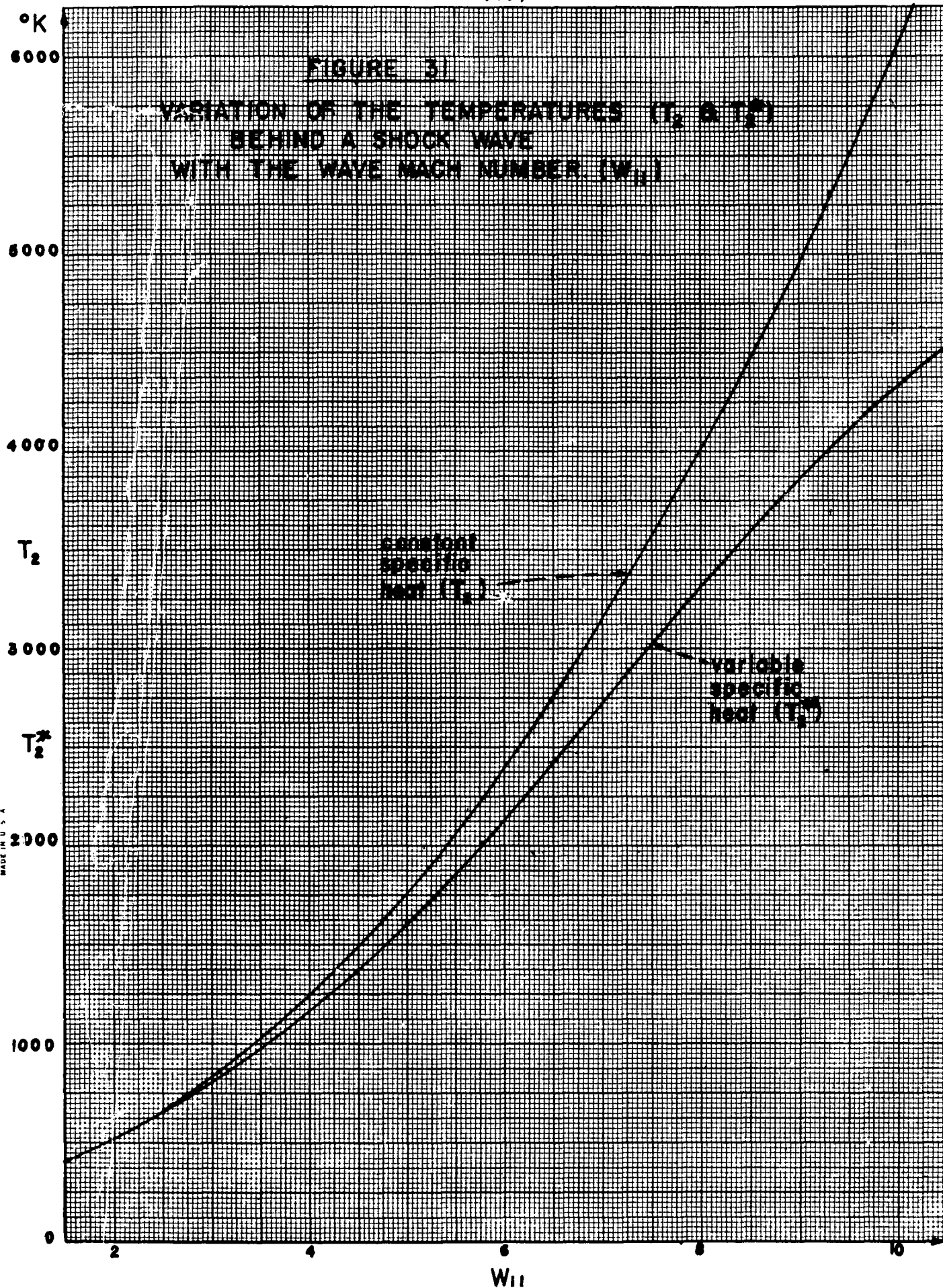
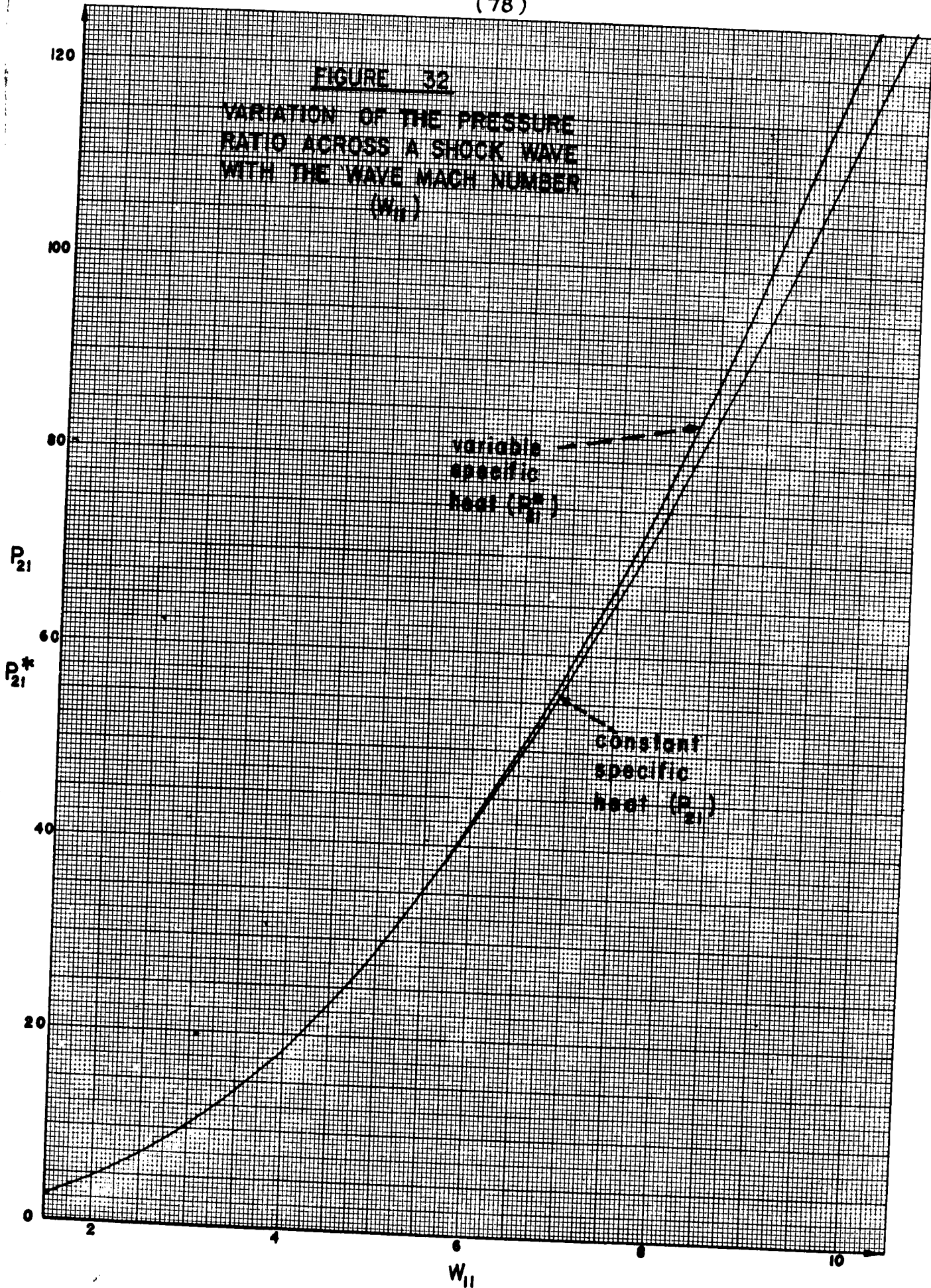
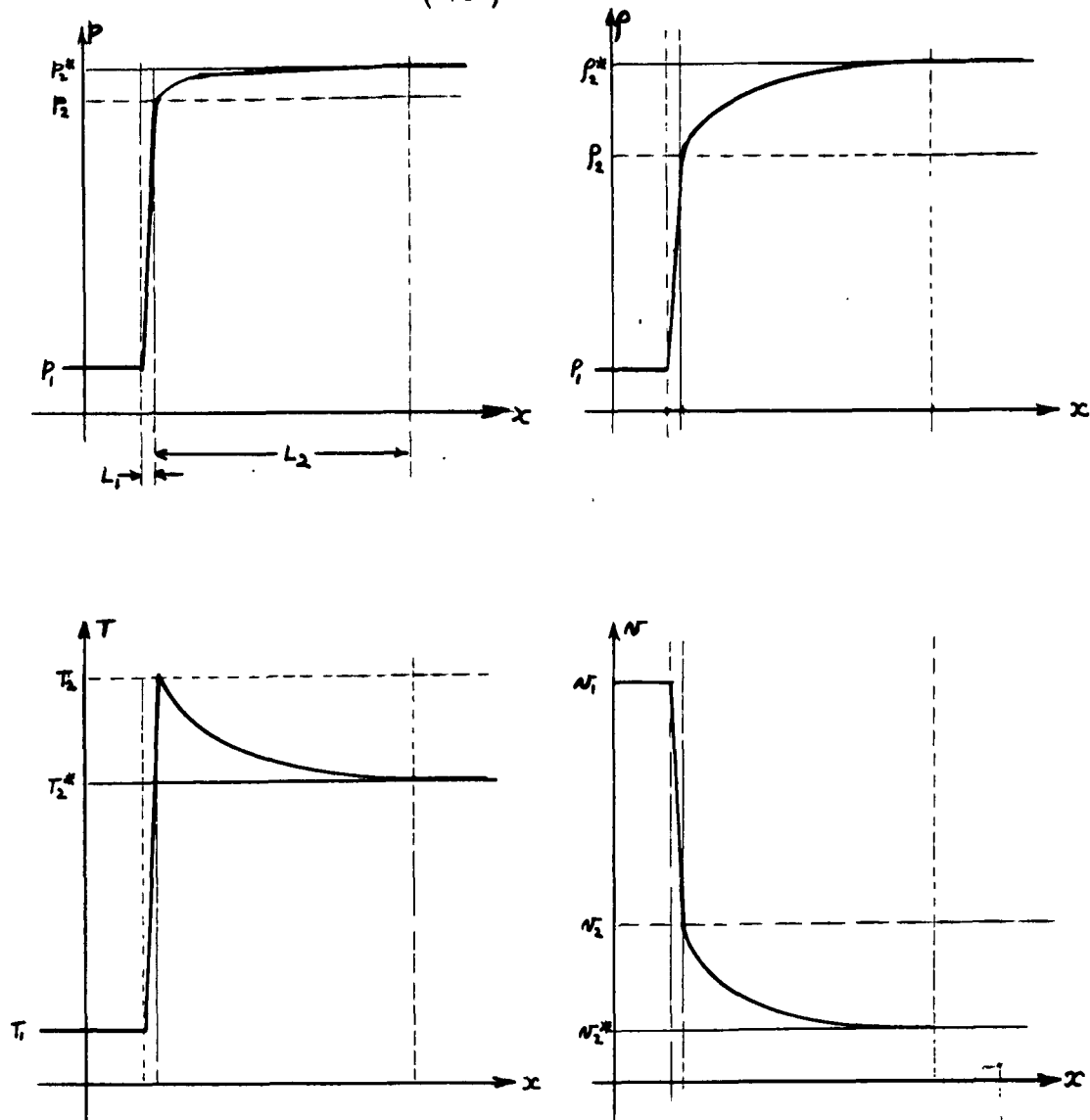


FIGURE 32

VARIATION OF THE PRESSURE
RATIO ACROSS A SHOCK WAVE
WITH THE WAVE MACH NUMBER
(w_{II})





----- Rankine-Hugoniot value (active degrees)

————— Equilibrium value (active and inert degrees)

L_1 = Shock thickness due to active degrees

L_2 = Shock thickness due to inert degrees

FIGURE 33

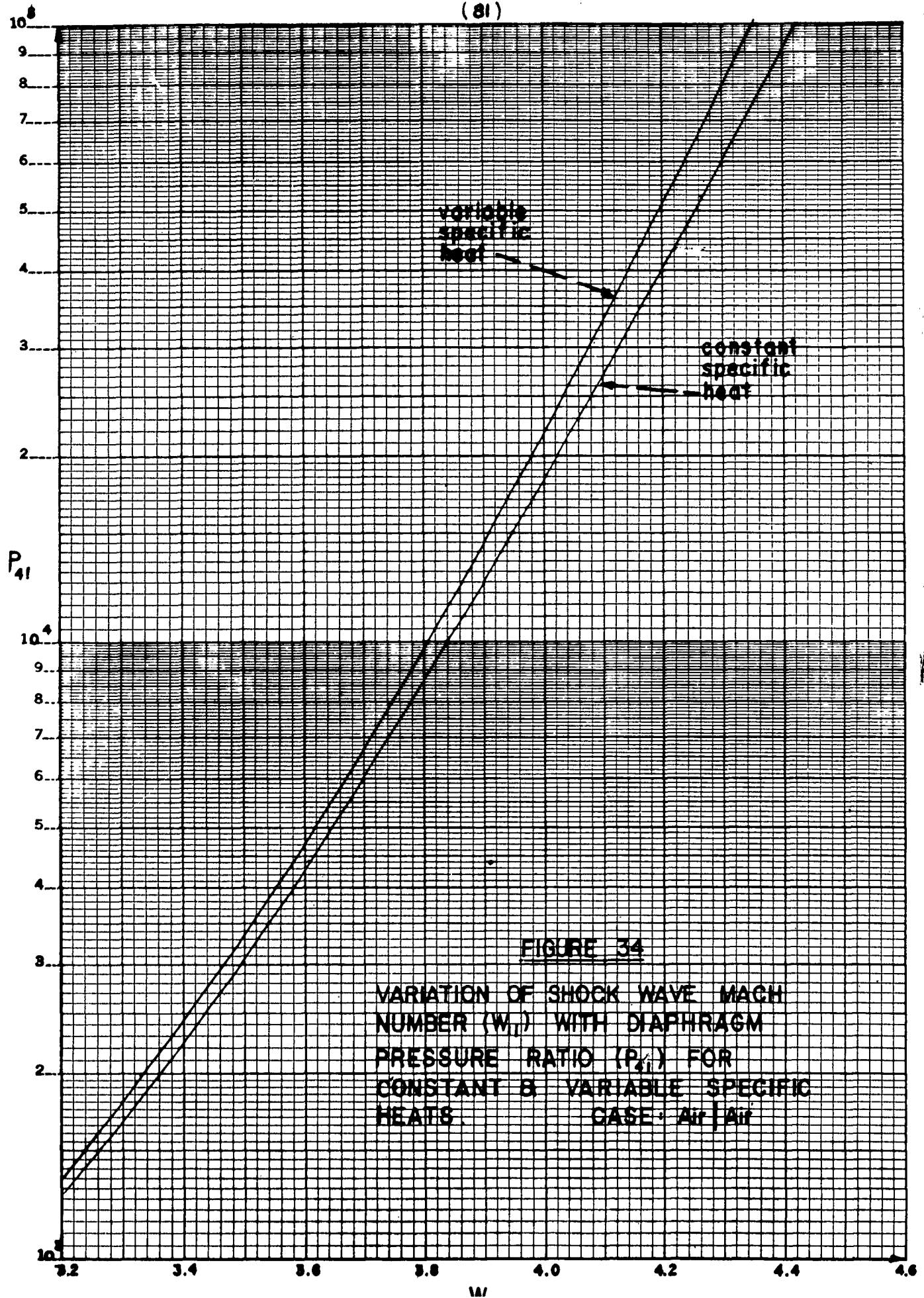
REPRESENTATION OF TRANSITION THROUGH A STRONG SHOCK FRONT.

It is possible now to determine a modified relation between the diaphragm pressure ratio and the shock pressure ratio based on the results from variable specific heat considerations. It is assumed that the flow velocity and the pressure are continuous across the contact surface. Therefore the velocity produced by the rarefaction wave must be equal to the flow velocity behind the shock wave, that is from equation (1.115)

$$v_1 - v_2^* \equiv u_3 = \frac{2a_4}{\gamma_4 - 1} \left[1 - \left(\frac{P_3}{P_4} \right)^{\frac{\gamma_4 - 1}{2\gamma_4}} \Phi \right]$$

and the pressure ratio across the rarefaction wave $P_3/P_4 = P_{34}$ now can be determined. For a given wave Mach number $v_1/a_1 \equiv W_{11}$, $P_2^*/P_1 = P_{21}^*$ is known and the diaphragm pressure ratio $P_{41} = P_{21}^*/P_{34}$ is similar to equation (1.61), except that the variable specific heat pressure ratio P_{21}^* is used instead of the Rankine-Hugoniot value, and the function Φ is used in the determination of P_{34} .

These relations are shown in figure 34 for Air/Air (the function Φ was taken as 1 in lieu of accurate data for air at very low temperatures). It is seen that the wave speed with variable specific heat for a given diaphragm pressure ratio, is less than the Rankine-Hugoniot value. However, the difference is small, and even at a diaphragm pressure ratio of 10,000 the wave speed is only about one percent slower than the Rankine-Hugoniot value. Thus from practical considerations for the case Air/Air the variation of the shock flow quantities due to deviations from thermal equilibrium are negligible. However, when He/Air and H₂/Air are used at a pressure ratio of 10,000 very high wave speeds are developed and the effects of a variable specific heat must be taken into account. In that case, for a given large diaphragm pressure ratio, the shock speed will start out with the value obtained from the Rankine-Hugoniot conditions and slow down during the relaxation period to the value predicted by the variable specific heat theory when the inert degrees have reached equilibrium (in about 50 μ sec at 5000°K). The contact surface velocity will be initially less than the equilibrium value by the same argument, and as a result the tail of the rarefaction wave will adjust itself during the relaxation period from a lower to a higher speed. In reality this idealized picture does not materialize due to the complex flow at the origin. The conditions across strong shock waves, however, as discussed above, do apply (references 9 and 16).



II. WAVE INTERACTIONS

In the previous sections the chamber and the channel were assumed to be of infinite length. In actual shock tube work the chamber and the channel are of finite length with open or closed ends. As a result, after a short time (milliseconds, depending on the channel length) the flow in a shock tube becomes quite complex due to the ensuing wave interactions.

When the diaphragm in a shock tube is ruptured, the shock wave proceeds along the channel and if it strikes a closed end it undergoes normal reflection in a non-linear manner. If the channel is open, then when the flow behind the shock wave is subsonic $M_2 < 1$, theoretically, a rarefaction wave is reflected back into the channel. Actually, due to the complex three-dimensional flow that takes place a shock wave is also reflected back into the channel. (Real flows at open chamber and channels will be discussed in Section 5). When the flow behind the shock wave is supersonic $M_2 > 1$, then theoretically a rarefaction wave cannot be reflected back from the open end of the channel.

In case of the rarefaction wave which is propagated into the chamber, if it encounters a closed end, then it undergoes normal reflection as a rarefaction wave; if it strikes an open chamber, then theoretically a reflected shock wave enters the chamber. Again, owing to the three-dimensional effects this is modified somewhat for a real flow (See Section 5).

Eventually, the reflected waves will interact with the contact surface and with each other and will give rise to a very complex flow pattern in the shock tube. As a result the reflected waves will determine the duration of the steady state flows in regions (3) and (2), and control the selection of the theoretical lengths of the chamber and channel of a finite shock tube for aerodynamic testing. Some of these interactions now will be considered in detail, assuming that γ is constant. It should be noted that the final states resulting from these interactions can be predicted from the (p, u) -plane solutions as outlined in section 1.03.

2.01 Normal Reflection of a Shock Wave

Figure 35 shows a simple shock tube with both ends closed and the resulting normal reflection of the rarefaction wave at the end of the chamber and the normal reflection of the shock wave at the end of the channel. From equation (1.63), the particle velocity behind the incident shock wave is

$$U_{21} = \frac{u_2}{a_1} = \frac{P_{21} - 1}{\gamma_1 [\beta_1 (\alpha_1 P_{21} + 1)]^{1/2}} \quad (2.1)$$

The boundary condition at the closed end of the channel is that the particle velocity after the head-on reflection must be zero. If this condition is to be satisfied then the particle velocity behind the reflected shock wave travelling into a gas at rest must be equal to the particle velocity behind the incident shock wave also entering a gas at rest. Hence,

$$u_2 = u_5 \quad (2.2)$$

$$\text{and} \quad U_{21} = U_{52} A_{21} \quad (2.3)$$

$$\text{or} \quad U_{21} = \frac{P_{52} - 1}{\gamma_1 [\beta_1 (\alpha_1 P_{52} + 1)]^{1/2}} \left[\frac{P_{21} (\alpha_1 + P_{21})}{1 + \alpha_1 P_{21}} \right]^{1/2} \quad (2.4)$$

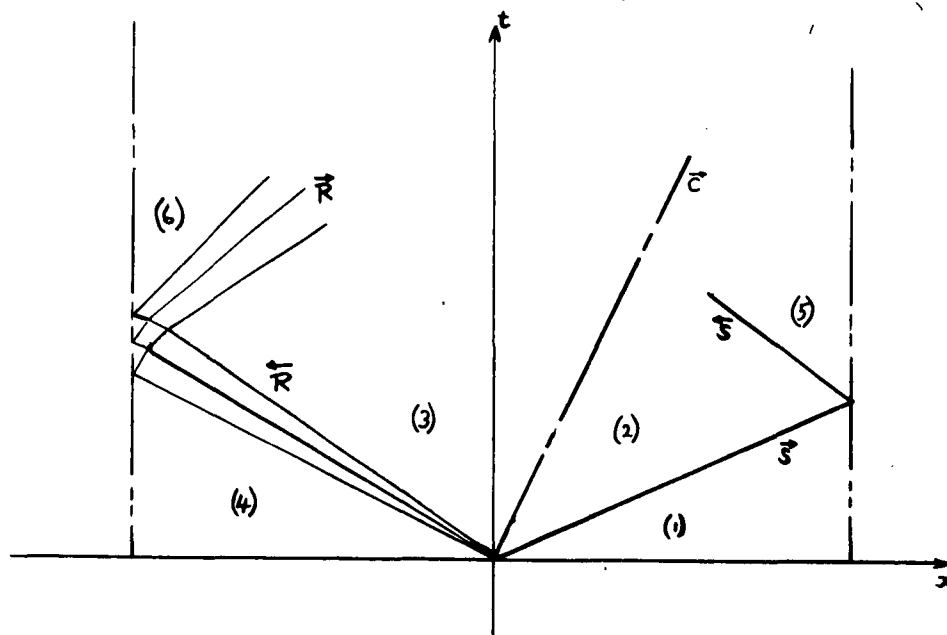


FIGURE 35

NORMAL REFLECTION OF A SHOCK WAVE AND RARE-
FACTION WAVE.

$$\text{or } \frac{P_{s1} - 1}{\gamma_1 [\beta_1 (\alpha_1 P_{s1} + 1)]^{1/2}} = \frac{P_{s2} - 1}{\gamma_1 [\beta_1 (\alpha_1 P_{s2} + 1)]^{1/2}} \left[\frac{P_{s1} (\alpha_1 + P_{s1})}{1 + \alpha_1 P_{s1}} \right]^{1/2} \quad (2.5)$$

$$\text{and } P_{s2} = \frac{\alpha_1 + 2 - P_{s1}}{1 + \alpha_1 P_{s1}} \quad (2.6)$$

Equation (2.6) gives the variation of the pressure ratio across the reflected shock wave in terms of the pressure ratio across the incident shock wave. It is seen that for an incident Mach wave $P_{s1} = 1$ and $P_{s2} = 1$. When the incident shock wave $P_{s1} \rightarrow \infty$, then $P_{s2} \rightarrow \alpha_1 + 2$. Thus for air, assuming a constant $\gamma = 1.40$, the strongest possible reflected wave $P_{s2} = 8$ (the limitations on the value of P_{s1} as outlined in table 2 should be noted).

The excess pressure ratio is defined as

$$\frac{P_2 - P_1}{P_2 - P_1} = 1 + \frac{P_{s1} (1 + \alpha)}{P_{s1} + \alpha} \quad (2.7)$$

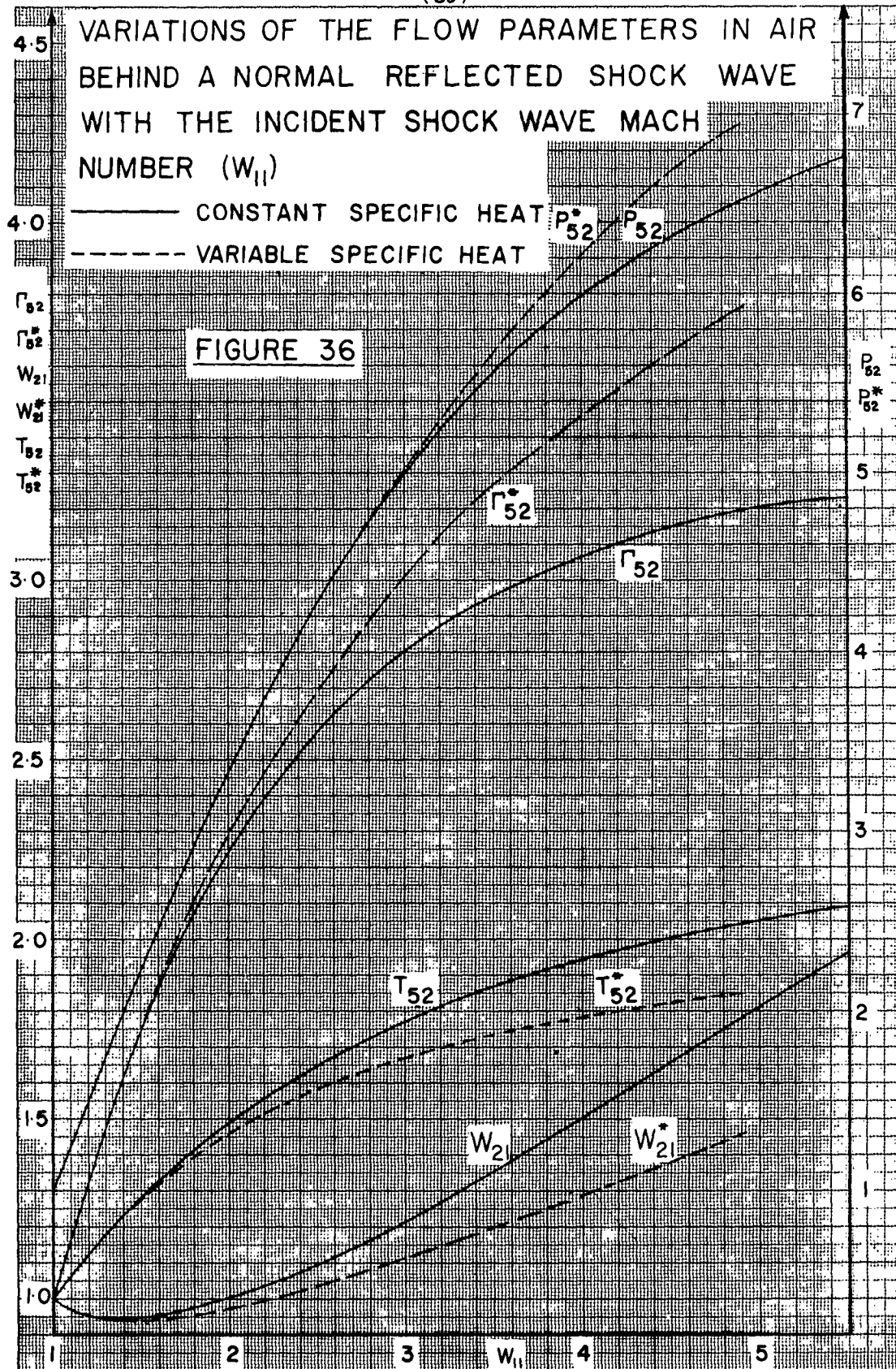
For a Mach wave $P_{s1} \rightarrow 1$ and the excess pressure ratio $\rightarrow 2$, which is the acoustic result for sonic reflection. If $P_{s1} \rightarrow \infty$, then the excess pressure ratio $\rightarrow P_{s2} \rightarrow 8$, as for (2.6).

The density ratio (Γ_{s2}) and the temperature ratio (T_{s2}) are obtained from equations (1.70) and (1.72)

$$\Gamma_{s2} = \frac{1 + \alpha_1 P_{s2}}{\alpha_1 + P_{s2}} \quad (2.8)$$

$$T_{s2} = \frac{P_{s2} (\alpha_1 + P_{s2})}{1 + \alpha_1 P_{s2}} \quad (2.9)$$

Thus, these ratios for $1 \leq P_{s2} \leq 8$ are identical with the values given for $1 \leq P_{s1} \leq 8$ on figure 21.



The limiting values of the above ratios when $P_{21} \rightarrow \infty$ and $P_{52} \rightarrow 8$, for air (assuming constant specific heat) are

$$\left[\frac{P_2}{P_1} \right]_{P_{21} \rightarrow \infty} = 3.500$$

$$\left[\frac{T_2}{T_1} \right]_{P_{21} \rightarrow \infty} = 2.286$$

The variation of these flow parameters with the initial shock wave Mach number (W_{11}) is shown on Figure 36.

The ratio of the incident shock wave speed (W_{11}) to the reflected shock wave speed (W_{21}) may be determined in a similar manner. The incident wave speed,

$$\frac{w_1}{a_1} = W_{11} = \left[\beta_1 (1 + \alpha_1 P_{21}) \right]^{\frac{1}{2}} \quad (1.73)$$

The reflected wave speed, if the gas in state (2) were at rest would be given by

$$\frac{w_2}{a_2} = \left[\beta_1 (1 + \alpha_1 P_{52}) \right]^{\frac{1}{2}}$$

From this the particle velocity u_2/a_1 must be subtracted to obtain the absolute velocity $|W_{21}|$, which is directed along the negative x-axis.

Thus

$$\left| \frac{w_2}{a_1} \right| = |W_{21}| = \frac{w_2 - u_2}{a_1} = \frac{w_2 a_2}{a_2 a_1} - \frac{u_2}{a_1} \equiv W_{21} \quad (2.10)$$

or

$$W_{21} = \left[\beta_1 (1 + \alpha_1 P_{52}) \right]^{\frac{1}{2}} \left[\frac{P_{21} (\alpha_1 + P_{21})}{1 + \alpha_1 P_{21}} \right]^{\frac{1}{2}} - \frac{P_{21} - 1}{\gamma_1 \left[\beta_1 (\alpha_1 P_{21} + 1) \right]^{\frac{1}{2}}} \quad (2.11)$$

Substituting for P_{52} from (2.6)

$$\text{then } W_{21} = \frac{P_{21}(\gamma_1 - 1) + 1}{\gamma_1 [\beta_1(\alpha_1 P_{21} + 1)]^{1/2}} \quad \text{or} \quad W_{21} = \frac{2 + (\alpha_1 - 1)P_{12}}{[(\alpha_1 + 1)P_{12}(\alpha_1 + P_{12})]^{1/2}} \quad (2.12)$$

$$\text{and } \frac{W_{21}}{W_{11}} = \frac{P_{21}(\gamma_1 - 1) + 1}{\gamma_1 \beta_1 (\alpha_1 P_{21} + 1)} \quad \text{or} \quad \frac{W_{21}}{W_{11}} = \frac{2 + (\alpha_1 - 1)P_{12}}{\alpha_1 + P_{12}} \quad (2.13)$$

For weak shock waves $P_{21} \rightarrow 1$ and $\frac{W_{21}}{W_{11}} \rightarrow 1$.

For infinitely strong shock waves $P_{21} \rightarrow \infty$ and

$$\left(\frac{W_{21}}{W_{11}} \right)_{P_{21} \rightarrow \infty} \rightarrow \frac{2}{\alpha_1} \quad (2.14)$$

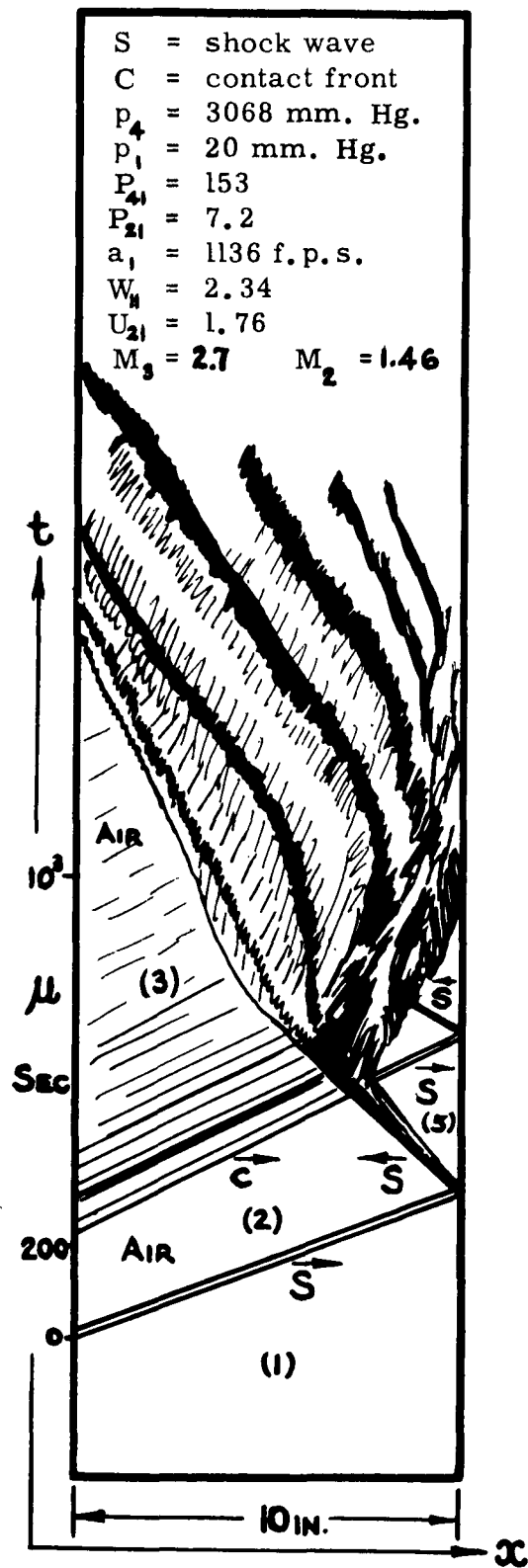
For air with constant specific heat, $\gamma_1 = 1.40$, $\alpha_1 = 6$ and

$$\left(\frac{W_{21}}{W_{11}} \right)_{P_{21} \rightarrow \infty} = \frac{2}{\alpha_1} = \frac{1}{3}$$

The reflected shock wave has a speed equal to the incident wave when they are both Mach waves (sound waves). The speed of the reflected wave then decreases as the incident wave strength increases until it reaches the value of one-third the incident wave velocity as $P_{21} \rightarrow \infty$.

For the case of Air/Air with $E_{14} = 1$, $\left(\frac{W_{21}}{W_{11}} \right)_{P_{21} \rightarrow \infty} = .351$, which is the minimum value of the wave speed ratio, and $W_{21} = .351 \times 6.16 = 2.16$.

It is of interest to note that in case of normal reflection the ratios P_{52} , Γ_{52} , T_{52} and $\frac{W_{21}}{W_{11}}$ remain finite when $P_{21} \rightarrow \infty$. These may be compared with the equivalent ratios in table 2, for the incident shock wave. A typical (x, t)-plane schlieren photograph of a normal reflected shock wave is shown on plate 2.



NORMAL REFLECTION, REFRACTION AND
 PROGRESSION OF A SHOCK WAVE THROUGH THE COLD
 REGION BEHIND THE CONTACT
 SURFACE.

PLATE 2.

When variable specific heat is considered then equation (2.12) is no longer applicable. The shock velocity is found in a step-by-step manner as outlined in section 1.06. For a given incident shock speed, the equilibrium values of the flow parameters are found from equations (1.134) to (1.136) or from figures 29 to 32. These flow quantities are now considered as the initial conditions for the reflected shock wave. Several final temperatures (less than the Rankine-Hugoniot values) are chosen for state (5) behind the reflected shock wave and equations (1.134) to (1.36) are utilized again. The boundary condition that the particle velocity in state (5) be zero, then is applied to the trials for a solution. The results for air, without dissociation, appear on Figure 36.

2.02 Normal Reflection of a Rarefaction Wave

The rarefaction wave which is formed when the diaphragm is ruptured travels along the chamber and undergoes normal reflection at the closed end (see figure 35).

It is shown in reference 38, that a steady state (6) is theoretically possible behind the reflected rarefaction wave if the initial diaphragm pressure ratio produces a rarefaction wave such that the speed of the tail of the wave $\frac{dx}{dt} \leq 2a_4$ for a diatomic gas and $\frac{dx}{dt} \leq a_4$ for a monatomic gas. At the limiting value of $\frac{dx}{dt}$, a total vacuum is produced in state (6) and $p_6 = 0$.

The physical quantities in state (6) behind the reflected rarefaction wave may be determined from the following considerations.

For a backward facing rarefaction wave from equation (1.26)

$$u_3 + \frac{2a_3}{\gamma_3 - 1} = u_4 + \frac{2a_4}{\gamma_4 - 1} \quad (2.15)$$

Similarly for a forward facing rarefaction wave

$$u_6 - \frac{2a_6}{\gamma_6 - 1} = u_3 - \frac{2a_3}{\gamma_3 - 1} \quad (2.16)$$

The boundary conditions are that initially $u_4 = 0$, and finally $u_6 = 0$ behind the reflected rarefaction wave. Subtraction of the above two equations yields

$$\frac{4a_3}{\gamma_4 - 1} = \frac{2}{\gamma_4 - 1} (a_4 + a_6) \quad (2.17)$$

or
$$\frac{a_6}{a_4} = \frac{2a_3}{a_4} - 1 \quad (2.18)$$

but
$$\frac{a}{a_4} = \left(\frac{T}{T_4}\right)^{1/2} = \left(\frac{P}{P_4}\right)^{\frac{\gamma_4 - 1}{2}} = \left(\frac{P}{P_4}\right)^{\frac{\gamma_4 - 1}{2\gamma_4}} \quad (1.30)$$

Therefore
$$P_{64}^{\beta_4} = 2P_{34}^{\beta_4} - 1 = 2(P_{14}P_{21})^{\beta_4} - 1 \quad (2.19)$$

Similarly
$$T_{64}^{1/2} = 2P_{34}^{\beta_4} - 1 \quad (2.20)$$

$$\Gamma_{64}^{\beta_4 \gamma_4} = 2P_{34}^{\beta_4} - 1 \quad (2.21)$$

Thus the flow quantities in state (6) may be determined from the known pressure ratio ($P_{34} = P_{14}P_{21}$) across the incident rarefaction wave. Also from equations (2.15) and (2.16),

$$\frac{2u_3}{a_3} = \frac{2}{\gamma_4 - 1} \left(\frac{a_4 - a_6}{a_3} \right) \quad (2.22)$$

$$M_3 = \frac{2}{\gamma_4 - 1} \left(\frac{1 - \frac{a_6}{a_4}}{\frac{a_6}{a_4} + 1} \right) \quad (2.23)$$

or
$$P_{64} = \left[\frac{\frac{2}{\gamma_4 - 1} - M_3}{\frac{2}{\gamma_4 - 1} + M_3} \right]^{1/\beta_4} \quad (2.24)$$

$$T_{64} = \left[\frac{\frac{2}{\gamma_4 - 1} - M_3}{\frac{2}{\gamma_4 - 1} + M_3} \right]^2 \quad (2.25)$$

$$\Gamma_{64} = \left[\frac{\frac{2}{\gamma_4 - 1} - M_3}{\frac{2}{\gamma_4 - 1} + M_3} \right]^{\frac{1}{\gamma_4 \beta_4}} \quad (2.26)$$

The above relations give the flow parameters in state (6) as a function of the known Mach number in state (3). It was noted above that in case of Air/Air a steady state region (6) is still possible for a rarefaction wave which has a tail with a characteristic slope of $\frac{dx}{dt} = 2a_4$. In this case it takes an infinite time for the state to form and the pressure $P_6 = 0$, i.e., a complete vacuum results. This limiting value may be achieved (equation 2.19) when $P_{34} = (\frac{1}{2})^7 = .00781$, or from equation (2.24) when $M_3 = 5$. This occurs at a diaphragm pressure ratio $P_{41} = 1620$ when the shock pressure ratio $P_{21} = 12.63$ for the case Air/Air, $\gamma = 1.40$, at $E_{14} = 1$. The values of the flow quantities in state (6) are plotted on figure 37. The dimensionless time (τ_6) of formation of the steady state (6) is given in reference (38) for the case of a monatomic gas in the chamber as,

$$\tau_6 = \frac{a_4 t_6}{L} = \frac{1 - 2P_{34}^{1/5} + 2P_{34}^{4/5}}{(2P_{34}^{1/5} - 1)^3} \quad (2.27)$$

and for a diatomic gas in the chamber

$$\tau_6 = \frac{a_4 t_6}{L} = \frac{1}{(2P_{34}^{1/2} - 1)^3} + \frac{6P_{34}^{3/2}(1 - P_{34}^{1/2})^2}{(2P_{34}^{1/2} - 1)^5} \quad (2.28)$$

where L = chamber length

t_6 = time state (6) forms from instant the diaphragm is ruptured. For example, case Air/Air, with $P_{41} = 10.5$ and $P_{21} = 2.90$, the tail of the rarefaction wave has a slope $\frac{dx}{dt} = 0$ and $M_3 = 1$. If $a_4 = 1130$ f.p.s. (22°C) and $L = 1$ ft., then $t_6 = 3.82$ milliseconds; for $P_{41} = 100$, $P_{21} = 6.35$, $t_6 = 71.1$ milliseconds. The variation of τ_6 with P_{41} for the combinations He/Air, A/Air and Air/Air is shown on Figure 38.

The duration of state (6) will be governed by the reflection of the reflected rarefaction^{or shock} wave from the contact surface, or in the case of a short channel by the reflected shock wave, and must be determined for a given experiment when state (6) is to be investigated (see fig. 40).

A typical normal reflection of a rarefaction wave appears on plate 3.

2.03 Interaction of a Shock Wave and a Contact Surface.

When the incident shock wave undergoes normal reflection at the end of the channel, it eventually interacts with the contact surface as shown on figure 39, plate 4 and plate 5.

FIGURE 37

VARIATION OF THE FLOW PARAMETERS
IN STATE (6) WITH THE PRESSURE
RATIO (P_{64}) ACROSS THE INCIDENT
RAREFACTION WAVE

 T_{64}

0.7

0.6

 Γ_{64}

0.5

0.4

 P_{64}

0.3

0.2

0.1

0

NOTE: In $P_{64} = 0.00812$ ($T_{64} = \Gamma_{64} = P_{64} = 0$)

 $\times 10^{-3}$

2

4

6

8

10

 $\times 10^{-2}$

2

4

6

8

10

 $\times 10^{-1}$

2

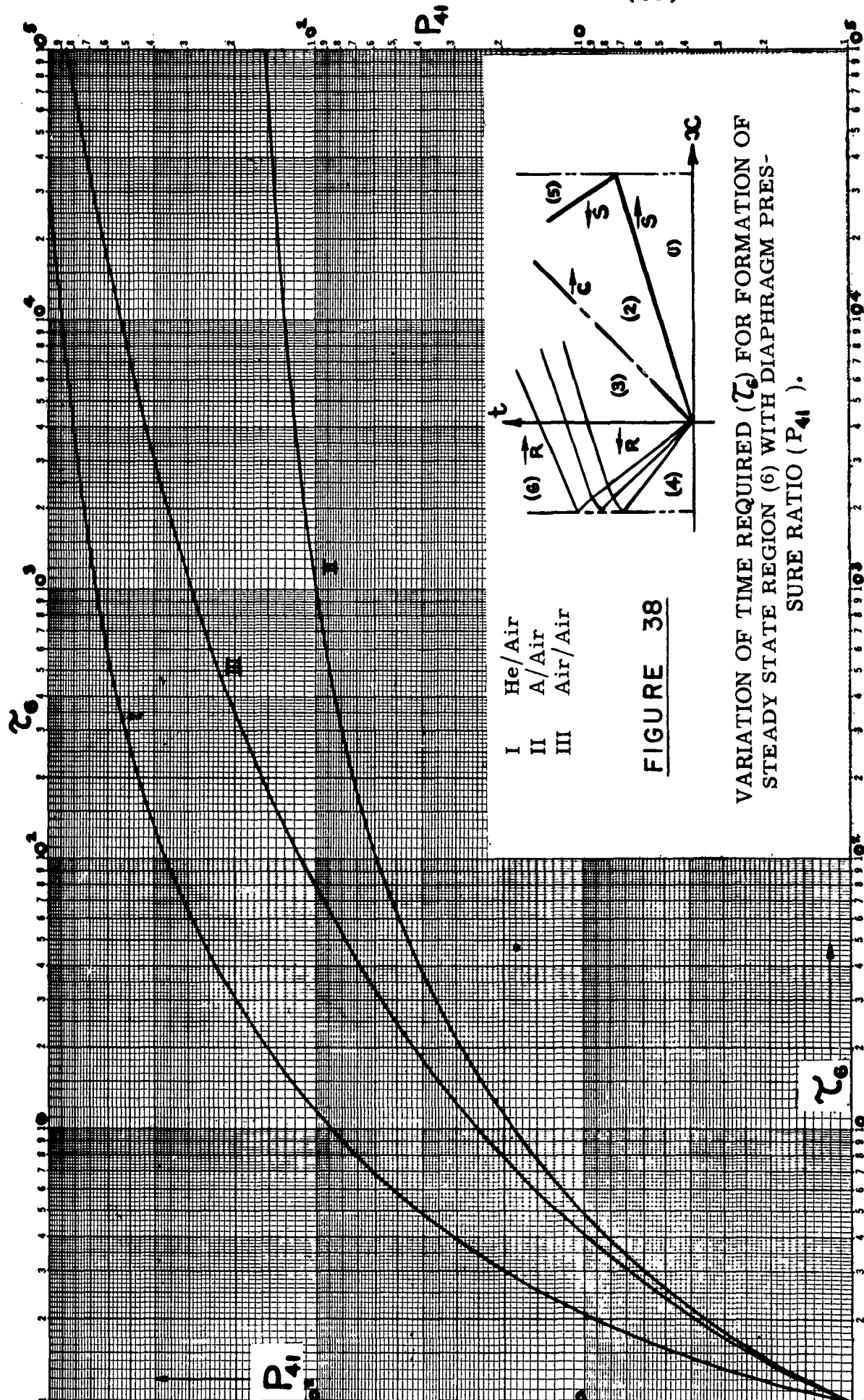
4

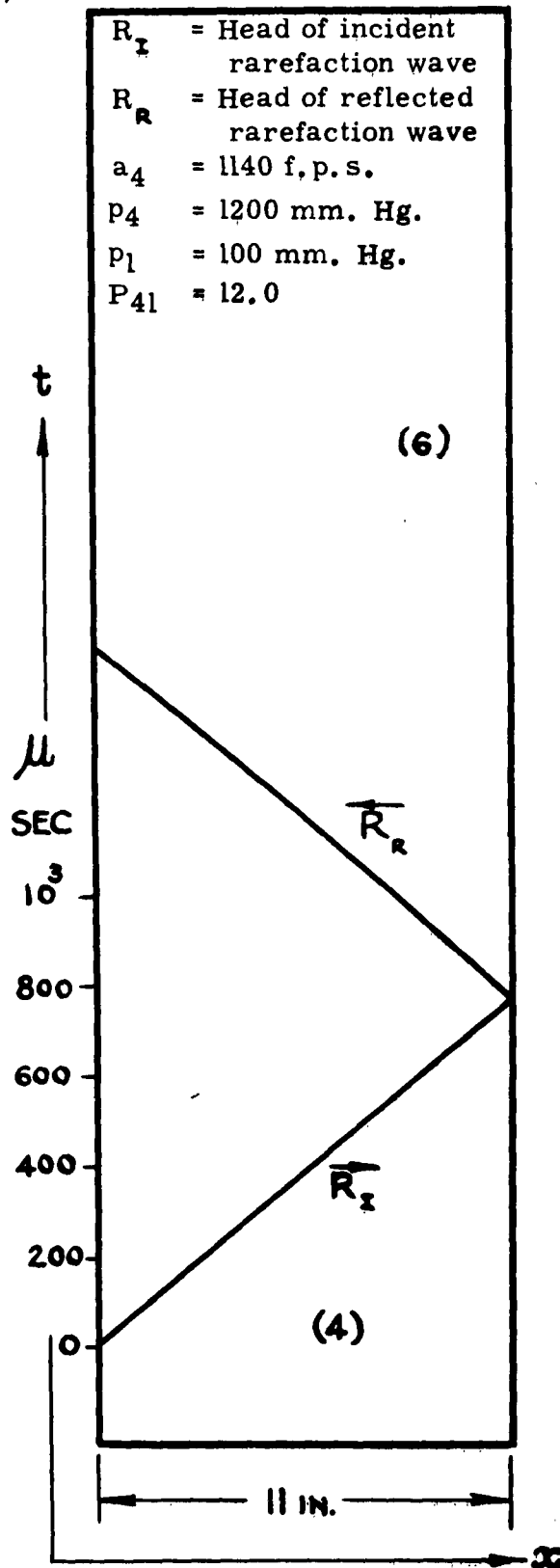
6

8

10

 P_{64} T_{64} Γ_{64} P_{64}





NORMAL REFLECTION OF A RAREFACTION WAVE
 AIR/AIR



S = Shock Wave
 C = Contact surface
 (He) $p_4 = 3080$ mm. Hg.
 (Air) $p_1 = 4.9$ mm. Hg.
 $P_{21} = 27.2$
 $W_{21} = 4.8$
 $a_1 = 1128$ f. p. s.

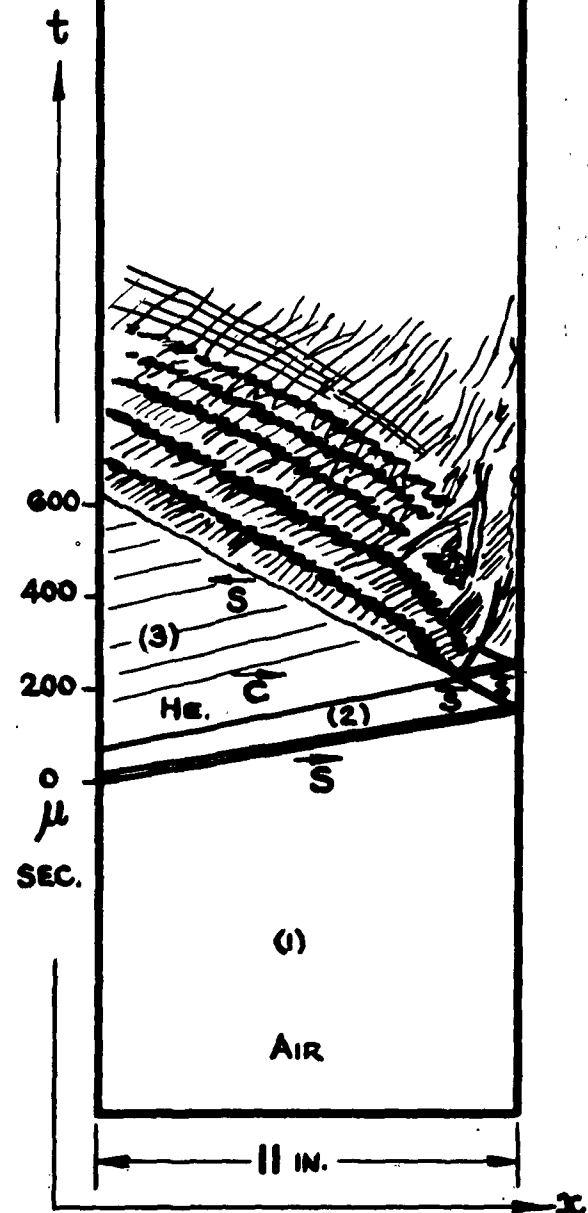


PLATE 4.

NORMAL REFLECTION AND REFRACTION OF A SHOCK WAVE
 AT AN AIR//HE CONTACT SURFACE



$P_{41} = 10$ $p_1 = 100 \text{ mm. Hg. (Air)}$ $p_4 = 1000 \text{ mm. Hg. (He)}$

$P_{21} = 4.60$ $W_{11} = 2.02$

PLATE 5.

THE REFRACTION OF A SHOCK WAVE AT AN AIR // He
CONTACT FRONT PRODUCED BY BREAKING THE DIAPHRAGM.

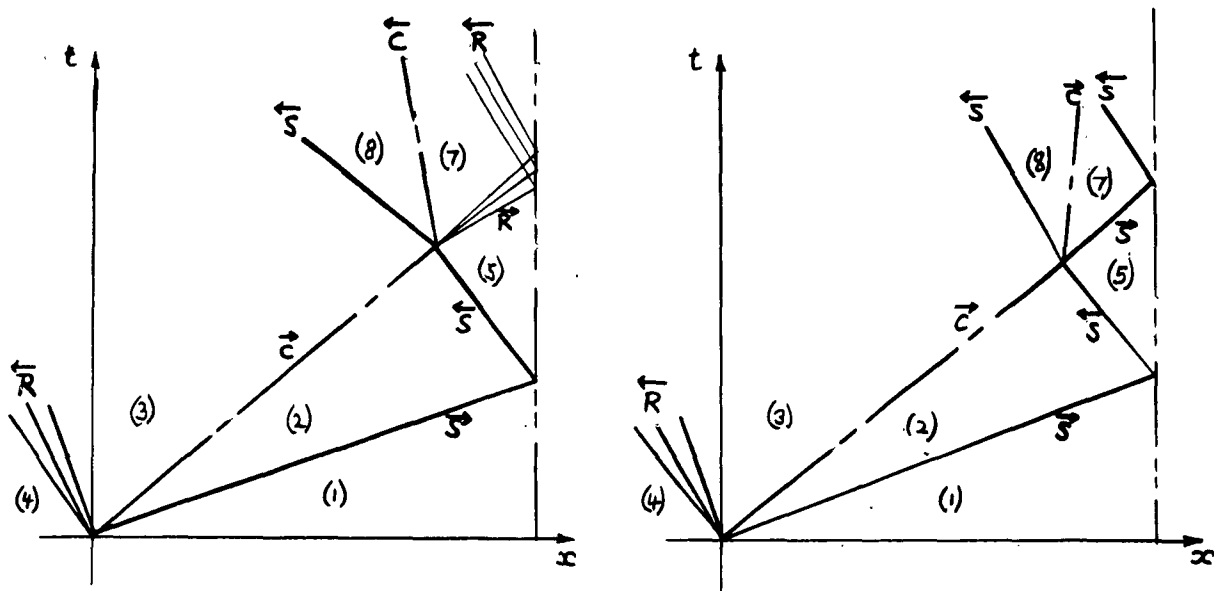


FIGURE 39

INTERACTION OF A SHOCK WAVE AND A CONTACT SURFACE.

The resulting refraction produces a transmitted shock wave and a reflected rarefaction wave if

$$E_{32_{min}} = \left[\frac{(C_v T)_3}{(C_v T)_2} \right]_{min} \geq \frac{\alpha_4 + P_{25}}{\alpha_1 + P_{25}} \quad (2.29)$$

or a reflected shock wave if

$$E_{32_{max}} \leq \frac{\alpha_4 + P_{25}}{\alpha_1 + P_{25}} \quad (2.30)$$

In the case of Air/Air, $\alpha_1 = \alpha_4$, $E_{32_{max, min}} = 1$, and since $E_{32} < 1$ a shock wave is always reflected back. The problem has been treated in detail theoretically and experimentally in references 11 and 12. The problem of shock wave refraction when extended to a finite layer of gas results in an overall absorption or attenuation of the incident shock wave pressure ratio, if the initial states are at room temperature. This case is illustrated on plate 6, for Air//He//Air, where the artificial microfilm contact surfaces are stationary, and will be discussed in section 5.

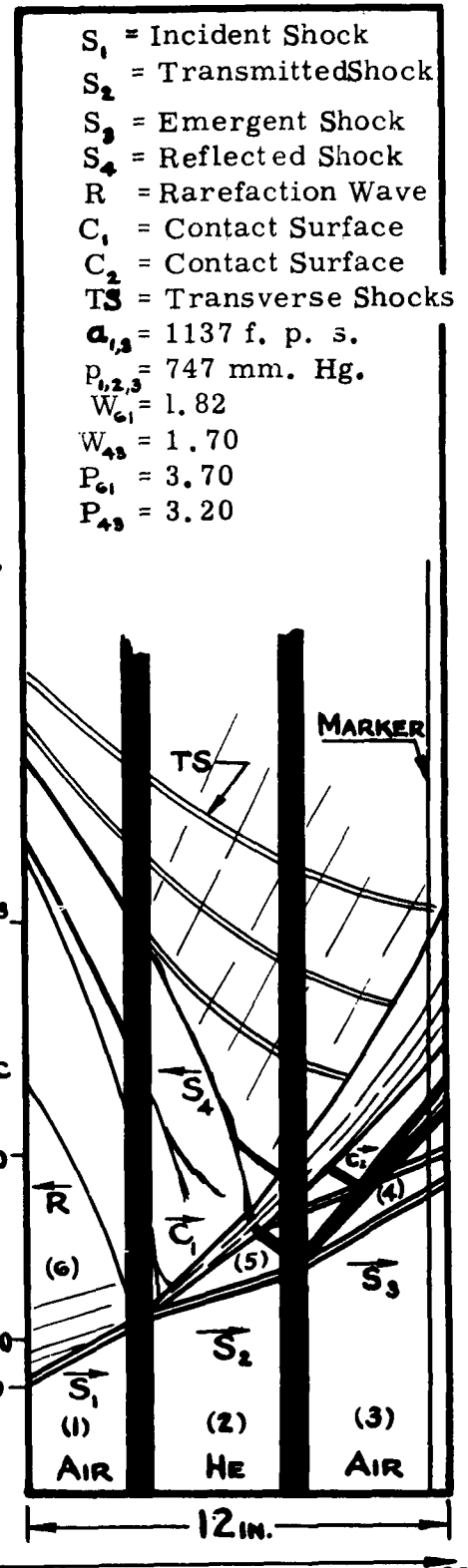


PLATE 6.

THE REFRACTION OF A SHOCK WAVE AT A LAYER OF HELIUM
 CASE Air//He//Air

2.04 Interaction of a Rarefaction Wave and a Contact Surface

The interaction of a rarefaction wave and a contact surface in a shock tube is shown in figure 40, and is produced by the initial rarefaction wave reflecting from the end of the chamber. The resulting refraction gives rise to a transmitted rarefaction wave and a reflected rarefaction wave if

$$E_{23\max} \leq \frac{\beta_1}{\beta_*} \left[\frac{1 - P_{63}^{\beta_*}}{1 - P_{63}^{\beta_1}} \right]^2 \quad (2.31)$$

or a transmitted rarefaction wave and a reflected shock wave (compression wave) if

$$E_{23\min} \geq \frac{\beta_1}{\beta_4} \left[\frac{1 - P_{63}^{\beta_4}}{1 - P_{63}^{\beta_1}} \right]^2 \quad (2.32)$$

The energy ratio is given by

$$E_{23} = \frac{(C_v T)_2}{(C_v T)_3}$$

In the case of Air/Air or H_2/N_2 , $\beta_1 = \beta_u$, $E_{22 \max, \min} = 1$ and since

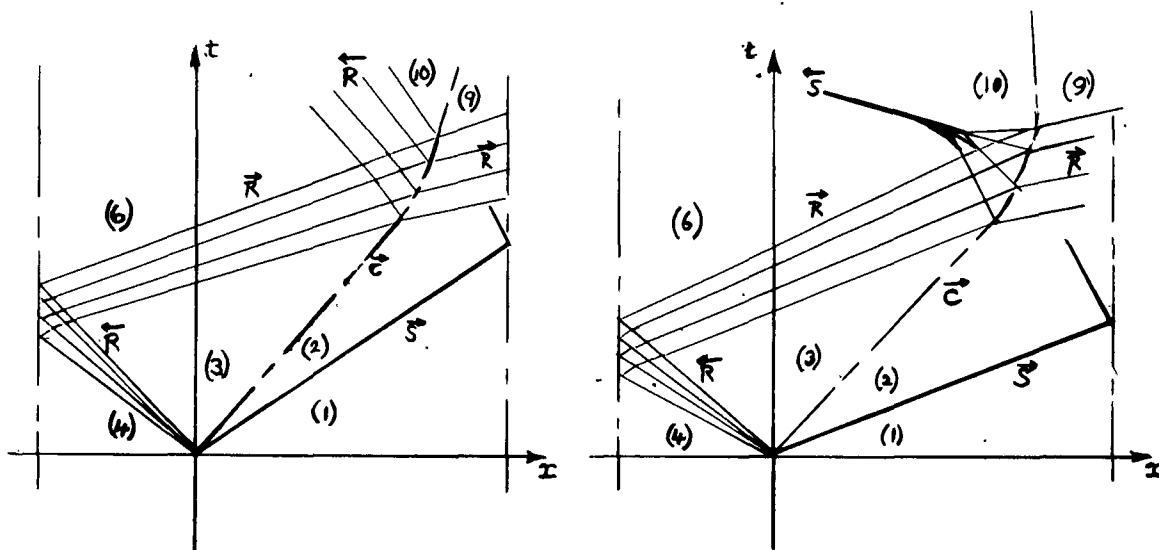


FIGURE 40

INTERACTION OF A RAREFACTION WAVE AND A CONTACT SURFACE

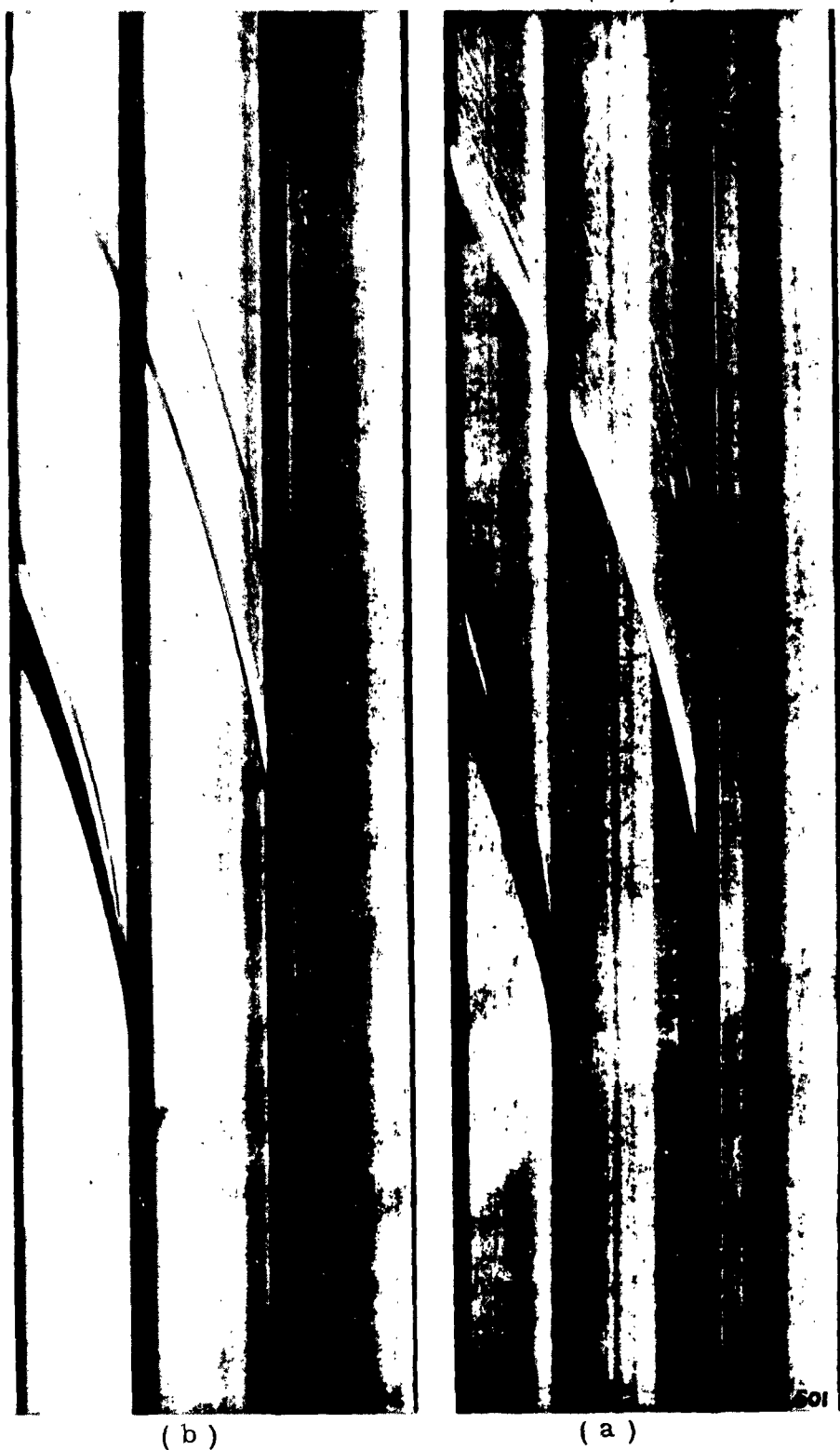
$E_{23} > 1$, a compression wave which forms a shock wave is always reflected back from the contact surface. To verify this type of interaction a method analogous to plate 6 can be utilized by using the simpler case of stationary contact surfaces, and this is illustrated for an actual case on plate 7. This interaction will be investigated at the Institute of Aerophysics at a later date.

Other basic wave interactions can also be studied in a shock tube (or wave interaction tube) with two chambers and a channel or two channels and a chamber (references 8 and 16). The most important of these interactions are:

- a) The head-on collision of two shock waves (the normal reflection of a shock wave from a rigid wall is obtained from the symmetric case of this interaction when the two waves are of equal strength.) An excellent account of the theoretical and experimental treatment of this problem appears in reference 16;
- b) The head-on collision of a shock wave and a rarefaction wave. The theoretical and experimental results are also given in reference 16.
- c) The overtaking of two similarly-facing shock waves (reference 40). This problem is difficult to set up in a shock tube and has recently been substantiated experimentally at the Institute of Aerophysics (see plate 37).
- d) The head-on collision of two rarefaction waves (the normal reflection of a rarefaction wave from a rigid wall is obtained from the symmetric case of this interaction when the two waves are of equal strength). A complete analytical solution for a diatomic and monatomic gas is given in reference 38. So far, this problem has not been studied in a systematic manner.
- e) The interaction of a shock wave and a wire screen. This will be discussed in section 5.

2.05. Theoretical Requirements for the Chamber and Channel Lengths of a Shock Tube.

The theoretical results of the previous interactions can be applied to determine the best combinations of chamber and channel lengths of a shock tube for the investigation of wave interactions or the steady state regions (6), (3), (2) and (5). In order to accomplish this it is necessary to determine the following positions on the (x, t) -plane or, what is equivalent, the (X, τ) -plane (figure 41),



(b)

(a)

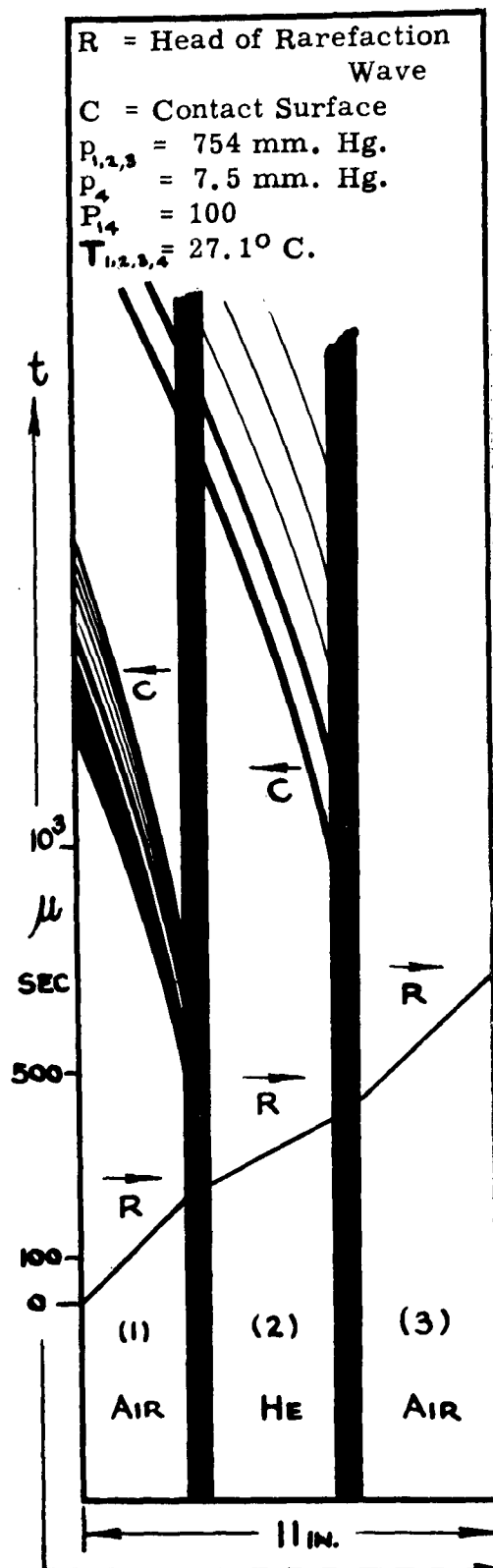


PLATE 7.

THE REFRACTION OF A RAREFACTION WAVE AT A LAYER OF HELIUM.

CASE Air || He || Air

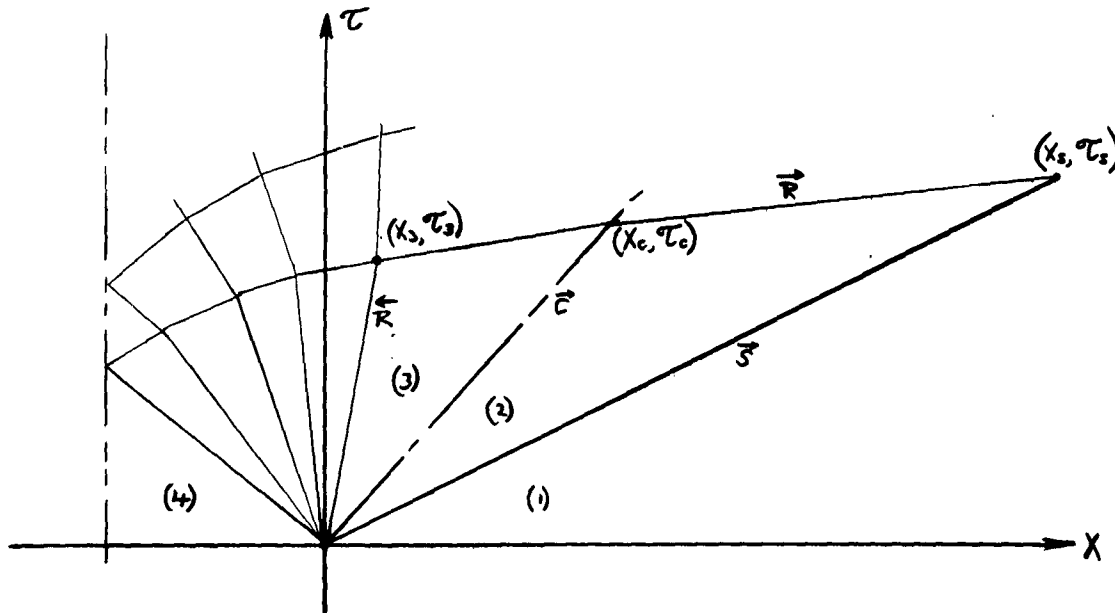


FIGURE 41.

POINTS IN THE (X, τ) -PLANE WHERE THE HEAD OF THE REFLECTED RAREFACTION WAVE OVERTAKES THE TAIL OF THE INCIDENT RAREFACTION WAVE (X_3, τ_3) , THE CONTACT SURFACE (X_c, τ_c) , AND THE SHOCK WAVE (X_s, τ_s) .

- a) Point (X_c, τ_c) where the steady state region (6) forms behind the reflected rarefaction wave.
- b) Point (X_3, τ_3) where the head of the reflected rarefaction wave overtakes the tail of the incident rarefaction wave.
- c) Point (X_c, τ_c) where the head of the reflected rarefaction wave overtakes the contact surface.
- d) Point (X_s, τ_s) where the head of the reflected rarefaction wave overtakes the shock wave.
- e) Point (X_s, τ_s) where the steady state region (5) forms behind the reflected shock wave.

The point (X_c, τ_c) is given by $(-1, \tau_c)$. The value of τ_c as a function of the diaphragm pressure ratio P_{41} is shown on figure 38 for different gas combinations.

The relations which determine the points (X_3, τ_3) , (X_c, τ_c) , and (X_s, τ_s) are developed in detail in reference 35, from which the following equations are quoted,

$$X_3 = (\alpha_4 - 1 - \alpha_4 P_{34}^{\beta_4}) P_{34}^{-\frac{\beta_4 \alpha_4}{2}} \quad (2.32)$$

$$\tau_3 = P_{34}^{-\frac{\beta_4 \alpha_4}{2}} \quad (2.33)$$

$$X_c = 2(\alpha_4 - 1)(1 - P_{34}^{\beta_4}) P_{34}^{-\frac{\beta_4 \alpha_4}{2}} \quad (2.34)$$

$$\tau_c = 2\tau_3 \quad (2.35)$$

$$X_3 = W_{11} A_{14} \tau_s \quad (2.36)$$

$$\tau_s = \frac{2A_{21} \tau_3}{U_{21} + A_{21} - W_{11}} \quad (2.37)$$

- where W_{11} , A_{21} and U_{21} are given by equations (1.73), (1.72) and (1.63) respectively and A_{14} is defined as for equation (1.64). The above values are plotted on figures 42 to 45 for different gas combinations against the diaphragm pressure ratio (P_{41}) for $T_{14} = 1$, i.e., the initial temperatures in the chamber and channel are equal.

It is interesting to note that the position where the head of the reflected rarefaction wave will overtake the shock wave has a minimum value at a low diaphragm pressure ratio, which in the case of Air/Air, $P_{41} \approx 4$ and for He/Air, $P_{41} \approx 5$. For a chamber length of one foot, the minimum channel length occurs for Air/Air at about 15 ft. and for He/Air at 4 feet. For diaphragm pressure ratios approaching one or infinity the overtaking process theoretically takes place at an infinite distance. If shock wave studies are conducted at the lower diaphragm pressure ratios, they should be made before the overtaking process takes place in order to prevent shock wave decay.

It may be seen from figure 46 that the maximum flow duration $\Delta\tau_3$ for the uniform state (3) occurs at X_3 for all diaphragm pressure ratios (P_{41}) for which $M_3 > 1$. If $M_3 < 1$, then the maximum occurs at $X = 0$. Similarly the maximum $\Delta\tau_2$ for region (2) occurs at X_c . These values may be obtained from figures 42 to 45. If aerodynamic testing is to be done in regions (3) or (2) then the maximum testing time, for a set

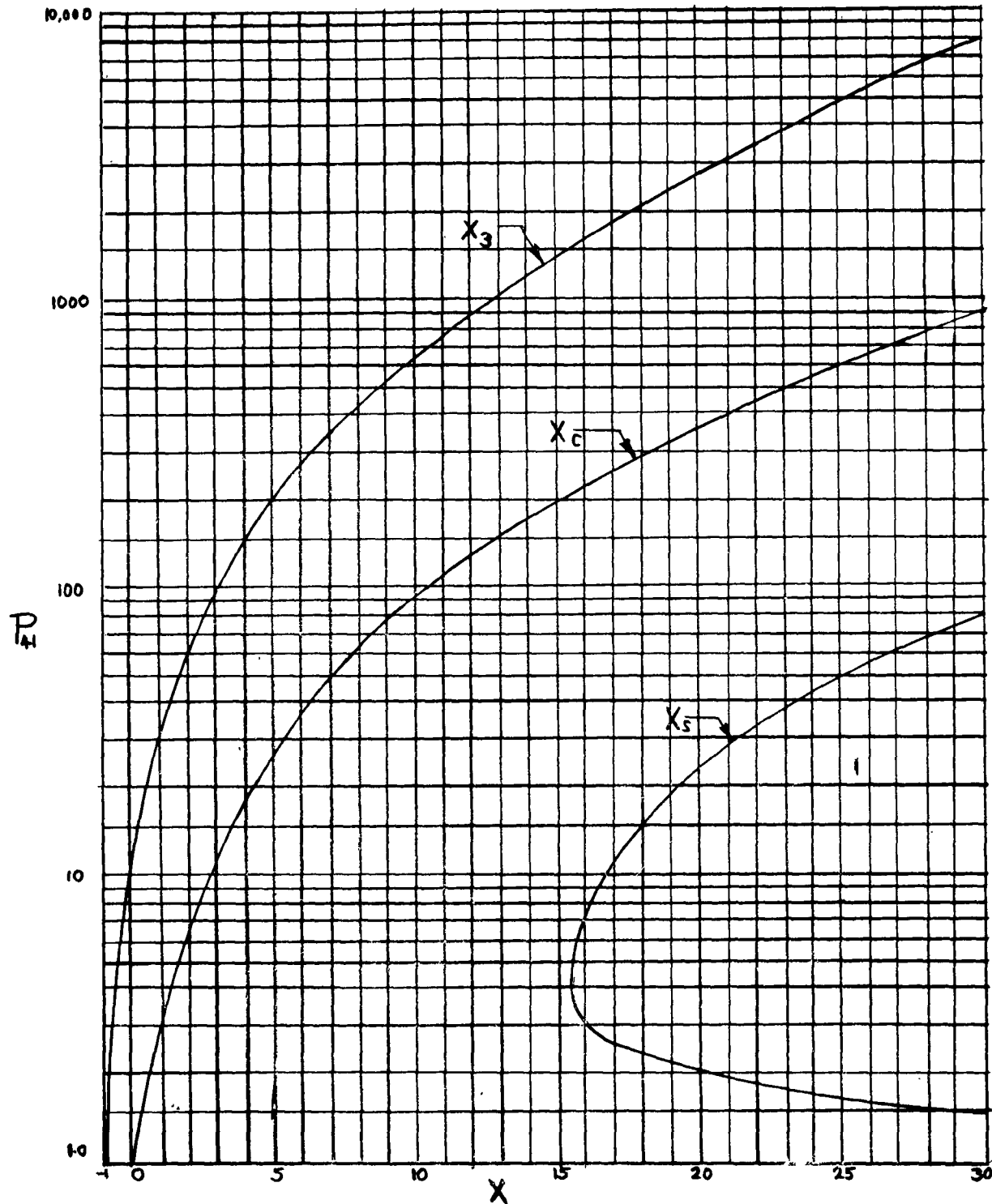


FIGURE 42

VARIATION OF X_3 X_c X_s WITH THE PRESSURE RATIO P_{41}
ACROSS THE DIAPHRAGM FOR AIR/AIR. $T_{14} = 1$ OR $E_{14} = 1$

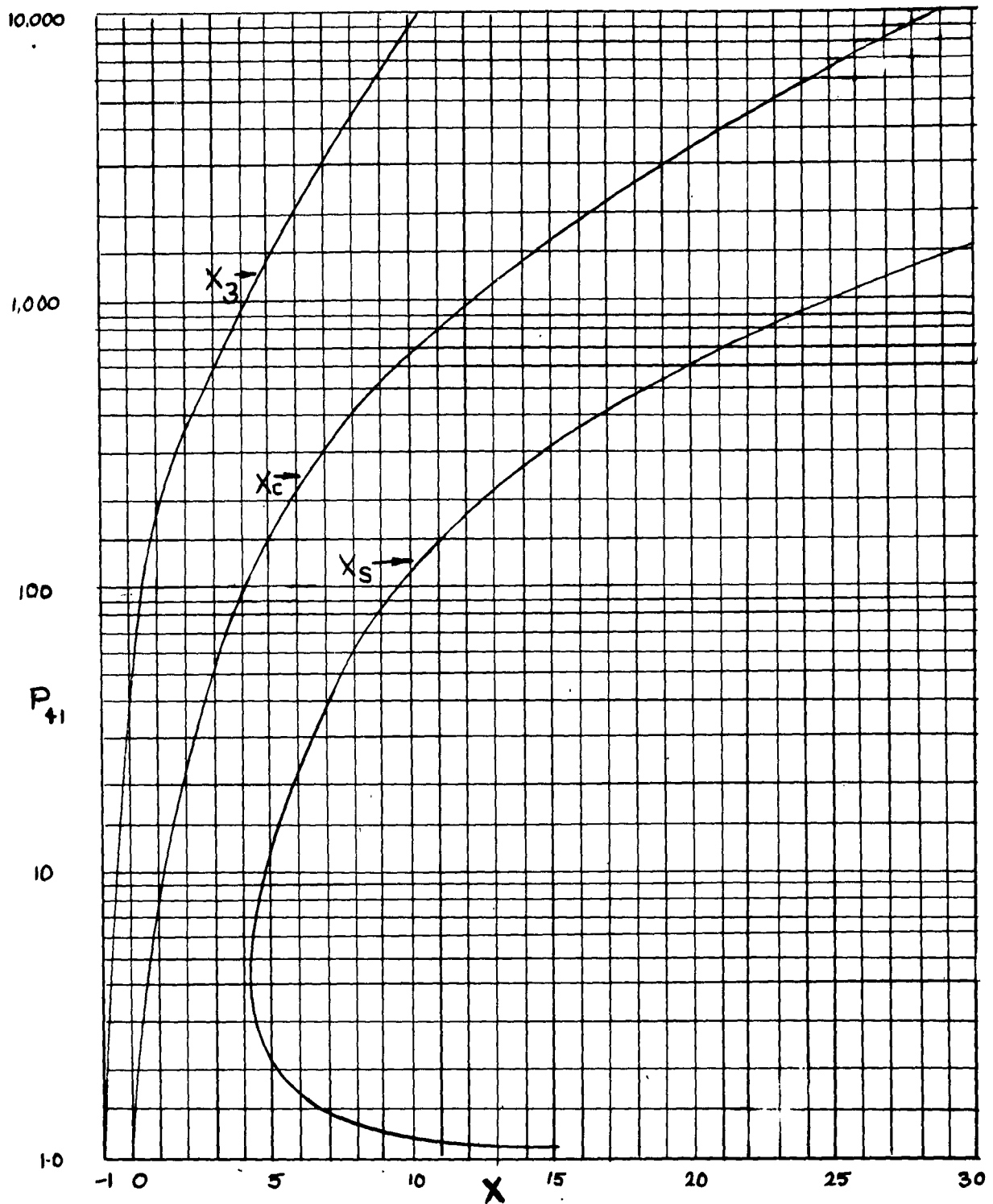


FIGURE 43

VARIATION OF X_3 , X_c , X_s WITH THE PRESSURE RATIO P_{41}
ACROSS THE DIAPHRAGM FOR HE/AIR. $T_{14} = 1.$

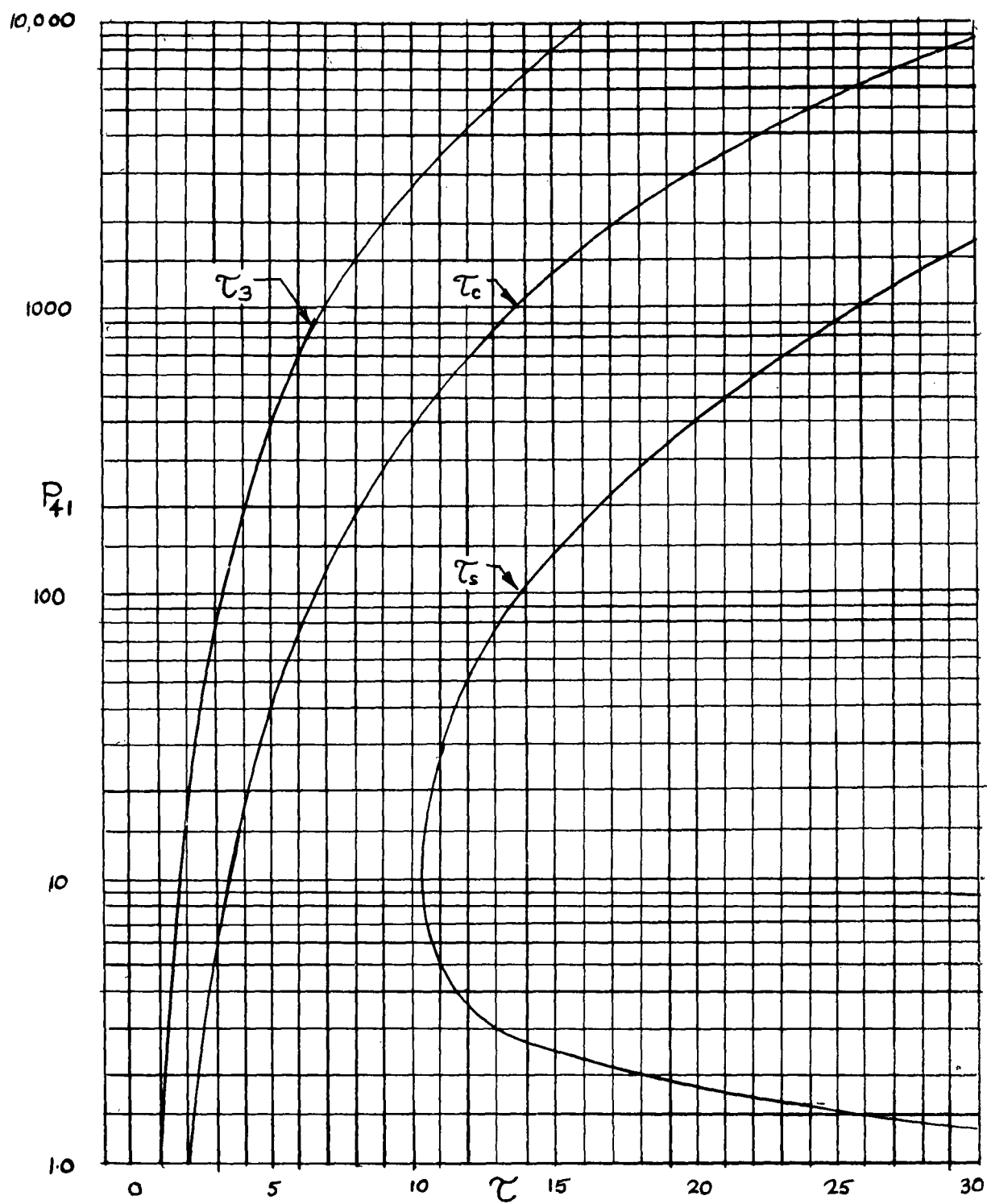


FIGURE 44

VARIATION OF τ_3 , τ_c , τ_s WITH THE PRESSURE RATIO P_{41} ACROSS THE DIAPHRAGM FOR AIR/AIR $T_{14} = 1$ or $E_{14} = 1$.

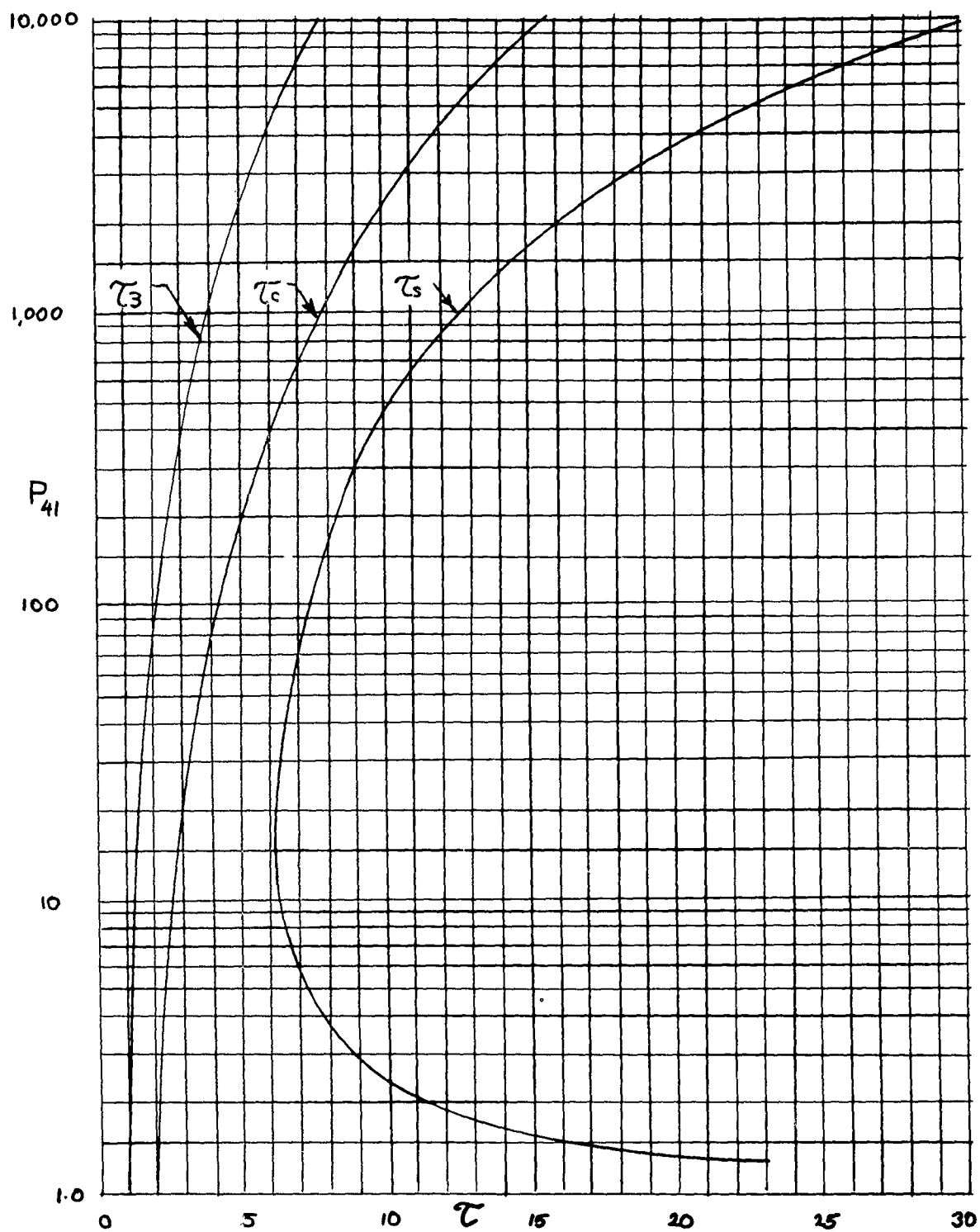


FIGURE 45

VARIATION OF τ_3, τ_c, τ_s WITH THE PRESSURE RATIO P_{41} ACROSS THE DIAPHRAGM FOR HE/AIR $T_{14} = 1$.



FIGURE 46

POINTS OF MAXIMUM FLOW DURATION X_3 AND X_c FOR REGIONS (3) AND (2) RESPECTIVELY

of initial conditions, is obtained by placing the model at X_3 and X_c respectively. In order to eliminate the possibility of the reflected shock wave decreasing the maximum flow duration $\Delta\tau_2$ for region (2), the channel should be of a length (X_5), such that the reflected shock wave meets the head of the reflected rarefaction wave at the contact surface, i.e., the point (X_c, τ_c). The length X_5 may be determined as follows. The dimensionless time (τ_c) it takes for the shock wave to hit the end of the tube, reflect and interact with the contact surface, follows at once from geometrical considerations:

$$\tau_c = \frac{X_5}{W_{11} A_{14}} + \frac{X_5 - X_c}{W_{21} A_{14}} \quad (2.38)$$

Solving for X_5 , one obtains the required channel length.

$$X_5 = \frac{\tau_c A_{14} + \frac{X_c}{W_{21}}}{\frac{1}{W_{11}} + \frac{1}{W_{21}}} \quad (2.39)$$

where W_{11} and W_{21} are the absolute magnitudes of the incident and reflected shock speeds as given by equations (1.73) and (2.11). Again, τ_c is given by equation (2.35).

In order to avoid excessive channel lengths when region (3) is under investigation it is sufficient to use a length X_2 , such that the reflected shock wave strikes the contact surface when the head of the reflected rarefaction wave overtakes the tail of the incident wave, i.e., the time τ_3 . This practical simplification eliminates the necessity of solving the complex shock-contact surface interaction. Since from equation (2.35) $\tau_c = 2\tau_3$, therefore

$$X_2 = \frac{1}{2} X_5 \quad (2.40)$$

The variation of X_5 with the diaphragm pressure ratio (P_{41}) is plotted on figure 47. It is seen that X_5 is only slightly greater than X_c , for the higher diaphragm pressure ratios (figures 42 to 45), because the reflected shock speed (W_{21}) decreases as P_{41} increases. If the channel length is increased beyond that required for maximum $\Delta\tau_3$ and $\Delta\tau_2$, then these values are unaffected; if they are decreased, the testing time is reduced by the wave interactions.

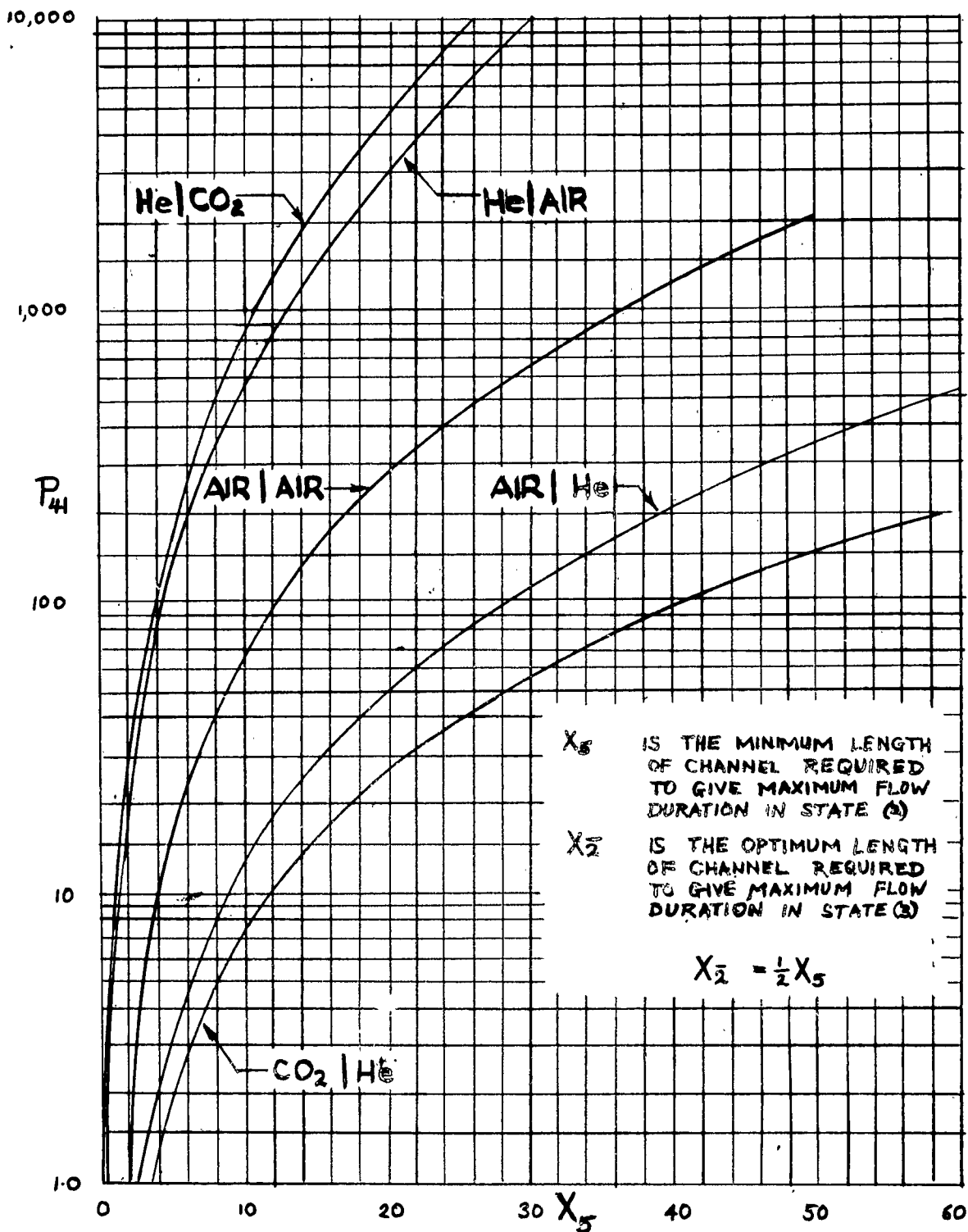


FIGURE 47

VARIATION OF X_5 AND X_2 WITH THE PRESSURE RATIO (P_{41})
ACROSS THE DIAPHRAGM FOR DIFFERENT GAS COMBINATIONS.

III. PRODUCTION OF STRONG SHOCK WAVES

In section 2 it was shown that to produce strong shock waves it was necessary that $P_{41} \rightarrow \infty$ and $E_{14} \rightarrow 0$. In practice the above ratios are governed by the experimental conditions. The magnitude of p_4 is limited by the structural strength of the chamber; p_1 is limited to about 0.5 mm. Hg., when the schlieren system is at its flow response limit. The energy ratio E_{14} can be reduced quite easily by using gas combinations such as H_2/A or H_2/SF_6 . Any further reduction may be achieved by heating the gas in the chamber and cooling the gas in the channel. If this is done by external or internal means (flame, electric elements, refrigeration devices) the simple shock tube soon becomes a complex piece of apparatus and these methods cannot be recommended.

However, it is possible to heat the gas in the chamber by three very convenient methods, which may be used in conjunction with high pressure ratios and effective gas combinations to produce strong shock waves.

(1) The gas in the chamber can be used in conjunction with other gases to produce a combustible mixture, which is ignited by means of a glow plug. At high pressures (400 p.s.i.) this can be accomplished by just rupturing the diaphragm, and no other ignition is required. Combinations such as one mole of oxygen to six of hydrogen or a stoichiometric mixture of oxygen and hydrogen diluted with 80 per cent helium produce a sizeable gain in shock Mach number (Mach numbers up to 17 have been produced at Cornell Aeronautical Laboratories in this manner), without undue modification of the existing shock tube (reference 29).

(2) The gas in the chamber can be heated rapidly to a high temperature by passing a high voltage discharge directly through it. This method has proven to be simple and successful, and shock wave Mach numbers $W_{11} > 30$, have already been produced (references 29 and 47).

(3) The gas in the chamber can be quickly heated by passing a very high current through fine copper wires stretched between two elements in the chamber. The wires are burned in the process. This method may be very useful when used in conjunction with method (1) in order to avoid detonation. The vaporized wire may, however, reduce the internal energy somewhat.

In combination with the above methods it is possible to obtain even stronger shock waves for a given set of initial conditions across the diaphragm by using shock tubes of varying cross-sections (see reference 37 where this problem was first advanced and treated in detail). The modification of the simple shock tube to produce stronger shock waves consists basically in using a chamber of larger cross-sectional area (A_4) than the

channel (A_1) as shown in figure 48. As in the simple shock tube, the origin or the plane of the diaphragm, represents a serious discontinuity, where shock wave diffraction, vortices and three-dimensional effects would be present, but this would tend to be smoothed out after a short time interval. As a result, a cylindrical chamber may be used advantageously with a channel of square or rectangular cross-section. It would be helpful to flare the channel section at the diaphragm in order to achieve the change in cross-section in a gradual manner, and thereby reduce discontinuous changes in the flow at the origin. This type of shock tube has already been used at Cornell University and Cornell Aeronautical Laboratory. However, the basic experimental data has not been reported to date.

The increase in shock strength is obtained from an additional two dimensional steady subsonic expansion in the plane of the diaphragm which converts thermal energy into kinetic energy.

If the initial conditions are such that behind the contact surface $M_3 > 1$, then sonic velocity (designated by $(*)$) is reached at the diaphragm ($x = 0$), (figure 48). Under these conditions M_5 is given by the

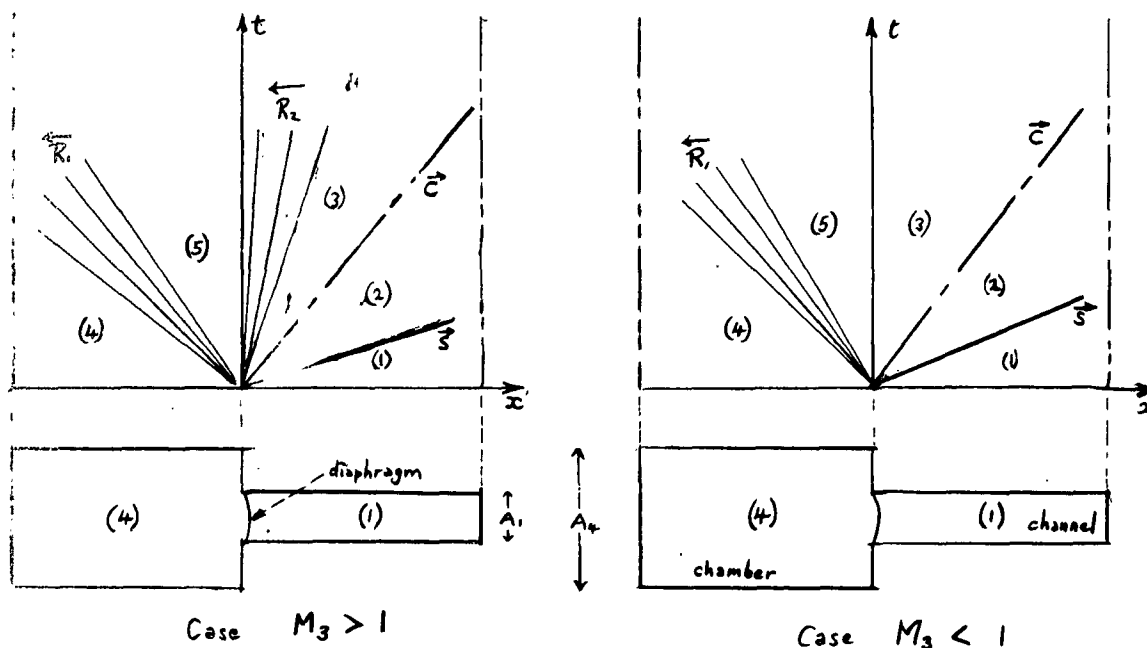


FIGURE 48

FLOW IN A SHOCK TUBE WITH A LARGE CHAMBER

one-dimensional steady flow equation

$$\frac{A_4}{A^*} = \frac{A_4}{A_1} = \frac{1}{M_5} \left[\frac{2 + (\gamma-1) M_5^2}{(\gamma+1)} \right]^{\frac{\gamma+1}{2(\gamma-1)}} \quad (3.1)$$

and $M_5 = 0$ when $\frac{A_4}{A_1} \rightarrow \infty$; when $A_4 = A_1$, $p_5 = p_3$.

The pressure ratio for a rarefaction wave (R_1) which accelerates the gas from rest to M_5 is given by the unsteady flow equation (see section 1)

$$\frac{p_4}{p_5} = \left(1 + \frac{\gamma-1}{2} M_5^2 \right)^{\frac{2\gamma}{\gamma-1}} \quad (3.2)$$

Further acceleration to reach sonic velocity in A_1 requires a pressure ratio given by the steady flow relations

$$\frac{p_4}{p_5} = \left(1 + \frac{\gamma-1}{2} M_5^2 \right)^{\frac{\gamma}{\gamma-1}} \quad \frac{p_4}{p^*} = \left(\frac{\gamma+1}{2} \right)^{\frac{\gamma}{\gamma-1}}$$

or

$$\frac{p_3}{p^*} = \left(\frac{\gamma+1}{2 + (\gamma-1) M_5^2} \right)^{\frac{\gamma}{\gamma-1}} \quad (3.3)$$

where p_4 is the conserved stagnation pressure.

Finally, to reach $M_3 > 1$, a second rarefaction wave (R_2) is required such that

$$\frac{p^*}{p_3} = \left(\frac{2 + (\gamma-1) M_3^2}{\gamma+1} \right)^{\frac{2\gamma}{\gamma-1}} \quad (3.4)$$

Thus when $M_3 > 1$ is given for a known tube geometry A_4 and A_1 , the overall pressure ratio across the rarefaction waves is given by

$$P_{43} = \frac{p_4}{p_3} \frac{p_5}{p^*} \frac{p^*}{p_3} \quad (3.5)$$

It will be noted when $\frac{A_4}{A_1} \rightarrow \infty$, $M_5 \rightarrow 0$, $P_{43} \rightarrow 1$ and the first rarefaction wave disappears and

$$P_{43} = \left(\frac{2}{\gamma+1} \right)^{\frac{\gamma}{\gamma-1}} \left(1 + \frac{\gamma-1}{2} M_3^2 \right)^{\frac{2\gamma}{\gamma-1}} \quad (3.6)$$

Similarly, to obtain the particle velocity u , then from the first rarefaction wave,

$$\frac{a_5}{a_4} = \frac{1}{1 + \frac{\gamma-1}{2} M_5^2} \quad (3.7)$$

For the steady expansion from A_4 to A_1

$$\frac{a^*}{a_5} = \left(\frac{p^*}{p_5} \right)^{\frac{\gamma-1}{2\gamma}} = \left(\frac{2 + (\gamma-1) M_5^2}{\gamma+1} \right)^{1/2} \quad (3.8)$$

For the second rarefaction wave

$$\frac{a_*}{a_3} = \left(\frac{p_*}{p_3} \right)^{\frac{\gamma-1}{2\gamma}} = \frac{2 + (\gamma-1)M_3}{\gamma+1} \quad (3.9)$$

Hence the particle velocity u_3 (contact surface velocity) is given by

$$\frac{u_3}{a_*} = \frac{u_2}{a_3} \frac{a_3}{a_*} = \frac{(\gamma+1)M_3}{2 + (\gamma-1)M_3} \quad (3.10)$$

or

$$\frac{u_3}{a_4} = \frac{u_3}{a_*} \frac{a_*}{a_5} \frac{a_5}{a_4} \quad (3.11)$$

when $A_4/A_1 \rightarrow \infty$, $M_5 \rightarrow 0$ and

$$\frac{u_3}{a_4} = \sqrt{\frac{\gamma+1}{2}} \left(\frac{M_3}{1 + \frac{\gamma-1}{2} M_3^2} \right) \quad (3.12)$$

For the subsonic case $M_3 < 1$, the pressure ratio across the first rarefaction wave (R_1) is given by

$$\frac{p_4}{p_5} = \left(1 + \frac{\gamma-1}{2} M_5^2 \right)^{\frac{2\gamma}{\gamma-1}}$$

The second rarefaction wave (R_2) is no longer required, and since the stagnation pressure p_4 is conserved, p_3/p_5 is obtained from M_5 and M_3 using the steady flow relations

$$\frac{p_5}{p_3} = \frac{p_5}{p_*} \frac{p_*}{p_3} = \left(\frac{2 + (\gamma-1)M_3^2}{2 + (\gamma-1)M_5^2} \right)^{\frac{\gamma}{\gamma-1}} \quad (3.13)$$

and M_3 is given by the area ratio

$$\frac{A_4}{A_1} = \frac{M_3}{M_5} \left(\frac{2 + (\gamma-1)M_5^2}{2 + (\gamma-1)M_3^2} \right)^{\frac{\gamma+1}{2(\gamma-1)}} \quad (3.14)$$

The overall pressure ratio p_{43} is obtained from

$$p_{43} = \frac{p_4}{p_5} \frac{p_5}{p_3} \quad (3.15)$$

When $\frac{A_4}{A_1} \rightarrow \infty$, $M_5 \rightarrow 0$ and

$$p_{43} = \left(1 + \frac{\gamma-1}{2} M_3^2 \right)^{\frac{\gamma}{\gamma-1}} \quad (3.16)$$

In a similar manner, the particle velocity u_3 may be determined. For the rarefaction wave (R_1),

$$\frac{u_5}{a_4} = \frac{u_5}{a_5} \frac{a_5}{a_4} = \frac{M_5}{1 + \frac{\gamma-1}{2} M_5^2} \quad (3.17)$$

From the one-dimensional steady continuity equation,

$$p_3 u_3 A_1 = p_5 u_5 A_4 \quad (3.18)$$

$$\text{or} \quad \frac{u_3}{u_5} = \frac{\rho_5}{\rho_3} \frac{A_4}{A_1} = \frac{M_3}{M_5} \left(\frac{2 + (\gamma-1)M_5^2}{2 + (\gamma-1)M_3^2} \right)^{1/2} \quad (3.19)$$

$$\text{But} \quad \frac{u_3}{a_4} = \frac{u_3}{u_5} \frac{u_5}{a_4} \quad (3.20)$$

When $A_1/A_4 \rightarrow \infty$, $M_5 \rightarrow 0$ and

$$\frac{u_3}{a_4} = \frac{M_3}{(1 + \frac{\gamma-1}{2} M_3^2)^{1/2}} \quad (3.21)$$

It is interesting to note that for $M_3 \geq 1$, and constant a_4

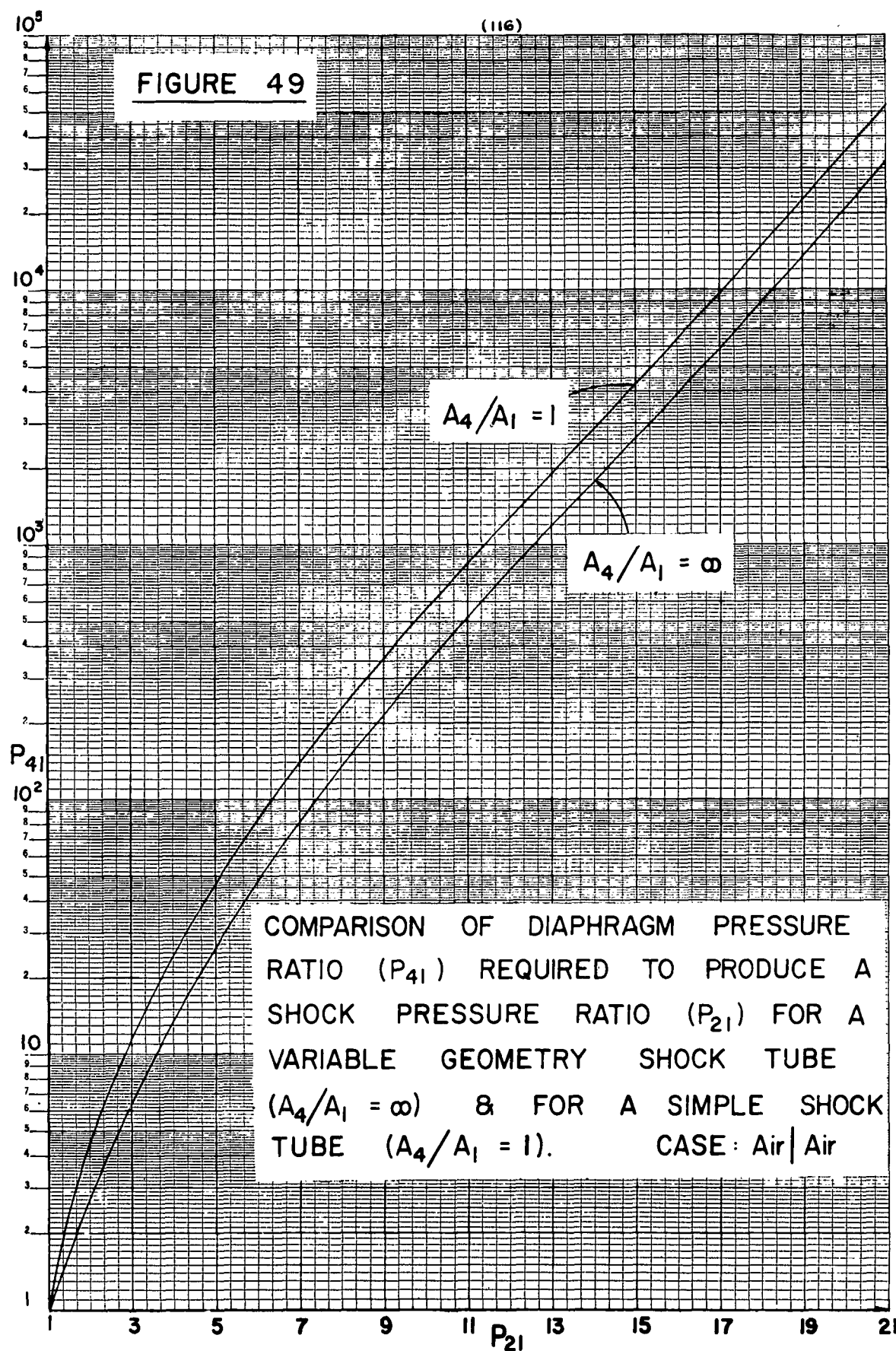
$$\left[\frac{[P_{34}]_{A_4/A_1 = \infty}}{[P_{34}]_{A_4/A_1 = 1}} \right]_{M_3 = \text{const}} = \left(\frac{\gamma+1}{2} \right)^{\frac{\gamma}{\gamma-1}} = 1.893 \text{ for } \gamma_4 = 1.40 \quad (3.22)$$

$$\left[\frac{[u_3]_{A_4/A_1 = \infty}}{[u_3]_{A_4/A_1 = 1}} \right]_{M_3 = \text{const}} = \sqrt{\frac{\gamma+1}{2}} = 1.096 \text{ for } \gamma_4 = 1.40 \quad (3.23)$$

Thus the pressure ratio (P_{34}) for a given M_3 increases with increasing area ratio and the particle velocity increases slightly, hence stronger shocks are produced, or conversely for the same strength shock a lower diaphragm pressure ratio is necessary. When $M_3 < 1$, the above ratios depend on M_3 . The variation of the shock pressure ratio P_{21} with the diaphragm pressure ratio P_{41} for the simple shock tube ($A_4 = A_1$) and for the modified shock tube ($A_4/A_1 \rightarrow \infty$) is shown on figure 49. The variable geometry tube also has the added advantage in that it takes longer for the reflected rarefaction wave to overtake the shock wave. Conversely, a slightly shorter chamber may be used for a variable geometry tube than for the simple shock tube in order to reach the same flow duration Δt_3 , in the steady state region behind the contact surface.

In addition to the increase in shock strength gained by using a tube with a large chamber area, it is possible to get a further increase by combining this technique with several diaphragms in steps (figure 50). If $\frac{A_4}{A_1}$ is very large, it may be assumed that the initial shock wave S_3 undergoes normal reflection when it strikes the second diaphragm and $u_4 = 0$. The rest of the problem is similar to variable geometry shock tube treated above. For example, using the initial conditions shown in Figure 50, the final shock wave Mach number $W_{11} = 3.9$ with two diaphragms. If the first diaphragm (D_1) is

FIGURE 49



omitted and using the same overall pressure ratio of 10^3 across the diaphragm D_2 , then $W_{11} = 3.3$. The gain in shock Mach number in this case is due to the decrease in the internal energy ratio E_{41} as compared with E_{81} , when diaphragm D_1 is not utilized. A complete experimental verification of these methods is still lacking.

Of course, all of the above methods may be combined, i.e. by using the gas discharge method with a favourable gas combination (He/Air) or (H_2/N_2) at high initial pressure ratios and a tube of variable geometry, in order to produce very strong shock waves (say $W_{11} \approx 50$).

The effects of strong shock waves on the thermal equilibrium of air have already been considered in section 1, where it was shown that dissociation, electronic excitation and ionization can take place for shocks of high Mach number.

In reference 29, it is reported that in the case of a very strong shock wave travelling in argon the shock front itself becomes highly luminous. From the previous discussion on the shock front with variable specific heat, it was indicated that the front consists initially of a very steep portion in which the Rankine-Hugoniot temperature is achieved in a few mean free paths, followed by a secondary region in which thermal equilibrium is reached in all states. In view of the few collisions taking place at the initial portion of the front, it does not appear theoretically possible for ionization and the resulting luminescence to take place. Nevertheless, the temperature at the initial portion of the shock front is greatest and may account for the observed luminescence in some manner. This phenomenon is not understood as yet. The same effects were observed for H_2 , He, Ne, N_2 and A in reference 47, by using a pulsed gas discharge tube.

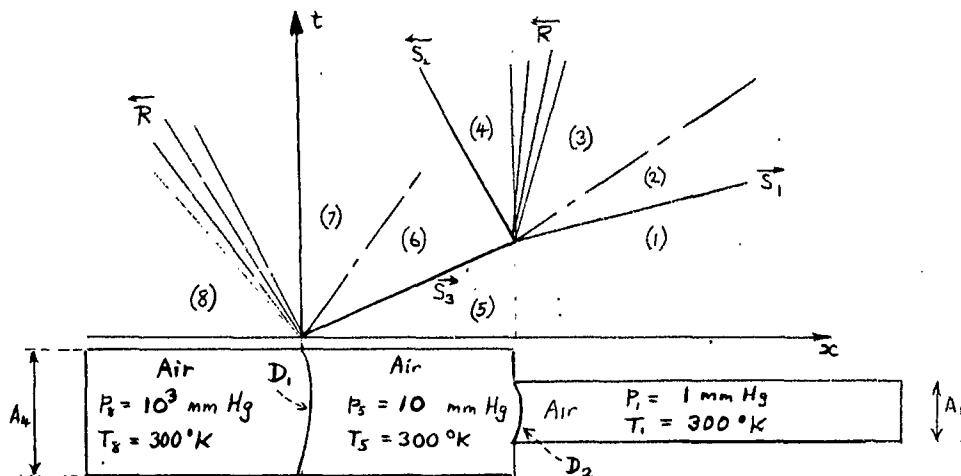


FIGURE 50

A STEP TYPE SHOCK TUBE UTILIZING A LARGE AREA CHAMBER AND TWO DIAPHRAGMS.

In addition, the shock front as well as the high temperature region up to and including the contact region was found to be a highly conducting gas. Spectra of the hot region behind the shock front indicate strong lines due to calcium, sodium and iron impurities (in the form of dust particles in the argon, of infinitesimal concentration). These elements would require much lower ionization potentials. The Stark effect in hydrogen lines was also noted. For very strong shocks the entire background of the spectrum becomes very intense and approaches a black body radiation.

From the above it has been amply demonstrated that the shock tube can also be utilized for the study of magneto-hydrodynamics, and may very well become a powerful instrument for the study of non-equilibrium phenomena in basic physics. This could lead to some new developments in the understanding of the kinetic theory of gases and molecular structure.

IV. DESIGN AND CONSTRUCTION CRITERIA FOR SHOCK TUBES

4.01. Shock Tubes in General

The literature on shock tubes has become so extensive in the past five years (reference 1 to 29), that it would be a rather lengthy task to review all the applications of the shock tube and the resulting design and construction criteria. Instead some general remarks will be made which are applicable to all shock tubes, and a particular application will be discussed in section 4.02.

The type of shock tube to be used is mainly determined by the funds available and the type of problem to be investigated. If shock waves, rarefaction waves and contact surfaces are studied, then a simple cylindrical metal tube plus an optical system is quite adequate (references 2, 8 and 23). If magneto-hydrodynamic effects produced by strong shock waves are investigated, then a cylindrical metal chamber and a glass channel is sufficient (reference 29). If flow studies over models are conducted in the steady state regions separated by the contact surface, it is necessary to use a square or rectangular metal tube, which will accommodate observation windows for the optical systems and will readily permit the installation of aerodynamic models, piezo-gauges and hot wire anemometers. The magnitude of the cross-sectional area will depend on the size of model to be tested or the Reynolds number to be attained in the shock tube. The wall thickness of the tube will be determined by the maximum pressure in the chamber. Welded structures should be avoided due to the resulting distortions. A combination of high pressure and large cross-section will result in a heavy shock tube and may require hydraulic or other means for moving the various sections. It is convenient to have a chamber of two or three feet and a channel composed of several sections of two to eight feet. The channel sections should be interchangeable and easily aligned by means of dowel pins so that they may be used in combinations, as required by a particular experiment.

The viewing windows can be installed in one or two sections. These may be coupled with the remaining channel sections to give an observation window located at a desired distance from the diaphragm and will thus give a predetermined flow duration. The windows may be of standard plate glass for shadowgraph and schlieren observations. It is important that the windows be selected and installed in a manner which will give uniform refraction due to the slightly wedged surfaces that are always present in this type of glass. If the wedge surfaces are not uniform in a given window, they should be discarded and monotonic wedge windows installed and matched until uniform schlieren illumination is obtained over the entire field. For interferometric work the windows should be plane and parallel optical flats. The windows may be installed with Woods

metal, rubber gaskets or recently developed plastic glass-to-metal bonding cement (for example, Hysol cement) to give a flush and vacuum tight installation.

The most satisfactory diaphragm materials are red-zip cellophane and cellulose acetate for low pressure work and copper and aluminum sheets for high pressure work. The red-zip cellophane has the best rupturing properties and leaves the smallest obstruction at the diaphragm cross-section. Unfortunately this material is not available in a range of thicknesses and must be used in several layers for higher pressure differences across the diaphragm. This gives rise to a small variation in the time it takes for all the diaphragms to rupture and results in an overlapping of several wave systems at the origin. This matter is discussed in more detail in Section 5.02.

The pressure differential at which a diaphragm will rupture depends on the material, cross-sectional shape and area, as well as on the gasket material used to hold the diaphragm. If metal diaphragms are used, gaskets are not necessary and the sharp edges of the channel section should be rounded to avoid cutting. If cellophane is used, then rubber gaskets are bonded to the tube sections with Pliobond or Armstrong cement. The gaskets should have enlarged cross-sections so that when the tube sections are fastened together, the gasket does not squeeze into the tube and cause a discontinuity at the origin.

Shadowgraph, schlieren and interferometric methods have now become standard equipment for shock tube investigations (references 8, 22, 27 and 28). The twin mirror, single pass, horizontal or vertical symmetrically offset schlieren system is most useful. First surface paraboloidal mirrors corrected to a quarter wave length of aperture F6 to F10 are necessary for good schlieren resolution. The type of light sources, continuous or spark, are described in the above references.

Initial conditions in a shock tube are obtained by measuring the pressure in the chamber by using mercury manometers or Heise type bourdon gauges, and in the chamber by using mercury or butyl phthalate manometers; McLeod, ionization and Pirani gauges or Wallace and Tiernan absolute pressure gauges. The temperature of the gases in the chamber and channel is generally room temperature. When gas at high pressure is admitted into the chamber, it should be allowed to reach thermal equilibrium (in about a minute) before the diaphragm is ruptured. Commercial cylinders of compressed gas (air, A, He, CO₂, H₂, N₂, O₂) are easily available and they have the advantage of a very low dew point (about minus 40° C, or lower), which eliminates extraneous effects due to water condensation.

Final conditions in the shock tube are obtained by measuring the shock wave velocity (W_{11}) continuously (references 2 and 8) or by measuring the time interval for the shock wave to travel over a given base (two accurately

measured points -- see reference 27 which contains an excellent summary of these methods). By utilizing the theoretical relations of section 1, the flow parameters can be determined. In addition, pressure profiles can be measured by using piezo-electric transducers (references 15, 17, 20 and 27), temperature profiles may be obtained with hot wire anemometers (reference 49), and flow Mach numbers are determined from shock angles over conical or wedge models. When strong shock waves ($W_{11} \approx 10$) are studied, the wave front itself becomes luminescent and its velocity may be self-recorded on a drum camera without the use of a shadowgraph or schlieren system (references 43 and 44).

To-date the wave speed results along with interferometric density distributions and Mach number measurements have supplied the means of verifying the shock tube theory. Piezo-gauge data and anemometry results have been confined, so far, to weak shock waves. Light scattering techniques have also been employed to give a measure of the degree of liquefaction in the cold region (3) behind the contact surface (reference 27).

4.02 3 inch x 3 inch Wave Interaction Tube.

The schlieren (x, t)-plane photographs, which are used to illustrate the various one-dimensional flow problems in this report, were obtained with the 3 inch x 3 inch wave interaction tube and the wave speed camera. The work described in reference 8 was done with a cylindrical tube of one-inch internal diameter. The rest of the ancillary equipment is common to both reports and is described in detail in the above reference. Although the one-inch diameter tube had certain desirable design and construction features, it was necessary to change to the 3 inch x 3 inch tube for the following reasons:

a) The lucite windows gave poor photographic results due to the longitudinal striations on the (x, t)-plane schlieren photographs.

b) It was not possible to use tourmaline piezo-gauges with the curved walls.

c) The high voltage spark gaps were erratic in operation at low pressure and were, therefore, unreliable as consistent diaphragm breakers. They also protruded into the tube and caused flow interference.

d) The method of coupling the various sections was slow and laborious, especially when changing diaphragms. The threaded type of couplings made it extremely difficult, if not impossible, to study the shock tube problem at the origin, absorption of a shock wave by a layer of gas or other complex wave interactions.

The manner in which these disadvantages were overcome will be described now in detail. The present wave interaction tube has been constructed with a great deal of care in design, and accuracy in machining and assembly. It has already proved to be a very versatile tube, which is simple to operate, and has yielded very satisfactory experimental results.

The tube consists of a number of sections or compartments all of the same cross-sectional area but of different lengths. The basic tube consists of four 12-inch sections, five 24-inch sections and a 30-inch test section. These sections may be coupled together to give any tube length desired. The 30-inch test section is fitted with glass windows 26" long and 1" wide for viewing the flow phenomena. An over-all view of the tube is shown in plate 8.

Each compartment consists of two side plates and two channels which, when assembled, form a square cross-section with dimensions 3 in. x 3 in. These dimensions were held to a tolerance of + .001 inch. The wall thickness of plates and channels is 0.5". Ground and hardened dowels are used to ensure correct alignment of the plates and channels. Dowels are also used in the end faces of each chamber so that the sections will be perfectly aligned when joined together. This method reduces the step between the sections to less than .0005". A typical tube section illustrating the above features is shown on figure 51.

The sides of each section are sealed by means of lead seals between the side plates and top and bottom channels. In order to obtain vacuum-tight joints when the tube sections are assembled, "O" rings are used in the dowelled end of each compartment. Vacuum and pressure outlets, piezo-gauge and diaphragm breaker stations are situated in the top and sides of the tube, and these outlets are also sealed by means of "O" rings. By this means of sealing the complete tube may be evacuated to very low pressures (0.4 mm. Hg. absolute, or less).

The windows used in the tube are ground from "water white" glass. Since commercial plate glass is not of constant thickness, the sets of windows were matched in a schlieren beam until uniform illumination was achieved over a desired length. The windows were cut from this portion, and ground to the shape shown on figure 51. The windows are retained in the grooves by means of "Wood's Metal", and a steel frame which is separated from the window itself by an 1/8 inch rubber gasket. This combination holds the window rigidly in place under both vacuum and pressure, and also provides an excellent seal.

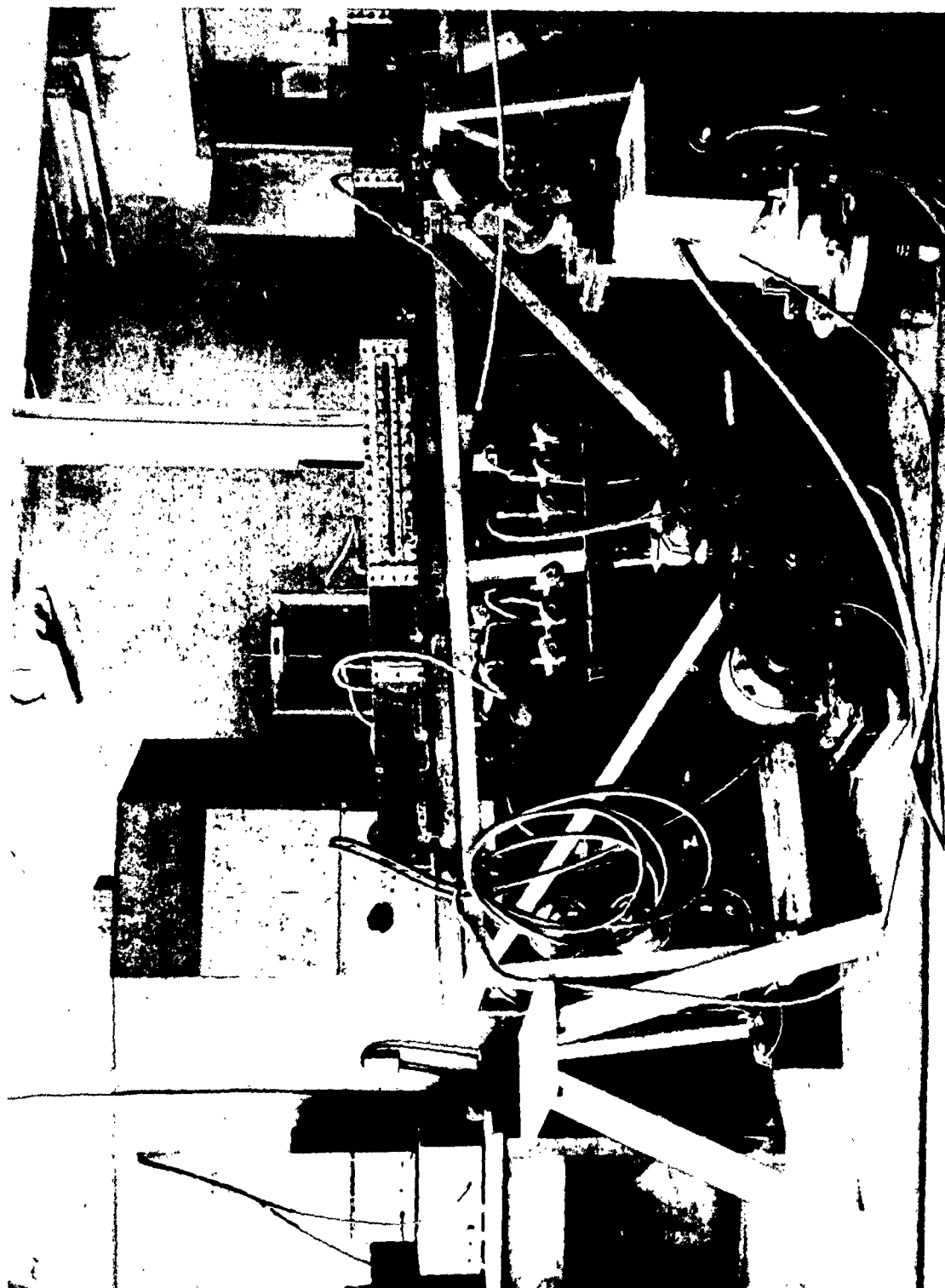


PLATE 8.

AN OVER - ALL VIEW
OF THE WAVE INTERACTION TUBE AND ANCILLARY EQUIPMENT

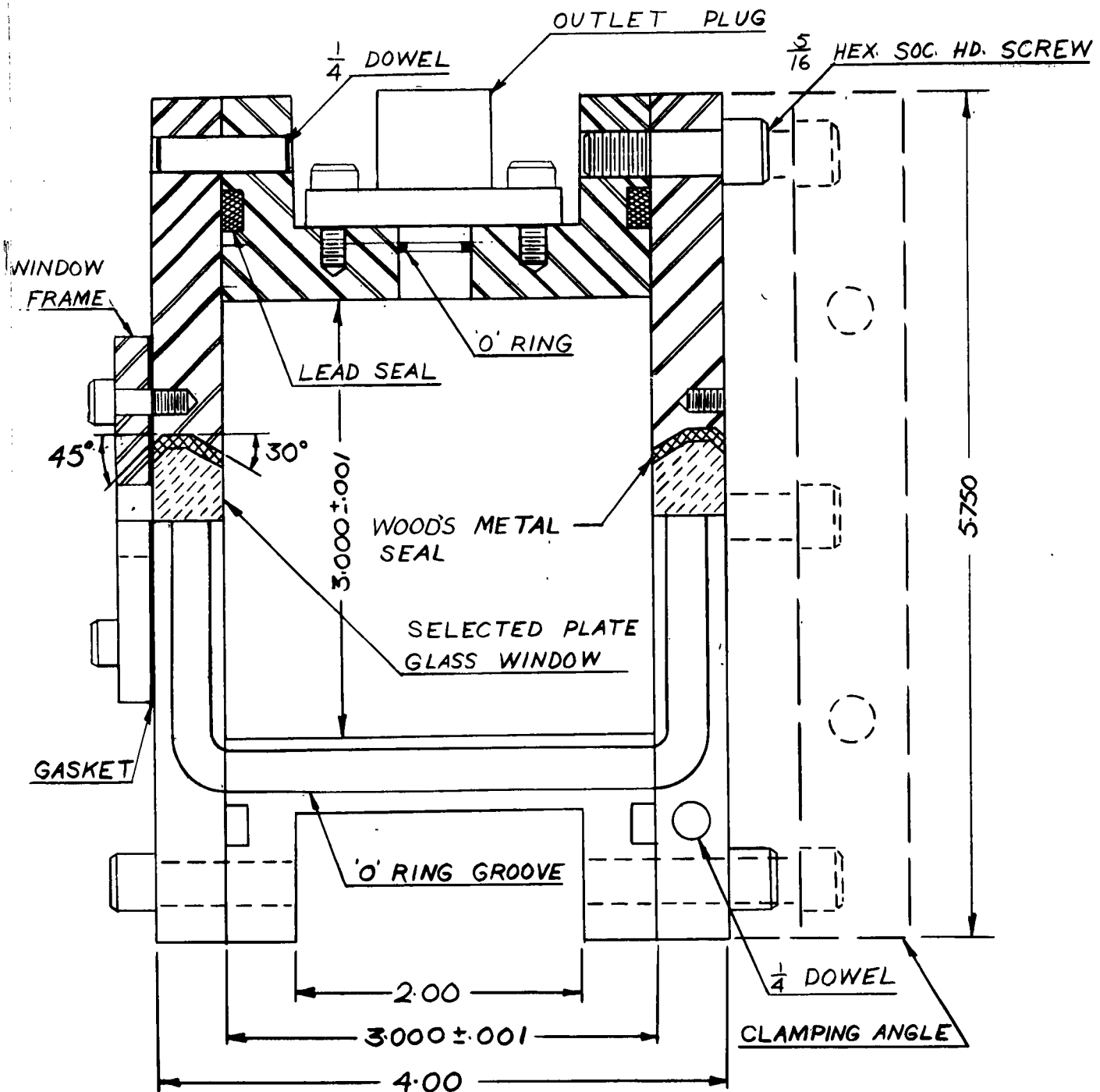


FIGURE 51.

CONSTRUCTION DETAILS OF 3 INCH x 3 INCH WAVE INTERACTION TUBE

The sections are joined together by means of ordinary hexagonal head bolts and heavy right-angle brackets. The sections can be assembled on the stand to give any tube length required. Four pairs of "Vise-Grip" pliers are used to clamp the chamber and channel at the diaphragm station. Rubber gaskets are used to retain the cellophane diaphragms, and this combination gives very good sealing, plus a rapid means of changing the diaphragms. The clamps are clearly visible on plate 9, along with the diaphragm breaker itself.

The flow is initiated by rupturing the diaphragm by means of a solenoid-operated mechanical plunger. The power for the breaker is supplied by a 6-volt automobile battery. A cross-sectional view of this diaphragm breaker is shown in figure 52. Two of these breakers are available in order that wave interaction studies may be conducted as well.

In addition to the basic tube, there are available two special 12-inch sections and a small 5-inch compartment. The special 12-inch section is fitted with glass windows 10" long and 1" wide. These windows are fitted with one end flush with the end of the section. Rubber gaskets may be cemented to the ends of these sections to form a diaphragm station. Each section contains a diaphragm breaker station so that the diaphragm may be ruptured from either side. These chambers make it possible to obtain a 12" field of view at the diaphragm station and thus enables the study of the origin in the (x, t) -plane. Plate 10 shows the 12-inch section with the diaphragm breaker installed for this purpose.

The two 12-inch sections and the 5-inch compartment when assembled together, afford a means of visually observing the refraction of a wave at a layer of gas. In this case the gas layer in the 5-inch compartment is separated from the gases in the two 12-inch sections by means of microfilm interfaces which are ruptured by the wave which is moving down the tube. Plate 11 shows an assembly of these three sections as set up for this purpose. Further details are given in section 5.

The vacuum system consists of a Kinney CVD-556 vacuum pump, two McLeod gauges and a set of Wallace and Tiernan absolute pressure gauges. These gauges cover the range from 0 to 810 mm. Hg. absolute pressure. The gauges are used extensively to measure pressures in the tube while the McLeod gauges are used to calibrate the Wallace and Tiernan gauges periodically. The pressure system utilizes bottles of high pressure gases which are commercially available. This method has proved to be the most convenient and also ensures a low moisture content for the gases used. Heise gauges with a range of 0 - 4000 mm. Hg. are used to measure the pressure in the chamber.

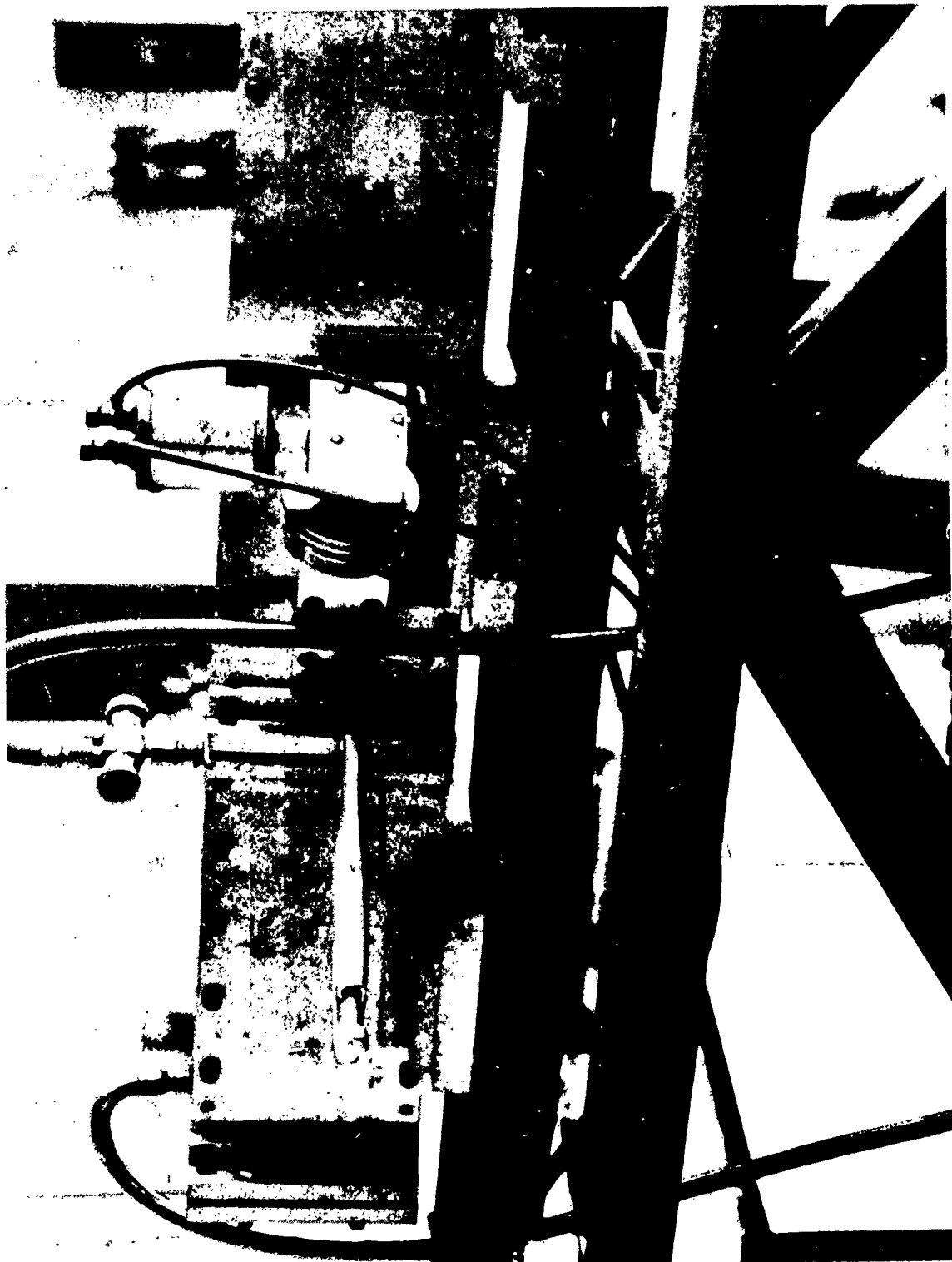
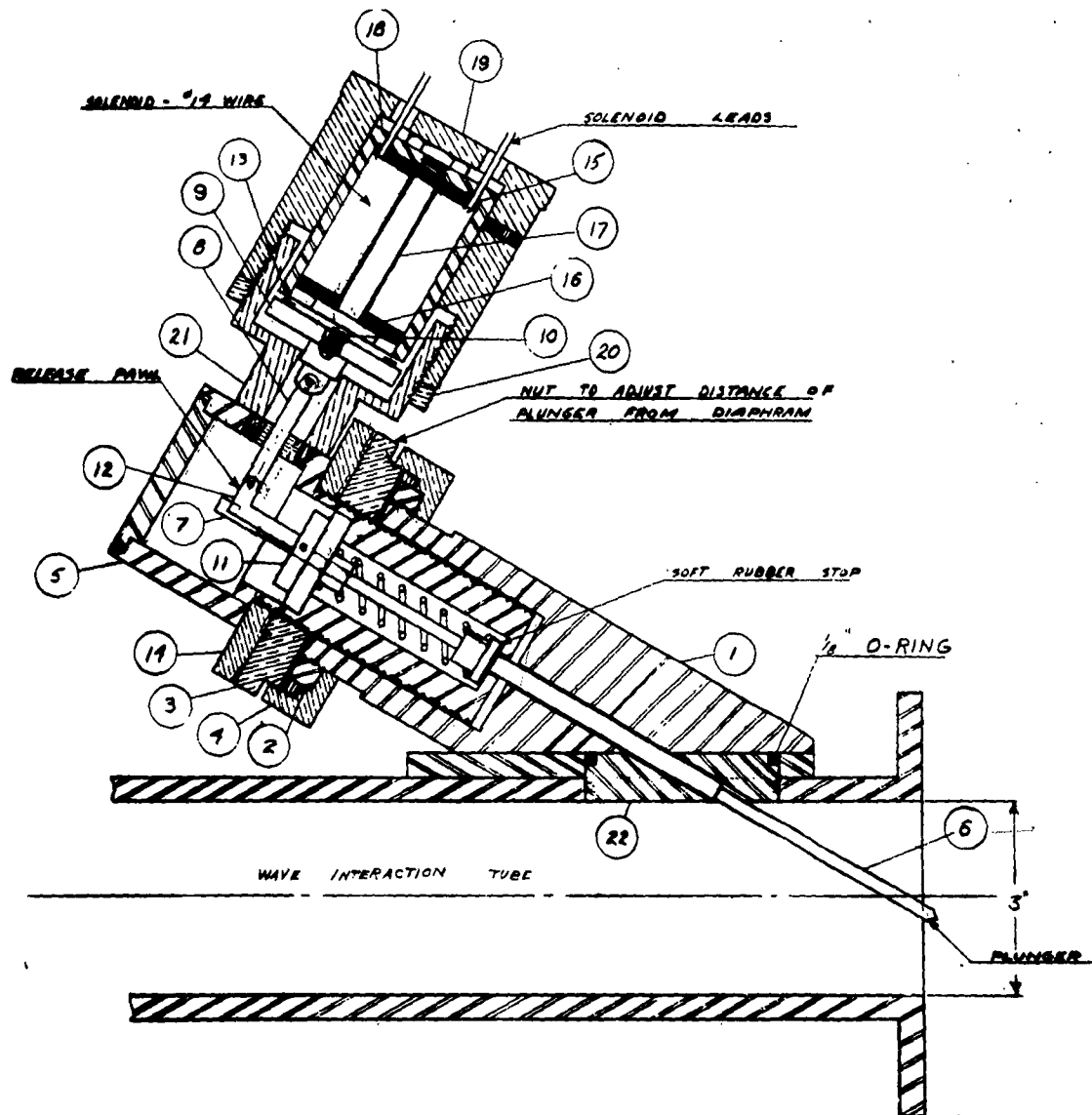


PLATE 9.

THE DIAPHRAGM STATION,
SHOWING THE DIAPHRAGM BREAKER AND CLAMPING PLIERS



ASSEMBLY DIAPHRAM BREAKER
FOR SHOCK TUBE

FIGURE 52.

CROSS-SECTIONAL VIEW OF DIAPHRAGM BREAKER

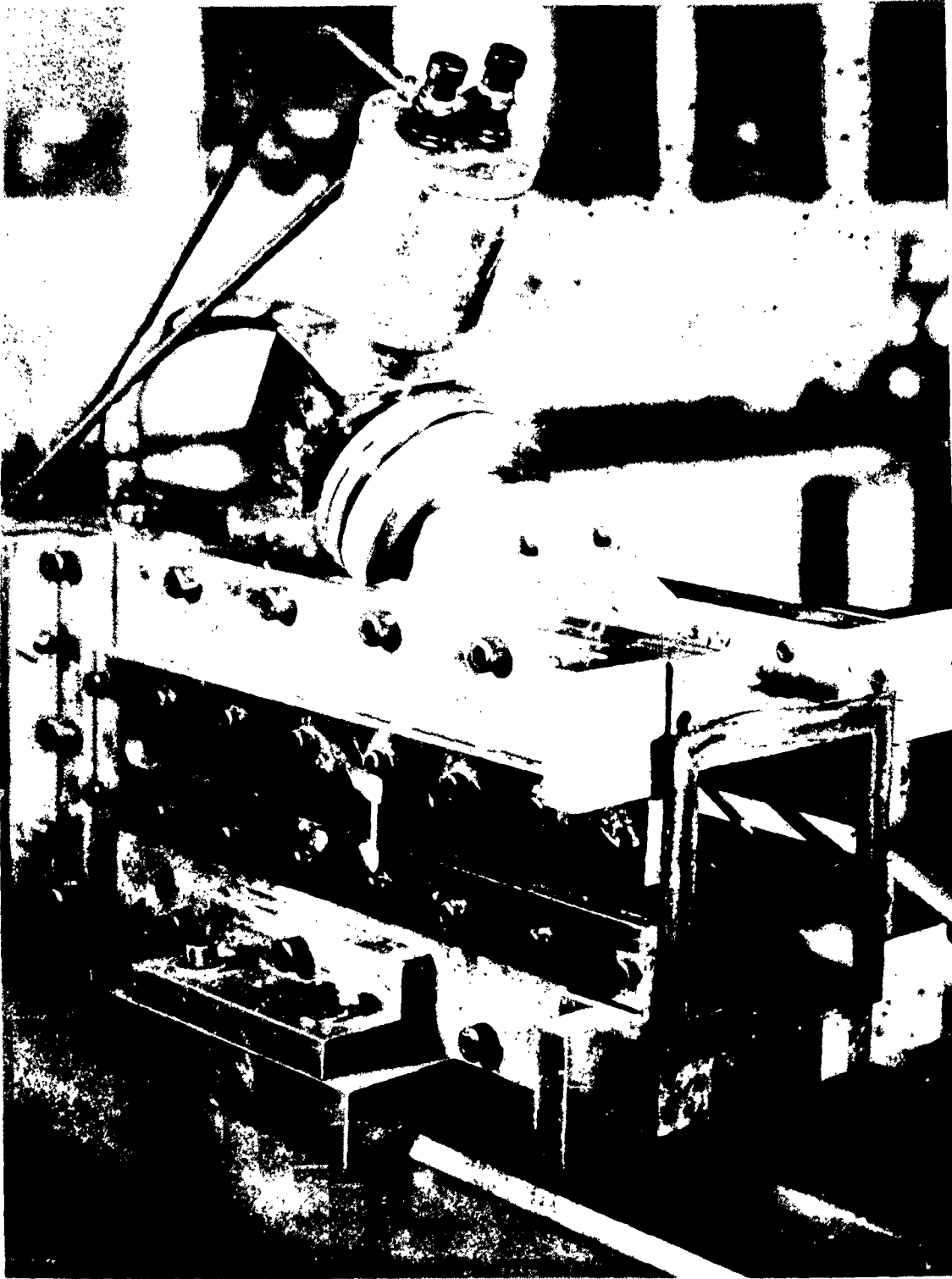


PLATE 10.

THE SPECIAL SECTION USED FOR THE STUDY
OF THE ORIGIN IN THE (x, t) - PLANE.

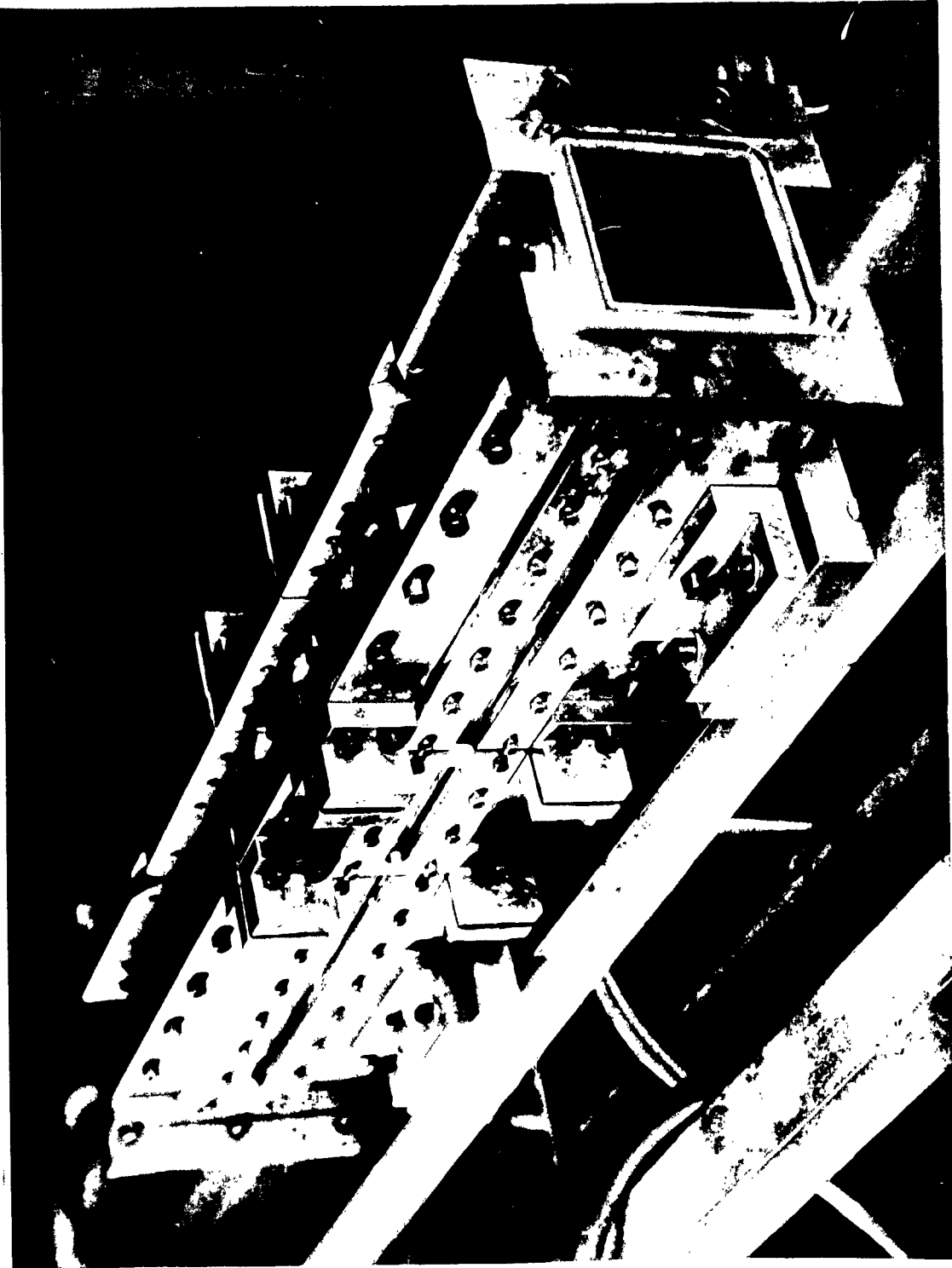


PLATE 11.

THE THREE SECTIONS USED FOR THE STUDY OF WAVE REFRACTION

(See Plates 6 and 7.)

The photographic records were obtained using a conventional schlieren system and a wave speed camera. The use of a wave speed camera gives a continuous distance-time (x, t)-plane record, and the wave velocity can be obtained directly by measuring the slope of the wave trace on the film, since the film speed and magnification factor are known accurately. The wave speed camera is illustrated on plate 12.

A more complete description of the schlieren system, wave speed camera and allied equipment may be found in reference 8, and a schematic diagram of the entire apparatus is shown on figure 53.

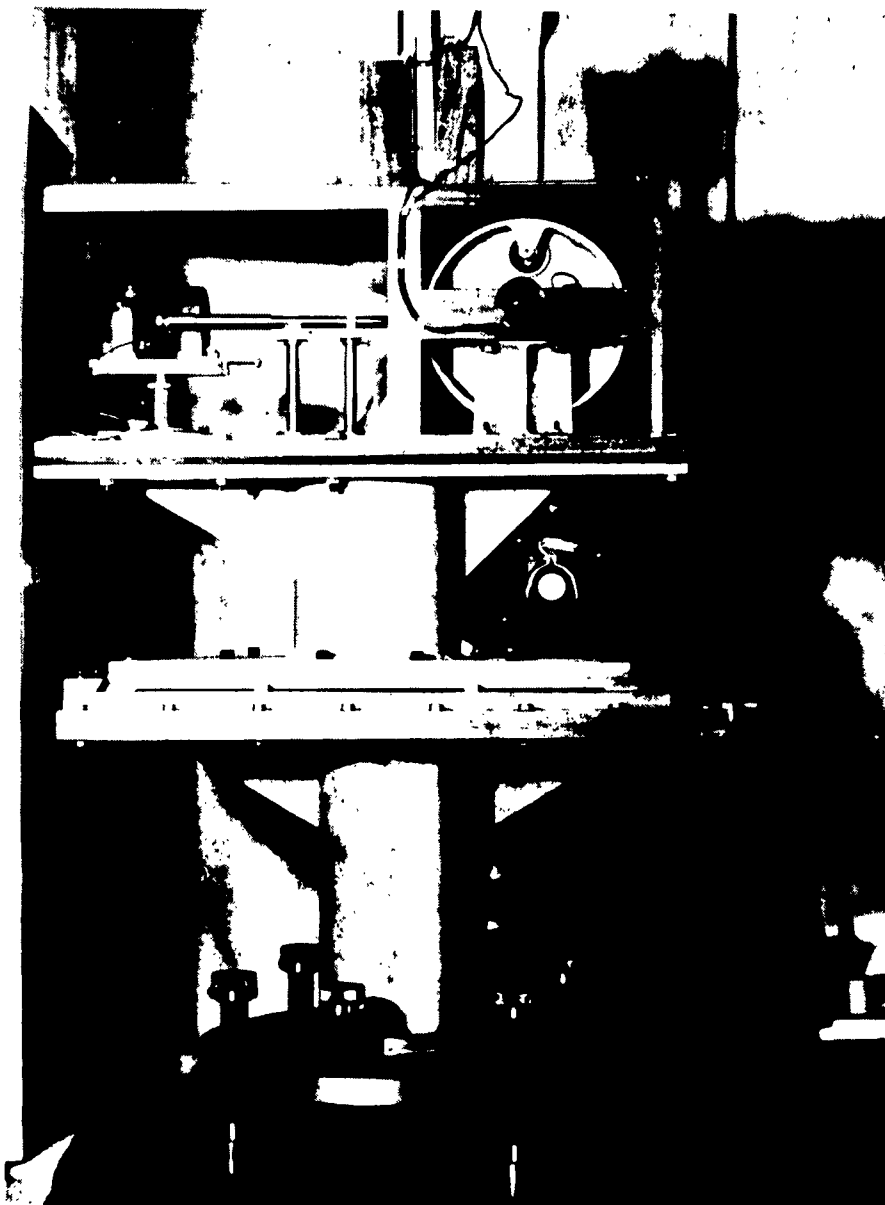
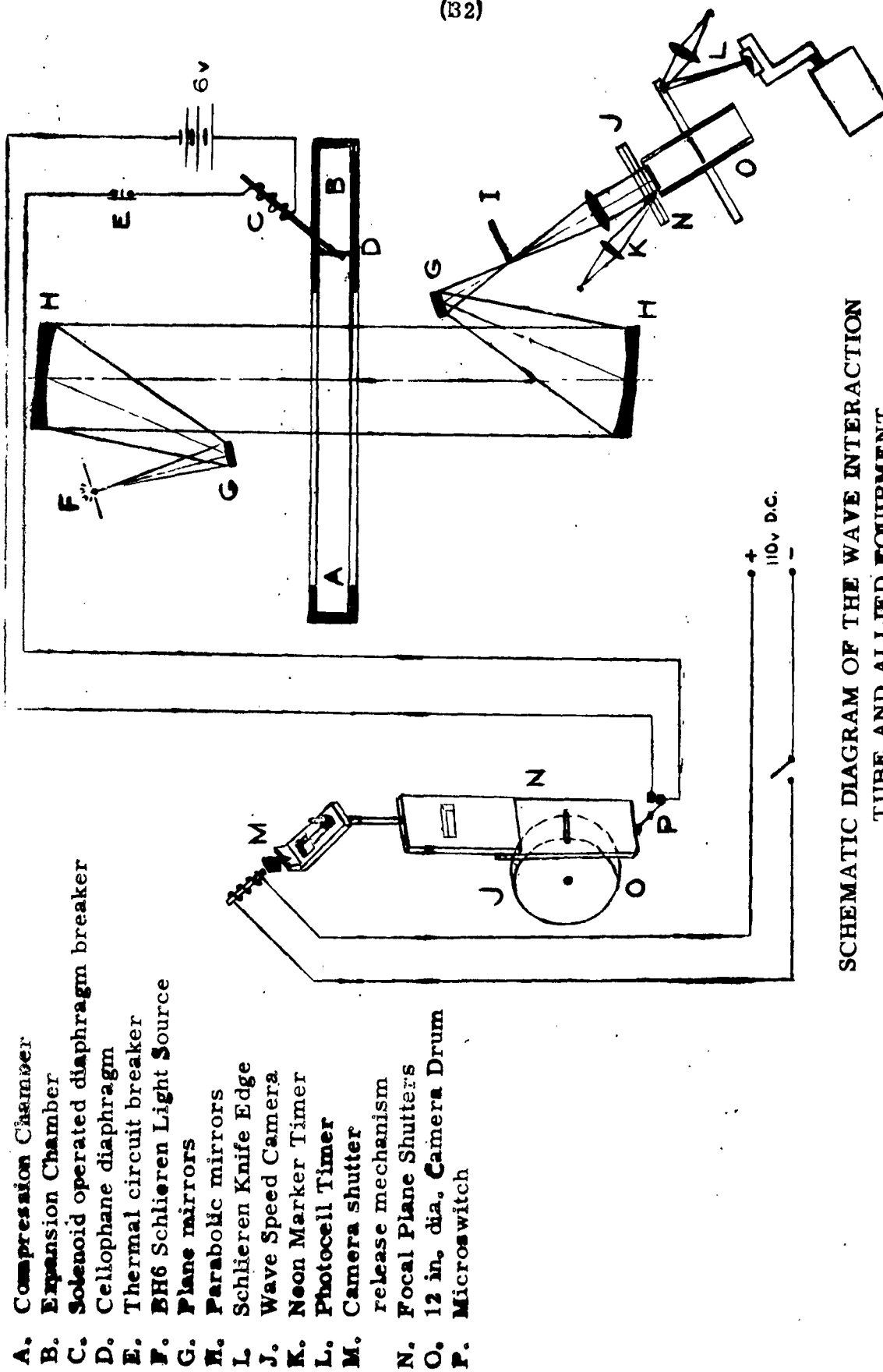


**PLATE 12. THE WAVE SPEED CAMERA WITH SIDE
PANELS REMOVED SHOWING FILM WINDER, LENS
AND KNIFE EDGE ASSEMBLY, AND NEON GLOW
LAMP TIMER.**

(32)



SCHEMATIC DIAGRAM OF THE WAVE INTERACTION
TUBE AND ALLIED EQUIPMENT

FIGURE 53.

V. COMPARISON OF THEORY AND EXPERIMENT

The present section deals with experiments on real flows in a shock tube. These experiments were designed to compare the actual data with the theoretical predictions discussed in sections 1 to 3 inclusive, and to evaluate critically the differences between ideal and real flows.

Entirely new results are given in sections 5.02 and 5.03, which deal with the origin problem in the (x, t) -plane and shock wave attenuation in tubes, respectively. The initial conditions were varied in a number of ways, in order to study the effects produced by diaphragm pressure ratio and diaphragm pressure difference at the origin and up to 12 feet beyond, on shock wave formation and attenuation. In addition, the deviations produced at the contact front and in the uniform states are also discussed.

The remaining sections 5.04 to 5.08 are devoted to a detailed discussion of the flows in the steady state regions, the rarefaction wave and wave interactions. Here, new data, as well as results obtained previously at the Institute of Aerophysics and other research establishments are given in an effort to present an integrated account of the present state of shock tube knowledge.

5.01. Experimental Procedure

The present data are mainly based on the wave speed measurements of the (x, t) -plane schlieren records obtained with the wave speed camera which is shown on plate 12. Essentially, these photographs show the propagation of discontinuities in the density derivative.

If the Rankine-Hugoniot conditions (equation 1.70) are assumed to apply across the shock wave, for example, then it is possible to calculate the physical parameters of the uniform states from the shock speed (relations 1.69 to 1.77). This procedure has the inherent weakness that the physical quantities are not measured directly. Where possible this gap has been narrowed by giving the few available actual measurements of physical quantities obtained in other shock tubes. It will be shown in later sections that the wave speed technique is reliable for basic calibrations and wave interactions, where variable specific heats are not too important. However, this should not be taken to imply that it is in itself a sufficient condition to determine the remaining flow parameters. Wherever possible these should be measured directly. When sufficient direct data of this type has been accumulated, the researcher may have a sounder basis for evaluating temperature, pressure and density from shock speed measurements.

The present schlieren records contain the traces of the basic wave elements found in a shock tube, such as, shock waves, contact surfaces, and rarefaction waves. In addition, traces of any discontinuity in the density

derivative produced by other flow phenomena such as, vortices, eddies, and boundary layer flow will also be recorded.

Since 12-inch paraboloidal mirrors are used in the schlieren system, the records cover approximately a 12-inch viewing section. The drum of the present camera is 12 inches in diameter, uses 70 mm. Linagraph Pan film and rotates at approximately 4200 R.P.M. This gives a maximum recorded flow duration of about 14 milliseconds. In practice, only about 2 milliseconds of the flow from the initial phenomenon is of interest, the remainder contains complex multiple interactions. It is seen that a continuous record is available for each experimental run over relatively large distances and long times.

The speed of any wave trace is determined from the relation

$$w = \frac{V \tan \alpha}{\mu}$$

where w = wave speed in feet per second (see figure 54)

V = film peripheral speed in feet per second

μ = magnification factor of the optical system

α = angle between the trace of the wave and the film velocity vector

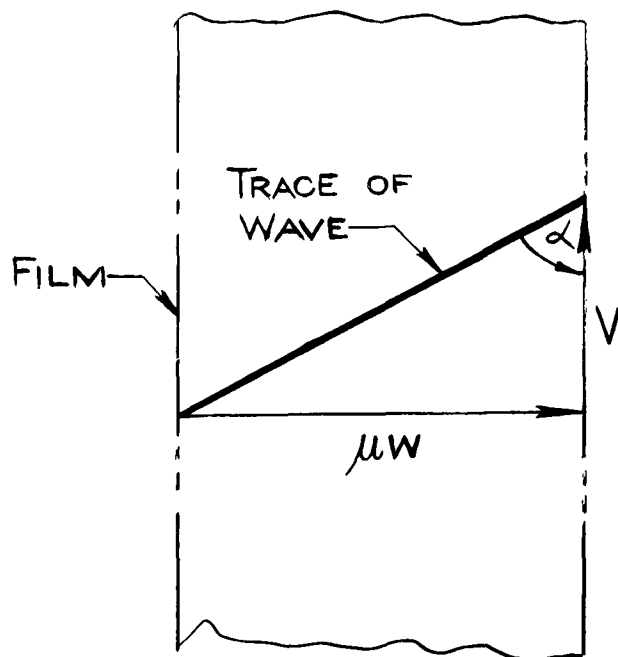


FIGURE 54

THE WAVE VELOCITY VECTOR DIAGRAM

The film speed is determined very accurately to about 0.07%. The diameter of the 12-inch drum is known to $0 \pm .001$ inch. The speed of the drum is measured by means of a photocell unit, an amplifier and a Potter chronograph to the nearest 10 microseconds. A blip circuit, which yields markers on the film every 5 or 10 microseconds is also available (see references 8 and 14).

The magnification factor may be determined to about 0.1%. It is found by attaching two razor blade markers to the window frame and photographing them within the schlieren records. The distance between the markers is over 11 inches and can be measured to the nearest $1/100$ or $1/64$ inch. The trace on the schlieren record may be measured with a travelling microscope to 10^{-4} inches.

The tangent of the included angle α , may be found with an accuracy of about 2% for large angles (75°) for high wave speeds, or less than 1/2% for low wave speeds or small angles (45°). The angles are measured on a Hilger T500 Universal Measuring Projector with a 10 x magnification lens. This shadow comparator enables the measurement of angles to 0.5 minutes or better. For diaphragm pressure ratios (P_{41}) of the order of 10,000 it is necessary to use absolute pressures in the channel of the order of 0.4 mm. Hg. This gives rise to faint schlieren shock traces, and it is essential to pin-point them for use in the comparator. The repeatability of the angle $\alpha^\circ \pm 20$ min. was always possible. Hence, the shock wave velocity even for strong waves could be measured to within 2% or better.

Chamber pressures could be read with an accuracy which varied from about 0.5% for the low pressures to about 0.05% for the high pressures. The pressures were measured on Heise bourdon gauges which are graduated in steps of 4 mm. Hg. Chamber pressures ranged from about 800 mm. Hg. to 4000 mm. Hg.

Low channel pressures were most difficult to determine accurately. For a pressure of 0.40 mm. Hg. an error of about 9% was possible. This was alleviated by taking several runs at these low pressures in order to determine an average value. The photographic reproducibility in these cases was quite good. Channel pressures were measured with Wallace and Tiernan absolute pressure gauges. They were calibrated against McLeod gauges in the range 0 to 15 mm. Hg. and 0 to 1.8 mm. Hg., and with manometers in the range 0 to 810 mm. Hg. The following gauges were employed:

- 0 to 20 mm. Hg. (with 0.1 divisions),
- 0 to 200 mm. Hg. (with 0.5 divisions),
- 0 to 410 mm. Hg. (with 2.0 divisions), and
- 390 to 810 mm. Hg. (with 2.0 divisions).

The difficulty of obtaining high accuracy at low channel pressures could be overcome in tubes designed to take higher pressures, but at the expense of economy, bulkiness and handling problems. In conclusion it may be stated that the present results at diaphragm pressure ratios of 10,000 are most subject to experimental error, and this was minimized by great care and repeated runs in order to ensure the greatest practical accuracy.

The tube configurations used during the experimental work, to be described in the following, are shown on plate 13.

5.02 The Wave System at the Origin in a Real Shock Tube.

The theoretical relations describing the flows in an ideal shock tube were developed in sections I and II. The present section will consider the flows in a real shock tube. An account will be given of the experimental work in order to compare the data obtained with the theoretical predictions.

Under the given assumptions, it was found that the ideal flow in a shock tube in the (x, t) -plane is represented by figure 1. Real flows in the same plane are modified considerably. This is shown by actual schlieren photographs of the (x, t) -plane, from the instant the diaphragm ruptures, on plate 14 (a) to (z) inclusive, for initial diaphragm pressure ratios (P_{41}) of 1.1 to 501. Plate 14 (x), (y), (z) illustrates the origin problem for the case of He/Air. Reversed schlieren records are included in order to show photographic detail. The differences between the ideal and real flows are quite noticeable, and will now be considered in some detail.

Under pressure the cellophane diaphragm becomes a curved surface. When it ruptures, three-dimensional effects are introduced in the form of shock wave reflection due to the curvature of the shock wave, diffraction about the remains of the diaphragm and interactions of the resulting waves. Viscous effects also show up immediately in the form of vortices, mainly downstream of the diaphragm. As a result one-dimensional inviscid flow does not exist at the origin.

The main features of all the schlieren records of the (x, t) -origin are similar. Instead of plane waves emanating instantaneously the moment the diaphragm is removed (see figure 1), the following actually takes place.

When the diaphragm ruptures, many compression waves are generated. These waves overtake, accelerate and combine to form the main shock front, which finally achieves a uniform velocity in a distance of a few cross-sectional widths. For diaphragm pressure ratios $P_{41} \approx 2$ the formation region appears to extend up to 12 in. and 1000 μ sec., due to the prominent transverse waves. The shock wave is well formed and of uniform speed about 12 inches beyond the origin. The formation region decreases to about 8 in., and the time to about 500 μ sec. at $P_{41} = 20$. For $P_{41} > 20$ the formation process is more rapid, but it loses photographic clarity (see plate 14 (w)), and the shock path is curved even after 18 in. beyond the origin. Thus the formation distance, in which the shock wave forms, accelerates and attains a straight path in the (x, t) -plane (uniform velocity), is only about 4 cross-sectional widths for weak waves and 8 for strong waves. The formation region is smaller when the diaphragm is stressed close to its breaking strength; that is, when the pressure difference is large. This is illustrated

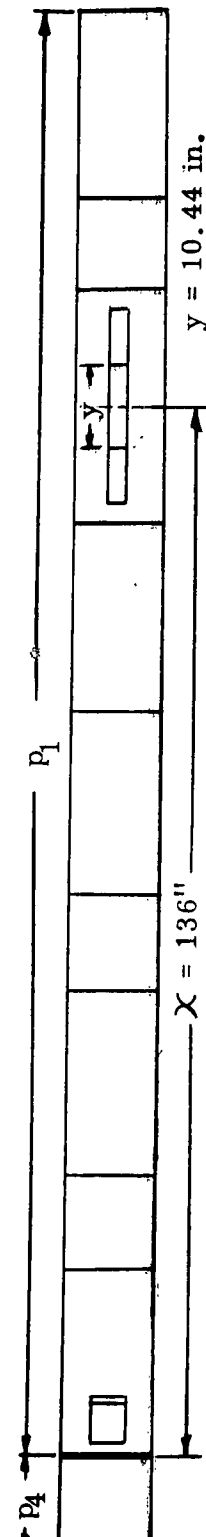
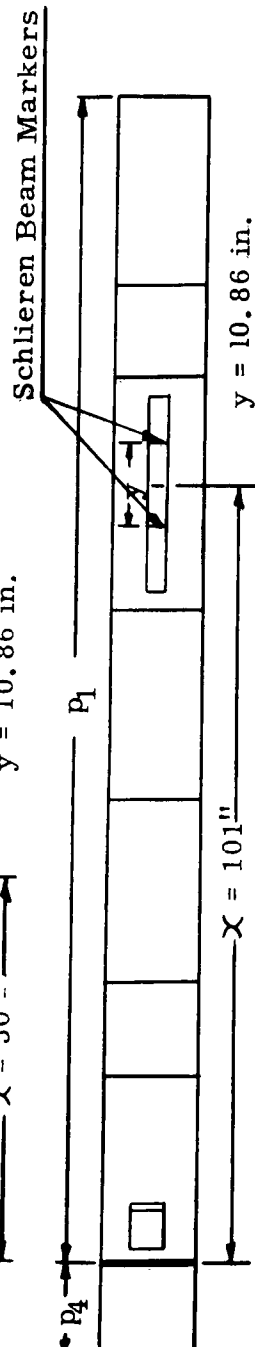
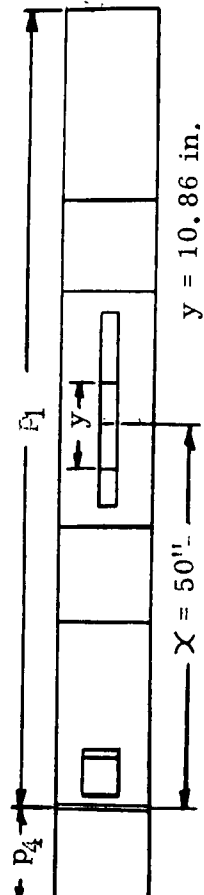
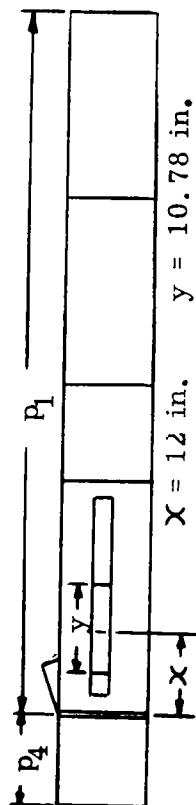
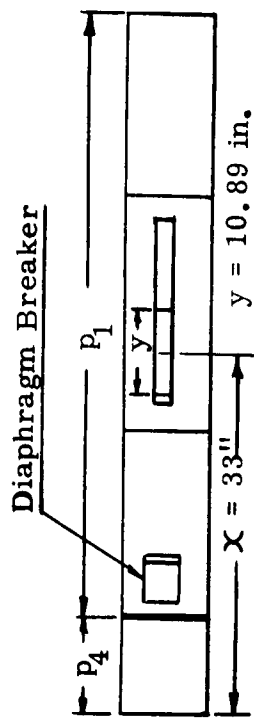
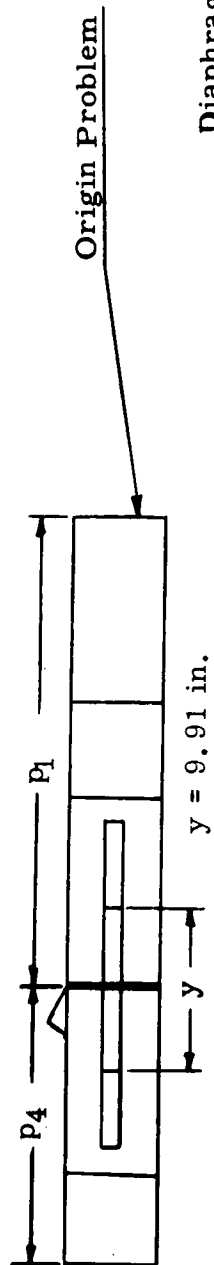


PLATE 13 -- TUBE CONFIGURATIONS USED DURING THE EXPERIMENTAL WORK

$p = 1500 \text{ mm. Hg.}$

$p = 1500 \text{ mm. Hg.}$
 $a_{41} = 1132 \text{ f.p.s.}$

$p_1 = 1365 \text{ mm. Hg.}$

$$P_{A1} = 1.10$$
$$P_1 = 1365 \text{ mm. Hg.} \quad P_{41} = 1.10$$

$$W'' = 1.02 \quad U_{21} = .034 \quad P_{21} = 1.05$$
$$P_{21} = 1.05$$

S = Shock Wave
C = Contact Front
R = Rarefaction Wave
D = Diaphragm
TS = Transverse Shocks

S = Shock Wave
 C = Contact Front
 R = Rarefaction Wave
 D = Diaphragm
 TS = Transverse Shocks

(3)
 (2)
 (1)
 (0,0)

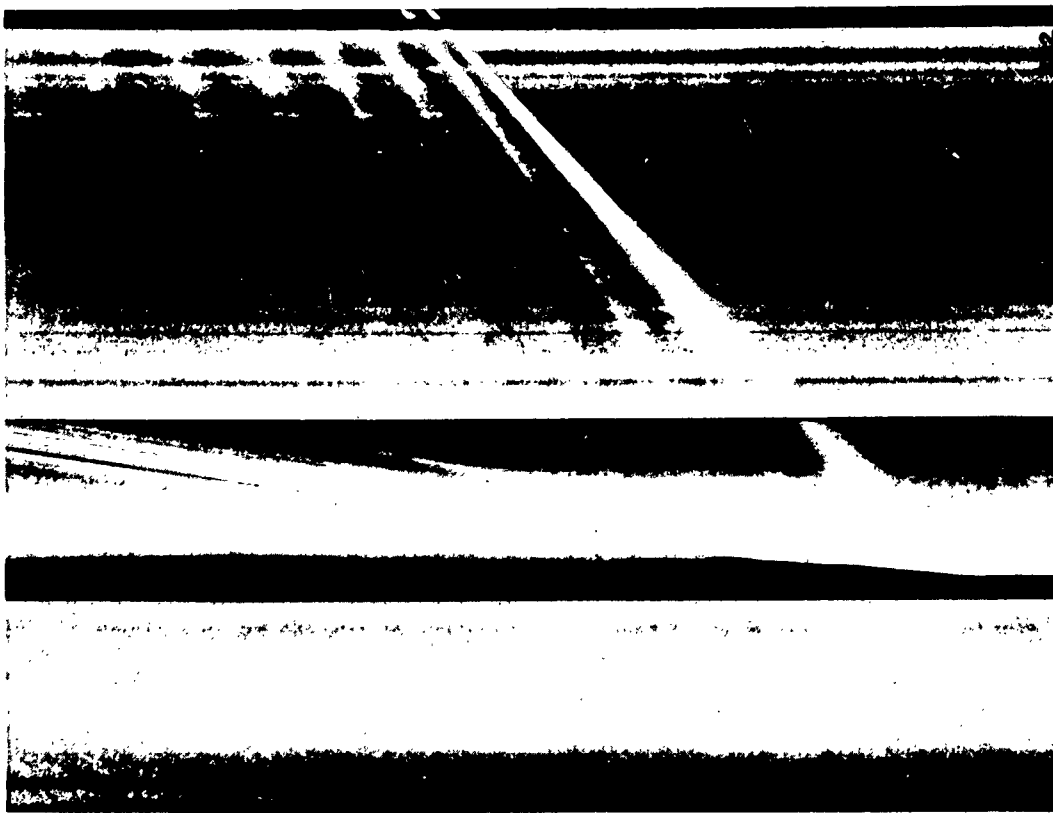
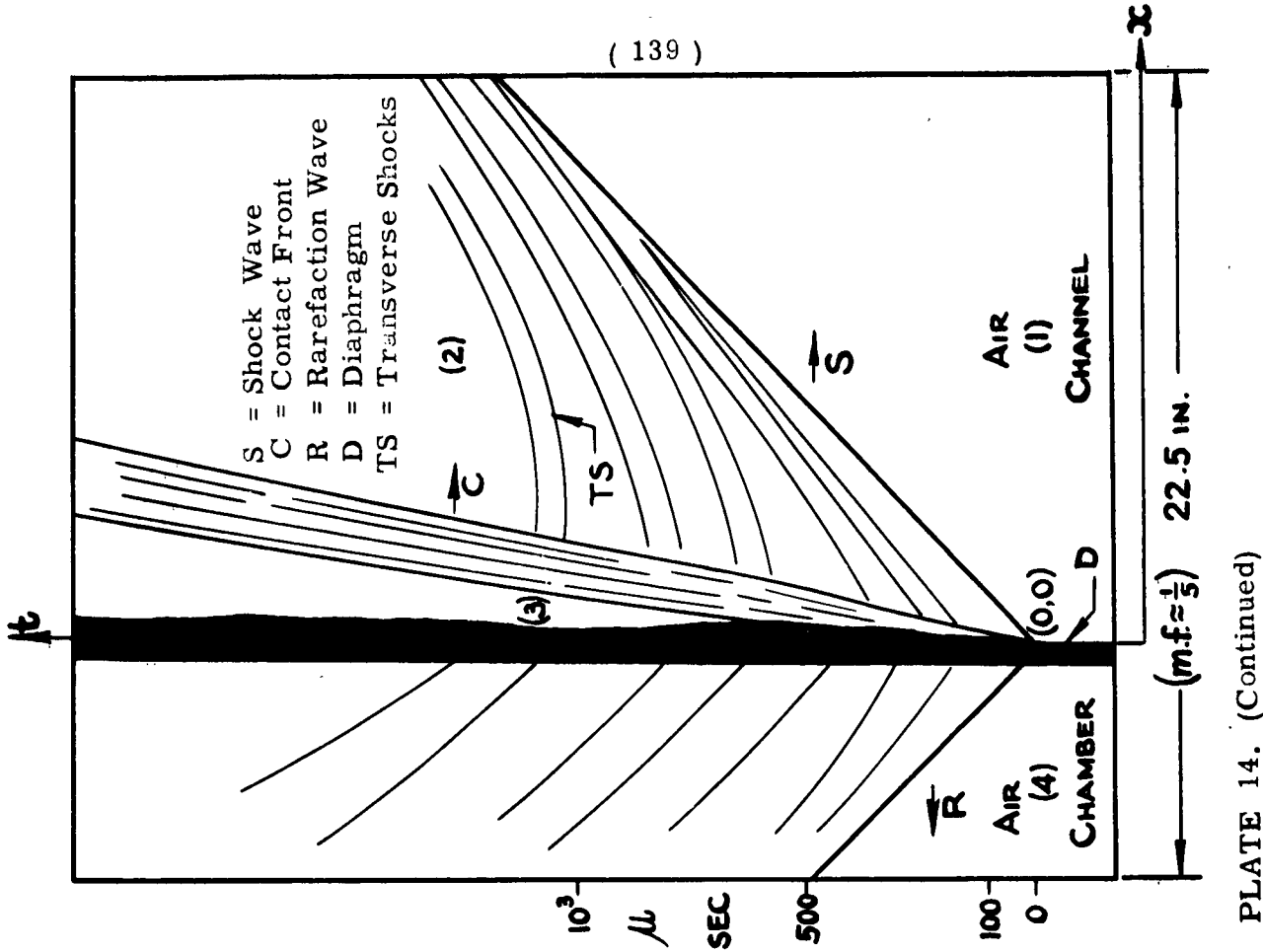
Air (4)
 Air (1)
 CHAMBER
 CHANNEL

SEC
 0
 100
 500

(m.f.s) 23 in.
 30

PLATE 14.

THE WAVE SYSTEM PRODUCED IN A REAL SHOCK TUBE FROM THE INSTANT THE DIAPHRAGM RUPTURES.



$$\begin{aligned}
 p_4 &= 1500 \text{ mm. Hg.} & p_1 &= 1000 \text{ mm. Hg.} & P_{41} &= 1.50 \\
 \rho_{41} &= 1132 \text{ f.p.s.} & W_1 &= 1.06 & U_{21} &= .20 & P_{21} &= 1.2
 \end{aligned}$$

THE WAVE SYSTEM PRODUCED IN A REAL SHOCK TUBE FROM THE INSTANT THE DIAPHRAGM RUPTURES.



(c)

$p_4 = 1000 \text{ mm. Hg.}$

$p_i = 514 \text{ mm. Hg.}$

$P_{4i} = 1.95$

$T_{4,i} = 17.6^\circ \text{ C.}$



(d)

$p_4 = 1009 \text{ mm. Hg.}$

$p_i = 500 \text{ mm. Hg.}$

$P_{4i} = 2.00$

$T_{4,i} = 22.8^\circ \text{ C.}$

PLATE 14. (Continued)



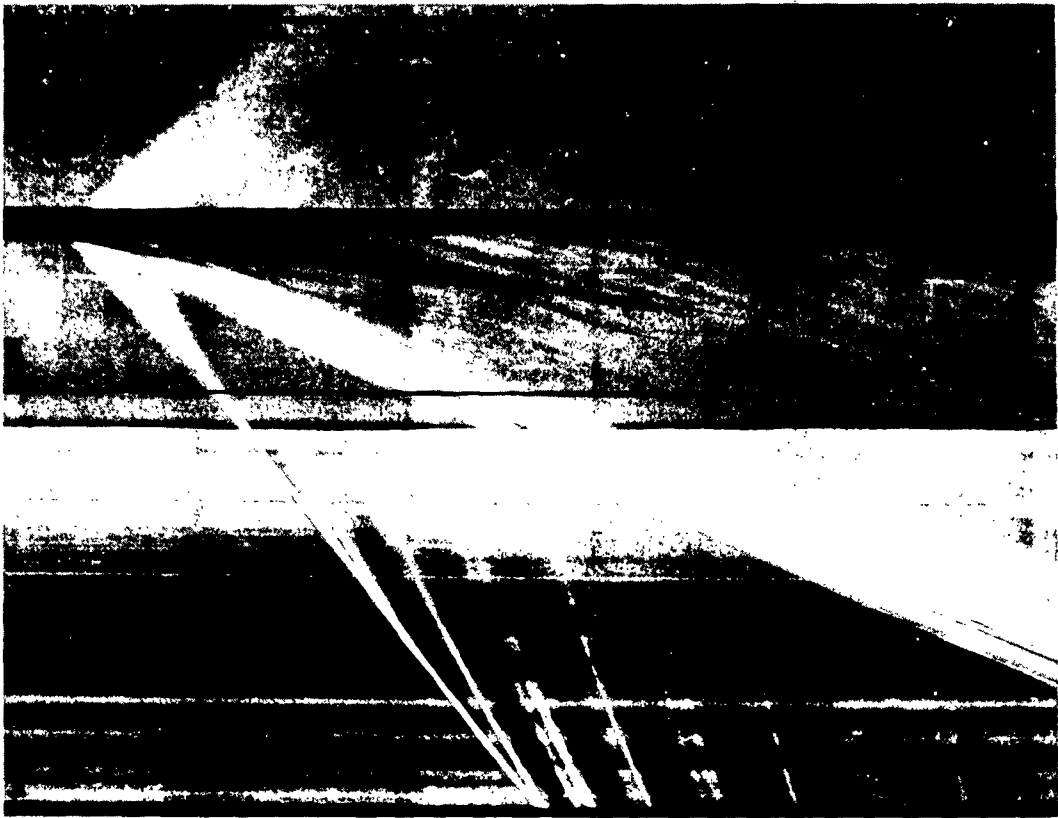
(e)

p_4 = 734.5 mm. Hg.
 p_1 = 367.3 mm. Hg.
 $P_{4,1}$ = 2.00
 $T_{4,1}$ = 23.8° C.



(f)

p_4 = 734.3 mm. Hg.
 p_1 = 367.3 mm. Hg.
 $P_{4,1}$ = 2.00
 $T_{4,1}$ = 22.8° C.



$P_4 = 1500 \text{ mm. Hg.}$ $P_1 = 500 \text{ mm. Hg.}$ $P_{41} = 3.00$
 $\alpha_{4,1} = 1132 \text{ f.p.s.}$ $W_{11} = 1.26$ $U_{21} = .44$
 $P_{21} = 1.7$ $M_2 = .38$ $M_3 = .45$

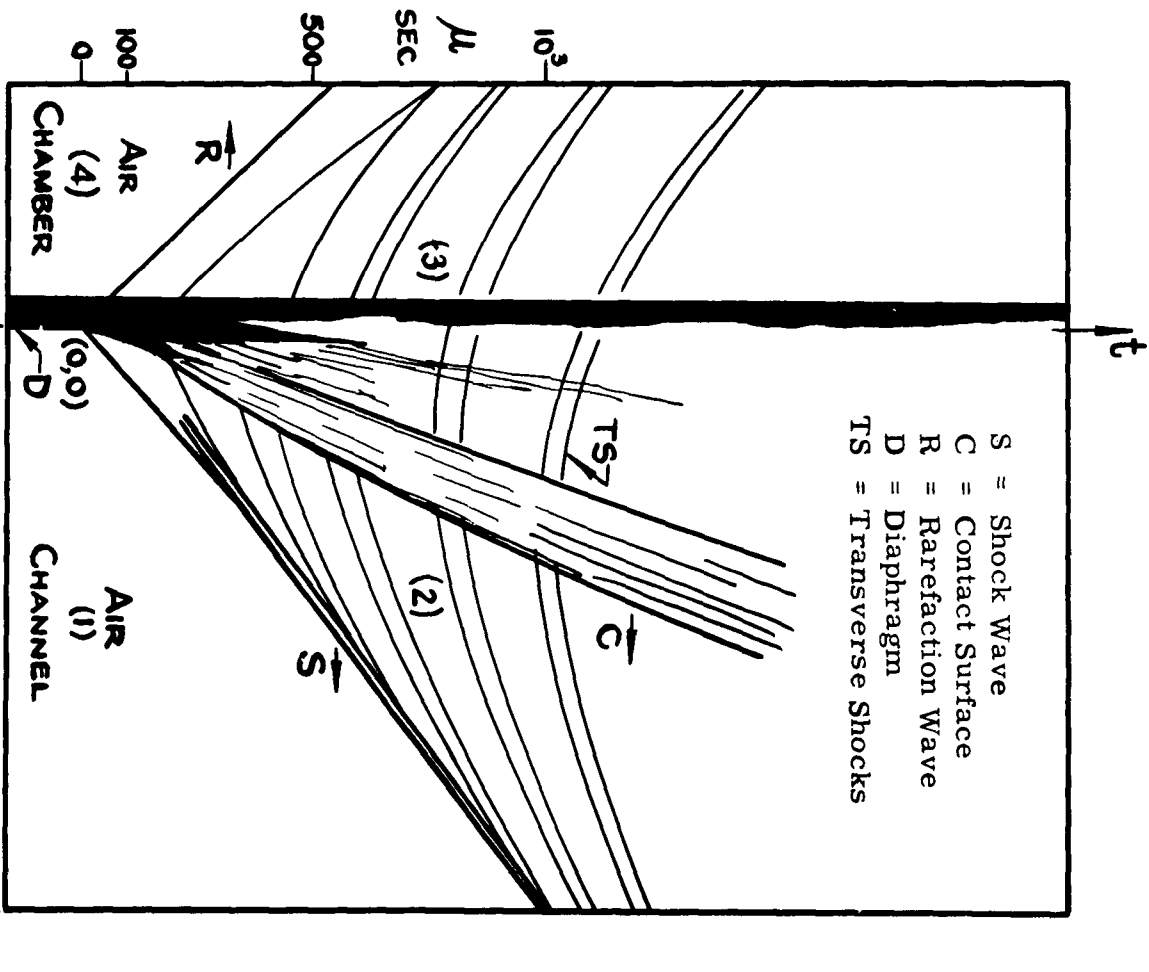


PLATE 14. (Continued)

THE WAVE SYSTEM PRODUCED IN A REAL SHOCK TUBE FROM THE INSTANT THE DIAPHRAGM RUPTURES.



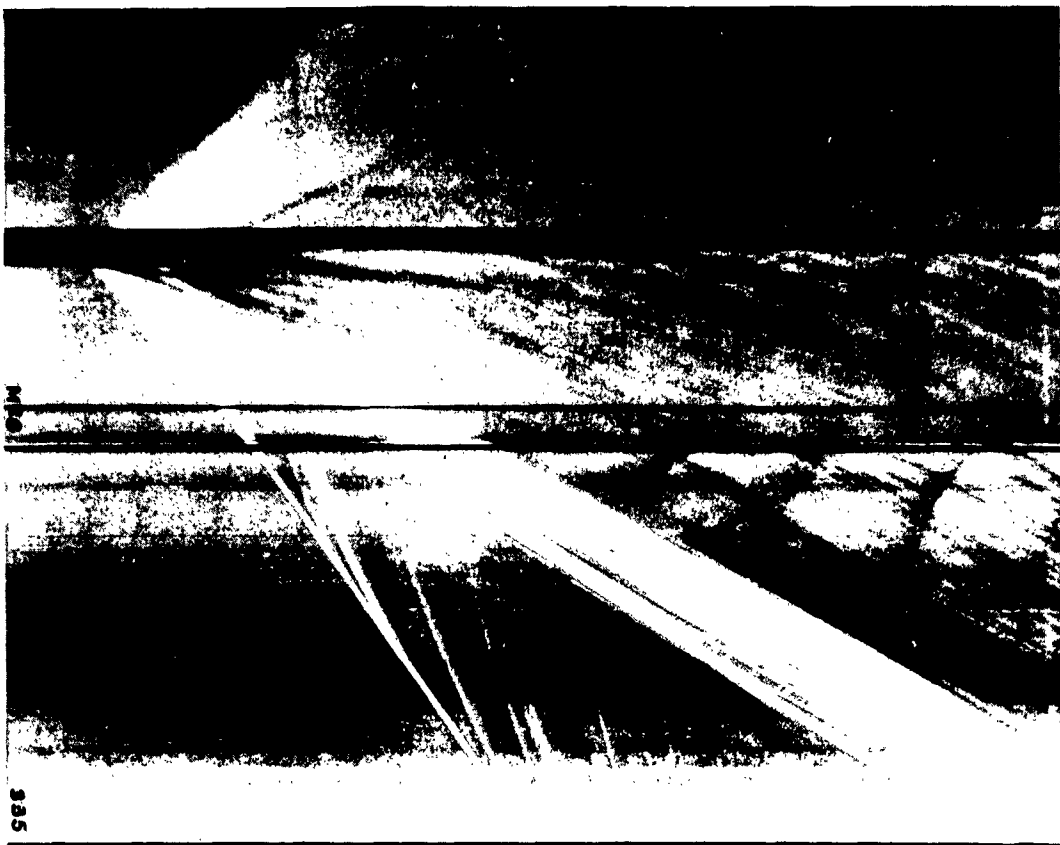
(h)

 $p_4 = 734.5 \text{ mm. Hg.}$ $p_i = 247.2 \text{ mm. Hg.}$ $P_{4,i} = 2.97$ $T_{4,i} = 23.5^\circ \text{ C.}$ 

(i)

 $p_4 = 734.5 \text{ mm. Hg.}$ $p_i = 247.2 \text{ mm. Hg.}$ $P_{4,i} = 2.97$ $T_{4,i} = 23.0^\circ \text{ C.}$

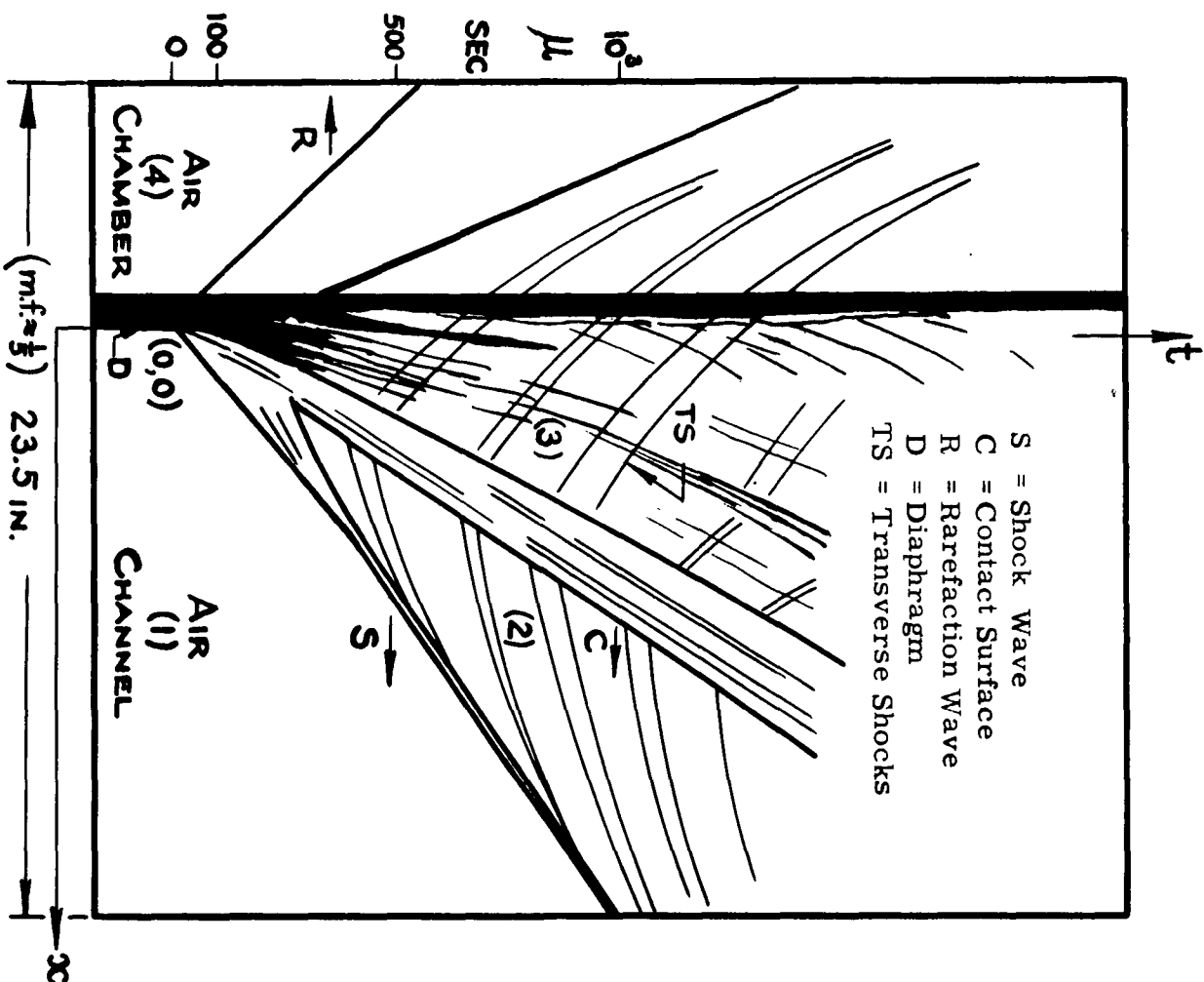
PLATE 14. (Continued)



$P_4 = 1500 \text{ mm.Hg.}$
 $Q_{41} = 1132 \text{ f.p.s.}$
 $P_{21} = 2.1 \text{ M}_2 = .50$

(j)
 $P_1 = 300 \text{ mm.Hg.}$
 $W_1 = 1.39$

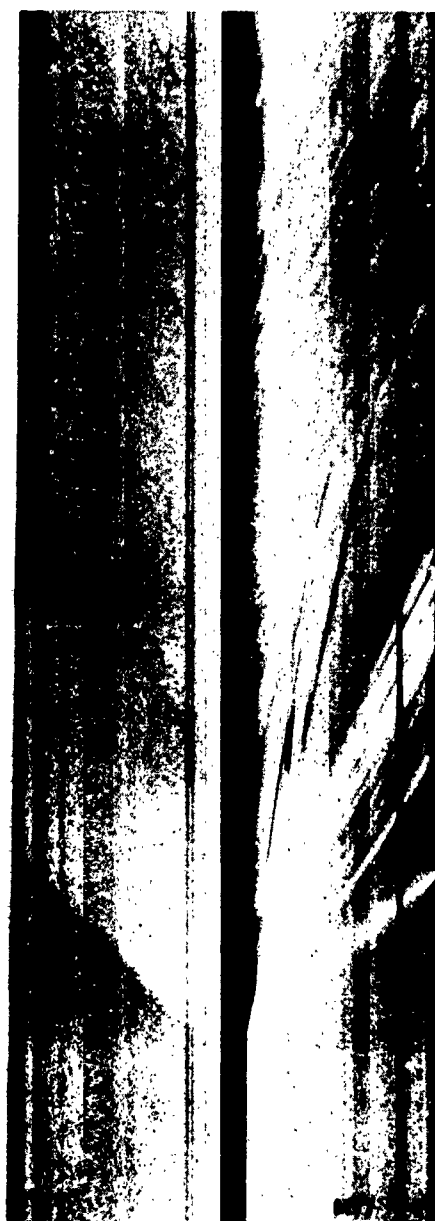
$P_{41} = 5.00$
 $U_{21} = .60$
 $M_3 = .65$





(k)

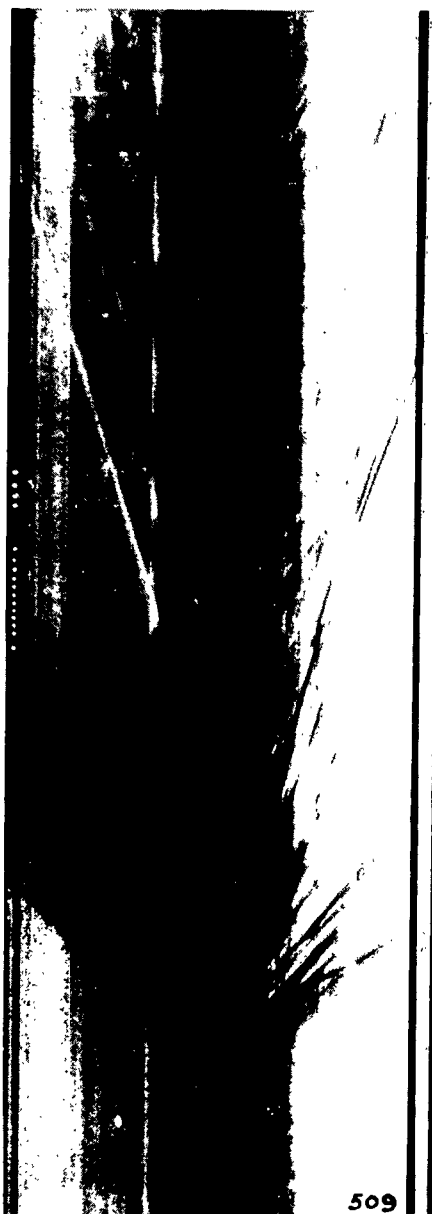
p_{Δ} = 746.8 mm. Hg.
 p_i = 149.4 mm. Hg.
 $P_{\Delta i}$ = 5.00
 $T_{\Delta, i}$ = 24.4° C.



(l)

p_{Δ} = 627 mm. Hg.
 p_i = 125 mm. Hg.
 $P_{\Delta i}$ = 5.02
 $T_{\Delta, i}$ = 21.8° C.

PLATE 14. (Continued)



(m)

$p_4 = 744.0 \text{ mm. Hg.}$

$p_i = 74.0 \text{ mm. Hg.}$

$P_{4i} = 10.0$

$T_{4i} = 25.0^\circ \text{ C.}$



(n)

$p_4 = 748.0 \text{ mm. Hg.}$

$p_i = 74.8 \text{ mm. Hg.}$

$P_{4i} = 10.0$

$T_{4i} = 23.6^\circ \text{ C.}$

PLATE 14. (Continued)



(o)

 $p_{\ast} = 1500 \text{ mm. Hg.}$ $p_i = 150 \text{ mm. Hg.}$ $P_{4i} = 10.0$ $T_{4,i} = 21.8^{\circ} \text{ C.}$ 

(p)

 $p_{\ast} = 1502 \text{ mm. Hg.}$ $p_i = 75.0 \text{ mm. Hg.}$ $P_{4i} = 20.0$ $T_{4,i} = 22.0^{\circ} \text{ C.}$

PLATE 14. (Continued)



(q)

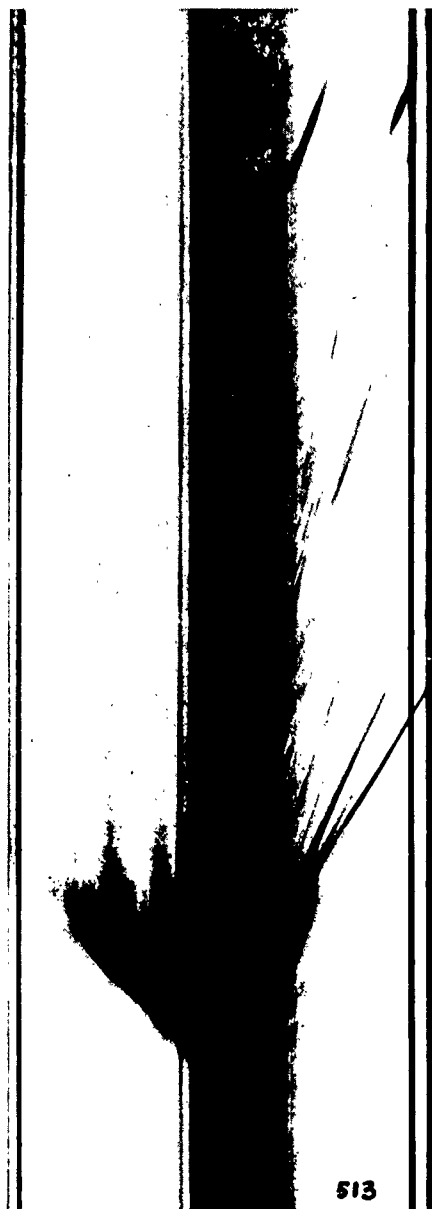
$P_4 = 748.2 \text{ mm. Hg.}$
 $P_1 = 37.4 \text{ mm. Hg.}$
 $P_{4,1} = 20.0$
 $T_{4,1} = 23.6^\circ \text{ C.}$



(r)

$P_4 = 748.0 \text{ mm. Hg.}$
 $P_1 = 37.4 \text{ mm. Hg.}$
 $P_{4,1} = 20.0$
 $T_{4,1} = 23.5^\circ \text{ C.}$

PLATE 14. (Continued)



(s)

$p_4 = 748.0 \text{ mm. Hg.}$
 $p_1 = 7.48 \text{ mm. Hg.}$
 $P_{4,1} = 100$
 $T_{4,1} = 26.2^\circ \text{ C.}$



(t)

$p_4 = 748.0 \text{ mm. Hg.}$
 $p_1 = 7.48 \text{ mm. Hg.}$
 $P_{4,1} = 100$
 $T_{4,1} = 23.4^\circ \text{ C.}$

PLATE 14. (Continued)



(u)

$p_4 = 514 \text{ mm. Hg.}$

$p_i = 5.00 \text{ mm. Hg.}$

$P_{4i} = 103$

$T_{4,i} = 21.5^\circ \text{ C.}$



(v)

$p_4 = 748 \text{ mm. Hg.}$

$p_i = 1.50 \text{ mm. Hg.}$

$P_{4i} = 498$

$T_{4,i} = 25.1^\circ \text{ C.}$

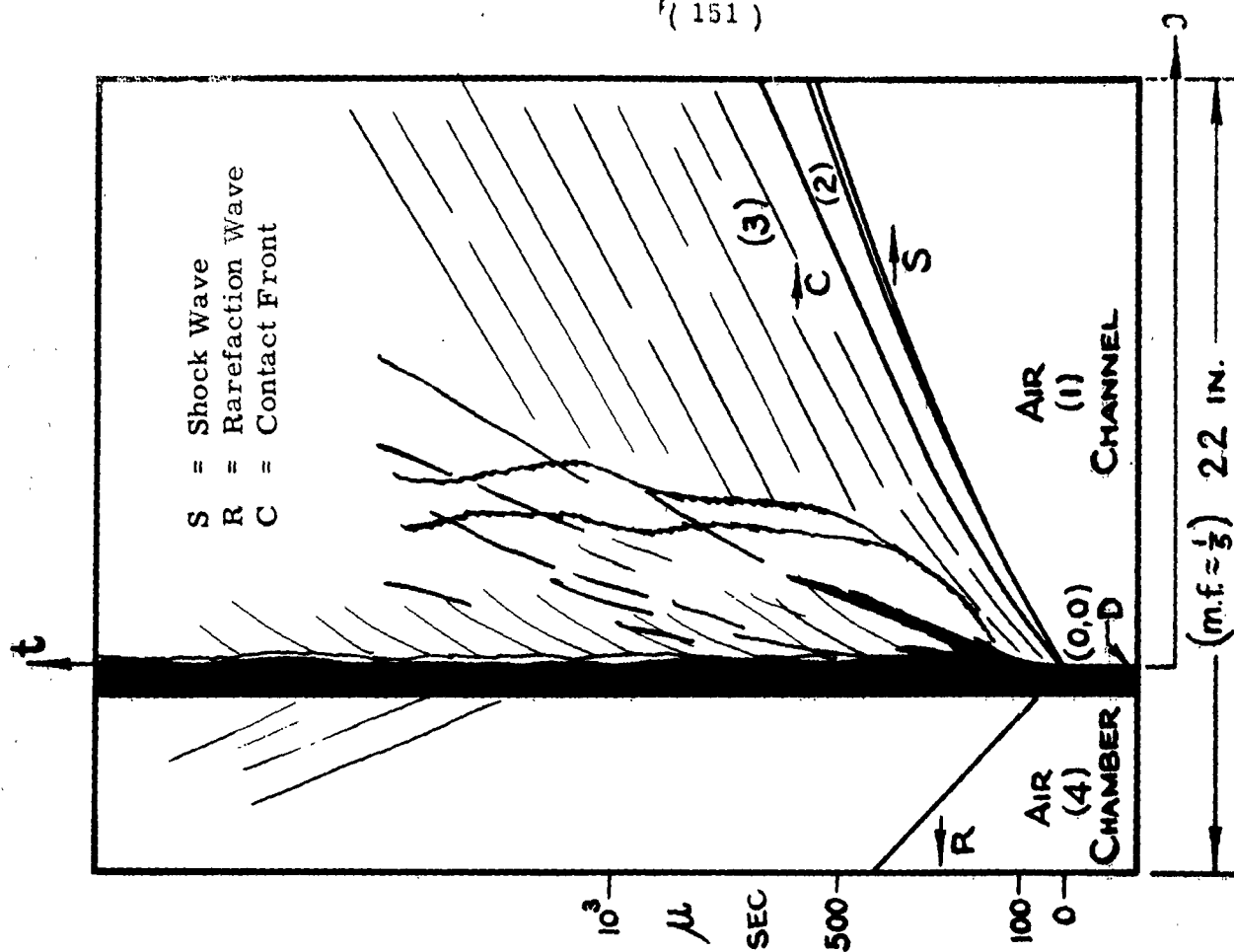
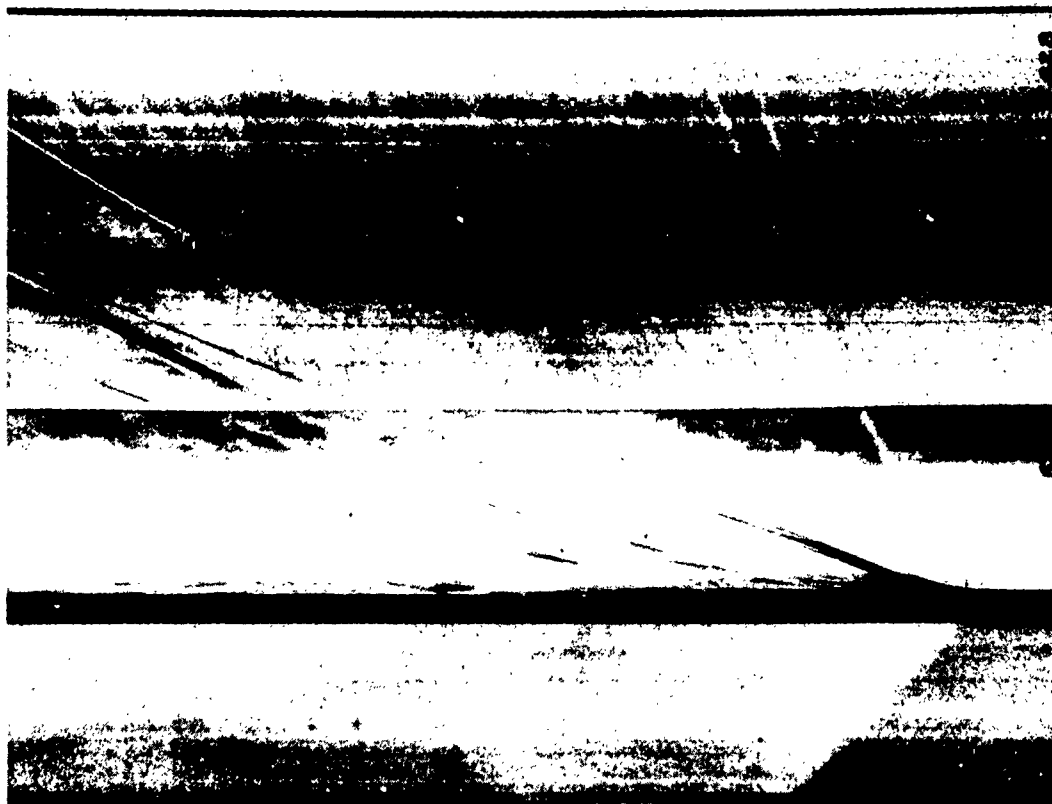


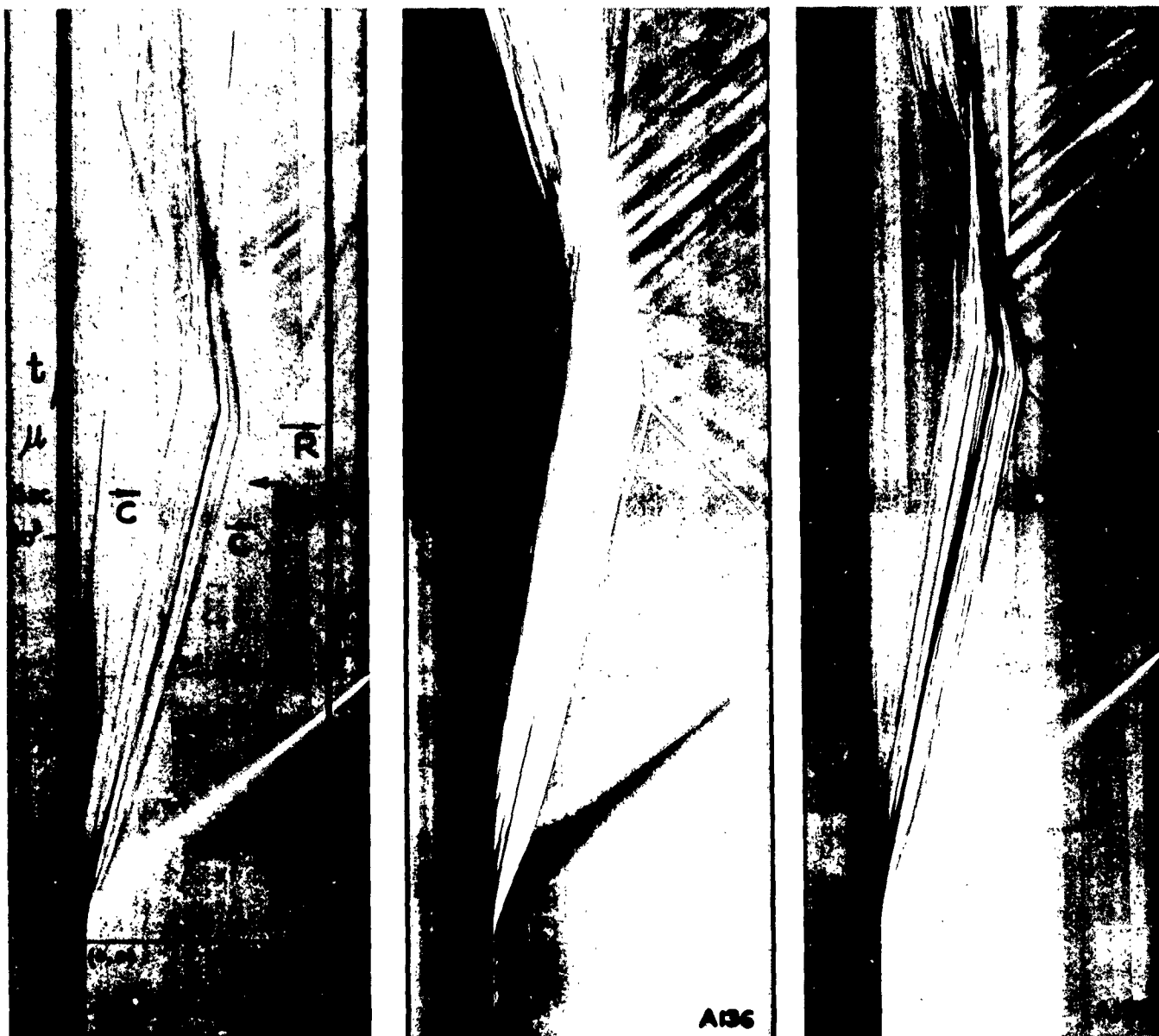
PLATE 14. (Continued)



(W)

$P_4 = 501$ mm. Hg.	$P_1 = 1.00$ mm. Hg.	$P_{41} = 501$
$a_{41} = 1141$ f.p.s.	$W_{41} = 2.54$	$U_{21} = 2.19$
$P_{21} = 7.4$	$M_2 = 1.22$	$M_3 = 2.80$

THE WAVE SYSTEM PRODUCED IN A REAL SHOCK TUBE FROM THE INSTANT THE DIAPHRAGM RUPTURES.



(x)

(y)

(z)

$P_{41} = 1.5$ $p_1 = 500 \text{ mm. Hg. (Air)}$ $p_4 = 750 \text{ mm. Hg. (He)}$

$P_{21} = 1.38$ $W_{11} = 1.18$

PLATE 14. (Continued)

THE WAVE SYSTEM PRODUCED IN A REAL SHOCK TUBE FROM
THE INSTANT THE DIAPHRAGM RUPTURES. CASE HE/AIR.

on plate 14 (j), (k) and (l) for $P_{41} = 5.00$. In (j) the pressure difference is 1200 mm. Hg., whereas in (k) it is close to 600 mm. Hg. and in (l) 500 mm. Hg. The formation region is much better defined in (j), and has a narrower contact front than in (k) or (l). The same phenomenon is illustrated on (g), (h) and (i) for a pressure ratio $P_{41} = 3.00$, and on (c), (d), (e) and (f) for a pressure ratio $P_{41} = 2.00$. On plate 14 (w) for $P_{41} = 501$, the origin is not so well defined. The shock front velocity becomes uniform after about 18 in. or 500 μ sec. Even at $p_1 = 1.00$ mm. Hg. the shock wave is well defined. The front of the contact region is clearly delineated, but for the higher diaphragm pressure ratios the rear boundary merges with the rough flow of state (3).

An examination of the photographic records shows that as P_{41} increases, the slope of the head of the compression wave becomes steeper than the head of the rarefaction wave. Thus the head of the compression wave is not a characteristic line, and it travels at supersonic speed. This is shown in table 7, which contains a summary of some data for the records used in plate 14 (a) to (z). (The run number appears on each schlieren record.)

It is seen that as the diaphragm pressure ratio (P_{41}) increases, the ratio of the speed of the head of the compression wave (C_1) to the speed of the head of the rarefaction wave (C_4 , the sound speed) also increases. For diaphragm pressure ratios up to 5, this difference is small, and for $P_{41} = 20$ it is quite large. For $P_{41} > 20$ the optimum shock speed is approached quickly from the start, and the shock formation region loses its former resolution. It will be noted that for three runs in the low P_{41} range, the speed ratio ($\frac{C_1}{C_4}$) was slightly less than unity. This is a reasonable deviation since a large number of records were not taken for each P_{41} to give a statistical result. It also points to the fact that every diaphragm break is somewhat different. This variation is also confirmed from the changes in the particle velocity (U_{21}), as determined from the front of the contact region. The speed of sound (a_1) was taken as $C_4 = a_4$ for each record. In all cases the value of U_{21} is higher than predicted by the theory when measured close to the origin. Several cross-sectional lengths beyond, the contact front velocity U_{21} does achieve good agreement with the theory, even for diaphragm pressure ratios (P_{41}) up to 100 (see section 5.03).

The channel observation window, which is located at the centre of the tube, permits a record of the phenomena in that plane. Initially, the small amount of air that escapes from the chamber as the diaphragm is pierced travels faster than the bulk of the air which follows the complete disintegration of the diaphragm. This is confirmed by an (x, y)-plane photograph of the bursting diaphragm (see plate 15) and explains the initial high velocity of the contact front.

At a first glance, the records indicate that it may be possible to determine the formation and growth of the shock wave by considering the front of the contact region as a piston path, in a manner similar to

TABLE 7

SUMMARY OF DATA ON FORMATION AND GROWTH OF SHOCK WAVES

RUN NO.	P_{41}	$\frac{C_1}{C_4}$	$U_{21} = U_{24}$	U_{21} (Theory)
M24	1.09	*	0.038	0.02
M3	1.50	0.992	0.204	0.14
M5	1.95	1.004	0.302	0.23
M8	2.01	1.026	0.345	0.24
526	2.00	1.008	0.381	0.24
531	2.00	1.015	0.364	0.24
533	2.97	1.004	0.583	0.39
528	2.97	1.021	0.612	0.39
532	3.00	0.976	0.494	0.40
M27	3.00	1.037	0.440	0.40
507	5.00	1.030	0.843	0.48
M28	5.00	1.043	0.670	0.48
M17	5.00	0.995	0.625	0.48
505	5.00	1.027	0.785	0.48
M47	10.00	1.057	0.884	0.82
518	10.00	1.141	*	0.82
509	10.00	1.127	*	0.82
512	20.00	1.136	*	1.07
519	20.00	1.139	*	1.07
M48	20.00	1.118	1.119	1.07

* not
measurable

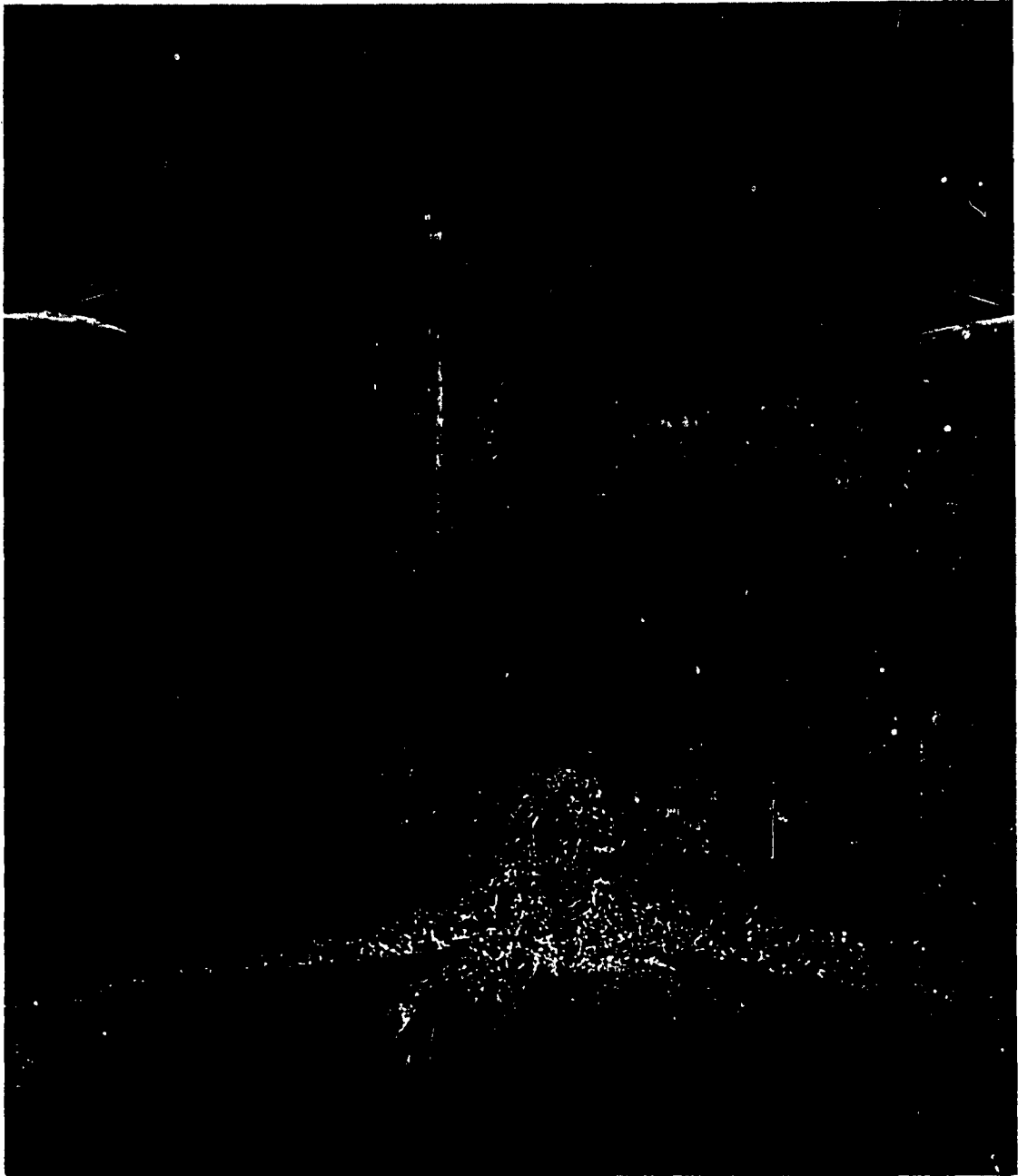


PLATE 15.

SHADOWGRAPH OF THE RUPTURING CELLOPHANE DIAPHRAGM
IN A 2 INCH x 7 INCH SHOCK TUBE AT A DIAPHRAGM PRESSURE
RATIO, $P_{41} = 2.0$. (from reference 7)

that presented in references 10 and 50. This was attempted with run no. 526, plate 14 (f), where the propagation of the first change in the density derivative at the contact front appears to give a reasonable piston path. This curve was measured with a shadowgraph comparator, having a magnification of ten. Distances could be measured to 10^{-4} inches, and angles to half a minute. The results are plotted on figure 55. It is seen that this is not a simple piston curve. For the first 65μ sec. the velocity remains quite uniform at 370 ft./sec. Between 65 and 230μ sec., the acceleration remains roughly constant (about 2×10^6 ft./sec.²). Beyond 230μ sec. the velocity appears to remain at 700 ft./sec. Theoretically, for a diaphragm pressure ratio $P_{41} = 2.00$, the shock wave speed $W_{11} = 1.16$ (1314 ft./sec.) and $U_{21} = 0.24$ (272 ft./sec.). It is seen that the initial propagation of the density derivative far exceeds the theoretical contact surface speed. This is due again to the initial jet of air which enters the channel from the chamber. As a result, it was not possible to obtain the shock formation by the method of characteristics (ref. 10) from this type of piston curve. Nevertheless, some interesting points do result from figure 55. The displacement curve indicates that initially there is an enormous acceleration which decreases to zero in about 230μ sec., although the diaphragm pressure ratio is low ($P_{41} = 2.00$). In the first 10μ sec. the acceleration is of the order of 7.4×10^7 ft./sec.². With a decelerating piston path the shock forms at the head of the compression front, and the birth point (x_s , t_s) may be determined approximately from the relations (see ref. 10):

$$t_s = \frac{2}{\gamma + 1} \cdot \frac{a_4}{\ddot{u}}$$

$$x_s = 0.4 t_s$$

$$a_4 = 1132 \text{ f. p. s.}$$

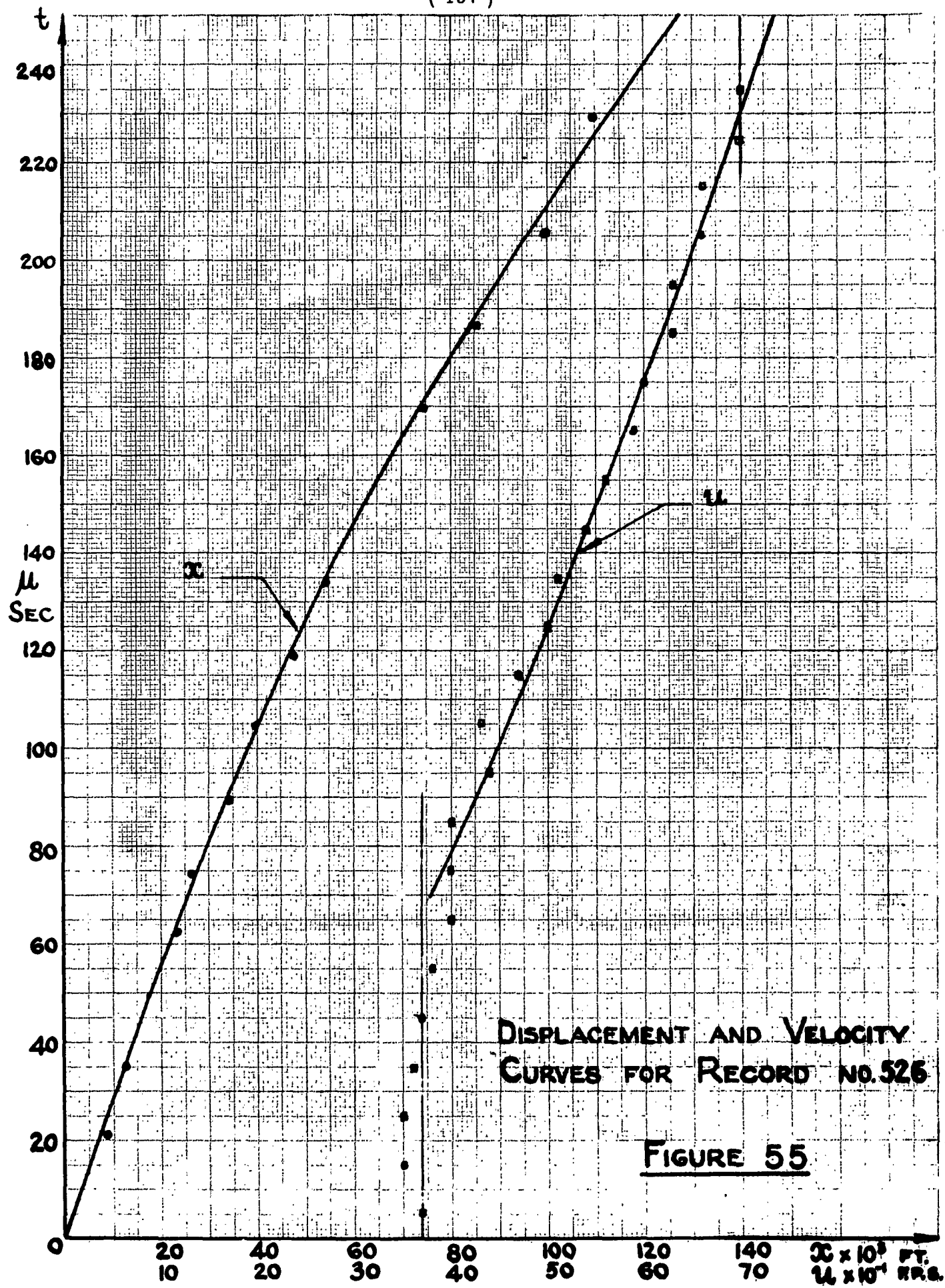
where \ddot{u} = piston acceleration.

$$\text{In this case } t_s = 12.7 \mu \text{ sec.}$$

$$x_s = 14.4 \times 10^{-3} \text{ ft.}$$

and it tends to agree with the theoretical assumption that the shock front forms almost instantaneously. Additional agreement also comes from table 7, which shows that the head of the compression front is supersonic even at very small diaphragm pressure ratios.

Two records are included on plate 16 in order to show the effects of using two diaphragms and diaphragms of different materials. In (a) two CIL MSC 300 cellophane diaphragms were used. It is seen that the second diaphragm burst about 400μ sec. later than the first. In this case the diaphragm breaker was located downstream of the diaphragm. The two heads of the rarefaction waves travel at almost identical speeds. The compression heads are both supersonic and the main shock wave really forms after the second diaphragm ruptures, and the second set of compression waves coalesce with the initial waves. Improved breaks due to a larger pressure difference and better shattering diaphragms are shown on plate 16 (b) and on plate 14 (o) and (p) where one CIL MSTL 600 and one CIL MSC 300 diaphragms were used. In the case of plate (p) the breaks are only of the order of 20 to 30μ sec. apart, nevertheless,





(a)

(b)

$p_4 = 1008 \text{ mm. Hg.}$ $p_1 = 500 \text{ mm. Hg.}$ $p_4 = 1501 \text{ mm. Hg.}$ $p_1 = 30.0 \text{ mm.Hg.}$
 $P_{41} = 2.00$ $T_{4,1} = 21.3^\circ \text{ C}$ $P_{41} = 50.0$ $T_{4,1} = 21.9^\circ \text{ C.}$

PLATE 16.

THE EFFECTS OF NON-SIMULTANEOUS RUPTURE
OF TWO CELLOPHANE DIAPHRAGMS.

they are discernible. As a result the red-zip CIL MSTL 600 cellophane diaphragms were used throughout singly or in multiple numbers because of their uniform, rapid and more complete breaking characteristics.

On the photographs the contact region appears as a thick layer which has an eddying structure. For low diaphragm pressure ratios the layer increases apparently from about 1 to 4 inches over a 6-inch channel length adjacent to the origin, as measured from the schlieren records. This can not be taken as a measure of its actual thickness, otherwise the shock front could also be measured directly from the records, and this certainly would be wrong. All that may be said is that the apparent thickness is that given by the propagation of the discontinuity in the density derivative at the front and rear of the contact region or shock front. A one-to-one mapping would be more likely in case of the contact region, which in practice is a finite layer and may in reality be as thick as it actually appears on the (x, t)-plane schlieren records.

In the case of plate 14 (x), (y), (z) the formation process is very similar, except that the contact front appears of opposite colour to the shock wave. This, of course, should be the case at low P_{41} since helium is only about one-seventh as dense as air. A piston was also inserted in the channel so that the normal reflected shock wave also appears and interacts with the contact front. The head of the rarefaction wave is not visible in the chamber due to the low density of the helium.

The term "eddying" is justified from the observation that this region has many black and white striations, and they are indicative of the propagation of changes in the density derivative throughout this area. Two-dimensional shadowgraphs of this layer confirms the swirling type of motion, as shown on plate 17, which is taken from reference 7. Very little is known about the transition properties through this front. An interferometric study has just been completed at the Institute of Aerophysics and yields some new facts on the physical structure of this type of contact layer. (See ref. 68).

Since the initial assumptions are not attainable at the origin, the rarefaction wave is not of the centred type. In all the records it was not possible to detect the tail of the rarefaction wave. Theoretically, this should have been possible whether the wave was centred or not, since the density derivative is roughly of the same order of magnitude as at the head of the wave for weak rarefaction waves (see table 4). A substantiated reason can not be given for the absence of this Mach line. Its appearance would have made it possible to determine the deviation from the ideal centred rarefaction wave, as well as some of the properties of state (3).

Plate 14 (a), (b), (g), (j) and (w) are all composed of two schlieren records having the same initial conditions. They represent a flow of about 6 inches upstream of the diaphragm and 18 inches downstream of the diaphragm. For all diaphragm pressure ratios (P_{41}), the compression waves overtake, coalesce and accelerate the shock front to a uniform speed. This condition



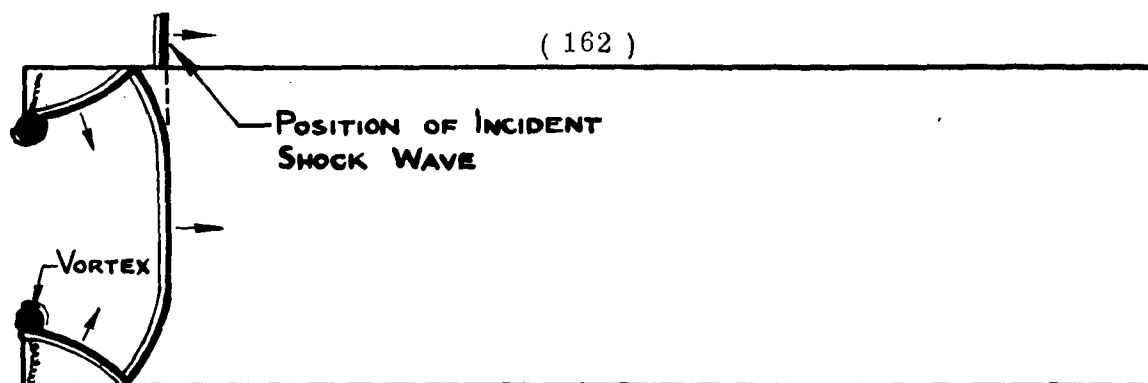
PLATE 17.

FLOW OVER A TWO-DIMENSIONAL 5° - $3'$ WEDGE SHOWING THE
ARRIVAL OF THE CONTACT LAYER (from reference 7)

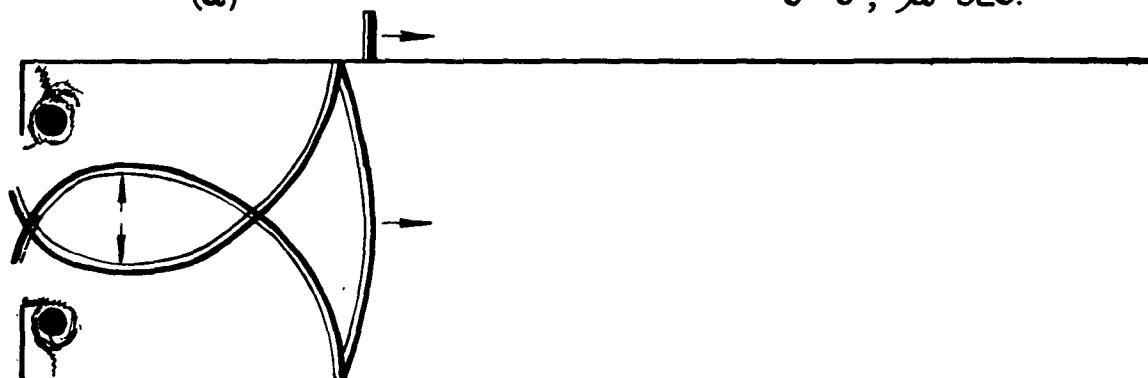
is achieved when the shock path is free from curvature and appears as a straight line. The duration of the formation process decreases with P_{41} . On the other hand, uniform velocity is achieved in a slightly longer time with P_{41} . (Compare plate 14 (b) and (w)). In addition, transverse shock waves also cover the field upstream and downstream of the diaphragm. This phenomenon is shown clearly on plate 14 (a), (b), (g), and (j). The origin and appearance of these waves may readily be accounted for with the aid of plate 18, as follows. Plate 18 was drawn from a series of photographs (figures 45 to 52) which appear in reference 53. It shows a shock wave diffracting through a channel placed in a 2 inch x 7 inch shock tube. The internal dimensions of the channel are given on plate 18 (h). Qualitatively, the series of figures from (a) to (h) illustrate what takes place in a shock tube from the instant the diaphragm is broken. In (a) and (b) the conditions are similar to the rupturing of the diaphragm. The shock wave is curved, and the angle it makes with the wall is not too large, hence regular reflection results and a transverse shock wave is formed. The well-defined vortices that are produced remain quite stationary and are similar to those appearing in the (x, t)-plane (see plate 1). In (b) the transverse waves have just crossed. In an (x, t)-plane schlieren photograph of the centre of the shock tube (for example plate 14 (j)), this would appear as a single point, at the moment the waves were tangent in the centre of the tube, that is, the lowest point in time for the concaved downward traces of the transverse waves. After this instant, for any other time, there would appear two points on the (x, t)-plane, corresponding to the two points of intersection of the waves. This would result in a parabolic type of family of traces as observed on the (x, t)-plane records. The upstream branch appears slower since it is travelling against the flow, and the downstream branch appears faster for the same reason.

This is confirmed by examining the upstream and downstream branches in the (x, y)-plane on plate 18 (b), (c) and (d). In (c) the angle of incidence of the shock wave with the wall has become so large that Mach reflection takes place. In (d) the main shock wave is plane and inverted Mach reflection as well as regular reflection can be observed. This transverse wave system is the mechanism which turns an initially curved shock wave into a plane wave. The wave becomes plane somewhere between (b) and (c) in a matter of about 150μ sec., and the time will vary directly as the size of the tube.

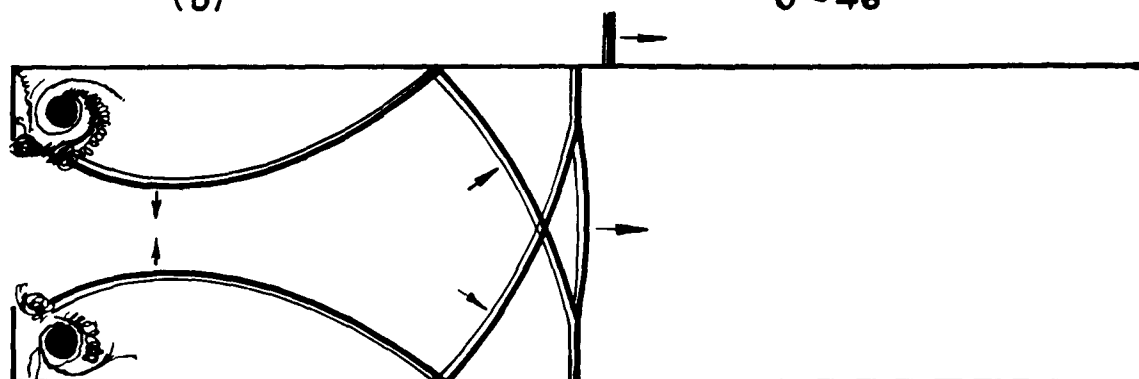
In (e), (f), (g) and (h) it is seen that these transverse waves do not vanish even after they are struck by the reflected shock wave from the closed end. Every incident transverse wave creates its own reflected counterpart. This is also shown on plate 19 (a) to (d) in the (x, t)-plane. These waves continue to follow the shock wave down the channel regardless of distance from the diaphragm (see (a) and (c)) which were taken at a distance of three and twelve feet from the diaphragm. The frequency of these waves on the (x, t)-plane increases with the distance from the diaphragm, due to the increase with time in the angle between the wall and the transverse wave adjacent to the main shock wave. This results in more frequent reflections.



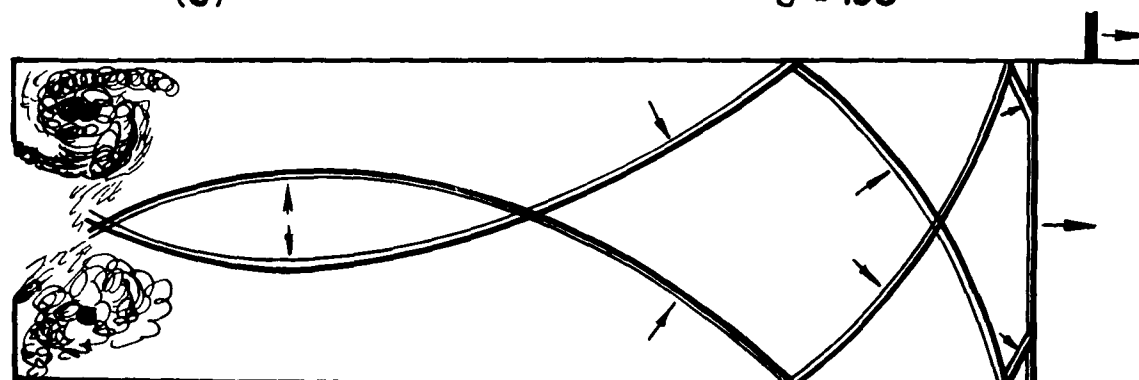
(a)

 $t = 0, \mu \text{ SEC.}$ 

(b)

 $t = 46$ 

(c)

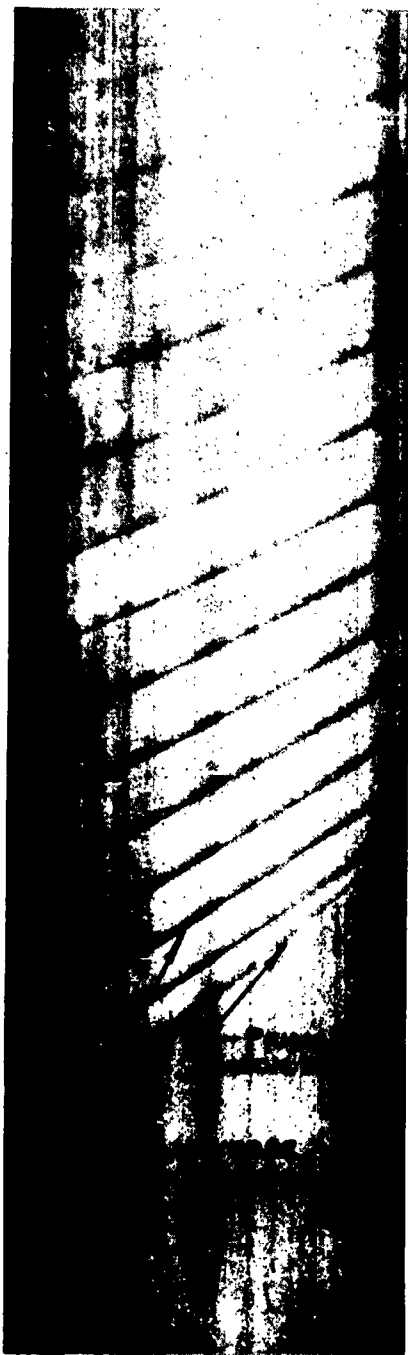
 $t = 100$ 

(d)

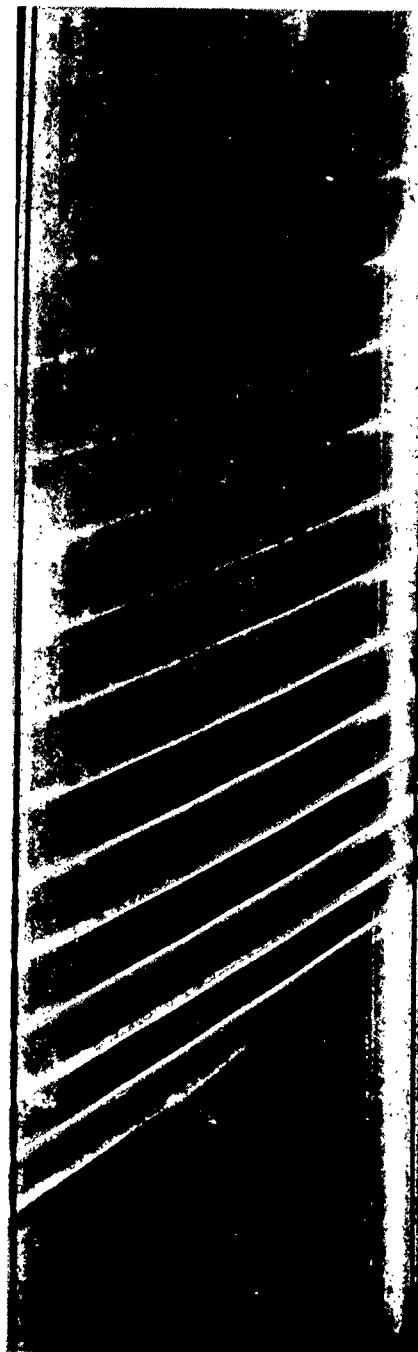
 $t = 201$ $p_1 \approx 750 \text{ mm. Hg. (Air)}$ $p_4 \approx 1500 \text{ mm. Hg. (He.)}$ $W_n = 1.19$ $M_2 = 0.27$ $P_{21} = 1.44$

PLATE 18.

THE TRANSVERSE WAVE SYSTEM FOLLOWING
AN INCIDENT AND REFLECTED SHOCK WAVE.



(a)



(b)

Distance from diaphragm = 39 inches

$$P_{41} = 2.00$$

$$P_{21} = 1.40$$

$$p_1 = 999 \text{ mm. Hg.}$$

$$W_{11} = 1.16$$

PLATE 19.

THE TRANSVERSE SHOCK WAVE SYSTEM GENERATED
BEHIND THE PRIMARY SHOCK WAVE.

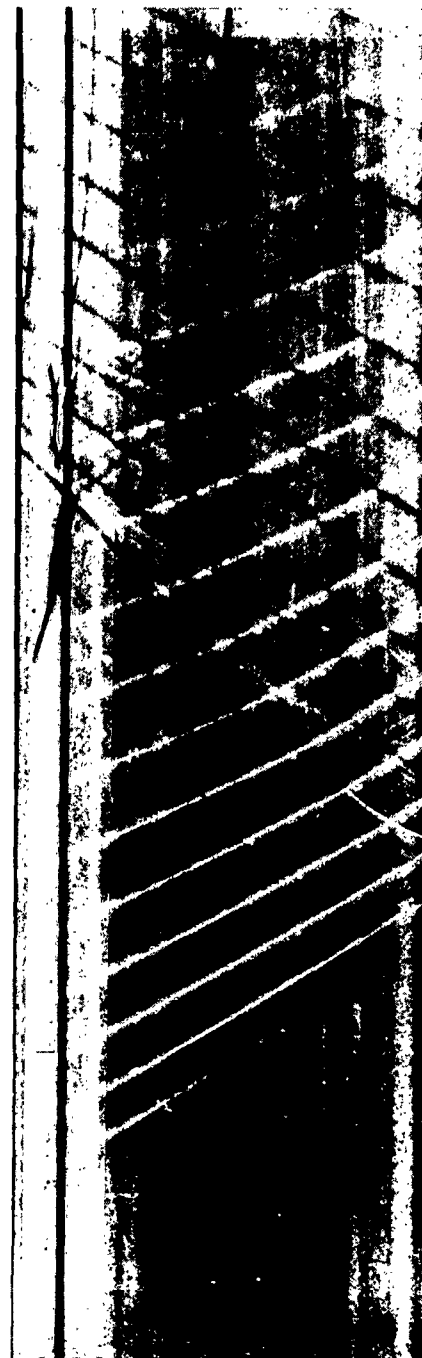


(c)

Distance from
diaphragm = 142 inches

$P_{41} = 2.02$ $p_1 = 744 \text{ mm. Hg.}$

$P_{21} = 1.40$ $W_{11} = 1.16$



(d)

Normal Reflection case
Distance from diaphragm = 44 in.

$P_{41} = 2.61$ $p_1 = 748 \text{ mm. Hg.}$

$P_{21} = 1.60$ $W_{11} = 1.23$

PLATE 19. (continued)



(e)

$P_{41} = 20.7$ $p_1 = 52.0$ mm. Hg.

$P_{21} = 3.80$ $W_{11} = 1.83$

$\rho_2 = 3.9 \times 10^{-4}$ slugs/cu. ft.



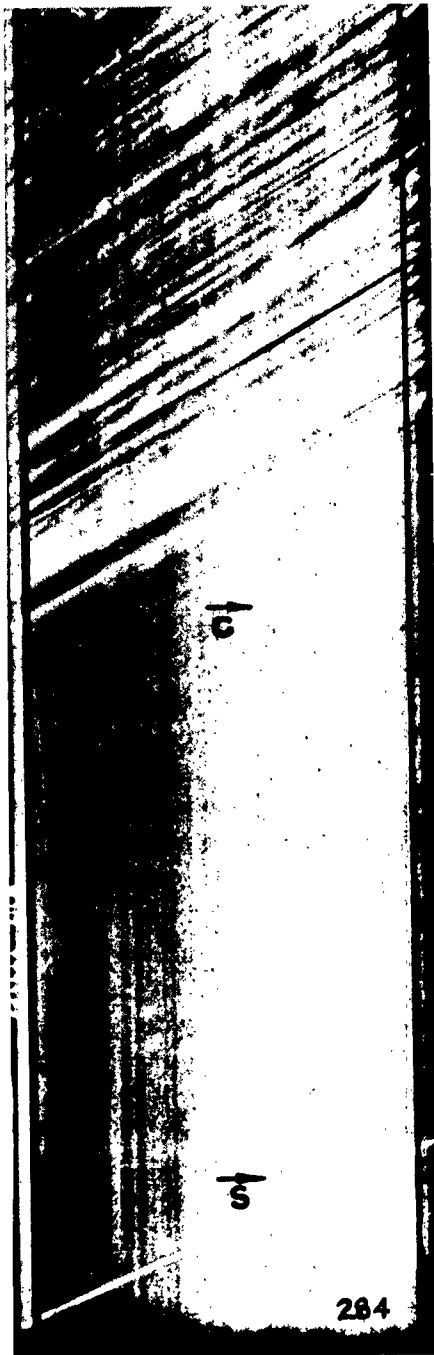
(f)

$P_{41} = 51$ $p_1 = 20$ mm. Hg.

$P_{21} = 5.20$ $W_{11} = 2.13$

Distance from diaphragm = 39 in.

PLATE 19. (continued)



(g)

$P_{41} = 100$ $p_1 = 15$ mm. Hg.

$P_{21} = 6.35$ $W_{11} = 2.37$

Distance from diaphragm = 142 in.



(h)

$P_{41} = 10,000$ $p_1 = 0.40$ mm. Hg.

$P_{21} = 17.0$ $W_{11} = 3.84$

$\rho_2 = 5.9 \times 10^{-6}$ slugs / cu. ft.

PLATE 19. (concluded)

Initially the radius of curvature of the transverse waves are small and they are really weak shocks. However, after a long time (3200 μ sec. for the 3 inch x 3 inch tube for $P_{21} = 1.8$, 3 feet from the diaphragm) the radius of curvature of the primary reflected transverse wave becomes very large, and it approaches a sound wave (see plate 18 (e) to (h)). This is easily confirmed by computing the time required for a sound wave to traverse the height of the tube. From (e) to (h) for the flattest wave, it is about 75 μ sec. and is in good agreement with the sound speed of 1186 f.p.s. in this region. This may also be checked from the (x, t)-plane on plate 19 (a) and (b) for the shallow transverse waves. The time to traverse the three-inch height is 210 - 220 μ sec. For a shock pressure ratio $P_{21} = 1.4$, the theoretical sound speed $a_2 = 1175$ f.p.s., and the time to traverse 3 inches is 213 μ sec., and checks quite well. It should be noted that the flatness of a transverse wave, contrary to a plane wave, is indicative of slow speed. A transverse wave with an infinite radius of curvature (sound wave) would cross the entire centre line of the tube uniformly and would appear as a horizontal line. For a plane wave this would mean infinite speed. Thus the wave speed camera yields true wave speed for plane waves only. Nevertheless, the frequency and the flatness of the transverse wave indicates whether it approaches a sound wave. This is also confirmed by the fact that when these waves are flat they fade and are not easily picked up by the schlieren system, since they are very weak.

The limit of visibility of these waves in the wave interaction tube, as shown on plate 19 occurs at a pressure in the channel $p_1 = 52$ mm. Hg. for $P_{41} = 20.7$ (see plate 19 (e)). Under these conditions $p_2 = 198$ mm. Hg., $\rho_2 = 3.9 \times 10^{-4}$ slugs/cu. ft. and $\rho_3 = 9.9 \times 10^{-4}$ slugs/cu. ft. It should not be implied that these transverse waves disappear at low density, but rather that they can no longer be detected with the schlieren system. The limit of the present schlieren system occurs at a channel pressure p_1 between 0.3 and 0.4 mm. Hg. Plate 19 (i) shows a run at $P_{41} = 10,000$ and $p_1 = 0.40$ mm. Hg., 12 feet from the diaphragm. The shock is just visible, and the physical quantities are $p_2 = 6.8$ mm. Hg., $\rho_1 = 1.25 \times 10^{-6}$ slugs/cu. ft., $\rho_2 = 5.9 \times 10^{-6}$ slugs/cu. ft., and $\rho_3 = 1.38 \times 10^{-3}$ slugs/cu. ft.

The question arises whether these waves affect the flow in any way. The answer is in the affirmative. The numerous criss-crossing of the flow by these transverse waves will alter the physical quantities in states (2) and (3) as well as the shock speed. This also can be seen from plate 18, where between (a) and (d), the diffracted shock wave inside the test channel racing against the incident shock wave velocity has decreased by as much as 6% over a distance of 3.24 inches in 201 microseconds. (This is based on a corrected scale measurement of the photographs, and yields an incident shock speed $W_{11} = 1.19$ and a shock speed inside the channel $W_{11} = 1.12$). As the shock tube dimensions will go down, the number of transverse reflections in a given time and tube section will increase. This will, in turn, cause a correspondingly greater viscous dissipation which will tend to reduce the shock speed or the pressure produced behind it. (See for example, some of the photographs and shock speed results in reference 8 for a one-inch diameter tube.)

Unfortunately, little work has been done to-date to determine the uniformity of states (2) and (3) separated by the contact region by measuring pressure, temperature or density directly, except for very low diaphragm pressure ratios. Hence it is not possible to give the magnitude of the effects these transverse waves produce in the uniform states. However, it may be predicted that these will be sizeable at the higher shock speeds. Recent piezo gauge measurements of the pressure in these states conducted at the Institute of Aerophysics tend to confirm this prediction (see ref. 68), but additional work is necessary to make it conclusive.

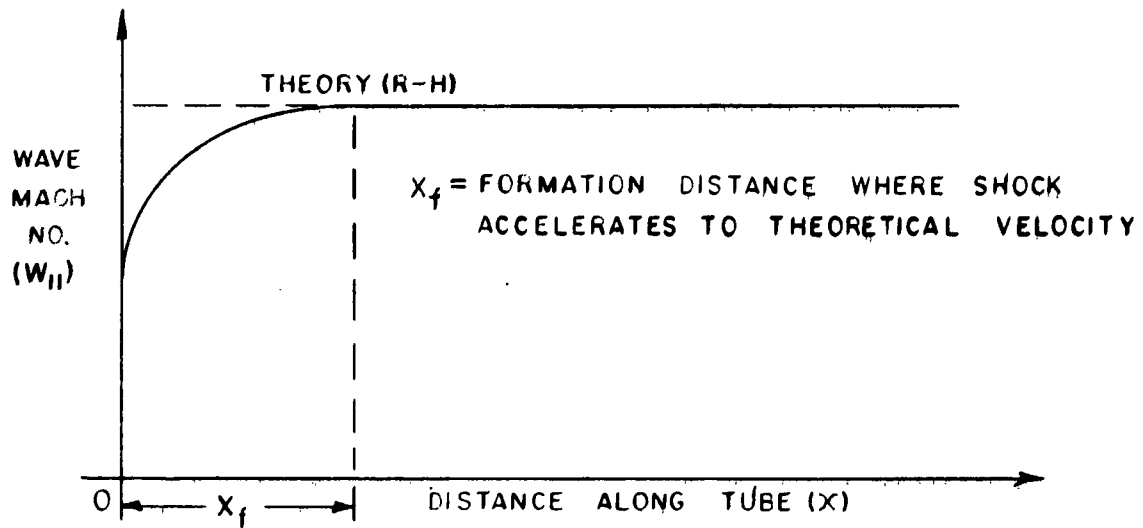
It should be noted that since these transverse waves are a portion of a curved surface (spherical or cylindrical) they will have a peak-type profile rather than a step-type profile. That is, they will have a rarefaction wave attached (see plate 19 (a) and (b), for example). Hence as they catch up to the shock wave, they will not only tend to weaken it by viscous dissipation of the flow behind it, but also by shock decay resulting from the overtaking of these peaked waves, where the attached rarefaction wave may have a far greater effect than the shock portion. Their absolute strength can not be assessed from schlieren observations alone. For instance, on plate 19 (a) the transverse waves appear more dense than the shock front itself, whereas on plate 19 (c) 12 feet from the diaphragm when the shock is weaker, they appear less dense and the appearance of an attached rarefaction wave is also gone. All that may be said is that the transverse waves are weak only if their radius of curvature is large. They will no doubt have an effect, say, on the determination of the shock thickness (ref. 23 and 24) and similar problems.

5.03. Some Experimental and Theoretical Aspects of Shock Wave Attenuation.

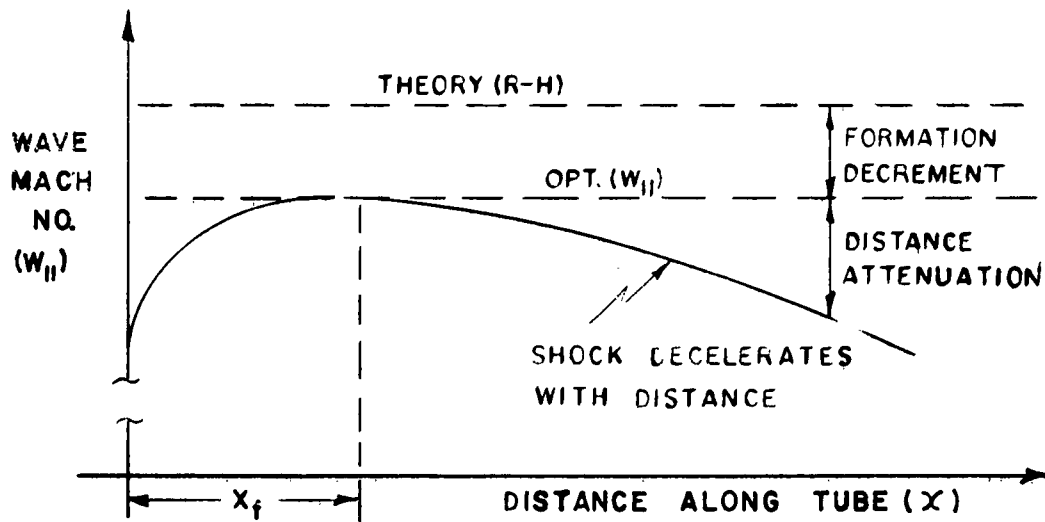
One of the first parameters to be measured by shock tube investigators was the shock wave velocity, because it was relatively easy to determine. It was shown in sections 1.04 and 1.05, that if the shock speed is known, then the pressure ratio (P_{21}) across the wave is determined from equation (1.73). If in addition the initial conditions are known, then the basic shock tube equation (1.65) can also be verified. This approach was followed by many investigators. They found that the agreement between theory and experiment was quite good for weak waves, but became progressively worse for strong shock waves.

This deviation has been referred to somewhat loosely as shock wave "attenuation". More rigorously the term "attenuation" may be considered from the following point of view. Associated with each weak or strong shock is a characteristic length x_f over which the shock forms, accelerates, and achieves a uniform speed. Based on the present results a weak wave will be defined as one for which $P_{21} < 3$. (It was shown in section 5.02 that the distance x_f is longer for strong shocks.) For the weak shock waves this uniform speed is the one predicted theoretically; that is, a given diaphragm pressure ratio (P_{41}) will produce a given shock wave speed (W_{11}) as shown on figure 20. (The wave speed for weak waves did not appear to change over the 142-inch length investigated during the present experiments, as suggested in figure 56(a).) For strong shock waves ($P_{21} > 3$) it is noticed that, although the shock achieves a uniform speed at the end of its formation distance, it never attains the theoretical wave speed corresponding to the given diaphragm pressure ratio. Instead it accelerates to some optimum wave speed, and beyond the formation length it decelerates, and the speed decreases monotonically with distance as sketched on figure 56(b). It should be noted that for the present experiments, strong shock waves were produced by using high diaphragm pressure ratios and low channel pressures. A low channel pressure causes a correspondingly high kinematic viscosity behind the shock. Therefore, it may be concluded that for strong shock waves the overall defect or total attenuation in shock speed consists of two portions; (a) a decrement due to formation, and (b) a further attenuation due to the distance traversed by the shock wave. These will be referred to as a formation decrement and distance attenuation, respectively.

It is reasonable to assume in the case of the strong shock waves (especially where the channel pressure is low and the kinematic viscosity behind them is high) that the formation decrement is due to viscous action during the shock formation process, and the distance attenuation results from a boundary layer build-up. The possible growth of the boundary layer in a shock tube is illustrated on figure 57. It is seen that at the position of the shock wave the boundary layer has zero thickness, since the particles in the tube have not been affected yet. At the contact front the boundary layer thickness (δ) is at a maximum, since these particles have been in



(a) WEAK SHOCK WAVES

 $(P_{21} < 3 \text{ or } W_{II} < 1.7)$


(b) STRONG SHOCK WAVES

 $(P_{21} > 3 \text{ or } W_{II} > 1.7)$

FIGURE 56.

TOTAL SHOCK WAVE ATTENUATION IN A SHOCK TUBE.

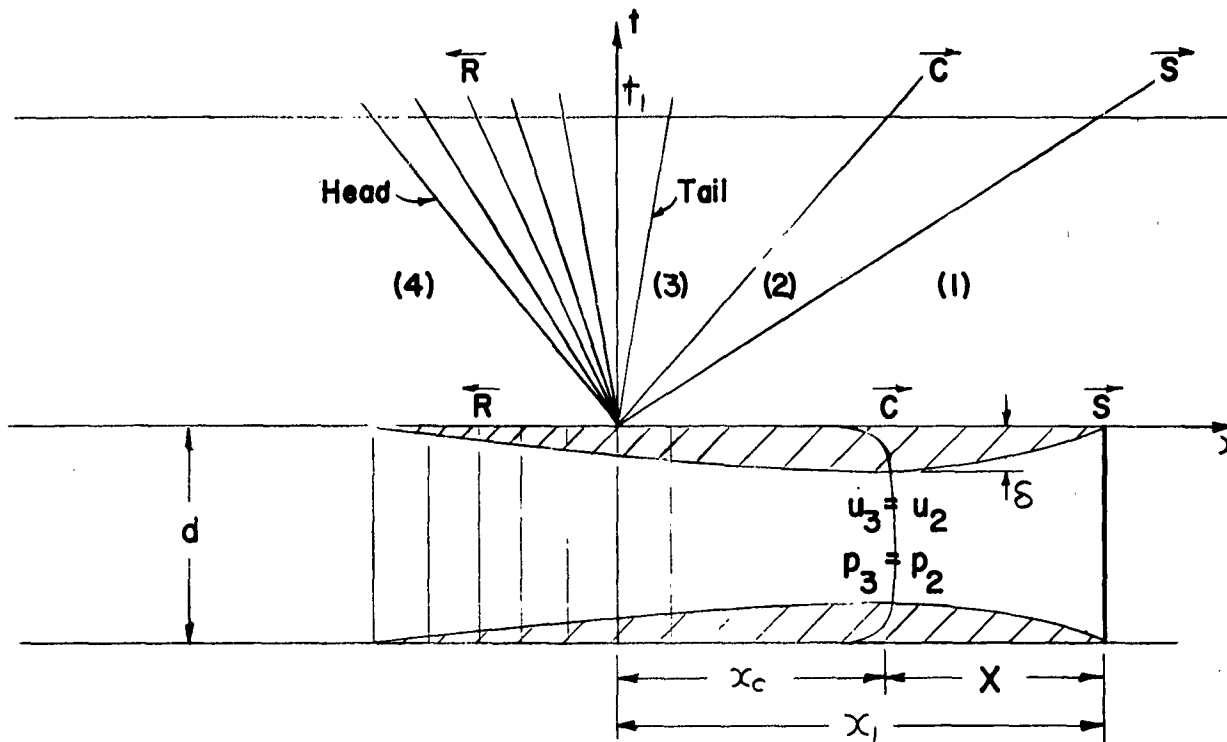


FIGURE 57.

BOUNDARY LAYER GROWTH IN A SHOCK TUBE AT $t = t_1$

motion with respect to the wall for the total length at time (t_1), under consideration. Just behind the contact front the Reynolds number increases discontinuously, and for an ideal flow without turbulence in region (3), it can be safely assumed that the boundary layer thickness will decrease in state (3) and through the rarefaction wave, until it is zero again at the head of the wave. Thus the boundary layer thickness in a shock tube at a given t is a function of x . The thickening of the boundary layer with time will diminish the induced mass flow behind the shock wave, and as a result its speed will be reduced to balance the lower mass flow. No definite mechanism for reducing the shock speed is postulated. However, since shock decay is caused by a rarefaction wave, it is generally considered that the contact front must slow up. The deceleration produces a rarefaction wave similar to the motion of a piston (see section 1). For real flows it will be shown that the front of the contact surface behaves in just the opposite manner; that is, it speeds up. This is the reason why the above assumption may appear rather artificial. Nevertheless, even if the mechanism

for slowing up the shock wave is not known, it is reasonable to state that the boundary layer growth reduces the mass flow, which reduces the shock speed and is the cause of attenuation with distance.

The present problem is somewhat analagous to Rayleigh's analysis of an infinite flat plate which has been started instantaneously from rest to a uniform velocity (u_i) at $t = 0$ (ref. 65). In the present analysis the equivalent problem is considered, that is, the plate is at rest and a flow is generated instantaneously such that its speed u is zero for $t \leq 0$ and $u = u_i$ for $t \geq 0$. This is illustrated for a cylindrical shock tube in figure 58, and has been solved in reference 21. It is seen that at small times the boundary layer is thin and uniform over the entire length of the tube. For large times the boundary layer approaches the centre of the tube and the motion becomes a pipe flow. In a shock tube the boundary layer does not grow uniformly and it occupies only a finite length of the tube. Furthermore, the end boundary conditions are complex due to the presence of the shock wave and the contact front. However, it can be shown that some useful results may be obtained by considering the two problems as identical.

A dimensional analysis of the instantaneously started smooth tube (fig. 58) shows that the boundary layer growth, neglecting heat transfer, is a function of the following quantities. (For a real flow the tube walls are cold and heat transfer exists between the gas and the walls, and here the Prandtl number also would be of importance.)

$$\delta = \delta(p, \rho, \mu, \gamma, u, d, t) \quad (5.01)$$

$$\text{or } F(\delta, p, \rho, \mu, \gamma, u, d, t) = 0 \quad (5.02)$$

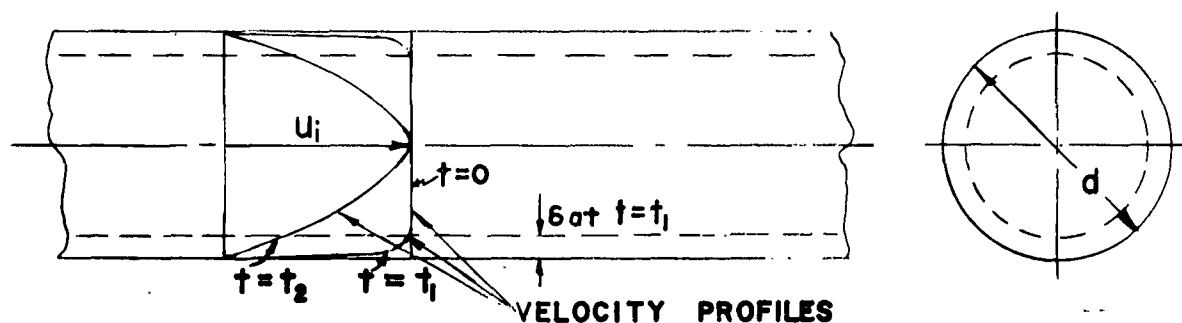


FIGURE 58

BOUNDARY LAYER PROFILES WITH INCREASING TIME FOR THE EQUIVALENT RAYLEIGH PROBLEM IN A CYLINDRICAL TUBE.

Therefore, there are five dimensionless Π -functions, such that equation 5.02 may be expressed in terms of the following dimensionless parameters as (ref. 70, Appendix A),

$$f\left(\frac{\delta}{d}, \frac{u^2}{\partial p/\rho}, \frac{\rho u d}{\mu}, \frac{\nu t}{d^2}, \gamma\right) = 0 \quad (5.03)$$

or

$$\frac{\delta}{d} = g\left(M, Re, \frac{\nu t}{d^2}, \gamma\right) \quad (5.04)$$

Hence for the distance attenuation, it may be expected that the boundary layer growth for a given gas (γ) without heat transfer would be a function of the Mach number (M), the Reynolds number (Re) and the time parameter ($\nu t/d^2$). It was pointed out above that the particles at the contact surface have been in motion with respect to the wall for the greatest length of time. Only this time will correspond to the time considered in the Rayleigh problem. If the total wave attenuation is assumed small, then from figure 57, the longest time for a shock speed w_1 and particle speed u_2 may be computed as any one of the following times, since they are all identical (fig. 57),

$$t_1 = \frac{x_c}{u_2} = \frac{x_1}{w_1} = \frac{X}{w_1 - u_2} \quad (5.05)$$

It is convenient to measure t_1 in terms of the distance of the shock position from the diaphragm $t_1 = \frac{x_1}{w_1}$, and the time parameter may be expressed for the shock tube case as

$$\frac{\nu_2 t}{d^2} \equiv \frac{\nu_2 X}{A w} \quad (5.06)$$

where A is the cross-sectional area proportional to d^2 .

In the series of experiments which will be described subsequently, the time parameter was varied by changing x . That is, the shock was observed over increasing distances from the diaphragm (x), while $\frac{\nu_2}{A w_1}$ was held constant for a given wave speed (w_1).

The above type of analysis can not be applied directly to the formation decrement, since it may also depend on the diaphragm bursting process, which is three-dimensional and of a complex nature.

In order to check some of the above factors which might contribute to the formation decrement, different types and combinations of diaphragms were used at the origin. In addition the influence of the static loading across the diaphragm was also investigated. This was accomplished by maintaining a constant pressure difference $\Delta p = p_4 - p_1$, of 100, 500 and 1000 mm. Hg., over a wide range of diaphragm pressure ratios P_{41} . A high pressure difference across the diaphragm gave the most complete ("clean") and uniform break, and had the nearest resemblance to the ideal case of instantaneous and complete removal of the diaphragm at $t = 0$.

Since the chamber pressure (p_4) in the present tube is limited to about 7 atmospheres, it was not possible to maintain a constant channel pressure (p_1) over a large P_{41} range. Instead p_4 was held constant while p_1 was varied to give a range of P_{41} , and the effects on the formation decrement were noted.

The influence of extraneous disturbances on the formation decrement, which may be produced by the ruptured diaphragm and the diaphragm breaker plunger, were also investigated. The broken cellophane diaphragm has a shredded edge which produces a discontinuity at the origin. In order to emphasize this property, protruding sheet metal frames were introduced at the diaphragm station, and their effects on the formation decrement were observed. Similarly, the diaphragm breakers were installed upstream and downstream of the diaphragm station, under identical conditions, and the effects produced on the shock velocity were noted.

Finally, to study the distance attenuation, the shock velocities were measured continuously over a 12-inch length at distance intervals between 0 and 142 inches (0 to 50 tube widths) from the diaphragm station. The range of diaphragm pressure ratio was simultaneously varied over the range $1 < P_{41} \leq 10,000$. (On the graphs that follow x is the distance from the diaphragm station to the centre of the 12-inch, schlieren beam.)

It is likely that a shock tube with poorly aligned compartments and non-uniform cross-sections could alter both the formation decrement and the distance attenuation. The present tube was therefore designed and constructed with utmost care and accuracy to ensure that faulty construction and poor alignment would not contribute significantly to shock wave attenuation.

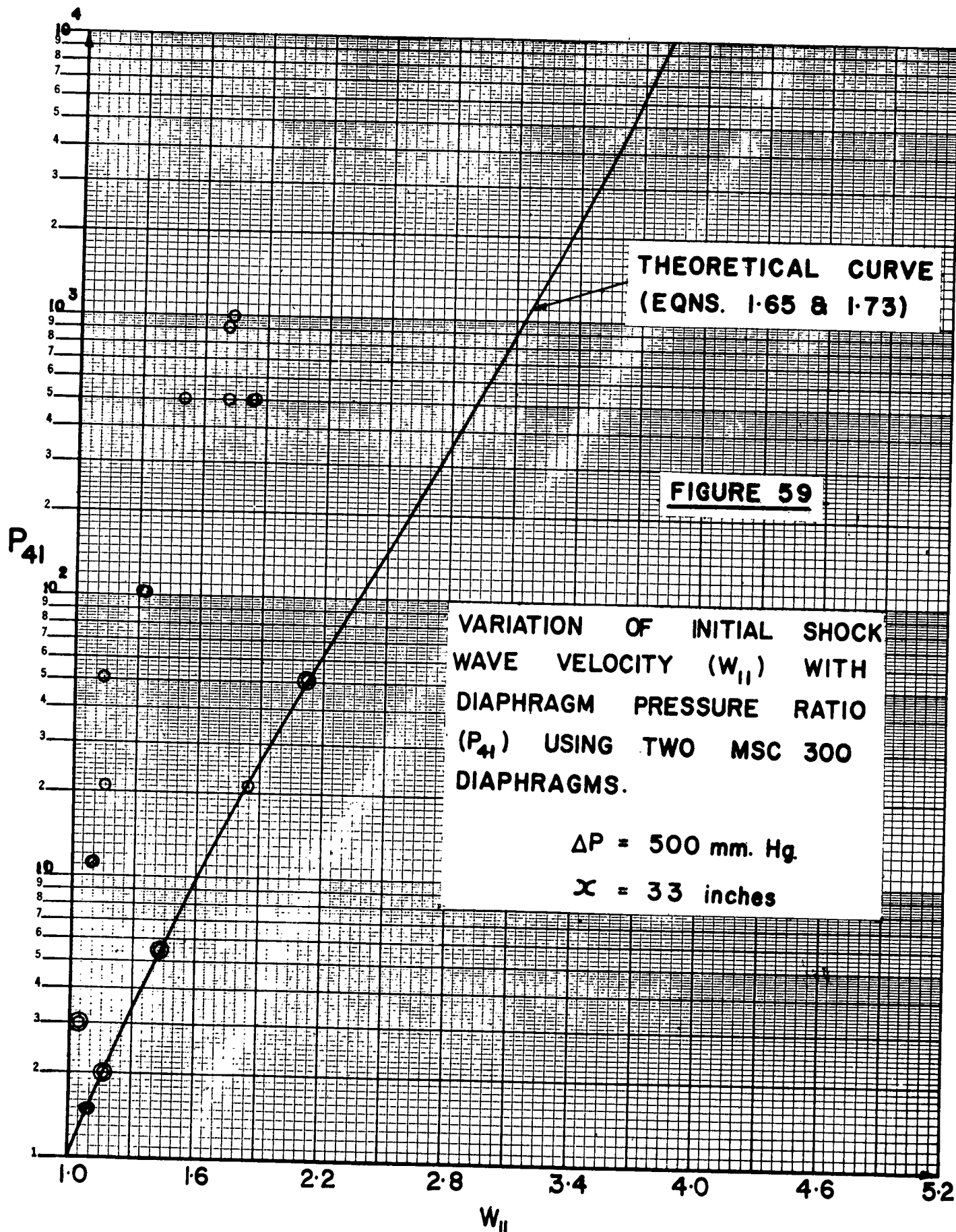
The arrangements of the wave interaction tube that were utilized during the attenuation experiments are shown on plate 13. The results obtained by introducing the above variable initial conditions will be discussed in some detail in the following.

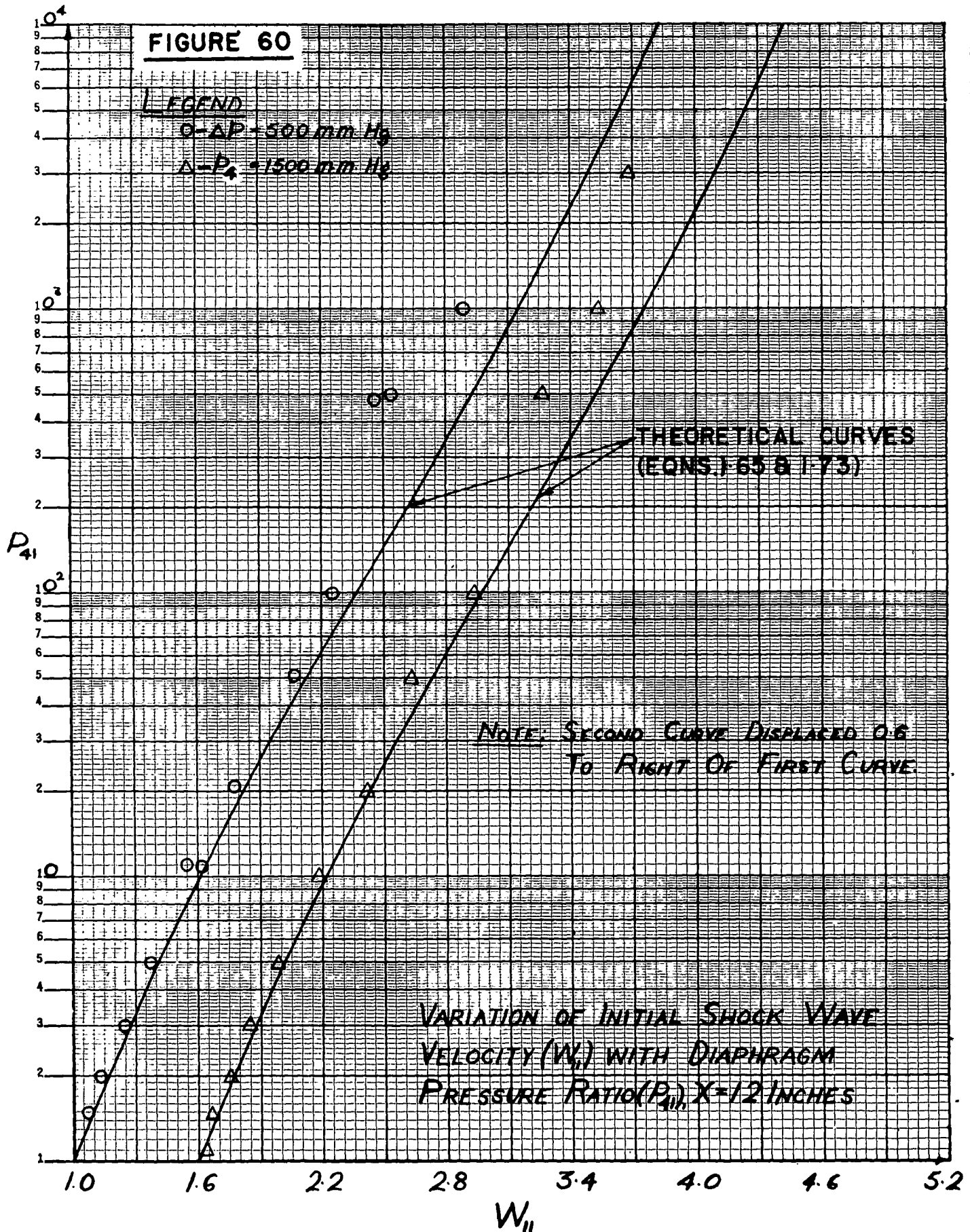
It was found early in the course of the experiments that the number type and combination of diaphragms had a definite effect on the shock wave velocity. Closest agreement with theory resulted from diaphragms that completely shattered and left as little material as possible at the diaphragm station. This occurred when the diaphragm was loaded close to its static breaking strength. When diaphragms of unequal thickness were used, it gave rise to one breaking ahead of the other (see plate 16(b)). Two MSC 300 diaphragms were used to obtain the record shown on plate 16(a). Although here both diaphragms are identical, again, one has broken before the other. In order to determine the effect of this poor break on the shock velocity a set of measurements were taken at 33 inches from the diaphragm. The results obtained are shown on figure 59 and are seen to be completely unreliable for calibration purposes. Therefore only MSTL 600 diaphragms were used throughout in combination or singly. The runs with $\Delta P = 100$ mm. Hg. are an exception. Here single MSC 300 diaphragms were utilized. Table 8 gives the static breaking strengths of various diaphragm combinations employed for this tube. Figure 60 shows the variation of W_{11} with P_{41} for a constant chamber pressure $p_4 = 1500$ mm. Hg. and $\Delta p = 500$ mm. Hg. at a distance $x = 12$ inches. It is seen that the

TABLE 8

A COMPARISON OF VARIOUS DIAPHRAGM COMBINATIONS ON THE BASIS OF THEIR APPROXIMATE STATIC BREAKING STRENGTH.

DIAPHRAGM COMBINATION	RUPTURING PRESSURE DIFFERENCE (in mm. Hg.)
One CIL MSC 300 0.001 inch red coloured cellophane	450
Two CIL MSC 300 0.001 inch red coloured cellophane	740
One CIL MSTL 600 0.0025 inch "red zip" cellophane	1300
One CIL MSC 300 0.001 inch cellophane and one CIL MSTL 600 0.0025 inch "red zip" cellophane	1550
Two CIL MSTL 600 0.0025 inch "red zip" cellophane	2500
Three CIL MSTL 600 0.0025 inch "red zip" cellophane	3700





two curves are essentially similar. Good agreement with theory is noted up to $P_{41} = 100$. Above this value the formation decrement becomes progressively greater. Since no apparent changes were noted by maintaining a constant chamber pressure, it was concluded that its influence was small. Thereafter a constant chamber pressure was not utilized as a basic condition.

Figure 61 shows the effect of diaphragm loading ($\Delta p = 1000$, 500 and 100 mm. Hg.) on shock wave attenuation at $x = 33$ inches. It is seen that for low P_{41} the effect of Δp is not very marked. For high values of P_{41} the diaphragm with the greatest loading gives the smallest formation decrement over the tested range of P_{41} . The maximum P_{41} for each of the three curves was limited by the low channel pressures. For example, for $\Delta p = 100$ mm. Hg. it was necessary to use channel pressures of 1.0 and 0.5 mm. Hg. in order to obtain a value of P_{41} of 100 and 200 respectively. In addition, the diaphragm could not be loaded near its static breaking strength for $\Delta p = 100$ mm. Hg. As a result the diaphragms split rather than shattered. This effect, along with the high kinematic viscosity in the channel resulted in a greater formation decrement at relatively low values of P_{41} when $\Delta p = 100$ mm. Hg.

It should be noted that the curve for $\Delta p = 500$ mm. Hg. has a lower shock wave formation decrement at $x = 33$ inches (figure 61) than at $x = 12$ inches (figure 60) in the range $10^2 \leq P_{41} \leq 10^3$. This confirms the representation on figure 56(b), that is, the shock wave does not reach its optimum velocity close to the diaphragm for high values of P_{41} . It should be emphasized that the exact position (x) of minimum formation decrement has not been established, but it lies between $x = 12$ and 33 inches from the diaphragm station over the range of P_{41} covered here. Plate 14 (w) also shows that for $P_{41} = 501$ the shock wave is accelerating, and its trace is still curved at $x = 12$ inches, which means a longer formation length at high P_{41} . The results of figure 60 were taken from the straightest portion of the shock path close to $x = 12$ inches. However, the shock path curvature at high values of P_{41} , could possibly introduce some error in the measurement of W_{11} near the diaphragm. The results for $x = 50$ appear on figure 62. It is seen that these values do not differ markedly from those of figure 61. Over the range $1 \leq P_{41} \leq 10^3$, the total wave attenuation changes very little with $\Delta p = 500$ and 1000 mm. Hg. This indicates that as long as the diaphragm is loaded to give a "clean" break, the resulting shock speed can be expected to be very consistent. If Δp is large, then the channel pressure (p_1) is correspondingly high for a given P_{41} . This is especially desirable for $P_{41} \approx 10^4$ in order to reduce the kinematic viscosity which contributes very considerably to the total attenuation.

Figure 62 also shows the effects of introducing extraneous disturbances into the flow. A frame of sheet aluminum foil was placed at the diaphragm station with a cut-out $2 \frac{1}{2}$ inches square in the centre, such

FIGURE 61

LEGEND

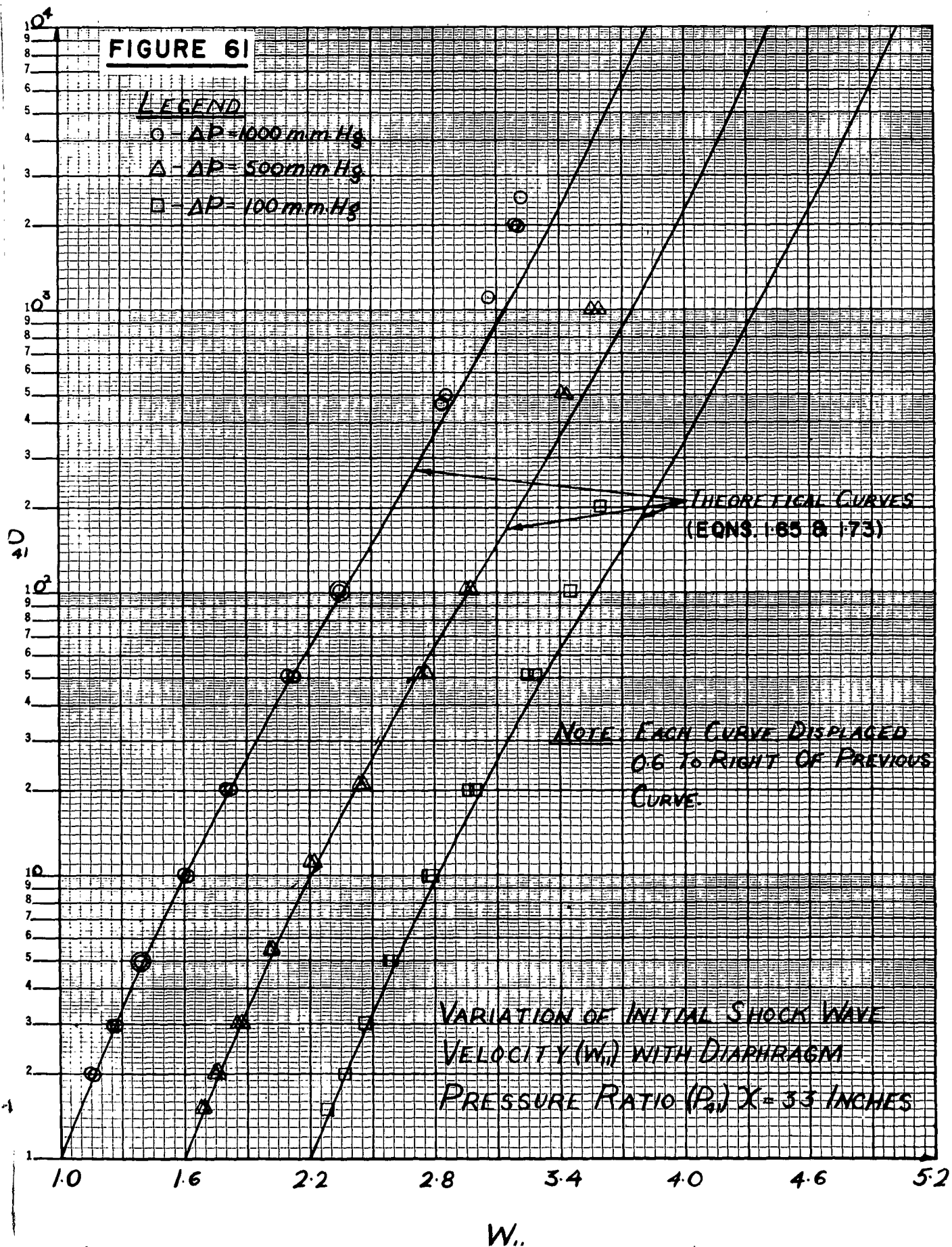
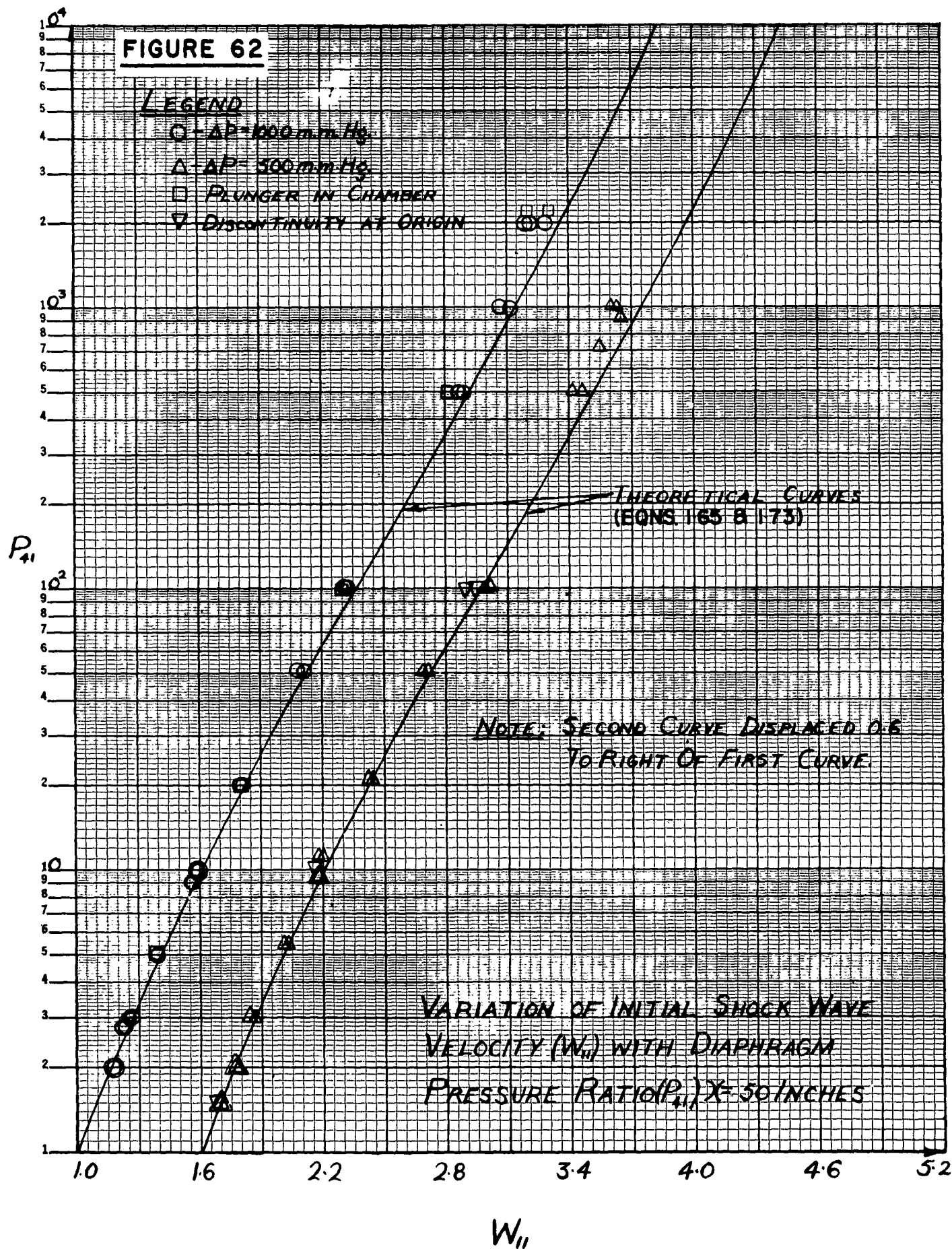
○ - $\Delta P = 1000 \text{ mm Hg}$ △ - $\Delta P = 500 \text{ mm Hg}$ □ - $\Delta P = 100 \text{ mm Hg}$ 

FIGURE 62



that 1/4 inch of the rigid foil protruded into the interior of the tube on all sides. This simulated the effects of a poor diaphragm break or an area discontinuity at the origin. The introduction of such a discontinuity appears to have a very small influence on W_{11} over the given range of P_{41} .

The effect of placing the diaphragm breaker (figure 52) upstream or downstream of the origin is also shown on figure 62. No discernible change is noted up to $P_{41} = 2000$, the maximum diaphragm pressure ratio tested. Therefore it may be concluded that these types of obstructions have a negligible effect on the final wave speed. From the above it may be inferred that the particles of cellophane will also have a secondary effect on the shock velocity. This does not exclude the possibility that these obstructions will give rise to diffracted shock waves and vortices which may in turn affect the uniformity of the two states separated by the contact front.

Figures 61 and 62 also show that as long as the diaphragm is reasonably stressed (1/2 or 1/3 ultimate breaking load), it does not affect the trend in the total wave attenuation at a given x . As a result it may also be inferred that the contribution of the energy from the shattered diaphragm to the flow is not significant.

In order to establish the profile of the formation decrement with P_{41} , the results of figures 61 and 62 were extended up to $P_{41} = 10,000$. In addition, these experiments were also enlarged to include the lengths of $x = 101$ and 136 inches. This provided the basis for the determination of the distance attenuation as well. The combined results appear on figure 63.

It is seen from figure 63 that for weak waves the formation decrement and the distance attenuation are absent. For strong waves, the formation decrement increases with P_{41} . The "dashed" curve shows the attenuation that would be produced as a result of variable specific heat. The curve was computed by the method outlined in section 1.06. It accounts for a very small portion of the experimental attenuation even at very high P_{41} . Thus figure 63 confirms the graphic representation of the total attenuation for strong shocks given on figure 56 (b).

In the present experiments it was necessary to use a channel pressure $p_1 = 0.4$ mm. Hg. in order to obtain a diaphragm pressure ratio $P_{41} = 10,000$. A low p_1 means a correspondingly high kinematic viscosity (ν_2) behind the shock wave. The dimensional analysis of this problem showed that ν_2 and x were two very important quantities affecting the distance attenuation and similarly ν_2 could also be expected to influence the formation decrement. These points are clearly brought out on figure 63.

In order to obtain an empirical relationship for the shock wave attenuation results, it was decided to approximate the theoretical curves and the experimental values by straight lines as shown on figure 64. An

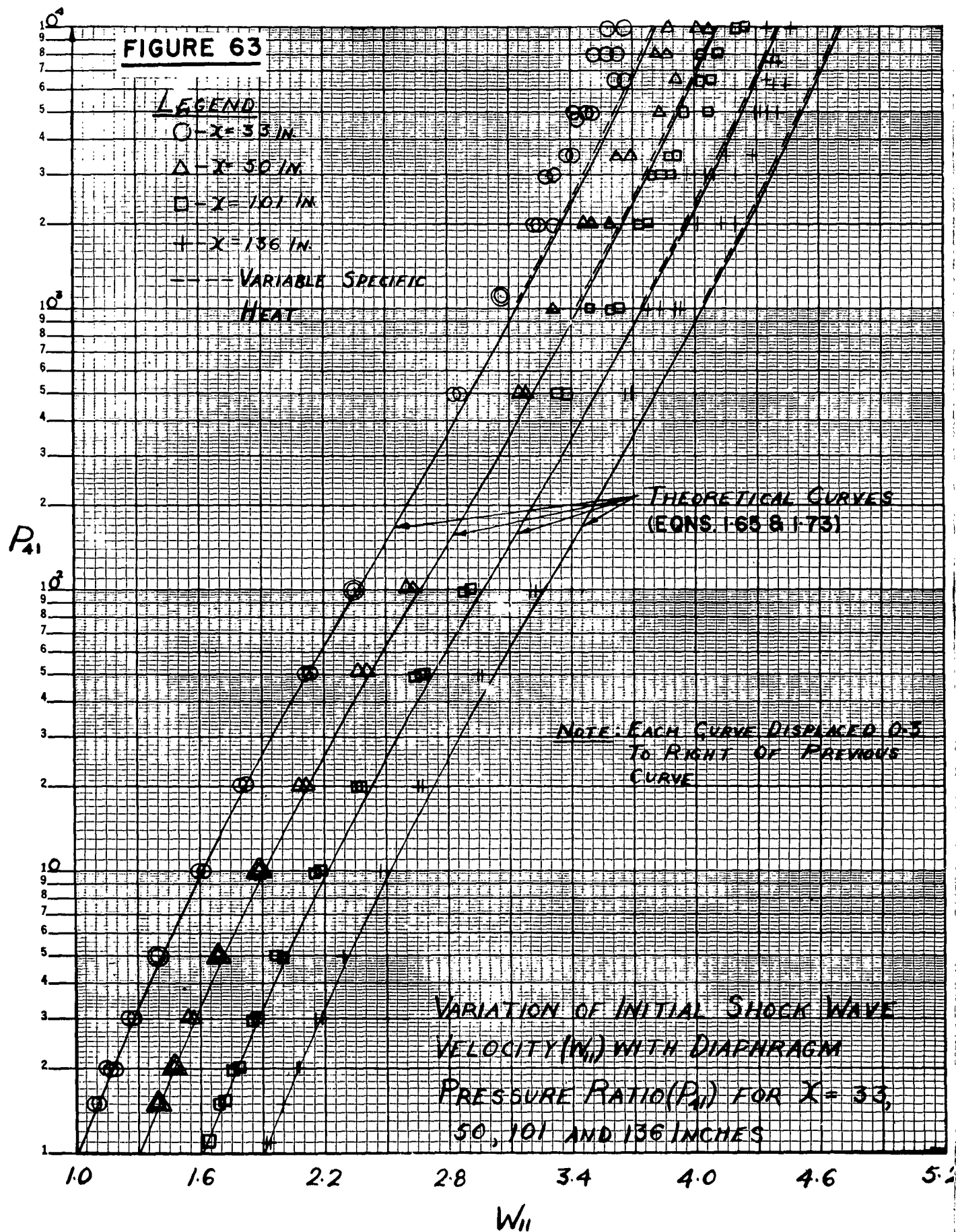
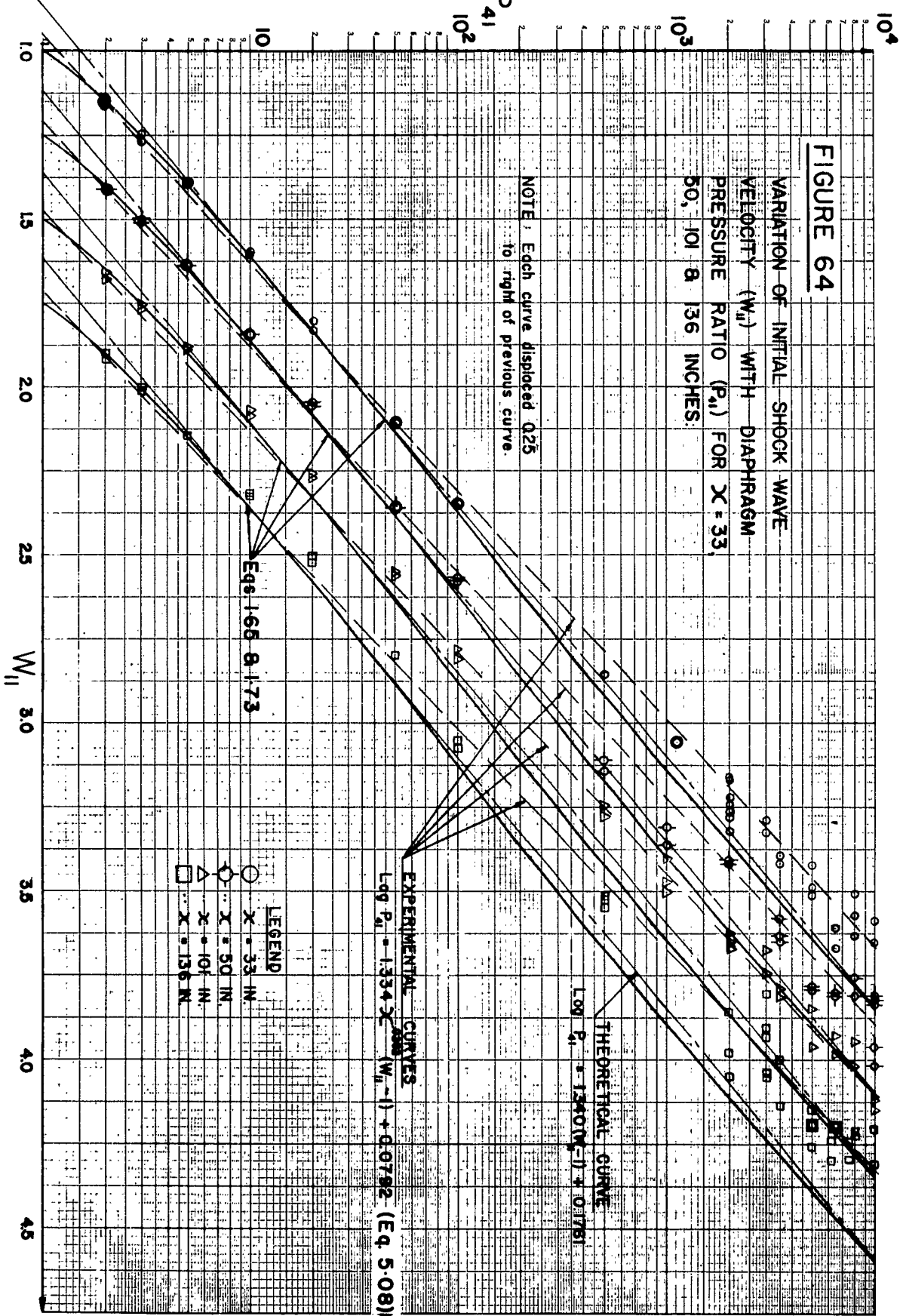


FIGURE 64

VARIATION OF INITIAL SHOCK WAVE
VELOCITY (W_{II}) WITH DIAPHRAGM
PRESSURE RATIO (P_{A1}) FOR $X = 33$,
50, 101 & 136 INCHES.

NOTE: Each curve displaced 0.25
to right of previous curve.



examination of these linear approximations show that they describe the theoretical and experimental results quite well over the entire P_{41} range plotted on figure 64. The ratio $(\frac{m_x}{m_t})$ of the experimental (m_x) and theoretical (m_t) slopes were plotted against x and yield a power curve of the form (see Appendix B),

$$\frac{m_x}{m_t} = 0.996 x^{.0282} \quad (5.07)$$

This relation predicts the slope of the line which approximates the experimental wave attenuation for any tube length x . Since each experimental line has the same intercept on the P_{41} axis (approximately 1.2), the family of lines may now be expressed as

$$\text{Log } P_{41} = 1.334 x^{.0282} (W_{11} - 1) + 0.0792 \quad (5.08)$$

or within present approximation

$$\text{Log } P_{41} = 1.33 x^{.03} (W_{11} - 1) + 0.08 \quad (5.09)$$

Although equation 5.08 describes the total wave attenuation in the 3 inch x 3 inch wave interaction tube under the given initial conditions, over the range of P_{41} , it was desirable to find a general relation that would be applicable to any shock tube. The first attempt in this direction was to follow the approach of approximating the shock tube flow in region (2) by a flow resulting from a tube which is started impulsively from rest, as outlined previously.

In the present case, the analysis was applied to a square tube of area A , (figure 65), since the wave interaction tube has this type of cross-section. Primarily, it is required to find the set of differential equations and the initial and boundary conditions for this type of flow. For a viscous, incompressible fluid without heat transfer, where the conditions are equivalent at any station x along the flow, the equation of motion is the only one of importance.

Thus the differential equation governing the flow for $u = u(z, y, t)$ is:

$$\frac{\partial u}{\partial t} = \nu \left(\frac{\partial^2 u}{\partial z^2} + \frac{\partial^2 u}{\partial y^2} \right) \quad (5.10)$$

The initial and boundary conditions are:

$$u(z, y, 0) = u_i \text{ for } 0 < z < z_0, \quad 0 < y < y_0$$

$$\left. \begin{array}{l} u(0, y, t) \\ u(z, 0, t) \\ u(z_0, y, t) \\ u(z, y_0, t) \end{array} \right\} = 0 \quad \text{for } t > 0$$

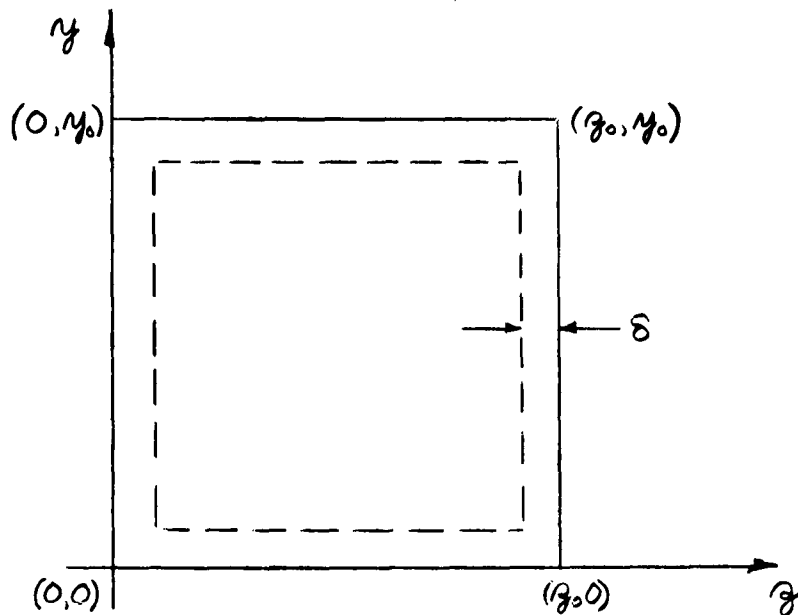


FIGURE 65

CO-ORDINATE SYSTEM FOR A SQUARE TUBE

The solution of this equation with the given initial and boundary conditions is known from the theory of heat conduction (ref. 59 and appendix B) and

$$\frac{U}{U_i} = \sum_{a=1}^{\infty} \sum_{b=1}^{\infty} \frac{4}{ab\pi^2} (1 - \cos a\pi) (1 - \cos b\pi) e^{-\nu t \left(\frac{a^2}{z_0^2} + \frac{b^2}{y_0^2} \right) \pi^2} \sin \frac{a\pi z}{z_0} \sin \frac{b\pi y}{y_0} \quad (5.11)$$

For a square tube $z_0^2 = y_0^2 = A$ or

$$\frac{U}{U_i} = \sum_{a=1}^{\infty} \sum_{b=1}^{\infty} \frac{4}{ab\pi^2} (1 - \cos a\pi) (1 - \cos b\pi) e^{-\frac{\nu t}{A} (a^2 + b^2) \pi^2} \sin \frac{a\pi z}{z_0} \sin \frac{b\pi y}{y_0} \quad (5.12)$$

At time $t = 0$ the mass flow $m_i = \rho u_i z_0 y_0$

At any other time t , the mass flow $m = \int_0^{z_0} \int_0^{y_0} \rho u \, dz \, dy$

Thus the mass flow ratio

$$\frac{m}{m_i} = \frac{4}{\pi^4} \sum_{a=1}^{\infty} \sum_{b=1}^{\infty} \frac{(1-\cos a\pi)^2 (1-\cos b\pi)^2}{a^2 b^2} e^{-\frac{\nu t}{A} (a^2+b^2) \pi^2} \quad (5.13)$$

The variation of $\frac{m}{m_i}$ with the time parameter $\frac{\nu t}{A}$ is plotted on figure 66.

It can be shown that the analogous problem for a flat plate over which a flow is started impulsively from rest has the solution (see ref. 65):

$$\frac{u}{u_i} = \operatorname{erf} \frac{y}{2\sqrt{\nu t}} \quad (5.14)$$

where

$$\operatorname{erf} x = \frac{2}{\sqrt{\pi}} \int_0^x e^{-r^2} dr$$

By definition the boundary layer displacement thickness is given as,

$$\delta^* = \int_0^{\infty} \left(1 - \frac{u}{u_i}\right) dy$$

and a substitution of (5.14) yields

$$\delta^* = \frac{2}{\sqrt{\pi}} \sqrt{\nu t} \quad (5.15)$$

For a cylindrical shock tube of radius R, if it is assumed that the defect in mass flow is due to the displacement thickness, then

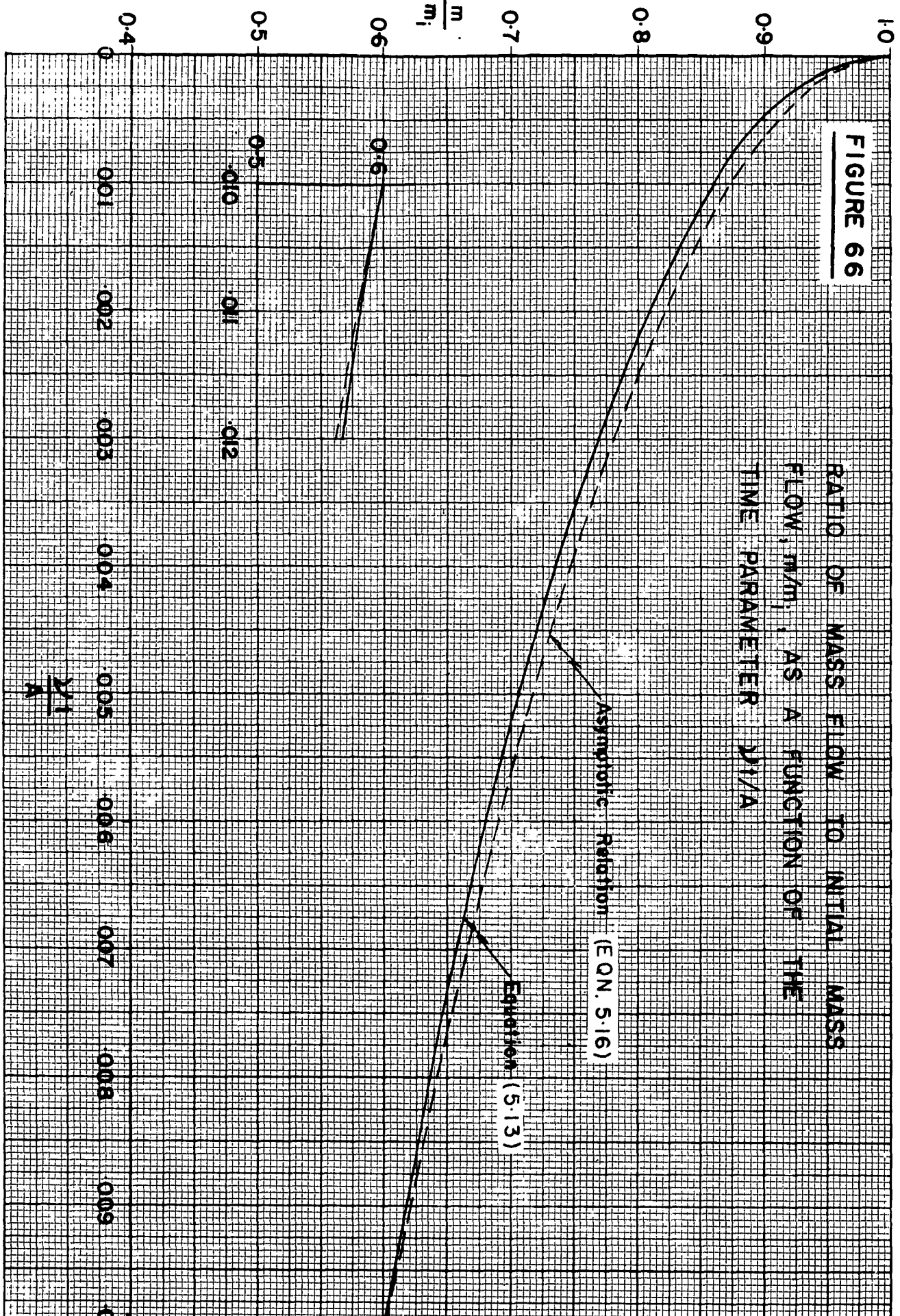
$$\frac{m}{m_i} = \frac{m_i - \Delta m}{m_i} = 1 - \frac{\Delta m}{m_i} = 1 - \frac{2\delta^*}{R}$$

Substituting, (5.15) results in

$$\frac{m}{m_i} = 1 - 4\sqrt{\frac{\nu t}{\pi R^2}} = 1 - 4\sqrt{\frac{\nu t}{A}} \quad (5.16)$$

This two-dimensional or asymptotic result compares very well with the present three-dimensional analysis over the entire range of $\frac{\nu t}{A}$ plotted

on figure 66. Strictly speaking this relation (5.16) is only valid when νt or δ^* is very small, otherwise the initial assumptions are violated. Nevertheless, the agreement with equation (5.13) is good even when δ^* is large. Figure 66 also shows that the two relations become identical when $\frac{\nu t}{A} \rightarrow 0$.



If the assumption is now made that the boundary layer produced between the contact front and the shock wave is identical to boundary layer produced in the Rayleigh problem, then the above relations may be applied to a shock tube in the following manner:

The initial mass flow behind the shock wave is free from boundary layer effects and is given by

$$m_i = (\rho_2 u_2)_i A$$

or for air

$$\frac{m_i}{\rho_i a_i A} = \frac{5}{\sqrt{7}} \sqrt{6(P_{21})_i + 1} \frac{(P_{21})_i - 1}{(P_{21})_i + 6} = \frac{5}{\sqrt{7}} n(P_{21})_i \quad (5.17)$$

where

$$n(P_{21}) = \frac{P_{21} - 1}{P_{21} + 6} \sqrt{6P_{21} + 1}$$

Any subsequent mass flow is given by

$$\frac{m}{\rho_i a_i A} = \frac{5}{\sqrt{7}} \frac{P_{21} - 1}{P_{21} + 6} \sqrt{6P_{21} + 1} = \frac{5}{\sqrt{7}} n(P_{21}) \quad (5.18)$$

$$\text{Thus } \frac{m}{m_i} = \frac{n(P_{21})}{n(P_{21})_i} = 4 \sum_{a=1}^{\infty} \sum_{b=1}^{\infty} \frac{(1 - \cos a\pi)^2 (1 - \cos b\pi)^2}{a^2 b^2 \pi^4} e^{-\frac{\nu t}{A}(a+b)\pi^2} \quad (5.19)$$

This is the relation which is shown in figure 66. The variation of the function $n(P_{21})$ with P_{21} appears in figure 67. If the viscosity is assumed to vary with the temperature in a manner given by

$$\mu \propto T^{0.76}$$

Then

$$\frac{\nu_2^t}{A} = \frac{(T_{21})^{1.76}}{P_{21}} \frac{\nu_1 \cdot x}{w_1 A} \quad (5.20)$$

where $t \approx \frac{x}{w_1}$, if the total attenuation is neglected. For a linear

variation of the viscosity with temperature, then (see ref. 21)

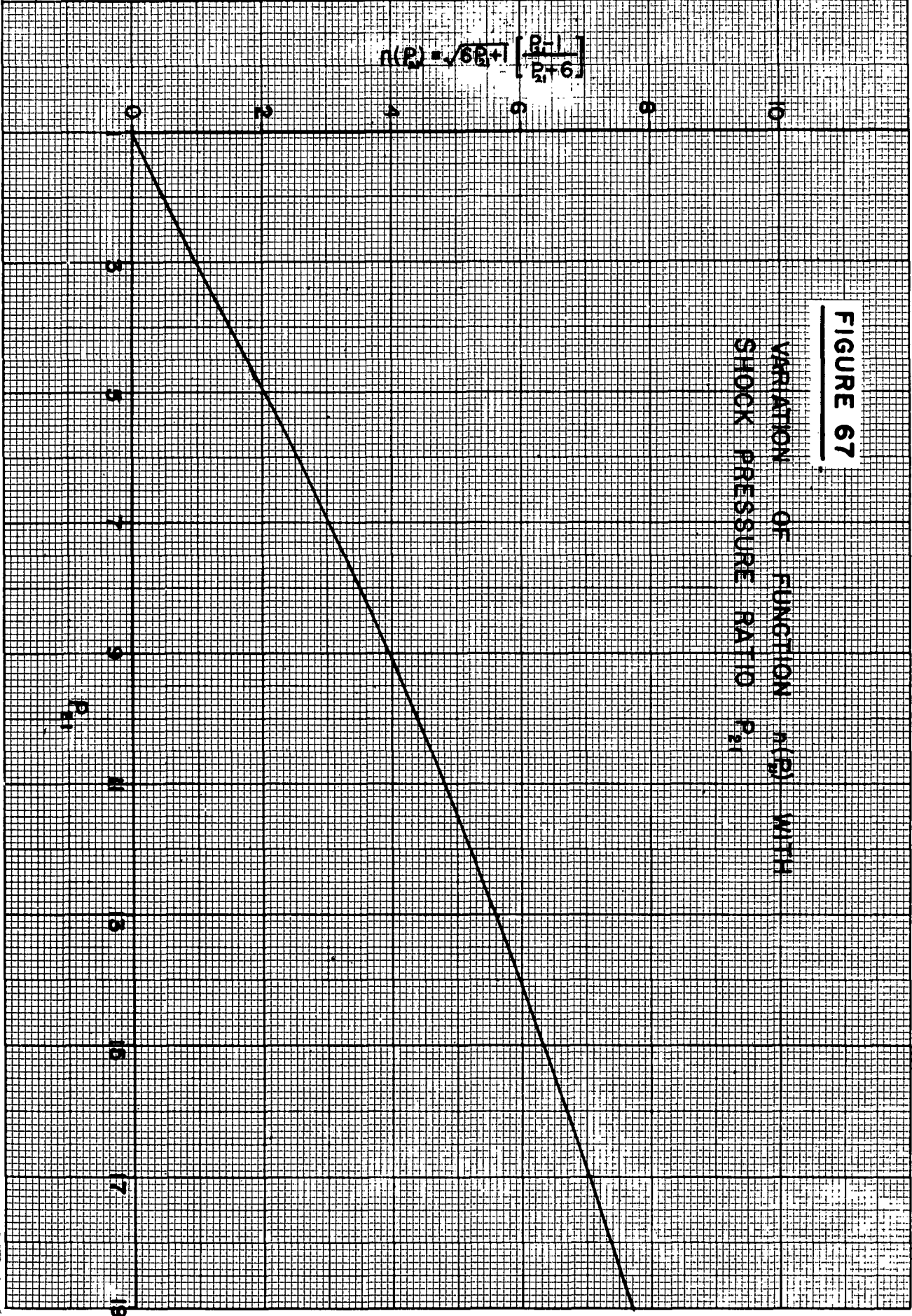
$$\frac{\nu_2^t}{A} = \frac{\sqrt{7} [(P_{21})_i + 6]^2 (P_{21})_i \nu_1}{[6(P_{21})_i + 1]^{2.5} a_i A} \quad (5.21)$$

Equation (5.21) is suitable only for weak shock waves, that is, $T_{21} \rightarrow 1$, as a result equation (5.20) was employed throughout the present calculations.

$$n(P_2) = \sqrt{6P_2 + 1} \left[\frac{P_2 - 1}{P_2 + 6} \right]$$

FIGURE 67

VARIATION OF FUNCTION $n(P_2)$ WITH
SHOCK PRESSURE RATIO P_2/P_1



The actual values of $\frac{\sqrt{2}t}{A}$ which existed in the present experiments for each length x , were computed from equation (5.20) and the given initial conditions. The results for $x = 136$ inches are listed in table 9, which is the extreme case of one attenuation problem considered here. Values of $\frac{m}{m_i} = \frac{n(P_{21})}{n(P_{21})_i}$ were then found from figure 66, and $n(P_{21})$ was determined. In turn P_{21} could be ascertained from figure 67. The results from the viscous flow analysis are plotted on figure 68 along with those obtained experimentally and the Rankine-Hugoniot curve. In order to obtain better graphical accuracy for this purpose figure 69 was drawn, and the experimental curve on figure 68 was constructed from this figure.

A study of figure 68 shows that this type of analysis over-emphasizes the effect of the boundary layer for strong shock waves, since it was assumed of uniform thickness, between the shock and the contact front. Agreement between the above analysis and experiment is very good only at low values of P_{41} (< 200) when the time parameter $\frac{\sqrt{2}t}{A}$ is small, i.e., when the boundary layer is thin. In this range the experimental results are in better agreement with the viscous flow analysis than with the Rankine-Hugoniot values. For $P_{41} > 200$ the attenuation predicted by the present analysis becomes progressively greater with increasing P_{41} . (The inflection point which occurs at $P_{41} \approx 3000$ is due to the increasing value of $\frac{\sqrt{2}t}{A}$, which comes about from the low channel pressures used at high P_{41}). Although this was a distance attenuation analysis, it is seen that the results for $x = 33$ inches are already far too great, and here the main effect is really due to the formation decrement.

Thus the viscous analysis follows the experimental results in the range of P_{41} where $M_2 \gtrsim 1$. However, in this range the experimental values of $\frac{\sqrt{2}t}{A}$ were also very small (about 10^{-4}). Therefore, $m \approx m_i$, and the distance attenuation would be negligible. Hence it should not be misconstrued that agreement is good in the incompressible range only, but that the total attenuation is small for weak waves. For large $\frac{\sqrt{2}t}{A}$ (strong shocks) the flow obtained from the Rayleigh analysis really ceases to be a boundary layer flow since the velocity distribution profile extends to the centre of the tube. It is, therefore, really a non-stationary "pipe flow" (see equation 5.13) and is somewhat analogous to the Poiseuille flow for the stationary case. Thus an analysis of this type would lend itself better to small diameter tubes. (This was shown partially in reference 21 for a 0.4 inch diameter tube over the limited range of $1.8 < P_{41} < 2.0$).

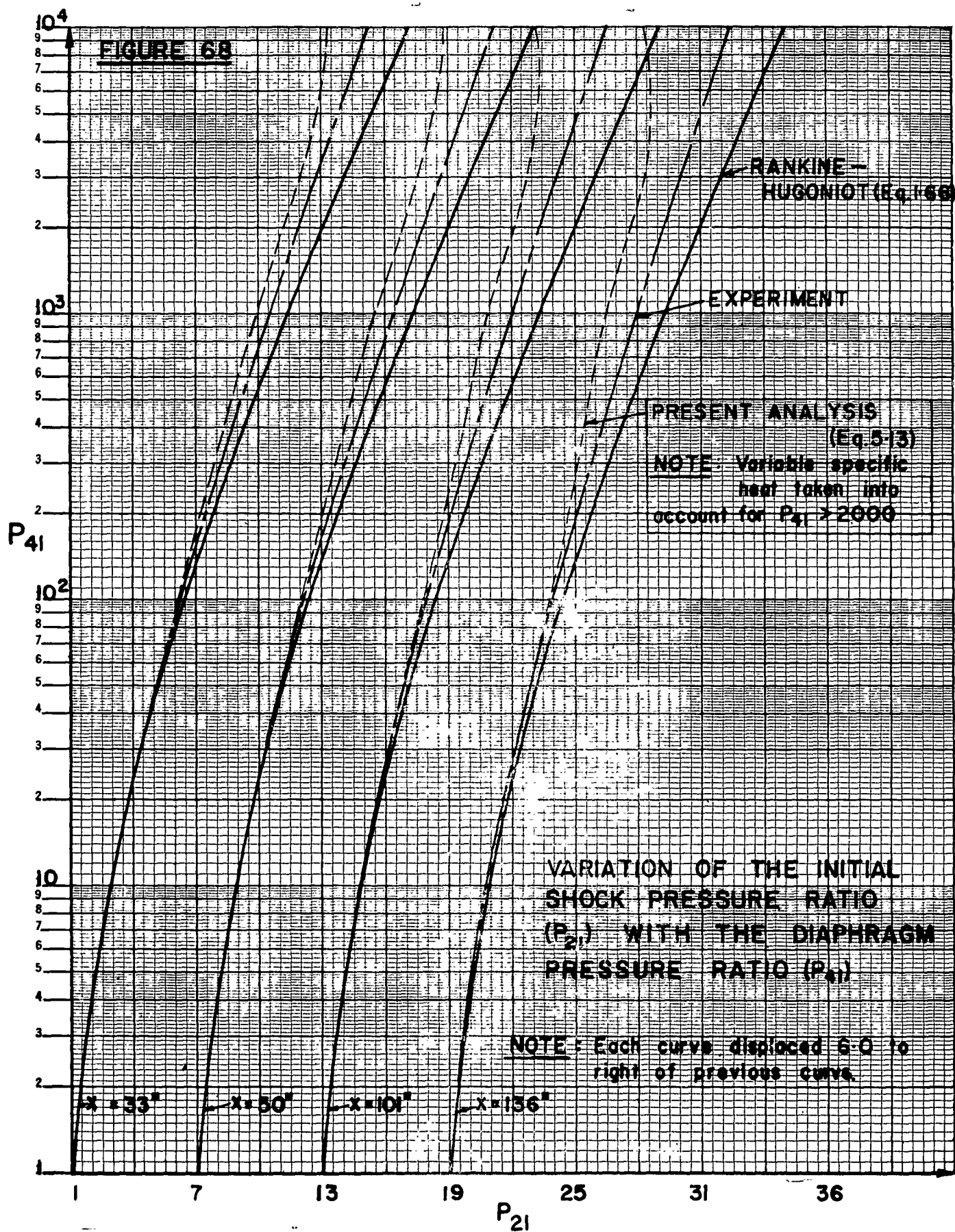
Since the Rayleigh incompressible analysis proved inapplicable when $\frac{\sqrt{2}t}{A}$ was large, an attempt was made to utilize the actual

$x = 136'' = 11.33'$

TABLE 9

Theoretical P_1	Theoretical W_1	Theoretical M_2	$\frac{\nu_2^t}{A} \times 10^3$	t m. sec.	ν_2 ft. 2/sec.	P_1 mm. Hg.	U_2 f.p.s.
17	3.837	1.520	7.73	2.60	.186	0.40	3373.3
15	3.606	1.482	4.11	2.77	.0930	0.80	3140.5
13	3.358	1.435	3.40	2.97	.0714	1.00	2890.6
11	3.093	1.374	3.58	3.24	.0690	1.00	2615.7
9	2.803	1.294	1.96	3.56	.0345	2.00	2309.1

Theoretical P_1	$Re = \frac{U_2}{\nu}$	Exp. $\delta^{*''}$	$\frac{d\delta^{*}}{dx}$	Asym. $\delta^{*''}$	Fourier $\delta^{*''}$	ν_1 ft. 2/sec.
17	18,100	.104	.00039	.264	.268	3.17×10^{-1}
15	33,800	.0974	.00040	.192	.202	1.59×10^{-1}
13	40,500	.0959	.00044	.175	.184	1.27×10^{-1}
11	37,900	.0880	.00044	.180	.188	1.27×10^{-1}
9	67,000	.0760	.00043	.133	.142	0.634×10^{-1}



total attenuation results (figure 69) in a more realistic approach to the problem based on a reasonable physical model. It was assumed that even at large values of $\frac{\gamma_2 t}{A}$, the flow still consisted of a viscous boundary layer defined by a displacement thickness δ^* , and a core of inviscid flow. The boundary layer thickness varies with x at a given t between the shock and the contact surface. But it was assumed that the boundary layer thickness at the contact front controlled the defect in mass flow, which in turn affected the shock speed. The mass flow ratio was then only dependent on the initial and final strength of the shock wave or $\frac{m}{m_i} = \frac{n(P_{21})}{n(P_{21})_i}$, which may be found from figure 67. Suppose that at the contact front the mass defect

$$\Delta m = \rho_2 u_2 \Delta A = \rho_2 u_2 \delta^* D$$

where δ^* = boundary layer displacement thickness at the contact front

D = perimeter of shock tube

Then, for a square tube (see fig. 65)

$$\frac{m}{m_i} = 1 - \frac{4 \delta^*}{y_0}$$

or

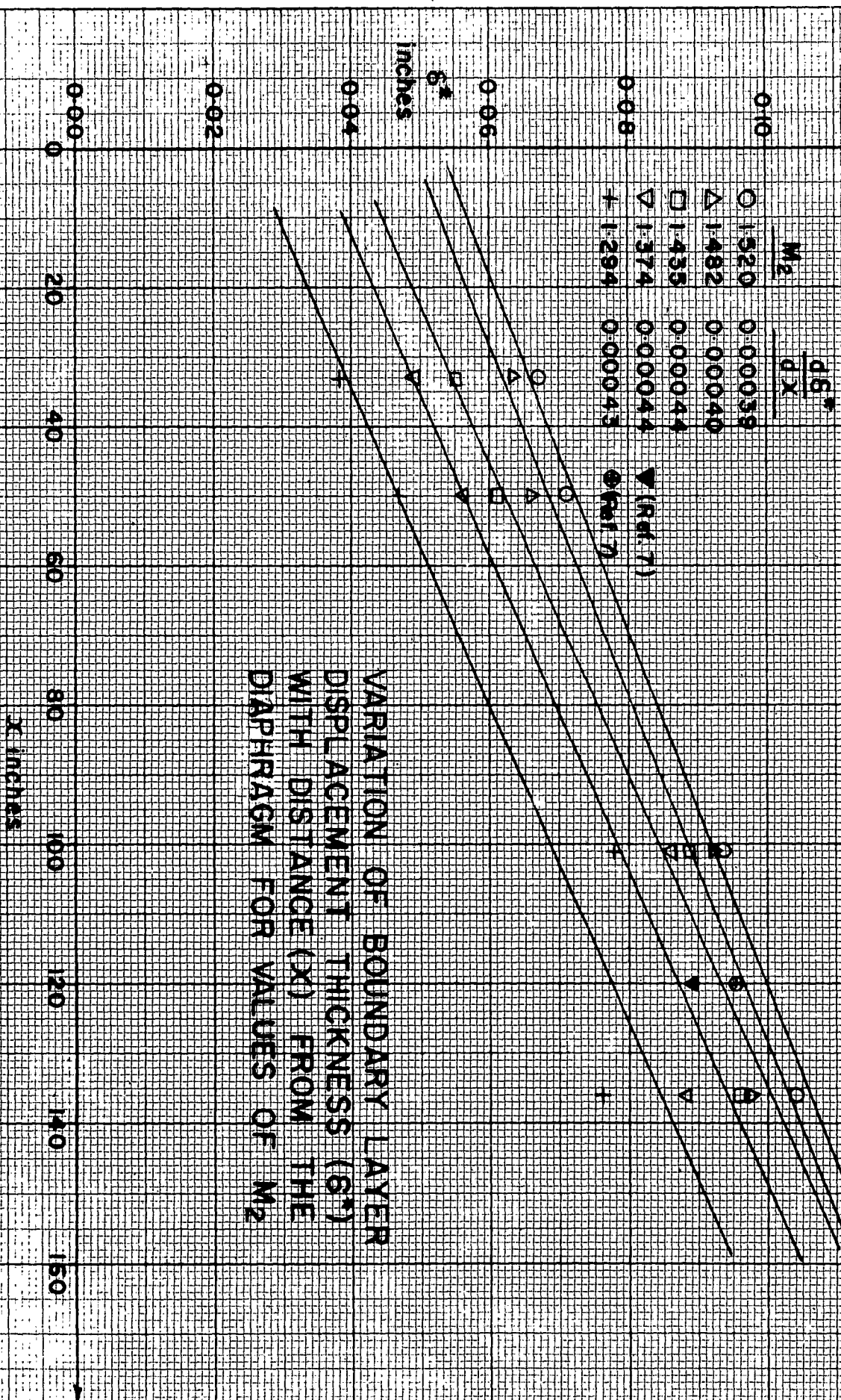
$$\delta^* = \frac{y_0}{4} \left(1 - \frac{m}{m_i} \right) \quad (5.22)$$

The assumption whether δ^* is the displacement thickness at the contact front may be questioned. It may be argued that it is really a fictitious thickness not varying with x (and ρ_2 and u_2 are constant with x), such that it accounts for the observed mass defect. Nevertheless, if the control of the mass flow is assumed to result at the contact front, in a manner analogous to the motion of a piston, then the definition of δ^* is not unreasonable if ρ_2 and u_2 are defined as the values at the contact front only and may vary everywhere else. However, δ^* could possibly be checked experimentally, say by interferometric means, to verify the validity of the definition.

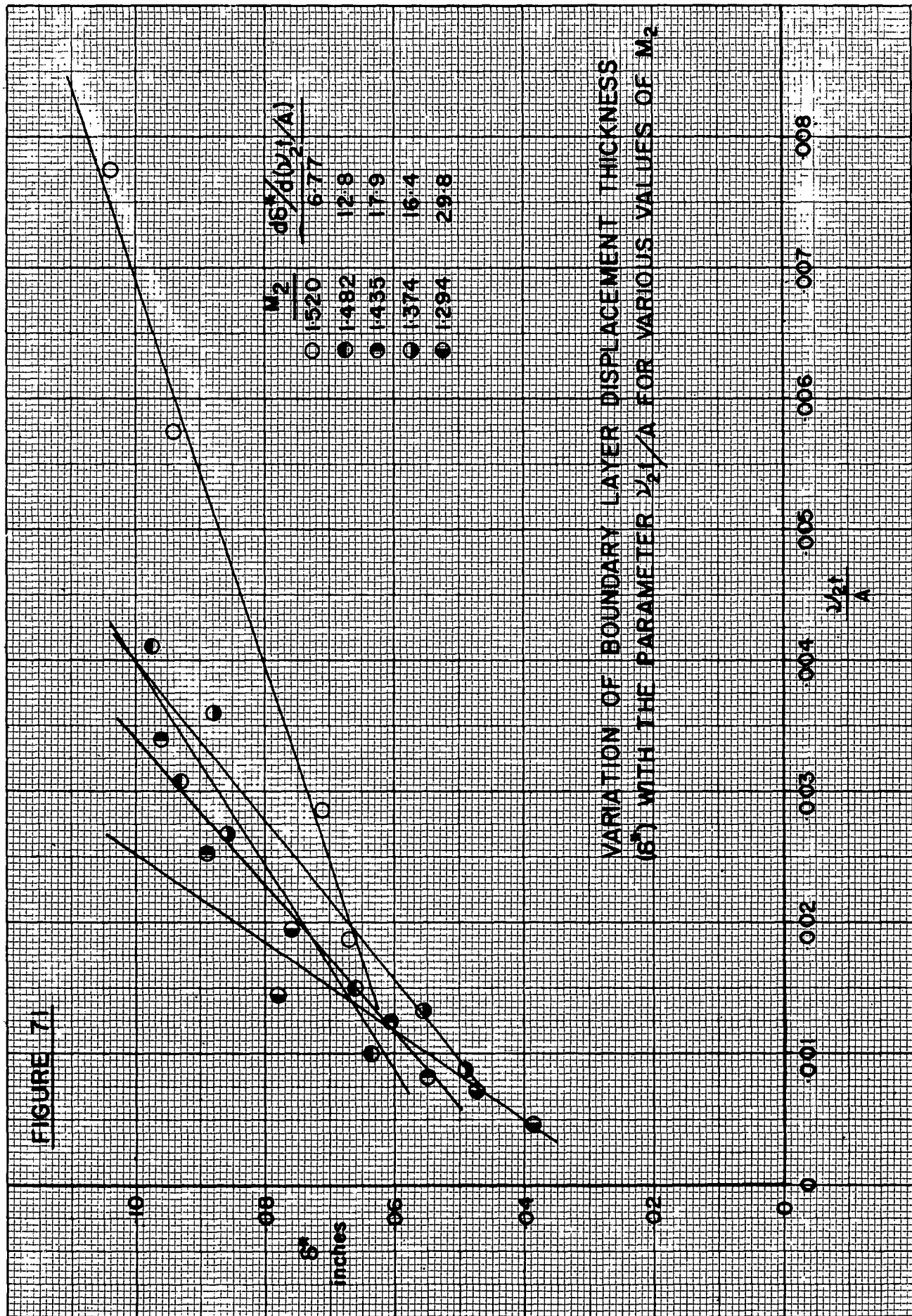
By using the experimental results of figure 69, it is possible to find the actual P_{21} for any P_{41} at any given length (x). From figure 67 $n(P_{21})$ and $n(P_{21})_i$ are found, and $n(P_{21}) / n(P_{21})_i = \frac{m}{m_i}$ is computed. Thus δ^* can be determined from equation (5.22), and a family of such curves of δ^* vs x for varying M_2 appears on figure 70, and of δ^* vs $\frac{\gamma_2 t}{A}$ appears on figure 71.

It is seen that at the higher values of M_2 (or P_{21}), the relation between δ^* and x or δ^* and $\frac{\gamma_2 t}{A}$ is linear. However, as M_2

FIGURE 70



VARIATION OF BOUNDARY LAYER
DISPLACEMENT THICKNESS (δ^*)
WITH DISTANCE (x) FROM THE
DIAPHRAGM FOR VALUES OF M_2



is decreased, there is considerable scatter, and below $M_2 = 1.29$ the scatter was too large to warrant a plot. This is brought about by the fact that the straight line approximations approach the actual curves and the distance between them is difficult to measure accurately (see fig. 69).

It should be noted that the variation of δ^* with x for constant M_2 , amounts in these particular experiments to keeping \mathcal{V}_2 constant, because the same initial conditions were maintained for each length (x). The dimensional analysis and the Rayleigh flow pointed to the basic importance of $\frac{\mathcal{V}_2 t}{A}$.

Therefore, since in this modified approach δ^* was found to be linear with x , it may be assumed that for a given M_2 and Re_2 , $\delta^* \propto \frac{\mathcal{V}_2 t}{A} = \frac{\mathcal{V}_2 x}{A w_1}$.

Therefore $\frac{d\delta^*}{dx} \propto \frac{\mathcal{V}_2}{w_1 A}$, and this slope should decrease considerably with decreasing M_2 or w_1 because \mathcal{V}_2 decreases more rapidly than w_1 , (see table 9 for values of w_1 and \mathcal{V}_2). This is not the case on figure 70 and perhaps may be due to the large scatter at lower M_2 for decreasing \mathcal{V}_2 . An approximate value for $\frac{d\delta^*}{dx}$ for all M_2 was found to be 0.0004. This figure is indicative of a trend and should not be taken as a finally determined quantitative value over the range $1.3 < M_2 < 1.5$. For stationary flow $\frac{d\delta^*}{dx}$ as obtained from the study of two-dimensional wind tunnel nozzles (see references 66 and 67), is about tenfold the present value.

Figure 71 shows the variation of δ^* with $\frac{\mathcal{V}_2 t}{A}$ for different M_2 (P_{21} or W_{11}). It is seen that although the points may again be approximated by straight lines, the lines have very rapidly increasing slopes. This is due to the fact that

$$\frac{d\delta^*}{d\mathcal{V}_2 t/A} = \frac{d\delta^*}{dx} \cdot \frac{w_1 A}{\mathcal{V}_2}$$

$\frac{d\delta^*}{dx}$ was found to be nearly constant. The parameter $w_1 A$ does not change too much with M_2 and \mathcal{V}_2 decreases much more rapidly than $\frac{d\delta^*}{dx}$. $w_1 A$ increases. Therefore the slopes of the lines of constant M_2 for δ^* vs $\frac{\mathcal{V}_2 t}{A}$ will increase with decreasing M_2 for the present experiments. This figure really restates the information given on figure 70, but not as clearly.

From figure 70 it appears that if the straight lines were extended towards the origin, then a large portion of δ^* is composed of the formation decrement. The decrement increases with M_2 or \mathcal{V}_2 , and this is quite sensible. The displacement thickness growth ($\frac{d\delta^*}{dx}$) exhibits an almost constant value, although an increase with \mathcal{V}_2 would have been more reasonable. The graph does illustrate that for strong shock waves there is a formation decrement followed by a distance attenuation which together make up the total wave attenuation. As the wave grows weaker, the formation decrement becomes smaller, and the distance attenuation from figure 69 remains almost constant.

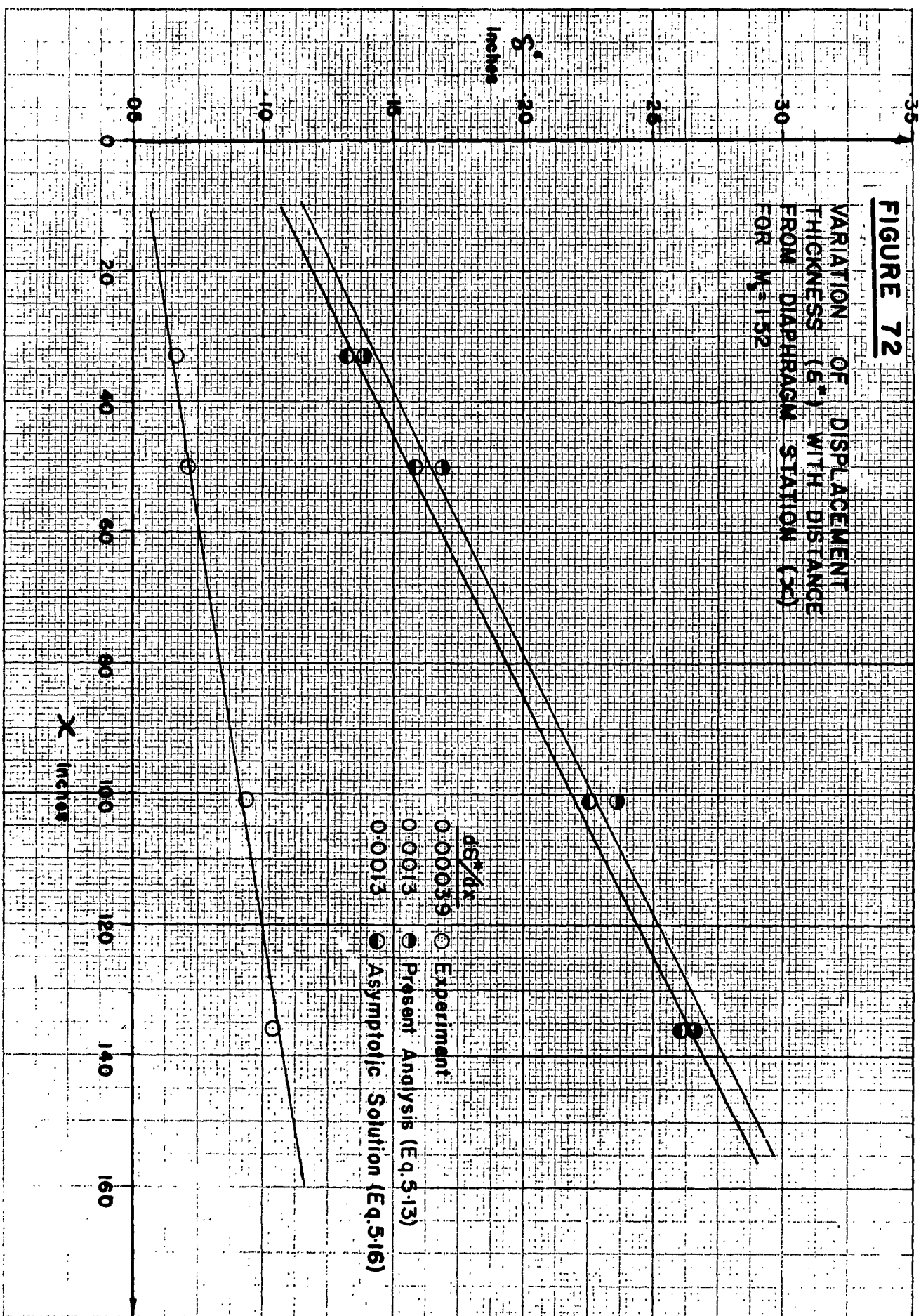
However, since only four distances are available on the graph to check the distance attenuation, the latter point can not be considered completely conclusive. Additional points for $50 < X < 150$ are required to establish uniquely the shape of the lines. Nevertheless, the results appear consistent for the high M_2 values.

Figure 72 shows the variation of δ^* with X for $M_2 = 1.52$. The experimental curve is taken from figure 70. By using the experimental values of $\frac{\nu_2 t}{A}$ it is possible to calculate the values of $\frac{m}{m_i}$ for the exact and the two-dimensional (asymptotic) solutions from figure 66. For comparison the values of δ^* is then computed from equation (5.22), and these are also shown on figure 72. It is seen that both theoretical predictions from the Rayleigh approach give values of δ^* which are about twofold greater than the experimentally based δ^* , and $\frac{d\delta^*}{dX}$ is about threefold greater. The variation of δ^* with X , really restates the results shown on figure 68, that is, that the Rayleigh analysis overestimates the viscous effects. The experimentally based $\delta^* \approx 0.1$ inches at 12 feet from the diaphragm appears reasonable, whereas the viscous result of 0.3 inches is too large.

In the present case it was shown that for a constant $\frac{\nu_2}{w_1 A}$, $\frac{d\delta^*}{dX}$ appeared linear for the high Mach numbers. This might be checked experimentally, in the following manner. At a given time, the shock and contact front will have definite positions in the shock tube, for a set of initial conditions. It is suggested to measure the boundary layer thickness (δ) at a number of X 's for the given t . A plot of δ vs. X would yield δ at the contact surface. If the velocity profiles were known, then δ^* would be found.

Since $\delta^* \propto \frac{\nu_2}{w_1 A}$, it would also be essential to conduct a series of experiments at a fixed diaphragm distance (X) and wave speed (w_1) but variable kinematic viscosity (ν_2), in order to determine the effect of ν_2 on total wave attenuation. The influence of the shock speed (w_1) could also be checked by varying the initial conditions such that $\frac{\nu_2 X}{A}$ was a constant and w_1 was varied over the range. These points will be the subject of further study.

Figure 73 shows the results of reference 7 and 8 as compared with the present work. For a distance of approximately two feet from the diaphragm there is close agreement with the data of reference 7 over the range covered. The shock tube utilized in reference 7 had a cross-section of 2 inch x 7 inch, approximately of the same order as the present tube. However, in reference 8 for a 1-inch diameter tube, the results agree only at the low values of P_{41} (small $\frac{\nu_2 t}{A}$), and the deviation for $P_{41} > 4$ becomes increasingly large (since $\frac{\nu_2 t}{A}$ was about tenfold).



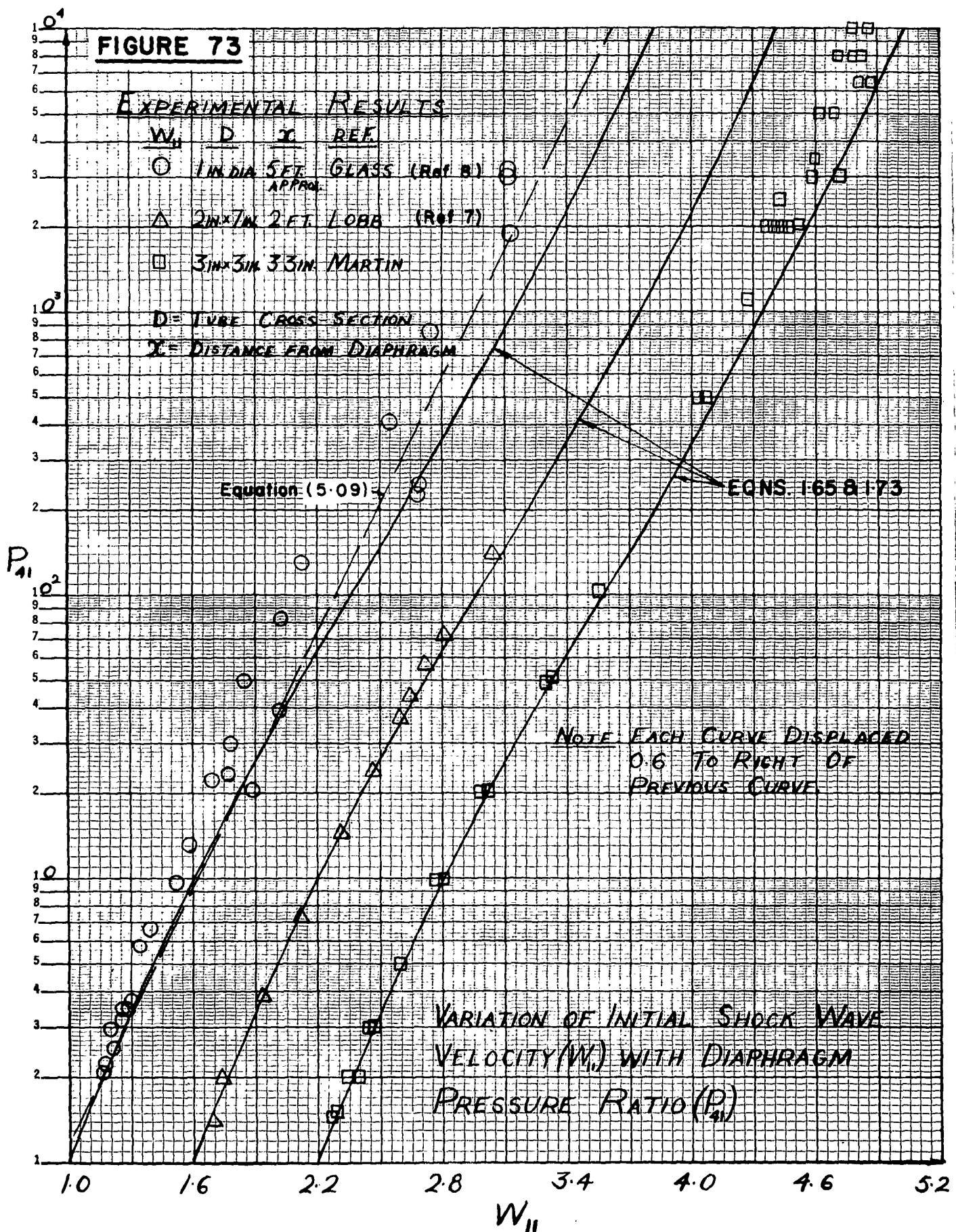


Figure 74 compares the present results with those of reference 7 at a distance of 10 and 11 feet from the diaphragm. There is close agreement at low P_{41} . At the higher values of P_{41} the attenuation is slightly greater for the experiments of reference 7, since somewhat higher values of $\frac{\nu_2 t}{A}$ had to be utilized for a corresponding P_{41} . This was due to the fact that the chamber pressure had to be kept to about two atmospheres on the welded tube. However, the results fit the present empirical relation (equation 5.09) shown as a "dashed" line. Therefore, this indicates again that for tubes in which $\frac{\nu_2}{w_1 A}$ is kept constant, the distance attenuation depends only on x . If, in addition, $\frac{\nu_2}{w_1 A}$ is of the same order as in the present results, then equation (5.09) describes the total attenuation quite well for any other shock tube.

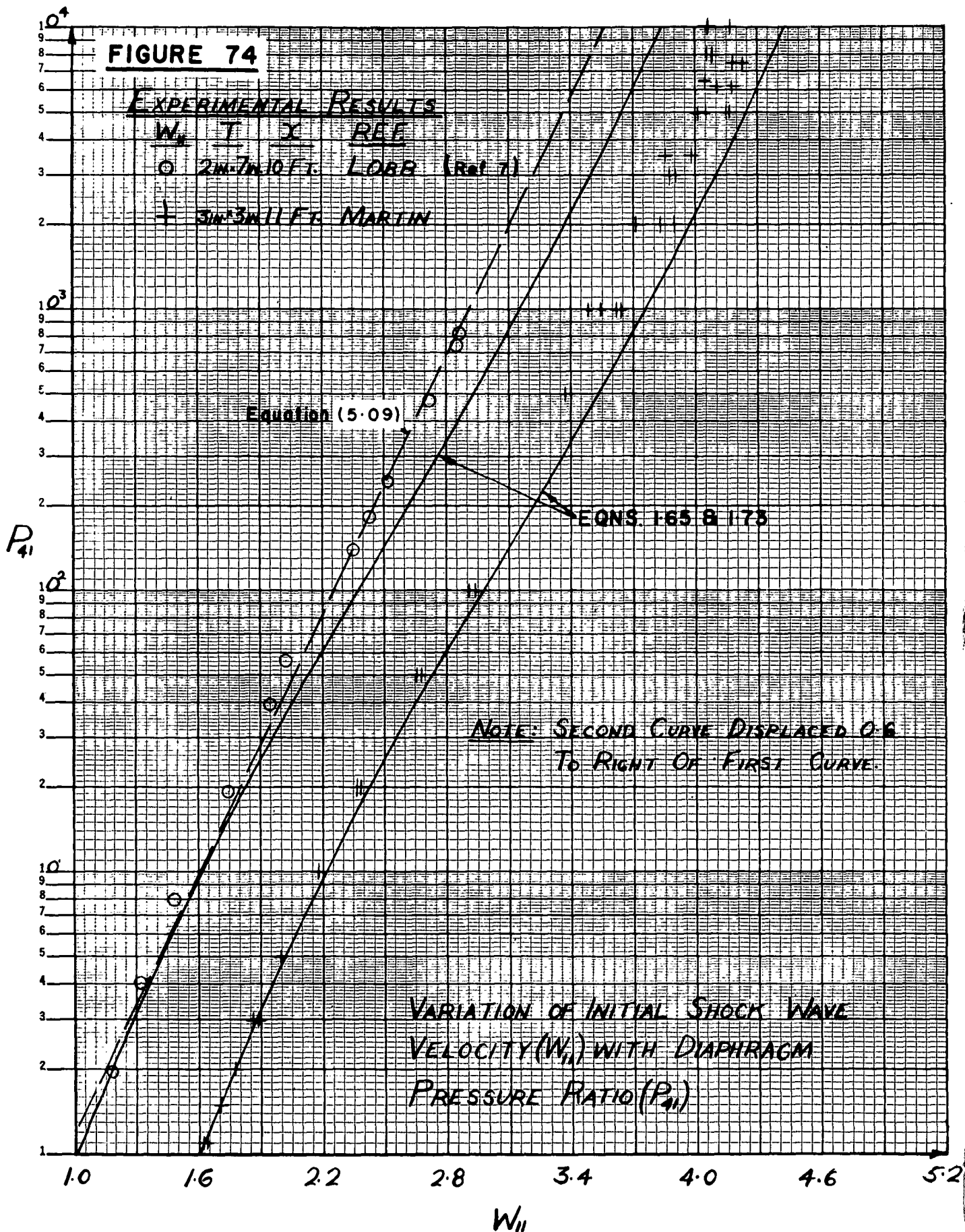
Equation (5.09) is also plotted on figure 73 for the values given in reference 8. In this case the agreement is not good since $\frac{\nu_2 t}{A}$ is about tenfold the present values, due to the small cross-sectional area A .

A computation of δ^* (equation 5.22) from the results of reference 7, for $x = 10$ feet at $M_2 = 1.37$ shows good agreement. For $M_2 = 1.29$ where scatter occurs, this value is greater. These points are shown on figure 70. A similar calculation of the results of reference 8 gave a value in excess of the scale used here and agrees with the previous remarks that the viscous flow analysis would be applicable to small shock tubes.

Table 9 is a summary of the important variables for $x = 136$ inches, where the total attenuation was greatest. It is seen that to obtain high values of P_{21} , it was necessary to use low channel pressures. This in turn produced relatively high values of $\frac{\nu_2 t}{A}$. Therefore $\frac{\nu_2 t}{A}$ increases with increasing wave speed W_{11} or Mach number M_2 . The time (t) will decrease with increasing wave speed, but ν_2 increases at a much faster rate so that the product $\frac{\nu_2 t}{A}$ is an increasing function of P_{21} . The Reynolds number per foot Re_L will decrease with increasing P_{21} due to the more rapid increase of ν_2 , as compared with u_2 , and effectively restates the greater viscous effects at lower Reynolds numbers, that is, theoretically for the two-dimensional case $\delta^* \propto \frac{x}{\sqrt{Re}}$ for a laminar boundary layer. The values of δ^* which were used to plot the curves on figure 70 are also given. The dimensional analysis indicated that for a given gas $\frac{\delta}{d} = \frac{\delta}{d}(M, Re, \frac{\nu_2 t}{A})$ and this is confirmed in the present table for δ^* . Thus δ^* increases with increasing M and $\frac{\nu_2 t}{A}$ and decreasing Re .

In conclusion it may be stated that to-date, the boundary layer effect on shock wave attenuation has not been settled either theoretically or experimentally. The incompressible viscous flow analysis of reference 21

FIGURE 74



was not adequately supported by experimental evidence, owing to the minute range of P_{41} (1.8 to 2.0), that was covered in a small tube of 0.4 in. diameter specifically used to give a high value of $\frac{\sqrt{2}t}{A}$. The results are therefore inadequate because the parameter $\frac{\sqrt{2}t}{A}$ was not fully tested over a range, say of $1 \leq P_{41} \leq 10,000$.

Another attempt has been made in reference 58 to determine the effect of the boundary layer on distance attenuation in a shock tube with smooth and rough walls. In this case, Karman's analysis of the steady boundary layer was used by defining a somewhat arbitrary distance x to correspond to the leading edge distance, in an effort to obtain some theory. The results are not satisfactory, and a far greater distance attenuation is predicted than was actually obtained. Here as well, the range of P_{21} (1.5 to 6) is only a very small portion of the range covered here. In this low range of P_{21} , for a smooth shock tube of large area, little attenuation of any kind takes place. It is the high shock strength range that is of importance from the point of view of large total attenuation.

Numerous investigations on distance attenuation and resulting empirical relations have also been reported in references 18, 19, 46, 56 and 63. However, there is no unifying theory to explain all these results.

In a later report an attempt will be made to extend the present analysis of a flow started impulsively from rest in a tube, by solving the compressible viscous flow equations in a manner similar to that outlined in references 60, 61, 62 and 63. The compressible displacement thickness could then be computed. This analysis would be more realistic for shock tube flows. However, in view of the fact that $\delta_{COMP}^* > \delta_{INCOMP}^*$ for a flat plate, very little improvement can be expected since the theoretical δ^* is already far too large.

It appears that the weakness in these analyses lies in equating the mass flow from the shock tube (equation 5.19) which exists over a finite length and a non-uniformly growing boundary layer (over this length) with an analysis for an infinite tube and a uniformly growing boundary layer. A new approach certainly appears as a necessary step.

5.04. Contact Front Velocity Measurements.

It was pointed out in section 1, that theoretically the transition through the contact front involves the solution of a set of non-linear differential equations in heat conduction. The solution indicates that the contact front is a phenomenon which grows in time due to the molecular transport of heat. As a result, the advance of the front of the contact region is

more rapid than the rear boundary (see reference 68 where this problem is treated theoretically and experimentally).

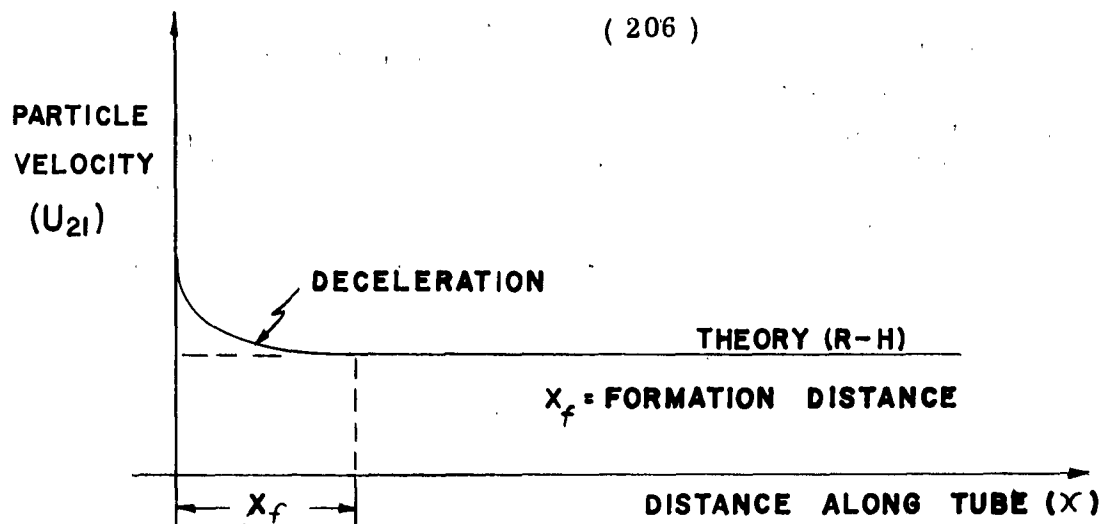
In a real flow (plates 1 and 14) the contact front which is obtained from the bursting diaphragm is very thick and irregular in appearance on a schlieren or interferometer record. Nevertheless, the discontinuity in the density derivative of the front of the contact region nearly always appears on a schlieren photograph of the (x, t) -plane. For high P_{41} values the rear discontinuity in the density derivative of the contact region merges with the rough and eddying flow of state (3), and is very difficult or impossible to discern. Under the same conditions it is often not possible to measure the front of the contact regions since the densities ρ_2 and ρ_3 are very small.

Figures 76 to 79 show the variation of the speed of the front of the contact region (or the initial particle velocity U_{21}) with P_{41} and X . Figure 76 exhibits the best agreement with theory when $X = 12$ inches, and when a constant chamber pressure $p_4 = 1500$ mm. Hg., or when a pressure difference $\Delta p = 500$ mm. Hg. was used. Figures 77 and 78 correspond to figures 61 and 62 for the shock wave velocity measurements. However, as P_{41} and X increase, this time the contact front velocity becomes increasingly larger than predicted by the theory. Figure 77 has some points, when the diaphragm plunger was in the chamber and the channel flow completely unobstructed. No changes are noted in the results.

Figure 79 corresponds to figure 63 for the shock velocity measurements. The combined results clearly show the marked trend of an increasing deviation from theory in the form of a contact front acceleration or speed up. An attempt was made to obtain a relation for the contact front of the form of equation (5.09). This did not prove successful owing to the non-linearity of the results.

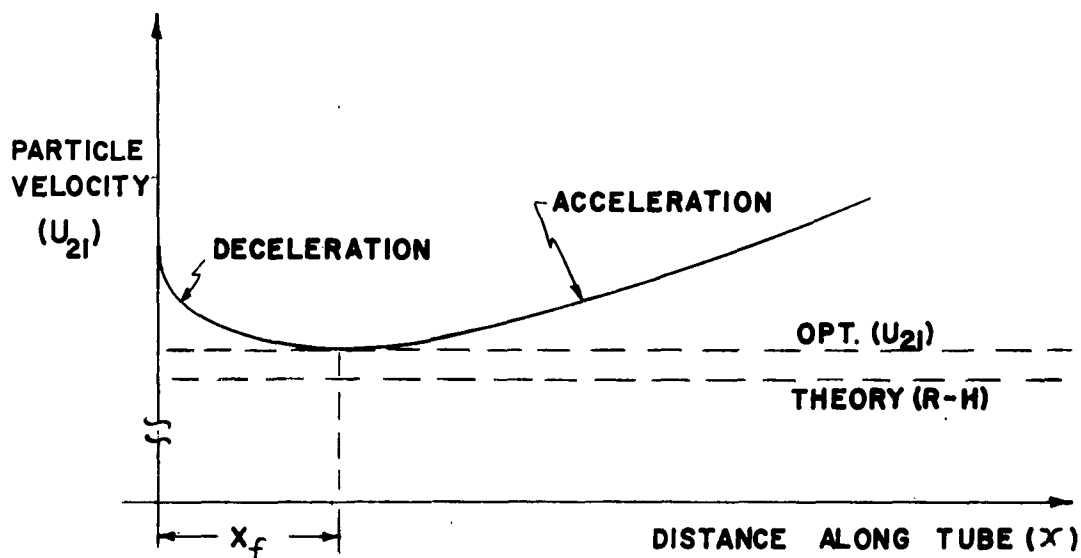
The contact surface results may be summarized graphically as shown on figure 75, and its behaviour is opposite to that shown for the shock wave on figure 56. For weak and strong contact fronts there is a deceleration of the initial jet following the breaking of the diaphragm. At the end of the formation distance an optimum velocity is reached. For weak contact fronts the optimum velocity is the one predicted by the Rankine-Hugoniot theory, and it appears independent of the distance traversed by the contact front. For strong contact fronts the velocity of the end of the formation distance is greater than the theoretical value and the velocity further increases with the distance travelled by the contact front.

The most striking feature of these measurements is that for strong waves for a corresponding P_{41} and X , the shock wave attenuates, and the contact front simultaneously speeds up. It was shown in the study



(a) WEAK CONTACT FRONT

$$(P_{21} < 3)$$



(b) STRONG CONTACT FRONT

$$(P_{21} > 3)$$

FIGURE 75. °

THE BEHAVIOUR OF THE CONTACT FRONT IN A SHOCK TUBE

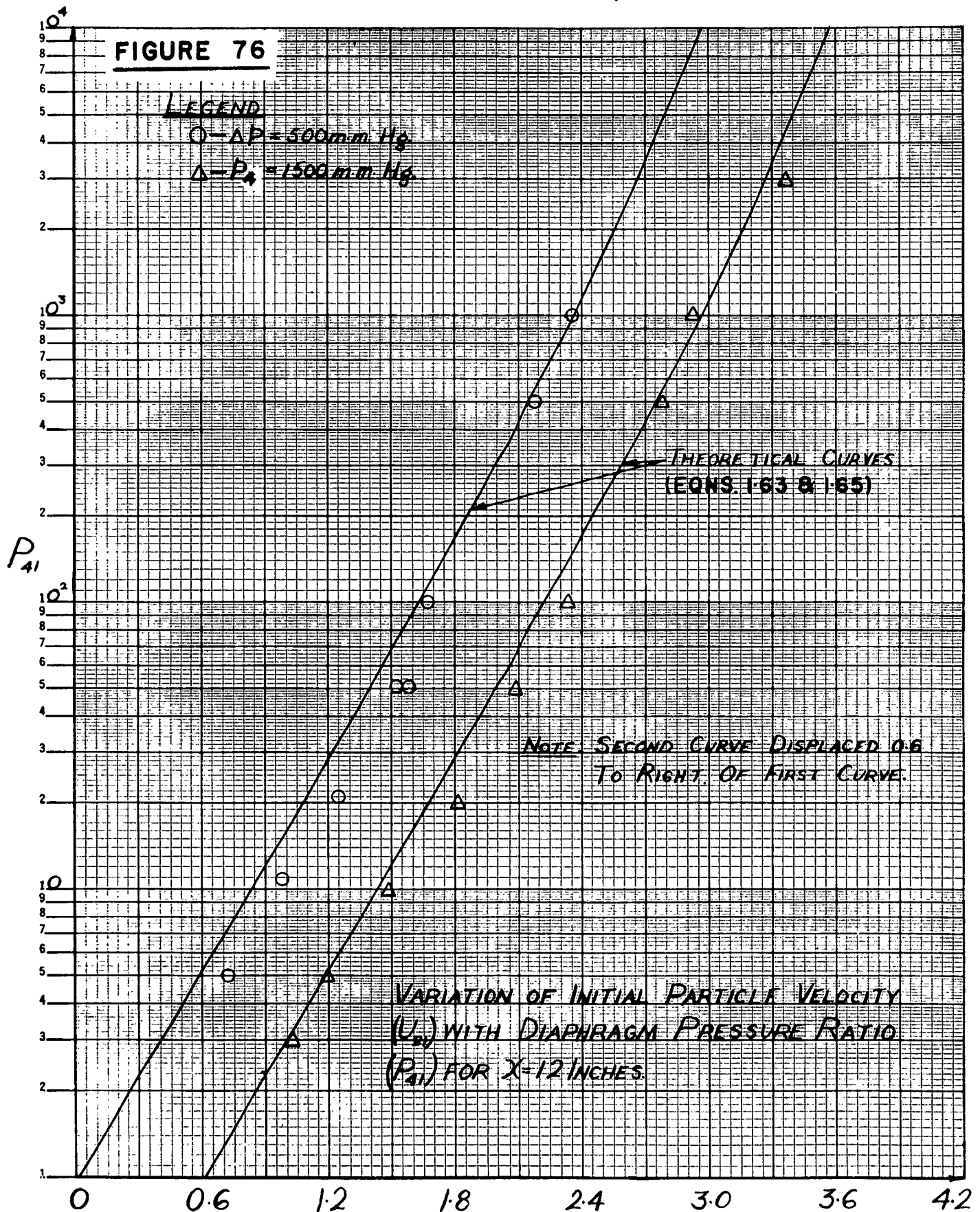


FIGURE 77

LEGEND

- - $\Delta P = 1000 \text{ mm Hg}$
- △ - $\Delta P = 500 \text{ mm Hg}$
- - $\Delta P = 100 \text{ mm Hg}$

THEORETICAL CURVES
(EQNS. 1.63 & 1.65)

NOTE: EACH CURVE DISPLACED
0.6 OF PREVIOUS CURVE.

VARIATION OF INITIAL PARTICLE
VELOCITY (U_{2i}) WITH DIAPHRAGM
PRESSURE RATIO (P_{2i}) $X = 33 \text{ INCHES}$

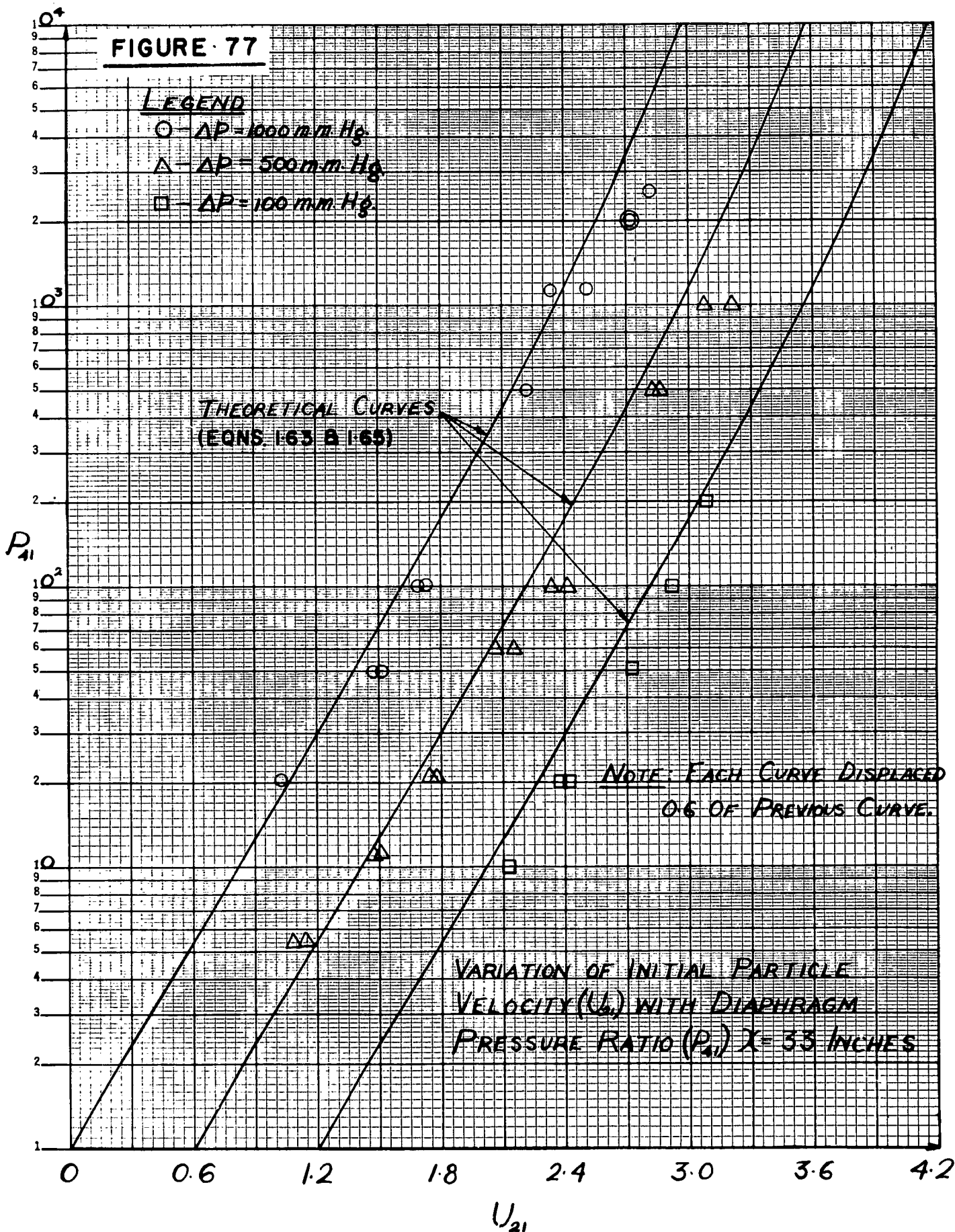
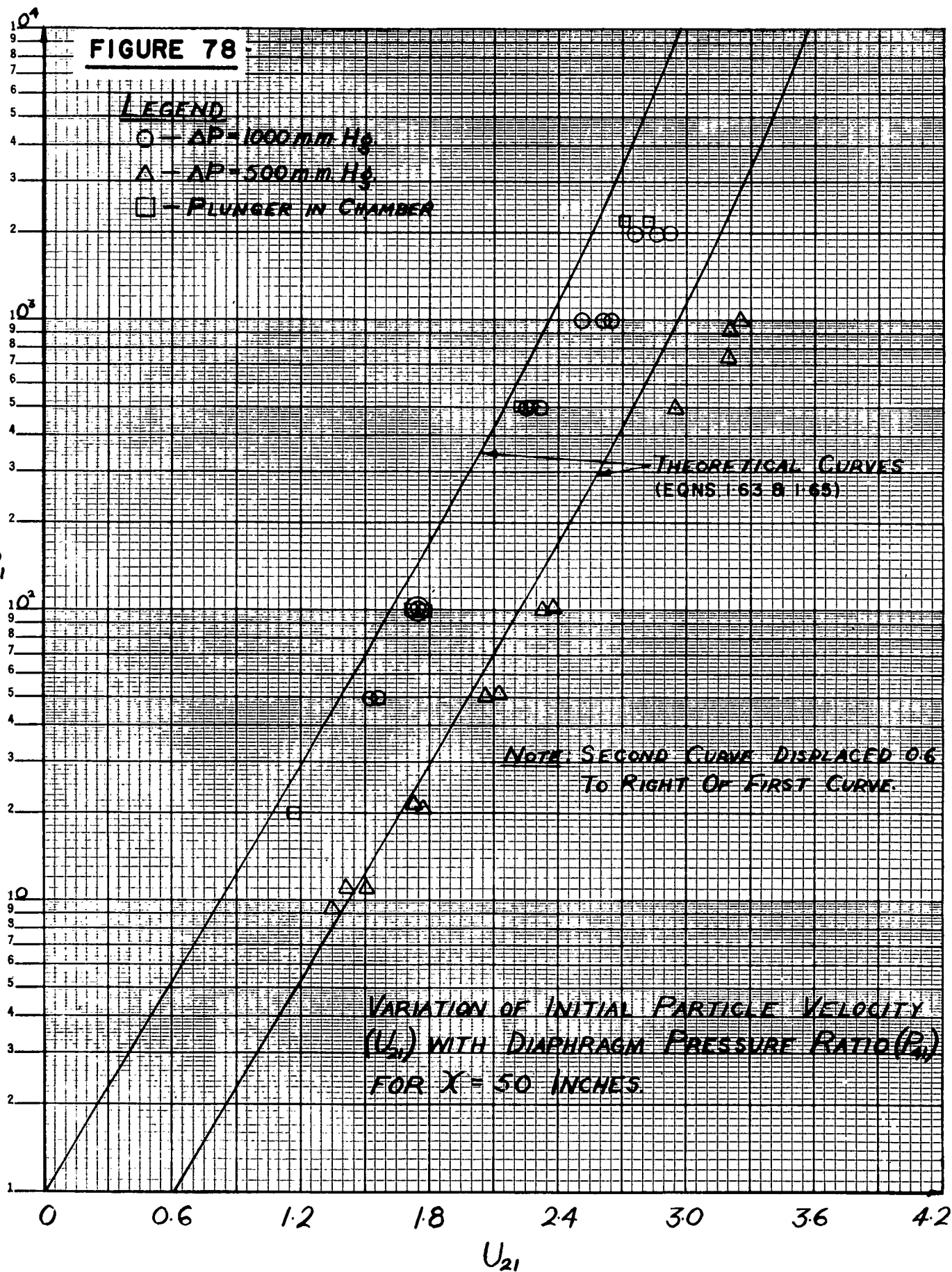


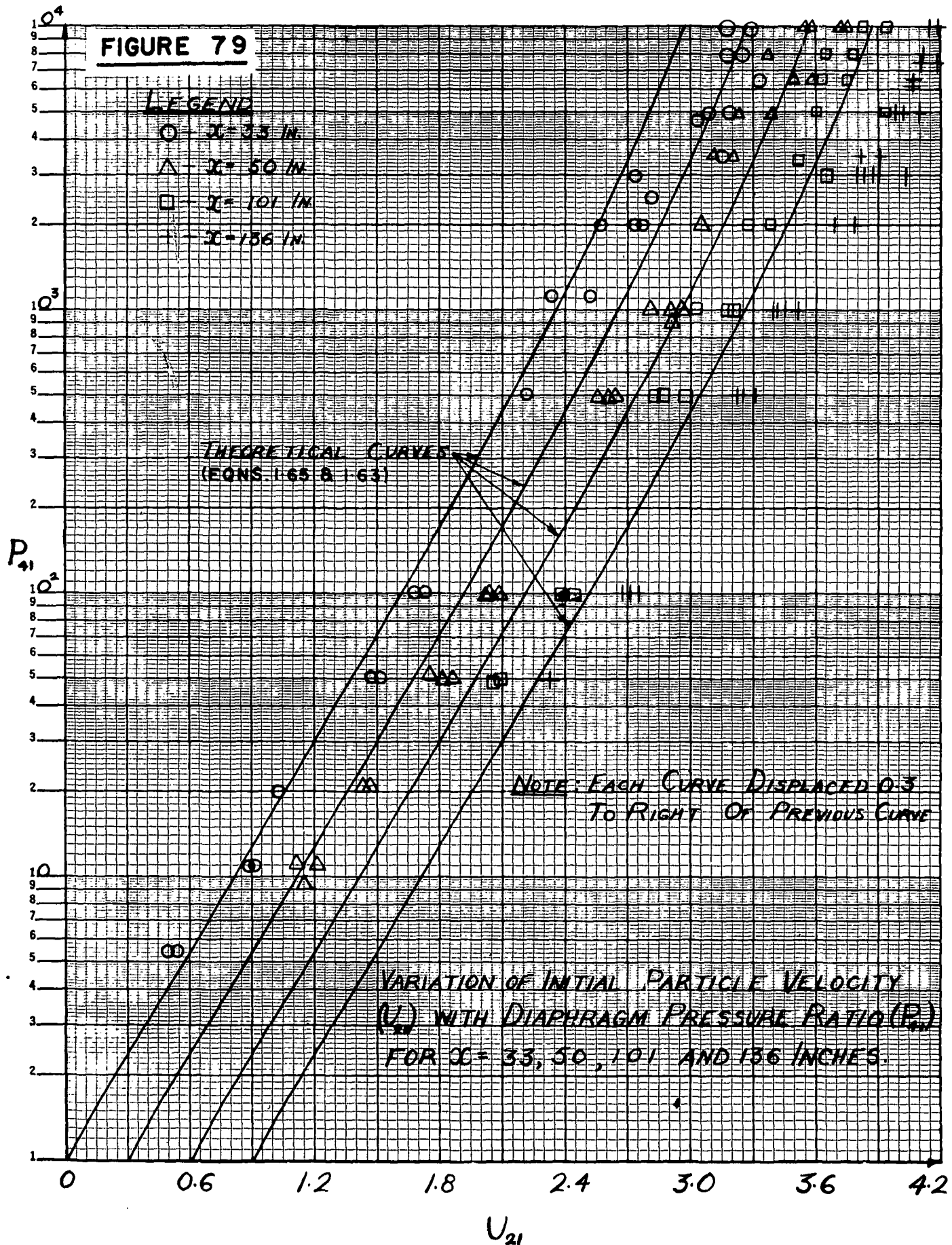
FIGURE 78

LEGEND

○ - $\Delta P = 1000 \text{ mm Hg}$ △ - $\Delta P = 500 \text{ mm Hg}$

□ - PLUNGER IN CHAMBER

 P_{41} THEORETICAL CURVES
(EQNS 1.53 & 1.55)NOTE: SECOND CURVE DISPLACED 0.6
TO RIGHT OF FIRST CURVE.VARIATION OF INITIAL PARTICLE VELOCITY
(U_{21}) WITH DIAPHRAGM PRESSURE RATIO (P_{41})
FOR $X = 50$ INCHES.



of the origin that there was an initial speed-up due to the small jet of air that escaped from the chamber as the plunger hit the diaphragm which disintegrated in a few microseconds. Later this velocity approached the theoretical value (fig. 76). Finally, the velocity of the front increased again when the shock was fully formed, and its velocity was quite uniform. The increase in speed can not be explained on the basis of the heat conduction solution for a "laminar" contact front alone, because on that basis its order of magnitude turns out to be very small (ref. 68). For real flows the contact region is turbulent, and its growth would be more rapid resulting in a greater advance of the front.

It is not known what effect this speed-up has on the flow in the shock tube. Nevertheless, here are two apparently contradictory physical phenomena, shock wave attenuation and contact surface speed-up, occurring simultaneously in the shock tube. Therefore, any theory that attempts to explain one effect should simultaneously explain the other, if it is to describe the real physical processes. (It should be emphasized that from the classical approach a retarded piston in a cylinder gives rise to a rarefaction wave, and an accelerating piston causes a compression wave. The contact front is essentially analagous to such a piston. Shock wave attenuation theory assumes that the contact surface decelerates. The reverse is true and this is rather paradoxical.)

5.05. Flow in the Uniform State Bounded by the Shock Wave and the Contact Surface.

It is not possible to give a final decision on the uniformity of the states (2) and (3) separated by the contact surface. The reason being, that to-date a systematic analysis of these states has not been conducted by measuring density, pressure and temperature directly, over a wide range of shock speeds. Most of the present data is based on a Mach number determination of the flow by means of two-dimensional wedges, using a schlieren or shadowgraph analysis. This method is not too useful for the determination of flow uniformity, especially at higher Mach numbers. For weak shock waves piezo gauge pressure profiles show that the flow in state (2) behind the shock is quite uniform (ref. 20). This has also been found from interferometer experiments. Work of a similar nature for strong shock waves has not been reported. Although, it is known from measurements conducted at Princeton, Toronto (see ref. 68) and Lehigh Universities that density and pressure changes do occur in these states, especially in small tubes. Some temperature profile measurements with hot wire anemometry are also reported in reference 49.

An examination of the (x, t) -plane flow records of reference 8, for a 1.00 diameter tube and the present results for the 3 inch x 3 inch tube shows that the entire region behind the shock wave is criss-crossed continuously by the transverse reflections of the Mach and regular reflected wave train which follows the main shock wave. It was pointed out in section 5.02 that these reflections will change the pressure, temperature and density in this state. (In the piezo records shown in reference 68 for stronger shocks, it is noted that total deviations of 30% of the pressure rise across the shock occurs.) The order of magnitude of the deviations that actually take place can not be determined from wave speed measurements and must be done by direct methods.

The variation of Mach number (M_2) with diaphragm pressure ratio (P_{41}), as determined from a two-dimensional wedge analysis (from ref. 7) is shown on figure 80, and a typical schlieren flow photograph of this region is shown on plate 20. The reason that the transverse Mach waves do not appear here is probably due to the fact that a low pressure was used in the channel. They are not really prominent unless a pressure (p_2) of about one atmosphere is utilized in shock tubes which are about two to three inches wide. It is seen that a noticeable deviation in Mach number (M_2) starts when the flow is just supersonic. These results indicate good agreement with theory, but it is not a direct indication of the variation in the flow quantities in state (2). All that may be said is that any deviation is likely to be small for weak shock waves.

5.06. Flow in the Uniform State Bounded by the Contact Surface and the Rarefaction Wave.

Very few results are available of direct measurements of flow quantities in state (3) (see ref. 68 for piezo pressure profiles over a sizeable range of P_{41}). The gas in this region was initially contained in the chamber, and during the expansion process the same gas passed through the jagged remains of the diaphragm into the channel. As a result the flow becomes quite rough, and is filled with velocity, pressure, temperature and density gradients. The entire region past the contact layer is covered by striations in the (x, t) -plane records. These indicate the propagation of fluctuating density gradients. The type of eddying flow in this region is also confirmed from spark schlieren photographs, as shown on plate 17. In addition, plate 2 which illustrates the refraction of a shock wave at an Air/Air contact front, indicates that the transmitted shock wave is broken up when it passes through this turbulent region. The records in reference 8 and the present results substantiate that this phenomenon takes place when the flow in state (3) has become supersonic. Since this type of flow is not seen at any time in state (2), which has a lower Reynolds number per foot and is therefore subject to greater viscous effects, it can not be attributed to a shock boundary layer interaction alone. That this type of flow is typical of the head-on collision of a shock wave with a jet and its

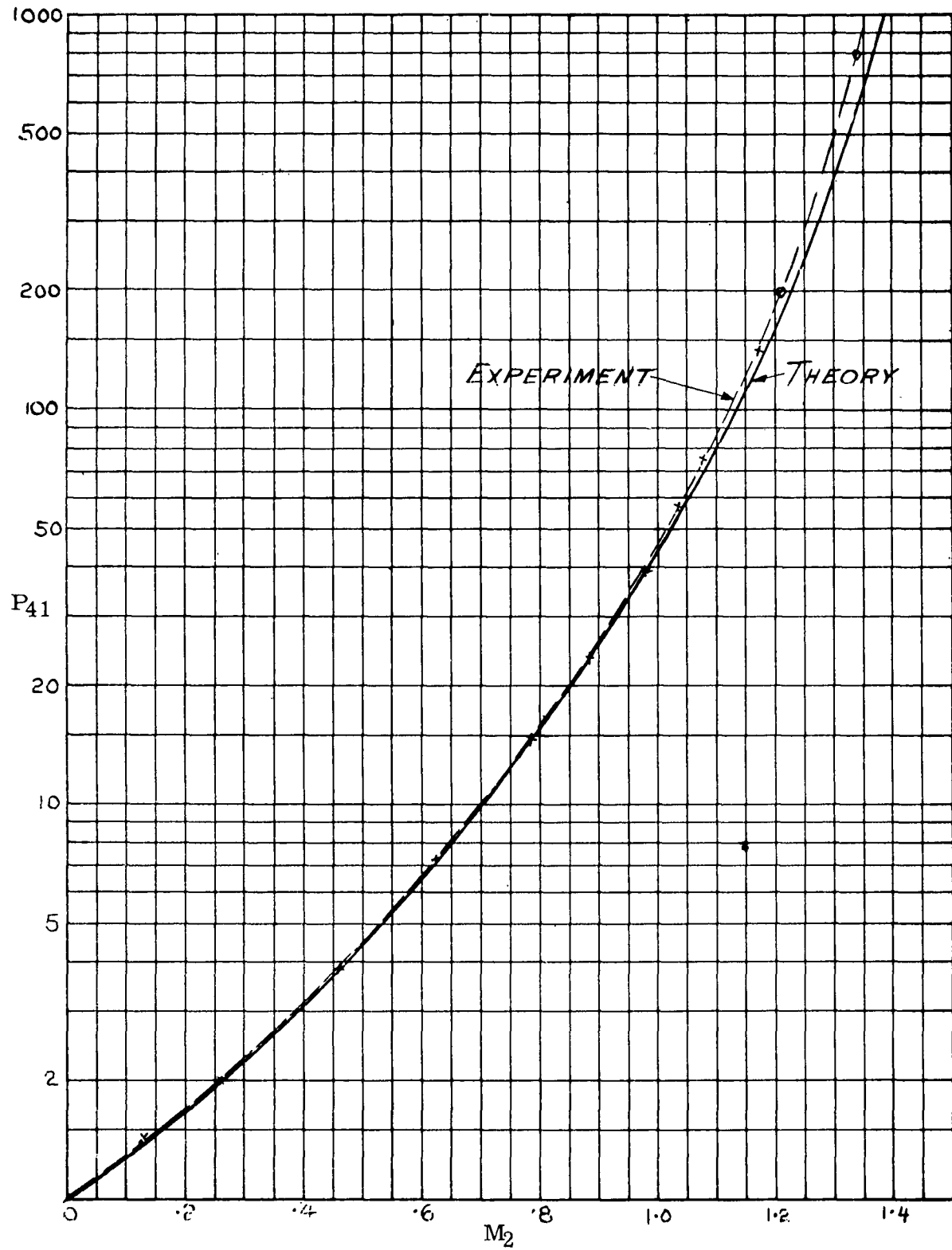


FIGURE 80

THE VARIATION OF MACH NUMBER IN STATE (2) (M_2) WITH
DIAPHRAGM PRESSURE RATIO (P_{41}). CASE AIR/ AIR.

(from reference 7)



PLATE 20.

TYPICAL SCHLIEREN PHOTOGRAPH OF THE FLOW IN STATE (2)
OVER A TWO - DIMENSIONAL 5° - $3'$ WEDGE. $P_{41} = 104.5$, $M_2 = 1.15$.

associated boundary layer has been shown in some shock tube experiments at John Hopkins University and from figures 54 to 56, in reference 53. The flow in state (3) may be considered as essentially of the same type and structure as a jet flow, that is, it has a mass flow which is turbulent in nature.

The available range of experimental results for state (3) from references 6, 7 and 27 are all based on the measurement of the Mach number by means of two-dimensional wedges. A typical flow photograph of this region is shown on plate 21. The experimental results from reference 7 of the variation of the Mach number (M_3) with diaphragm pressure ratio (P_{41}) is shown on figure 81. It is seen that beyond $M_3 > 3.5$, the deviation from theory becomes very rapid, and really high Mach numbers ($M_3 > 5$) have not been achieved to-date in this region. Substantiated reasons for this discrepancy have not been given to-date. In reference 27 it is pointed out that there may not exist an upper limit to the attainable Mach number (M_3). In any event, a decision on this point will have to wait until experimental results are available on the temperature, density and pressure distribution in this region. All that may be said, is that the uniformity of flow behind the contact surface is not nearly as good as the flow behind the shock wave.

There is evidence from work recently completed at the Institute of Aerophysics on shock wave refraction into this region (3) that points to the possibility that the low temperatures are not achieved in state (3). This would explain the unattainability of very high M_3 .

5.07. Rarefaction Wave Velocity Measurements.

Velocity measurements on rarefaction waves from (x, t)-plane schlieren records are described in detail in reference 14. It was shown in section 1, that because the rarefaction wave is a simple wave which separates two uniform states the density derivative is discontinuous at the head and at the tail of the wave. The order of magnitude of the density derivative at the head and tail of the wave is almost the same for weak rarefaction waves (see table 4). This implies that the head and tail of the wave should both appear in a schlieren photograph, regardless whether the rarefaction wave is centred or not. In practice this does not materialize and only the head of the wave appears (plate 14). The reason for the non-appearance of the tail of the wave can not be explained on the basis of a non-centred rarefaction wave alone. It was shown in section 5.01 that a piston type characteristic diagram could not be constructed at the origin for the case of a bursting diaphragm, due to the fact that the head of the compression region was already a shock wave. Therefore, although

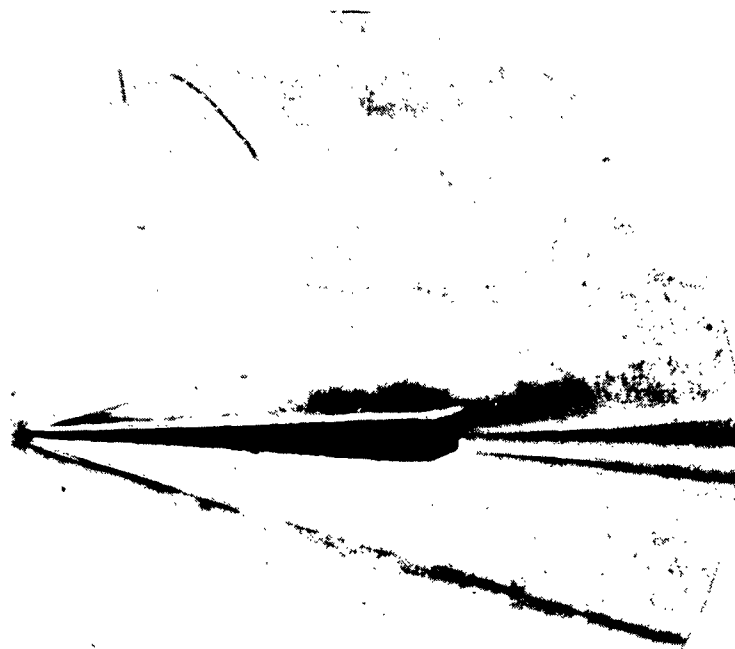


PLATE 21.

FLOW OVER A $5^\circ - 3'$ WEDGE IN THE HIGH MACH NUMBER
REGION (3). $P_{41} = 6960$, $M_3 = 4.38$ (from reference 7)

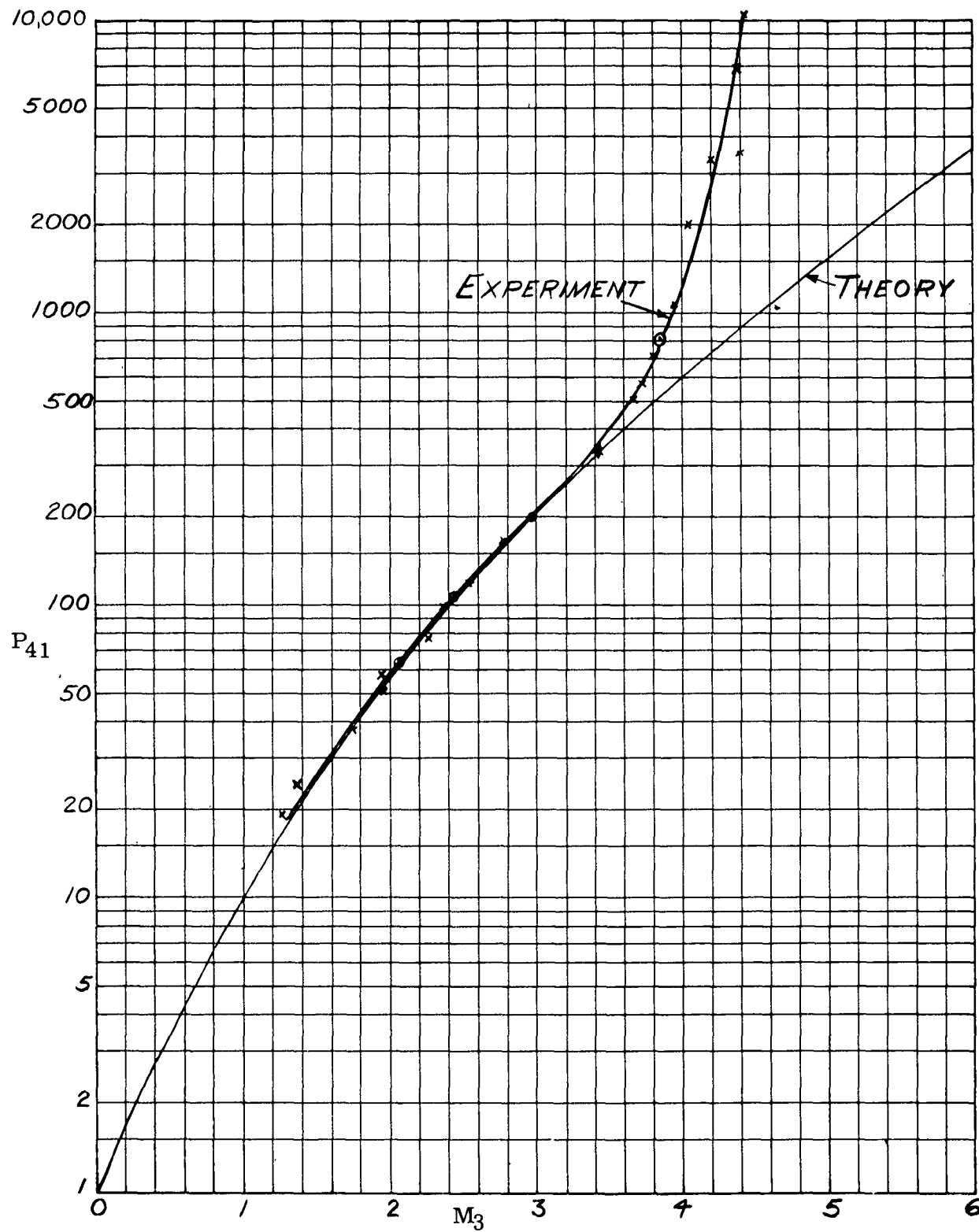


FIGURE 81

THE VARIATION OF MACH NUMBER IN STATE (3), (M_3) WITH
DIAPHRAGM PRESSURE RATIO (P_{41}). CASE AIR / AIR.

(from reference 7)

the rarefaction wave is not centred, it will not be very extended either. Thus a discontinuity in the density derivative will exist at the last characteristic line, and would be expected to show up for weaker rarefaction waves, when its absolute value is high.

It was thought that perhaps this may be due to the fact that at the tail of the wave the gas is in motion, and as a result the discontinuity in the density derivative is smoothed out by viscous effects. (On a piezo pressure record the curve at the tail of the wave does appear smooth.) However, later experiments have shown that the head of a rarefaction wave appears prominently when the gas into which it is progressing is in motion (see plate 23), and here viscous smoothing effects are not in evidence. Hence, it must be concluded that the disappearance of the tail of a rarefaction wave under schlieren observation must be due to some other cause. This is unfortunate because had this border Mach line appeared, it would have given an excellent means of determining the particle velocity, speed of sound and Mach number in the cold region as well as the deviation from a centred wave. It was possible, however, to determine the speed of sound of the gas at rest in the chamber from the head of the rarefaction wave. In this manner, the speed of sound considered from a gas dynamic viewpoint as outlined in section 1, was tested. The results reduced from about 23°C . to 0°C without correcting for the small variation in γ are as follows: $\bar{a}_{\text{air}} = 1087 \pm 2 \text{ f.p.s.}$, $\bar{a}_{\text{argon}} = 1009 \pm 1 \text{ f.p.s.}$, $\bar{a}_{\text{carbon dioxide}} = 844 \pm 1 \text{ f.p.s.}$ These values agree very well with acoustic results. It also bears out the previous observation that for weak shock waves (starting with a sound wave) the wave speeds are in excellent agreement with theory.

It should be noted that the dark lines on plate 14 (j), (o), (p), (r), (t) and (u) and the white lines (reversed schlieren) on plate 14 (m), (q), (s) and (v) in the vicinity of the rarefaction wave, are not to be confused with the tail of the rarefaction wave. The tail propagates into the channel for all diaphragm pressure ratios $P_{41} > 11$, for the case Air/Air. The observed lines all occur in the chamber and are really condensation shock waves. This is confirmed on plates 22 (a), (b) and (c) which show the effects of condensation at the origin and beyond. For the three recorded cases $M_3 \geq 1$, it is seen that the saturated air runs are all alike in that a marked condensation shock wave appears about $250 \mu\text{sec.}$ after the diaphragm breaks. In the dry air runs this phenomenon is absent. The shock trace has a straight path at a speed relative to the tube of 630 f.p.s. This speed was found to be constant for the three P_{41} cases tested. In the runs shown on plate 14 the condensation shock speed is again uniform, but their relative values differ, presumably due to the degree of initial saturation. The fact that the condensation shock wave does not curve (slow up) as it passes through the rarefaction wave is not understood (see ref. 69). The particle velocity opposing the shock is decreasing through the rarefaction wave, and simultaneously the pressure in front of the shock is increasing, and a degree of compensation may result. Secondary transverse condensation shocks are also visible.



DRY AIR

(a)



SATURATED AIR

$P_{41} = 10$ $P_{21} = 2.8$ $p_4 = 746 \text{ mm. Hg.}$ $T_{4, 1} = 298^\circ \text{ K}$
 $T_3 = 210^\circ \text{ K}$ $W_{11} = 1.61$ $M_3 \approx 1$
 chamber length = 4 feet channel length = 1 foot

PLATE 22.

CONDENSATION EFFECTS IN THE RAREFACTION WAVE



DRY AIR

(b)



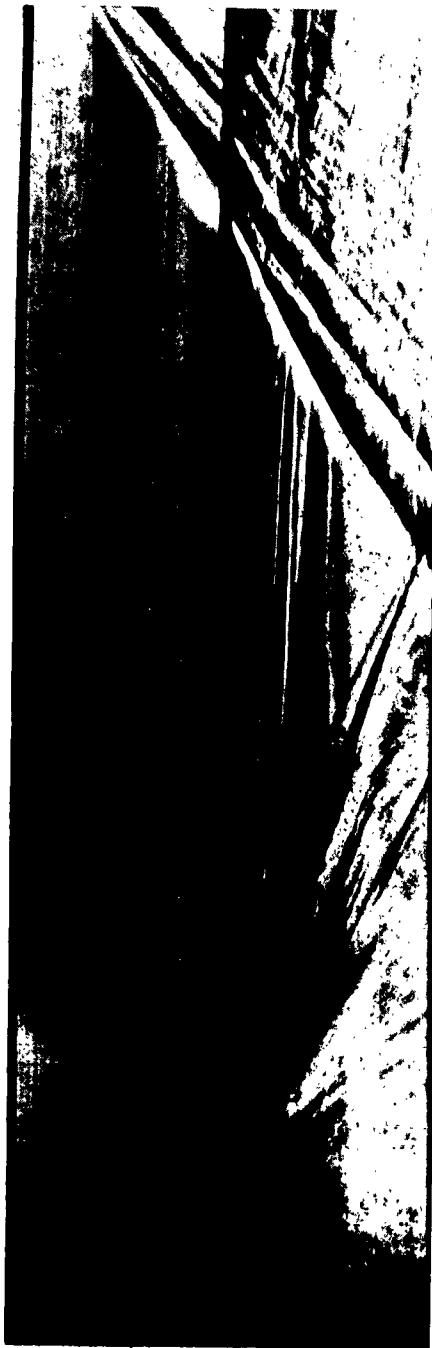
SATURATED AIR

A142

$$P_{41} = 25 \quad P_{21} = 4.0 \quad p_4 = 746 \text{ mm. Hg.} \quad T_{4,1} = 297^\circ \text{ K}$$

$$T_3 = 177^\circ \text{ K} \quad W_{11} = 1.90 \quad M_3 = 1.45$$

PLATE 22. (continued)



DRY AIR



A141

SATURATED AIR

(c)

$P_{41} = 50$ $P_{21} = 6.1$ $p_4 = 746 \text{ mm. Hg.}$ $T_{4,1} = 297^\circ \text{ K}$
 $T_3 = 138^\circ \text{ K}$ $W_{11} = 2.13$ $M_3 = 2.28$

PLATE 22. (concluded)

About 800 μ sec. after the diaphragm breaks the condensation nuclei are so numerous that the film is completely blacked out. This suggests that the wave speed records could be utilized for the study of the rate of formation of condensation nuclei with the aid of a photodensitometer.

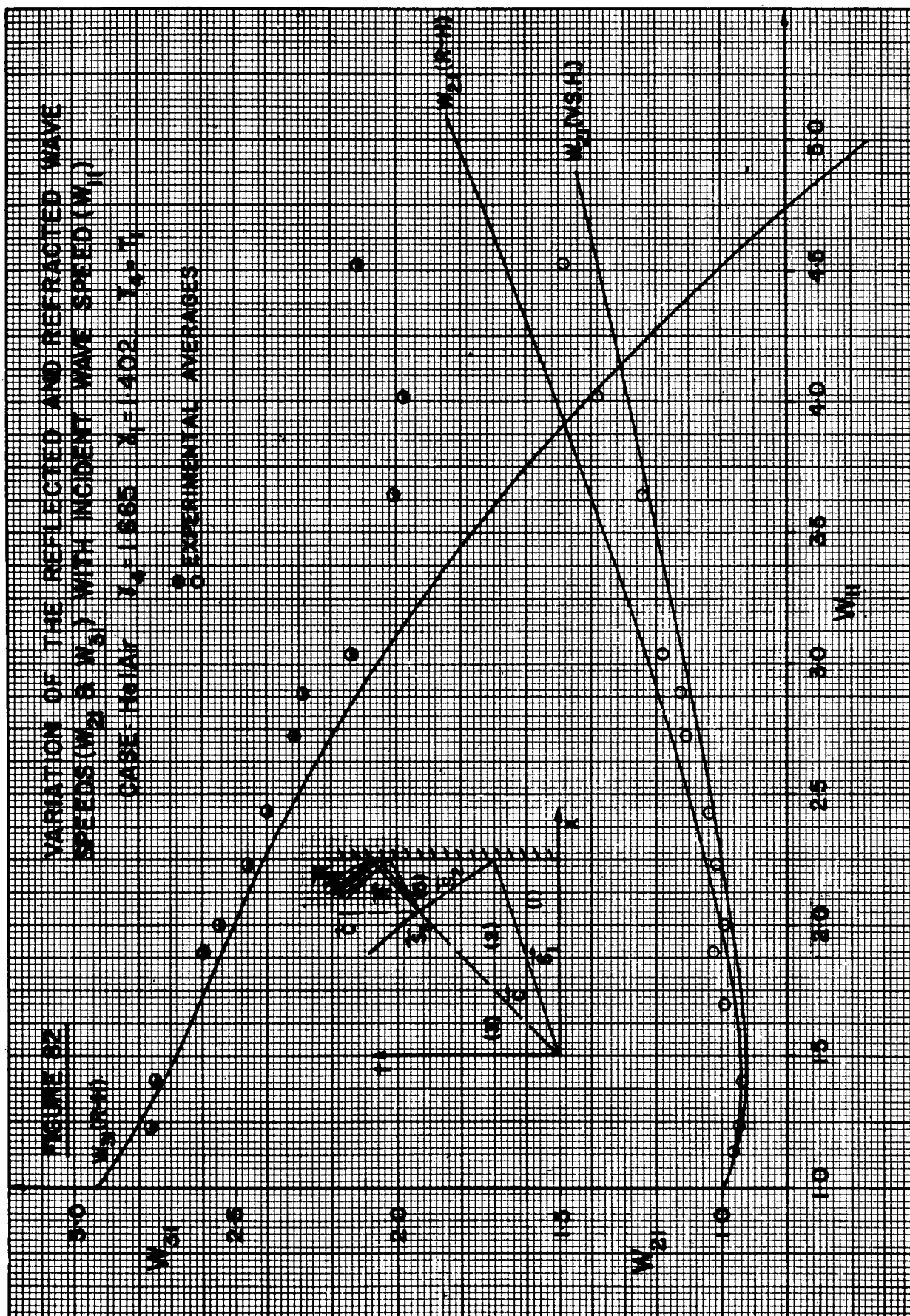
Despite the precautions to keep the chamber air dry for the records shown on plate 14 by employing commercial compressed air cylinders, some condensation (or liquifaction for the high P_{41} runs) did take place, and is quite evident from the records. This entire matter will require a detailed investigation.

5.08. Real Flows at an Open or Closed Chamber and Channel.

The basic shock tube as treated in section 1 may have an open or closed chamber or channel, depending on the problem under investigation. If the channel is closed, then normal reflection of shock waves may be studied, as shown on plates 2, 4 and 5. This type of reflection has been considered by a number of investigators, and the detailed results with air in the channel (from ref. 73) are shown on figure 82. These experiments were conducted at the Institute of Aerophysics in the 3 inch x 3 inch wave interaction tube. The strength of the incident shock was determined directly from the wave speed as measured from (x, t)-plane schlieren records, and thus eliminated the necessity for a tube calibration. The results are in agreement with the theory using constant specific heats for shock waves below a Mach number of $W_{11} \approx 2$. For strong shock waves the results approach the values determined from the modified shock tube theory with variable specific heats, (section 1.06). For an incident wave Mach number $W_{11} > 3$ and a density in the channel of several millimeters, luminescence may be observed behind the reflected shock wave. At the lower Mach numbers the light is due mainly to the ionization of impurities such as barium, calcium and sodium which require low ionization potentials (see refs. 43 and 44).

For a spectroscopic study of the ionized state behind the shock wave, Mach numbers of the order of six are necessary. In this case the magneto-hydrodynamic phenomena associated with strong shock waves may also be investigated (ref. 29).

If the channel is open, the shock wave emerges into the free atmosphere. Actual schlieren photographs of this type of flow are shown on plates 23 and 24. Plate 24 (c) shows the outflow from a 1-inch diameter tube and was taken from reference 8. Reversed knife edge positions are included in order to evaluate any possible schlieren overloading effects (ref. 45). The records show that when the plane shock wave emerges into the atmosphere, it diffracts, decelerates and tends to become spherical.



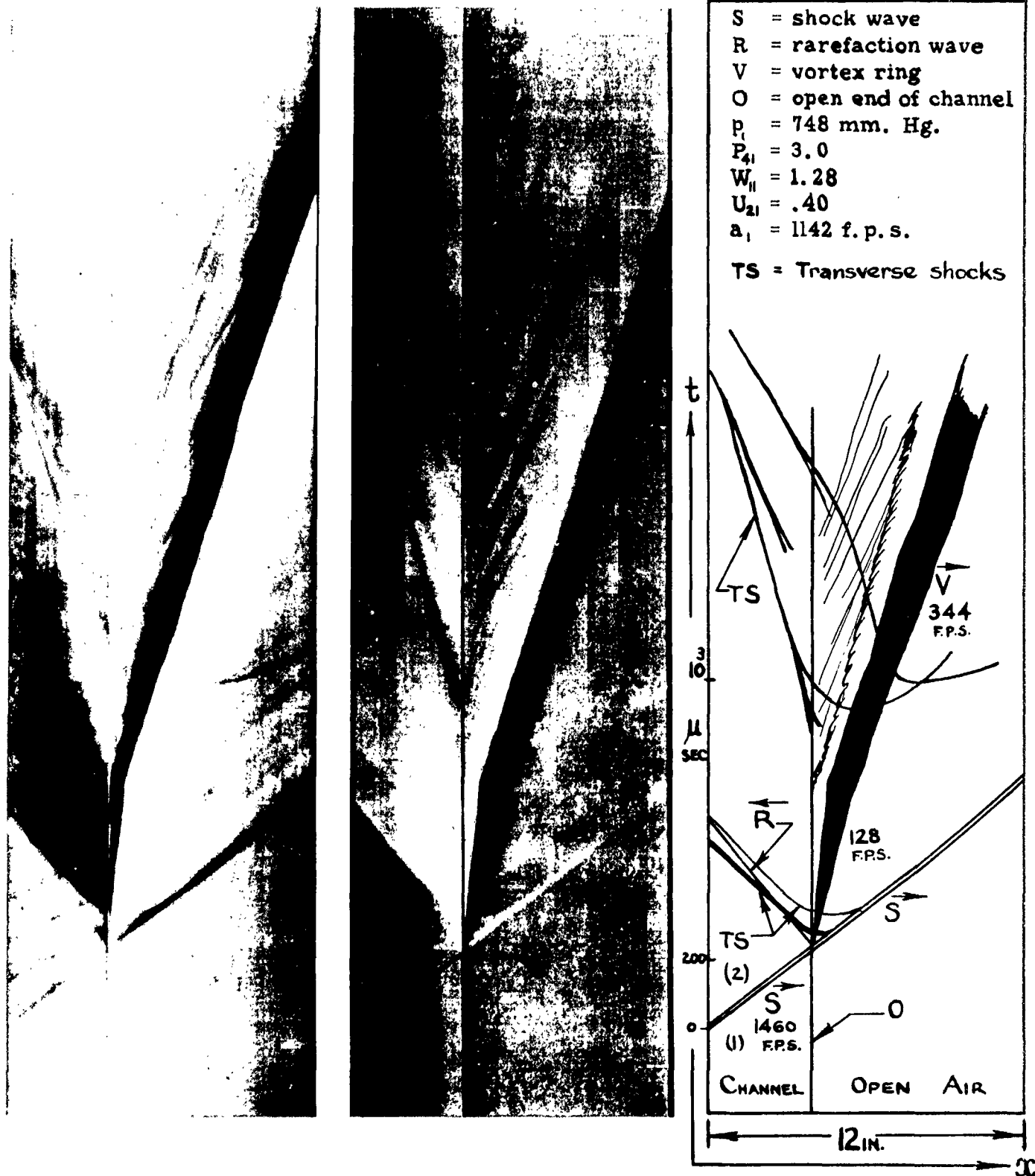


PLATE 23.

EMERGENCE OF A SHOCK WAVE FROM THE OPEN END OF A SHOCK
TUBE CHANNEL.



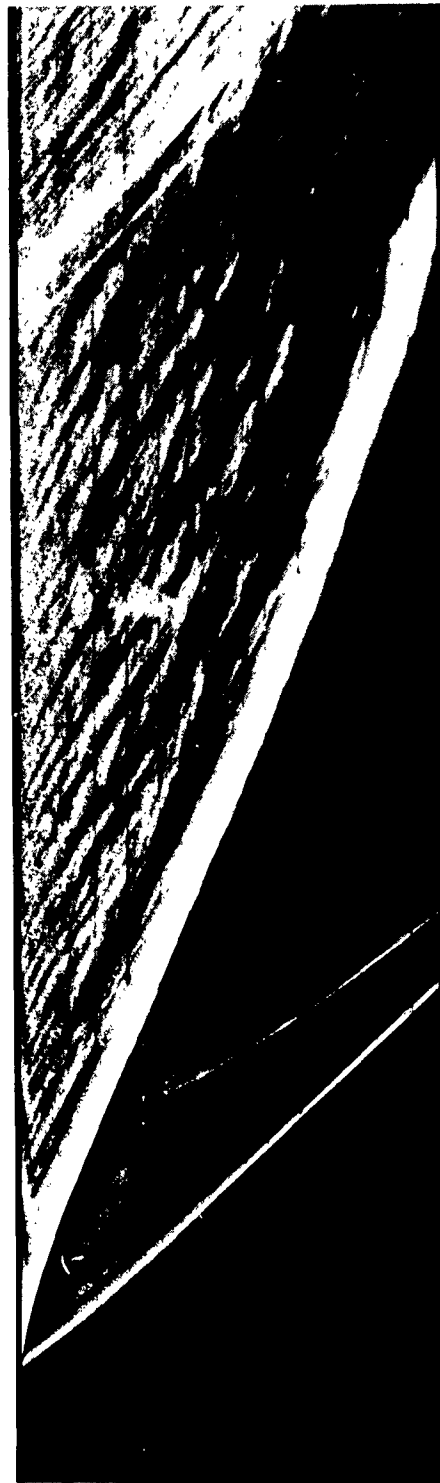
(a)

$$W_0 = 1.41$$



(b)

$$W_0 = 1.81$$



(c)

$$W_0 = 1.29$$

PLATE 24.

EMERGENCE OF A SHOCK WAVE FROM THE
OPEN END OF A SHOCK TUBE CHANNEL

The shock wave is followed immediately by an annular vortex (see also refs. 2 and 42). The vortex travels rather slowly for the first 500 μ sec. and then accelerates. At the point in the (x, t)-plane where this occurs transverse shock waves are seen to cross. Some of these waves coalesce and enter the shock tube. This is confirmed on plate 35 where the shock wave coming from the open end strikes the wire screen.

At the point of emergence of the shock wave from the channel a rarefaction wave is reflected back into the tube, and the head of the wave actually travels at the speed of sound in region (2), behind the incident shock wave. Shock diffraction and reflection also occurs at the open end, and a transverse shock wave is seen to overtake the head of the rarefaction wave.

This is a complex type of three-dimensional viscous interaction which will depend on the emergent as well as the reflected wave systems for a solution. It is intended to do a systematic investigation of this problem at a later date. The present flow photographs however, show that the wave systems are qualitatively similar for cylindrical and square tubes. Due to symmetry the vortex ring appears to have a smoother motion in case of the cylindrical tube. In all cases the flow behind the incident shock wave was subsonic.

If the chamber is closed, the rarefaction wave undergoes normal reflection at the chamber end. A typical photograph of this reflection is shown on plate 3. It was shown in section 1, that very low temperatures, densities and pressures may be obtained in the uniform region (6) which forms behind the reflected rarefaction wave. This has not been verified to-date. State (6) has been neglected almost entirely by experimentalists. It should receive much more attention since it offers research in a thermodynamic state with flow quantities of extremely low values.

If the chamber end is open, then the rarefaction wave emerges into the free atmosphere. Theoretically, a compression wave which steepens into a shock wave, is also reflected back into the chamber. This problem is treated graphically in the (x, t)- and (U , a)-planes by the method of characteristics, in reference 51. An actual flow of this type with reversed schlieren is shown on plate 25. The head of the rarefaction wave is clearly shown on both records. Since it is a sound wave, it propagates into the free atmosphere with unchanged speed. However, this or any other expansion characteristic fails to be reflected back from the open end as a compression characteristic. Instead, about 500 μ sec. from the time the head of the rarefaction wave emerges into the open air, a vortex is formed within the tube by the air inflow into the chamber. (This vortex is seen to unite with another vortex caused by the rupturing of the cellophane diaphragm). The flow of air into the tube appears to be quite rough as indicated by the transmission of density gradients (alternate black and white lines), and is similar in appearance to the flow through the ruptured diaphragm. This type of inflow is typical of unfaired subsonic entries, and changes very

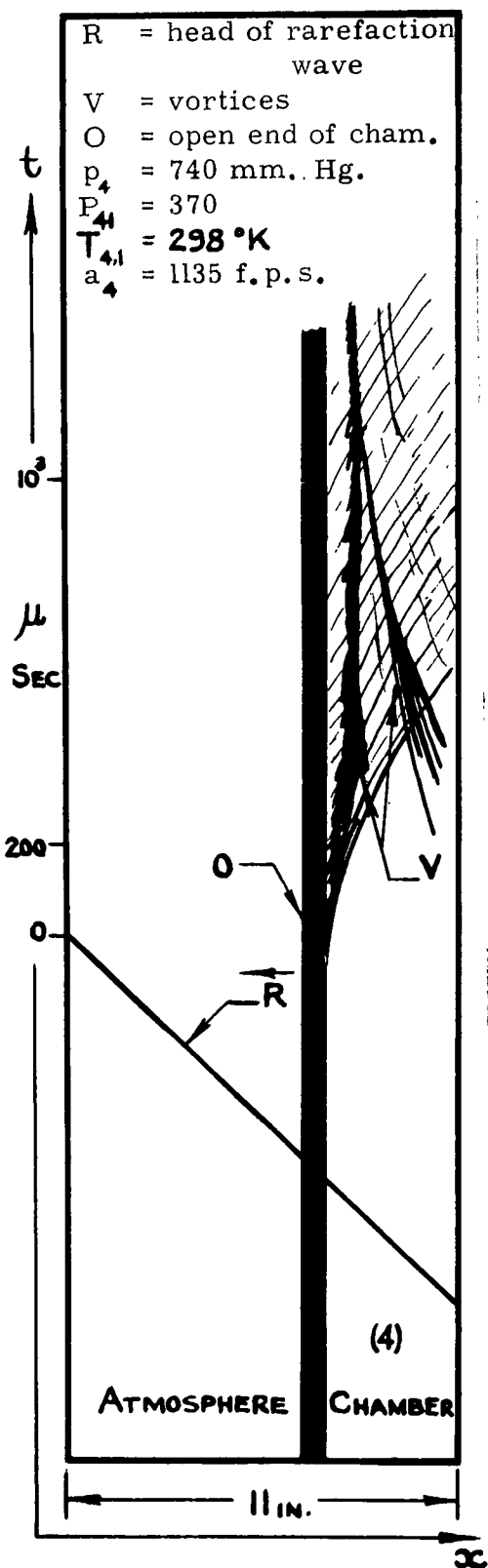


PLATE 25.

EMERGENCE OF A RAREFACTION WAVE FROM THE OPEN END OF A SHOCK TUBE CHAMBER, AIR/AIR.

little in appearance for various strengths of rarefaction waves. The absence of a reflected shock or compression wave can not be accounted for at present. It is hoped to investigate this problem in a more detailed manner at a later date. In this open-end case as well, three-dimensional and viscous effects impose difficult boundary conditions, and the ideal flow solution as given in reference 51 is not very realistic.

5.09. Experiments on One-dimensional Wave Interactions.

The previous subsections dealt with the basic flows in a real shock tube with open or closed ends. In the following a résumé will be given of the one-dimensional wave interactions that have been investigated at the Institute of Aerophysics.

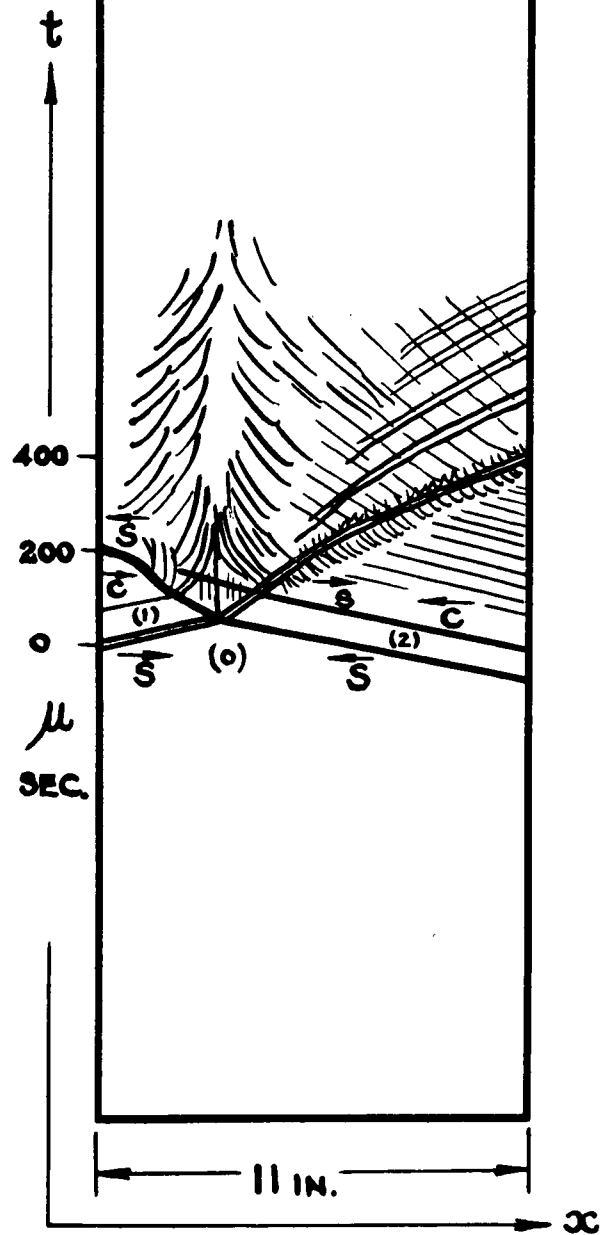
By using two chambers and a channel the head-on collision of two shock waves can be studied in the wave interaction tube. The cases of equal and unequal shock waves colliding are shown on plates 26 and 27. This problem has been considered in detail in reference 16 from which figure 83 is replotted. It is seen that agreement with constant specific heat is good up to wave Mach numbers $W_{11} \approx 3.5$. For stronger shock waves the results approach the variable specific heat solution. Relaxation times for the establishment of thermal equilibrium behind the shock wave were not measured in these experiments. Only about 50μ sec. were available on the schlieren records, and about 100μ sec. to 1000μ sec. are required to establish equilibrium under the experimental conditions. However, it was estimated that the theoretical values obtained in reference 36, for air, were quite good.

By using three tube sections with successively decreasing pressures, the head-on collision of shock and rarefaction waves has also been studied in reference 16. A typical interaction is shown on plate 28. Good agreement between theory and experiment is shown on figure 84, which is typical of the results obtained, for shock pressure ratios up to 7 and for rarefaction wave pressure ratios of 0.50 and 0.59.

The problem of shock wave refraction has been considered in detail in reference 12. Typical results shown on figure 85, were obtained by using artificial contact surfaces of cellulose nitrate dope of 1500 to 3500 angstrom units in thickness.

By reflecting the initial shock waves from the end of the channel the natural contact surface also may be employed to study shock wave refraction. For weaker shock waves ($M_3 < 1$) the interaction with the swirling flow in the cold state and its associated boundary layer is not as severe as those shown on plates 2 and 4, and only a single transmitted shock wave

S = Shock Wave
 C = Contact surface
 $p_o = 2.90$ mm. Hg.
 $P_{10} = 32.4 = P_{20}$
 $W_{10} = 5.2 = W_{20}$
 $a_o = 1136$ f.p.s.



COLLISION OF EQUAL SHOCK WAVES IN AIR
 PLATE 26.

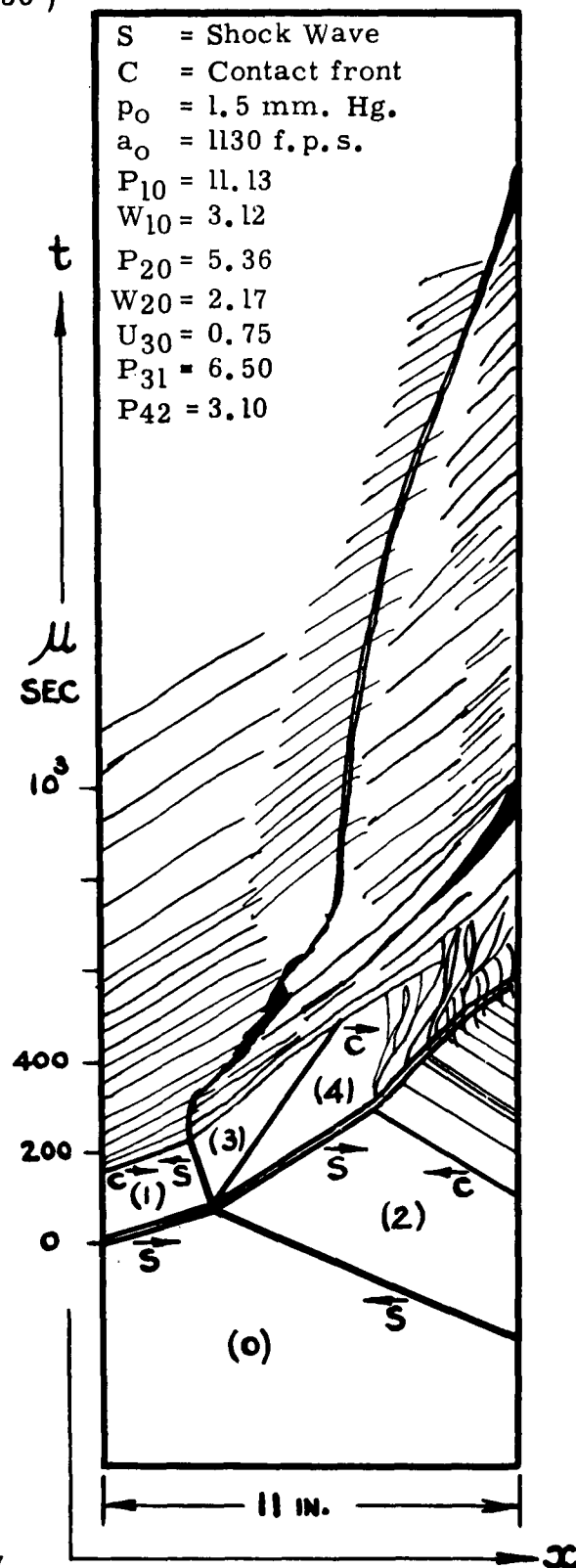
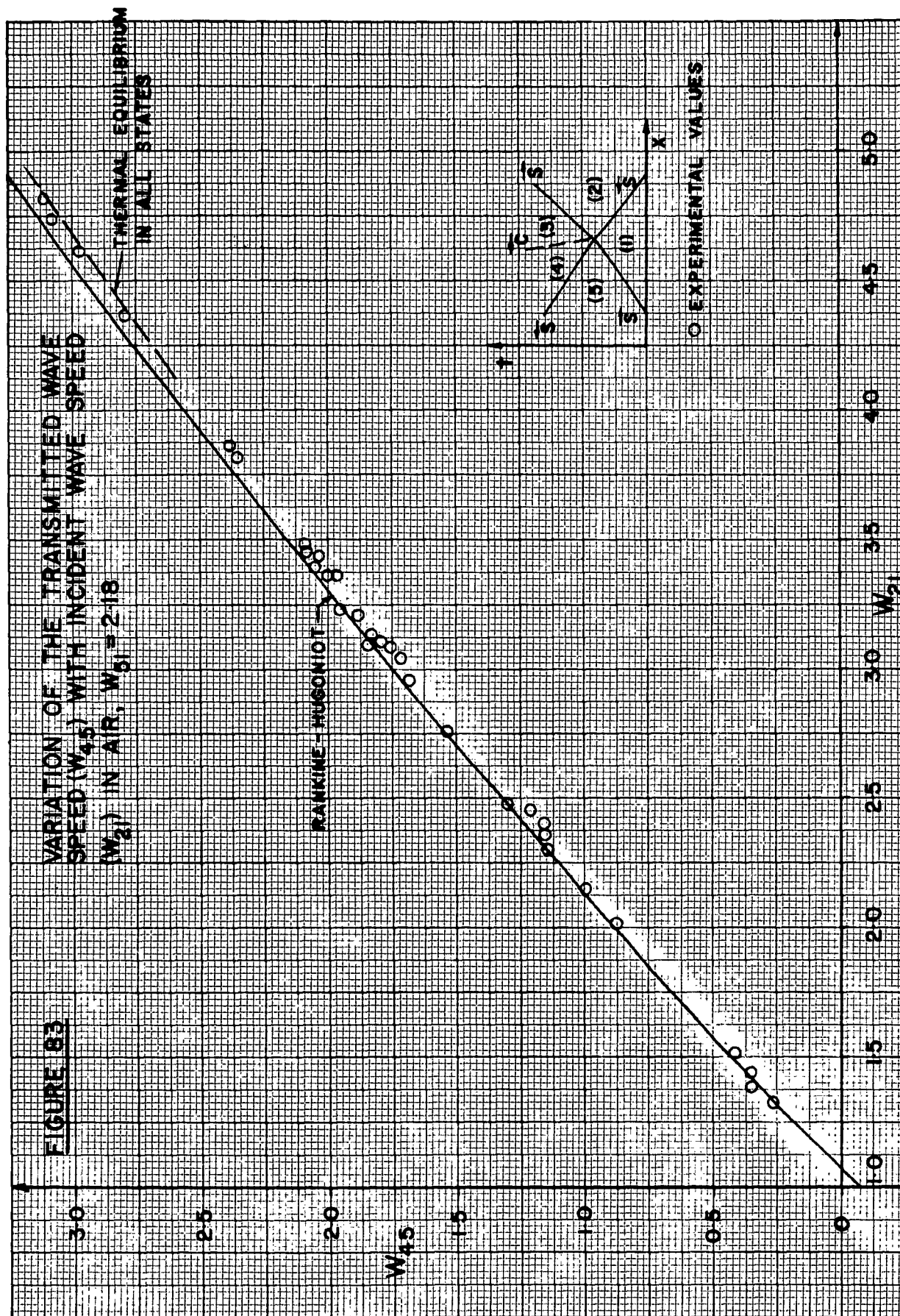


PLATE 27.

COLLISION OF TWO SHOCK WAVES IN AIR



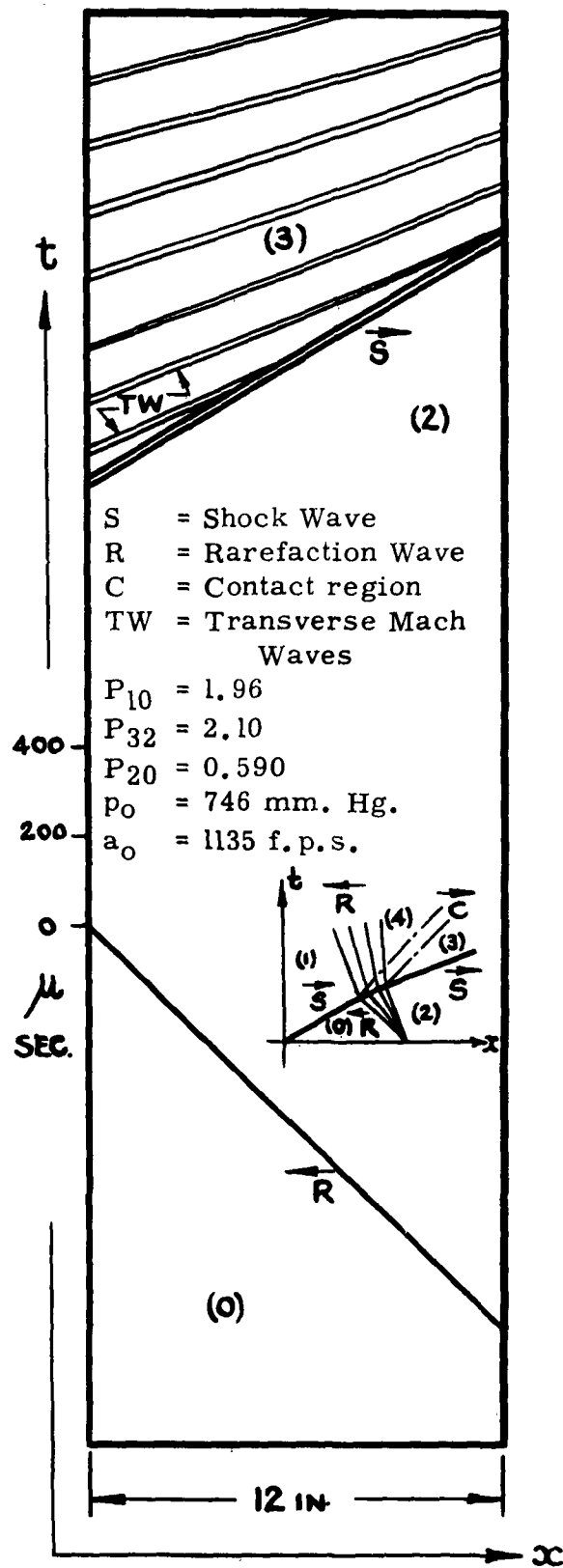


PLATE 28.

COLLISION OF A SHOCK AND A RAREFACTION WAVE
IN AIR

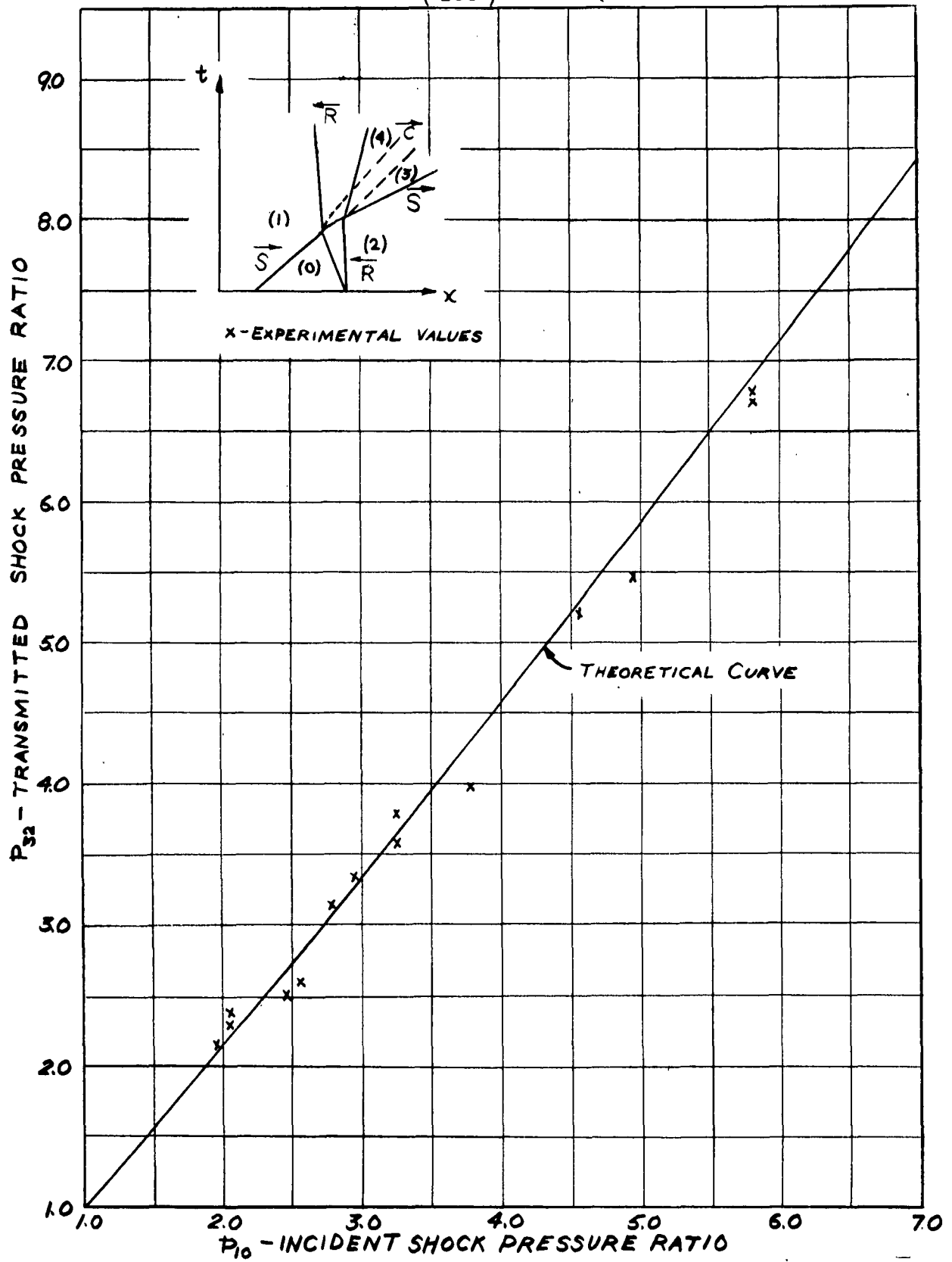


FIGURE 84.

COLLISION OF A SHOCK AND RAREFACTION WAVE.

Rarefaction Strength $p_{20} = 0.500$

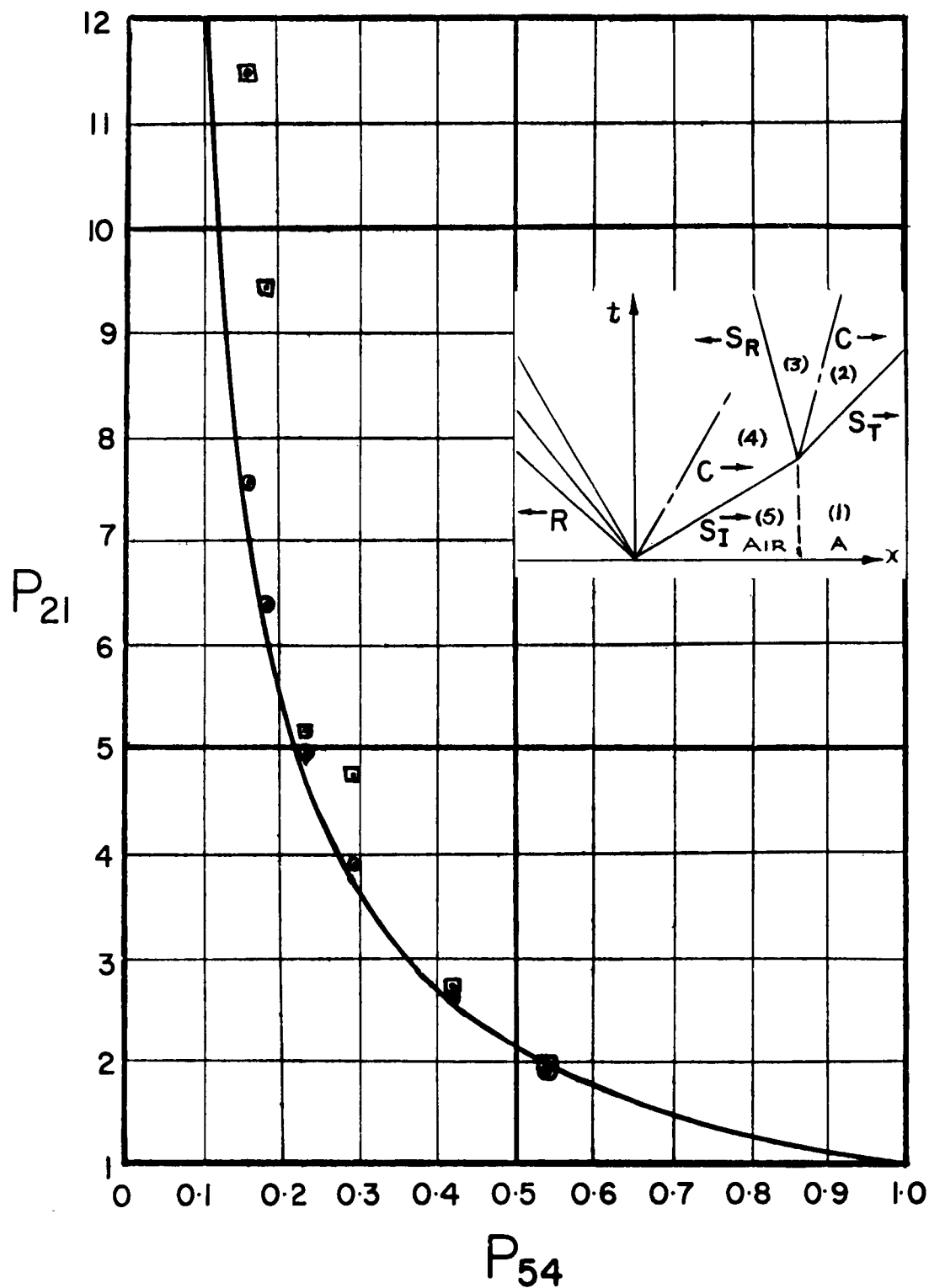


FIGURE 85.

VARIATION OF THE TRANSMITTED SHOCK STRENGTH, P_{21} ,
 WITH THE INCIDENT SHOCK STRENGTH, P_{54} , for $E_{15} = 0.431$.
 (CASE AIR//A) (from reference 12)

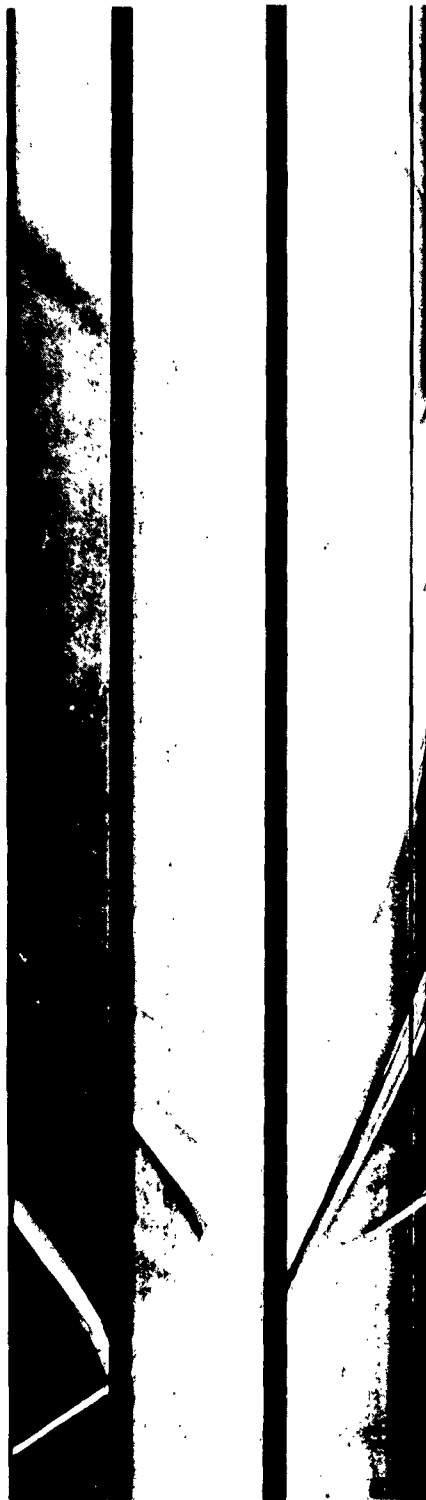
results (see plate 5). The agreement with theory for the records evaluated to-date is quite good, except for strong shock waves ($W_{11} \approx 3$). Figure 82 (ref. 73) shows the variation of the normal reflected and refracted wave speeds W_{21} and W_{31} as a function of the incident wave speed W_{11} . The reason why the refracted wave speed (W_{31}) does not follow the theoretical curve is not known. Perhaps the temperature does not reach the very low theoretical value. This would also account for the low theoretical values of M_3 . It should be noted that the variable specific heat (V.S.H.) curve for W_{31} is almost identical with the constant specific heat (R-H) curve.

Shock wave or rarefaction wave refraction at a contact surface can be extended to include the double refraction of these waves at a finite layer of gas. In the case of a shock wave passing through a layer of gas, it has been shown (ref. 11), that the pressure ratio of the emergent shock wave may be raised or lowered depending on the boundary conditions, just as it leaves the layer. This phenomenon has been called shock wave amplification and absorption or attenuation respectively. Beyond the layer overtaking shock waves catch up with the emergent wave and tend to bring up its strength to its initial value, in the absorption case. Typical results appear on plates 6 and 29. The agreement with theory for the waves tested is satisfactory. This problem has just been investigated in a systematic manner and will be published in the near future. (ref. 73.)

In addition to the refraction phenomena, some additional features may be noted on plates 6 and 29. It will be seen that when the incident shock wave S_1 , strikes the Air//He contact surface C_1 , a rarefaction wave is reflected. The rarefaction wave is bounded at the head and tail by two shock waves. The shock at the head of the rarefaction wave is mainly due to the presence of the 1500-3500 angstroms thick microfilm (determined by multiple beam interferometry). The existence of the shock at the tail of the rarefaction wave can not be adequately accounted for. This type of N wave is again generated about 400μ sec. later at the contact surface and appears to undergo periodic transverse reflection. The head and tail of the initial rarefaction wave are curved, indicating that the reflected rarefaction wave is catching up, as a short chamber was used for this particular experiment.

This problem has also been applied to a rarefaction wave passing through a layer of gas. The criterion for the reflection of a compression wave or rarefaction wave from a contact surface was given in section 2.04. Plates 7, 30 and 31 show the refraction of a rarefaction wave at a layer of helium, argon and carbon dioxide. All gases separated by the gas layer are at atmospheric pressure and temperature. With these boundary conditions a rarefaction wave refracts at an Air//A contact surface to give a reflected rarefaction wave; at an Air//He contact surface a shock wave is reflected back; and for an Air//CO₂ contact surface, which is a borderline region, a shock should also be reflected.

From the above plates it is seen that in the case of argon a converging type of compression wave appears from the second (A//Air) contact surface, not at the point of impingement, but several hundred μ sec. later. These results

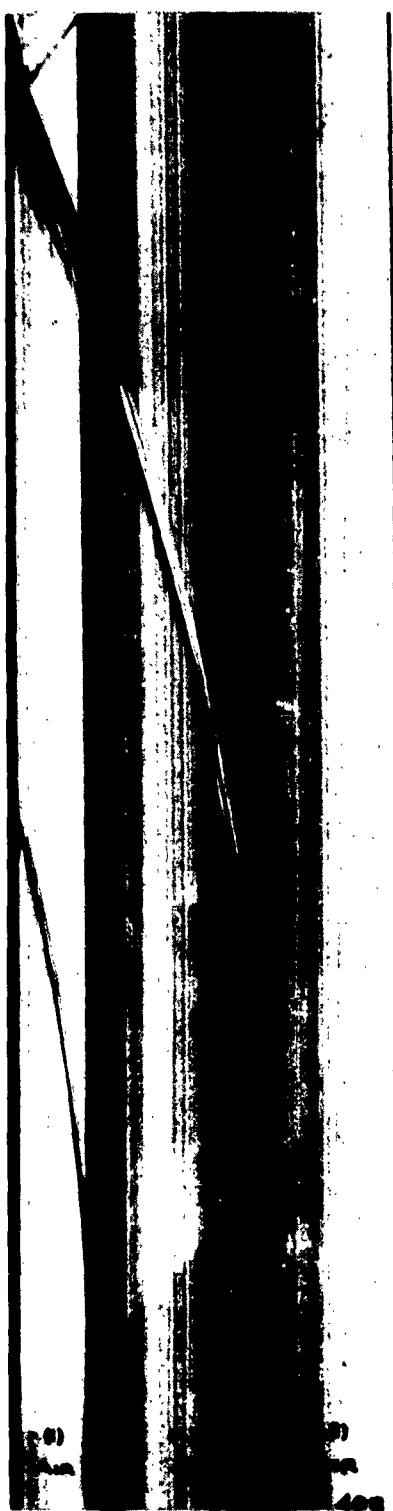


$$W_{II} = 1.52$$

$$W_{31} = 1.42$$

PLATE 29

THE REFRACTION OF A SHOCK WAVE AT A LAYER OF HELIUM
CASE Air//He//Air



(a)



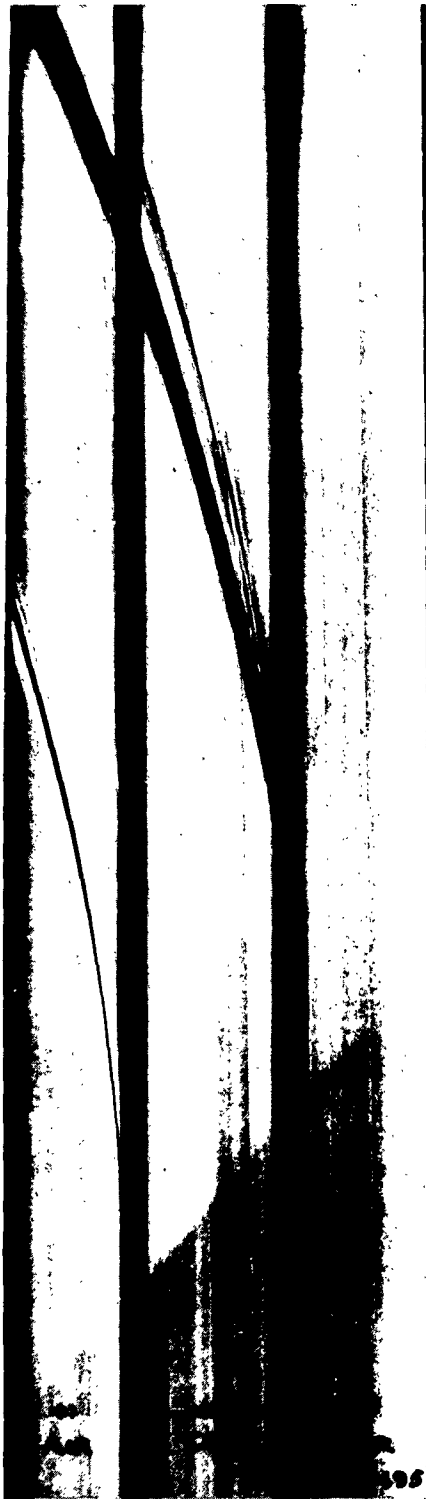
(b)

$p_4 = 742 \text{ mm.Hg.}$ $p_{1,2,3} = 185 \text{ mm.Hg.}$ $p_4 = 754 \text{ mm.Hg.}$ $p_1 = 7.5 \text{ mm.Hg.}$
 $P_{41} = 4.0$ $T_{1,2,3,4} = 27.1^\circ \text{ C.}$ $P_{41} = 100$ $T_{1,2,3,4} = 25.2^\circ \text{ C.}$

PLATE 30.

THE REFRACTION OF A RAREFACTION WAVE AT A LAYER OF ARGON.

CASE Air | A | Air



(a)



(b)

$p_4 = 741 \text{ mm.Hg.}$ $p_1 = 185 \text{ mm.Hg.}$ $p_4 = 741 \text{ mm.Hg.}$ $p_1 = 70.5 \text{ mm.Hg.}$
 $P_{41} = 4.0$ $T_{1,2,3,4} = 27.0^\circ \text{ C.}$ $P_{41} = 10.5$ $T_{1,2,3,4} = 27.0^\circ \text{ C.}$

PLATE 31.

THE REFRACTION OF A RAREFACTION WAVE AT A
 LAYER OF CARBON-DIOXIDE. CASE Air \parallel CO₂ \parallel Air.

can only be viewed as qualitative. A quantitative analysis is essential and will require a considerable amount of theoretical and experimental work and may be done at a later date. The contact surface stability for the case of a helium layer is demonstrated rather well on plate 7, where the front which is being accelerated into the helium remains very stable, whereas the front going into the air becomes unstable (see ref. 54).

Recently, the interaction of a shock wave with a wire screen has been examined with the wave speed camera. Typical results appear on plates 32 to 35. In subsonic aerodynamics the wire gauze has been utilized to study the mechanism of free stream turbulence, to reduce turbulence in wind tunnels and as a means of diminishing losses in sharp bends and diffusers. Very little is known of the characteristics of screens in compressible flow. This type of interaction may offer some interesting possibilities in that direction.

Most of the present experiments were conducted on number 8, 30 and 40 mesh screens with blockage coefficients, β of .50, .42 and .28 respectively. The subsonic definition of the blockage coefficient is given by $\beta = (1 - \frac{d}{\ell})^2$, where d is the wire diameter and ℓ is the mesh length. For incompressible flow these screens would have a resistance coefficient $K = \frac{p_1 - p_2}{\frac{1}{2}\rho u_1^2} \approx \frac{1 - \beta}{\beta^2} = 2, 3 \text{ and } 9$ (reference 55). Where $(p_1 - p_2)$ is the static pressure drop across the screen, and u_1 is the flow velocity (greater than 30 f.p.s., if this relation is to apply).

The preliminary results can be described as follows. When a shock wave strikes a screen, a shock is transmitted and a shock is reflected. In order to maintain the co-existence of the two adjacent states behind the two shock waves of different strength, a contact surface must form. This is confirmed by the experimental records. It is seen that at the point of impingement the two shock waves are formed very rapidly. Shock wave diffraction also takes place. The primary reflected and transmitted shock waves are also followed by their respective transverse waves which criss-cross the tube. In addition, a vortex sheet is formed. For weak waves it remains nearly stationary and hugs the wire screen (plate 32). For strong incident shock waves, the vortex sheet is swept out beyond the screen by the high particle velocity (plate 34). On plate 34 for about 100 μ sec. the vortex travels at constant speed, suddenly decelerates and remains almost stationary. The deceleration is probably due to some type of wave interaction, but it is not discernible from the flow photographs. There is no evidence of wakes being shed from the wire elements as from a grid nozzle in steady flow. As a matter of fact the flows in all states appear as uniform as those behind the incident shock waves. However, on plate 32 it can be seen that every transverse wave generates its own contact front when it is stronger than a sound wave. Also, if the gauze is coarse, then each wire element generated its own transverse waves by diffraction and gives

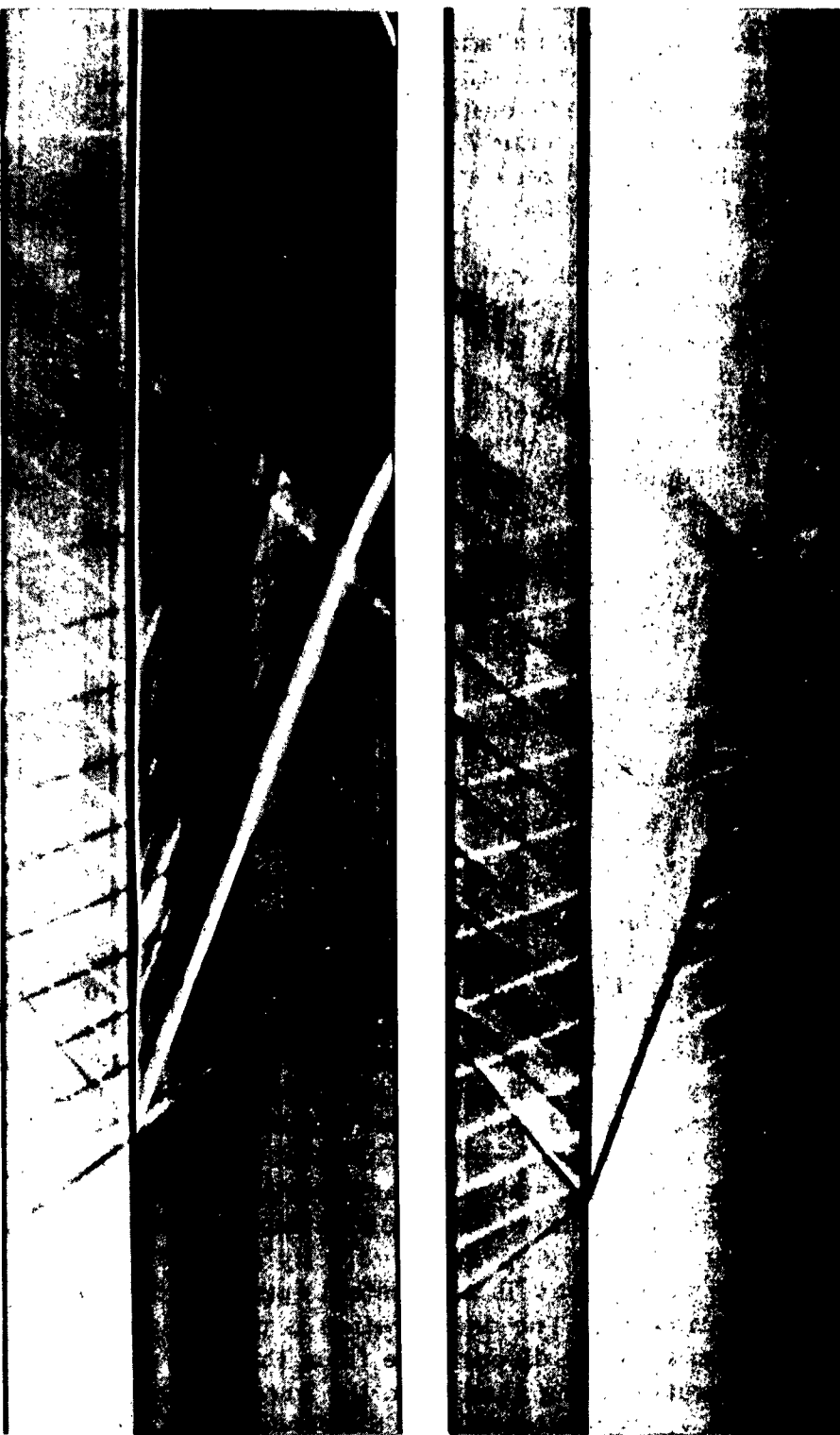
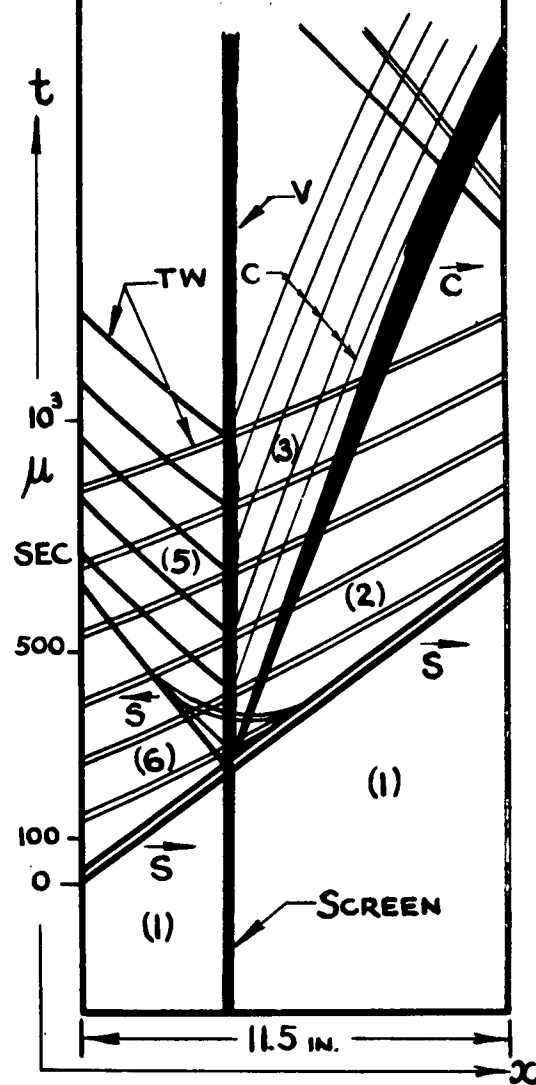


PLATE 32.

S = Shock Wave
 C = Contact Surface
 V = Vortex
 TS = Transverse Shocks
 $a_1 = 1137$ f. p. s.
 $p_1 = 747$ mm. Hg.
 $P_{71} = 4.00$ $W_{56} = 1.15$
 $W_{61} = 1.34$ $M_6 = .42$
 $W_{21} = 1.26$ $M_2 = .33$
 $U_{21} = .36$ $M_5 = .18$
 $p_2 = p_3 = 1280$ mm. Hg.
 $p_6 = 1400$ mm. Hg.
 $p_5 = 1935$ mm. Hg.



THE INTERACTION OF A SHOCK WAVE WITH A NO. 40 MESH SCREEN.



$W_{61} = 1.34$ $W_{21} = 1.32$ $U_{21} = .44$ $M_5 = .26$
 $p_1 = 747 \text{ mm. Hg.}$ $P_{71} = 4.00$ $p_5 = 1810 \text{ mm. Hg.}$ $p_{2,3} = 1360 \text{ mm. Hg.}$

PLATE 33.

THE INTERACTION OF A SHOCK WAVE WITH A No. 8 MESH SCREEN.

S = Shock wave

C = Contact surface

V = Vortex

$a_1 = 1138$ fps.

$p_1 = 16.1$ mm. Hg.

$P_{v1} = 46.5$

$W_{e1} = 1.98$ $U_{21} = 1.07$

$W_{21} = 1.82$ $U_{41} = .54$

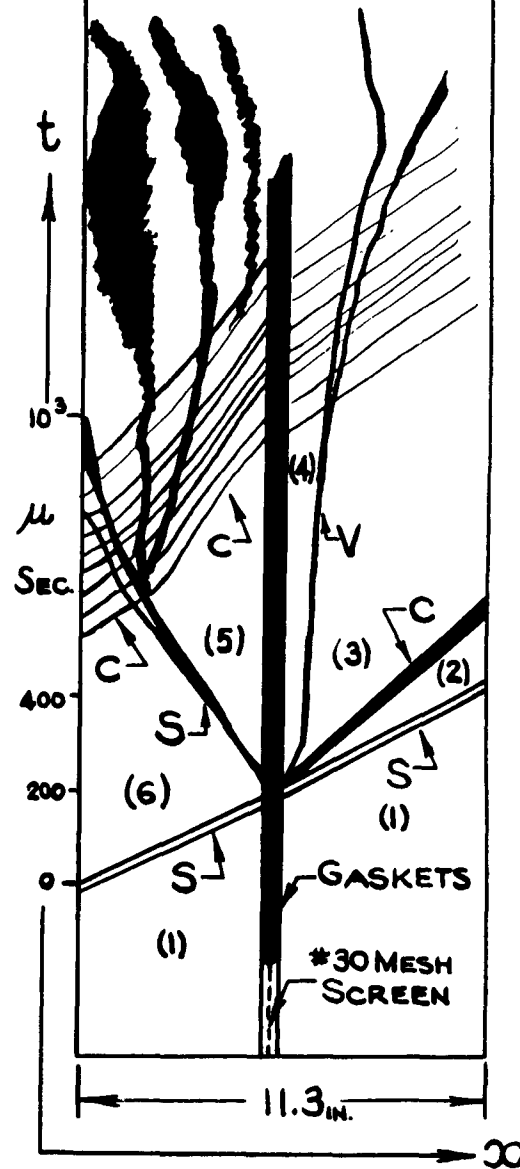
$M_e = .96$ $W_{56} = 1.48$

$M_2 = .85$ $M_5 = .25$

$p_2 = p_3 = 59.5$ mm. Hg.

$p_6 = 71.6$ mm. Hg.

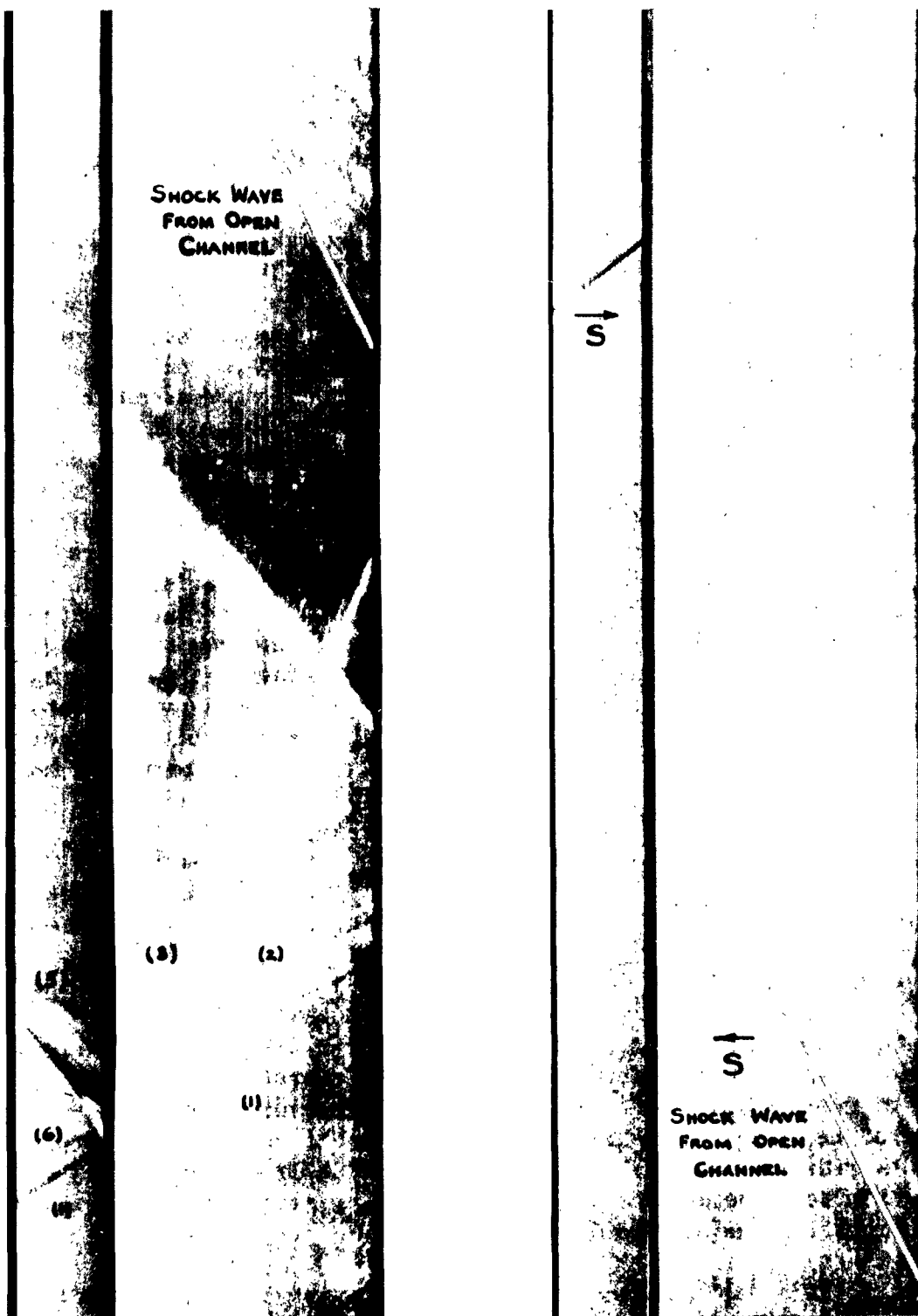
$p_7 = 172$ mm. Hg.



462

PLATE 34.

INTERACTION OF A SHOCK WAVE WITH A WIRE SCREEN



$$\begin{aligned}
 W_{61} &= 1.53 & W_{21} &= 1.45 & U_{21} &= .65 \\
 p_1 &= 752 \text{ mm.Hg.} & p_5 &= 3810 \text{ mm.Hg.} & p_{2,3} &= 1767 \text{ mm. Hg.}
 \end{aligned}$$

PLATE 35.

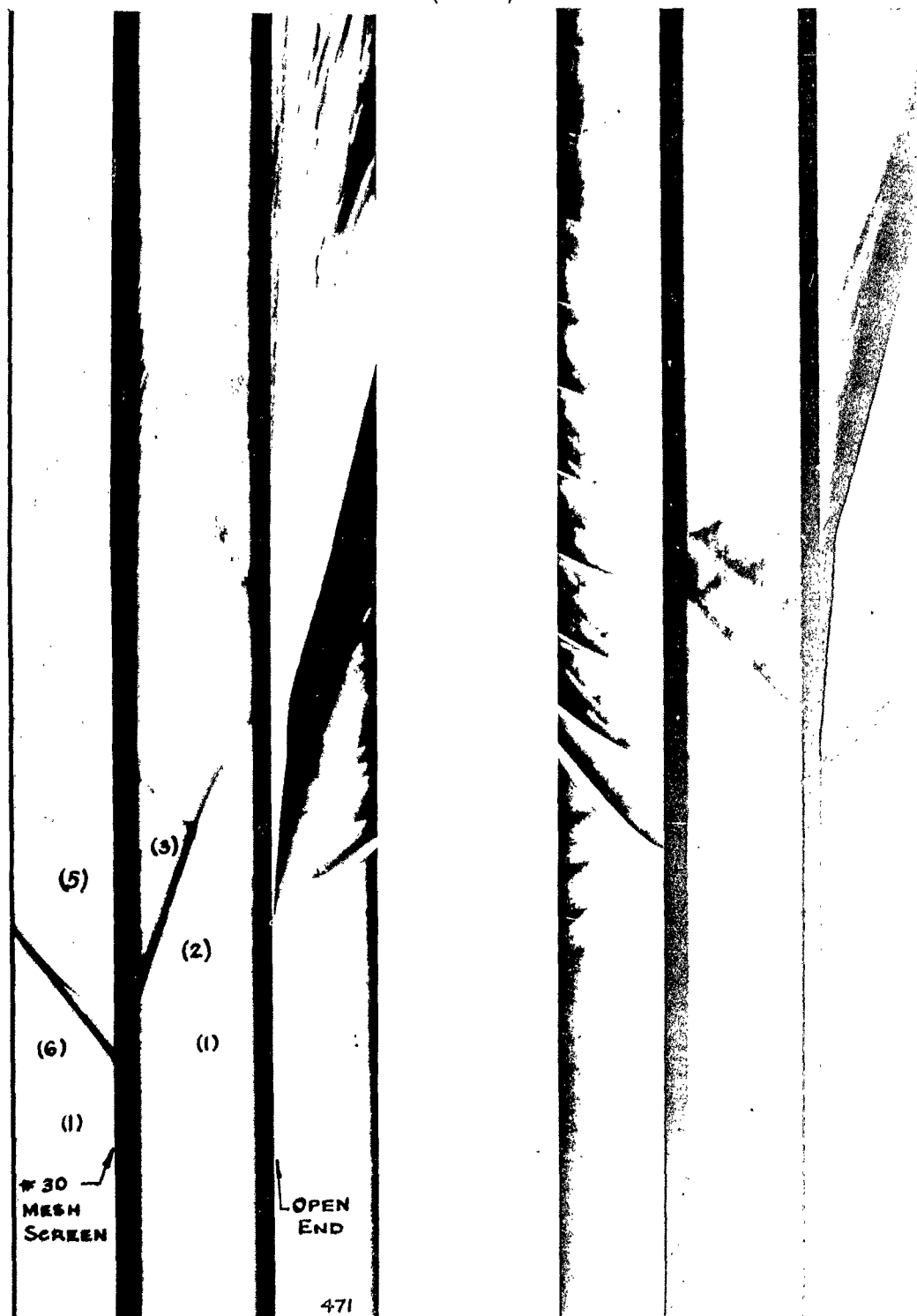
THE INTERACTION OF SHOCK WAVES WITH A NO. 30 MESH SCREEN.

rise to a very fine trace structure on the schlieren record (see plate 33) of transverse waves and contact surfaces. In addition a diffusion process occurs about the screen on the same plate. For the finer mesh gauzes this line structure becomes too close to be discernible but it probably exists nevertheless.

From the various records that were taken, it has been tentatively established that the Mach number in region (5) between the reflected shock wave and the screen (M_5) remains a constant for a screen with a given blockage factor. That is, if the blockage coefficient is zero (solid wall) the Mach number is zero; if the blockage coefficient is 1 (no screen), the Mach number is M_6 , corresponding to the incident wave strength. The schlieren photographs also show that region (3) is at a lower density than region (2). Since the pressures in (3) and (2) are equal, the temperature $T_3 > T_2$. This is reasonable, since state (5) has undergone two shock compressions. The measured velocity of the contact front agrees with the particle velocity (U_{21}) for the transmitted shock wave. The pressure in (5) is very high, and the particle velocity is very low by comparison with region (3). (Compare the initial contact surface velocity with the contact front velocity on plate 34.) Hence a rarefaction wave must exist between state (5) and (3) in order to reduce the pressure and increase the particle velocity from U_5 to U_3 . The rarefaction wave can not be seen. The vortex sheet at the screen is probably produced by shock wave diffraction, but its effect on the flow is not known, and hence state (4) is completely undetermined from a wave speed analysis.

An attempt has been made in reference 44, to compare this type of interaction with the magneto-hydrodynamic interaction of a shock-wave and a magnetic field. The equations of continuity, momentum and energy are applied. Only the momentum equation is changed by the pressure drag due to the screen or the strength of the magnetic field. The resulting solution is interesting. Since viscosity was neglected and viscous effects are very apparent in all the flow records, it must be concluded that this theory should be applied with caution to real screen interactions. Since the pressure drop across the screen is not uniquely determined owing to the existence of the vortex at the screen, it was not possible to check the present results with the curves given in reference 44. This problem may be investigated in some detail at a later date by using piezo gauges and a hot wire anemometer in addition to the wave speed camera.

In order to ascertain additional properties of the waves that are reflected back from the open end of a channel when the shock wave emerges into the atmosphere as well as the wave system produced by the shock impinging on a screen, plate 36 is also included. In this experiment the two problems were combined. It shows the stability of the contact region produced from the screen interaction. It also demonstrates the diffraction



$$W_{61} = 1.27$$

$$W_{21} = 1.19$$

$$U_{21} = .37$$

PLATE 36.

THE INTERACTION OF A SHOCK WAVE WITH A NO. 30 MESH SCREEN COMBINED WITH THE EMERGENCE OF A SHOCK WAVE FROM THE OPEN END OF A CHANNEL.

that is produced at the screen and at the open end of the channel. This in turn causes the production of new trains of transverse waves. It also indicates the possibility of studying the interaction of the vortex ring produced at the open end of the channel with a contact front produced by a screen. The refraction of the rarefaction wave, produced from the open end of the channel, at the screen contact front could also be studied. It should be noted that in this case as well, the reflected wave, as a result of refraction, is also absent.

It has become possible only very recently to set up the problem of the overtaking of two similarly facing shock waves (ref. 40). This interaction is shown on plate 37. It is seen to agree with the theory that a shock is transmitted, a rarefaction wave is reflected, and an almost ideal contact surface is separating the two uniform states between the two waves. The quantitative results are also quite good, and this work will be issued as a separate report in the near future (ref. 73).

A study of figure 1 of reference 40 shows that this is an excellent method of producing very strong shock waves, because in the case of two equal shocks (pressure ratios between 20 and 100) overtaking, the transmitted shock has a strength which is of the order of half the product (the ratio approaches one for very weak shocks) of the pressures of the initial shock waves. For example, when two equal shocks of a pressure ratio of 100 overtake, the transmitted shock wave has a pressure ratio of 4200 and the reflected rarefaction wave has a pressure ratio of .42.

The appearance of the wave system on the (x, t) -plane following the overtaking interaction is similar to the one generated by the bursting diaphragm. However, for the equivalent case in a shock tube with a diaphragm pressure ratio of 10,000 (compared with two equal overtaking shocks of 100 which also have an overall measure ratio of 10,000) a strong rarefaction wave ($P_{34} = .0017$) and a relatively weak shock ($P_{21} = 17$) are produced. Whereas, in the case of two overtaking shock waves a weak rarefaction wave (pressure ratio of 0.42) and a very strong shock wave (pressure ratio 4200) are generated.



S_1 = Incident Shock
 S_2 = Overtaking Shock
 S_3 = Transmitted Shock
 C = Contact Front
 R = Rarefaction Wave
 a_1 = 1130 f. p. s.
 p_1 = 747 mm. Hg.
 T_1 = 21.9 ° C.
 W_{51} = 1.65 W_{45} = 1.03
 W_{21} = 1.69 U_{21} = .90
 C_{41} = 0.28 (R.W. Head)
 P_{84} = 0.97

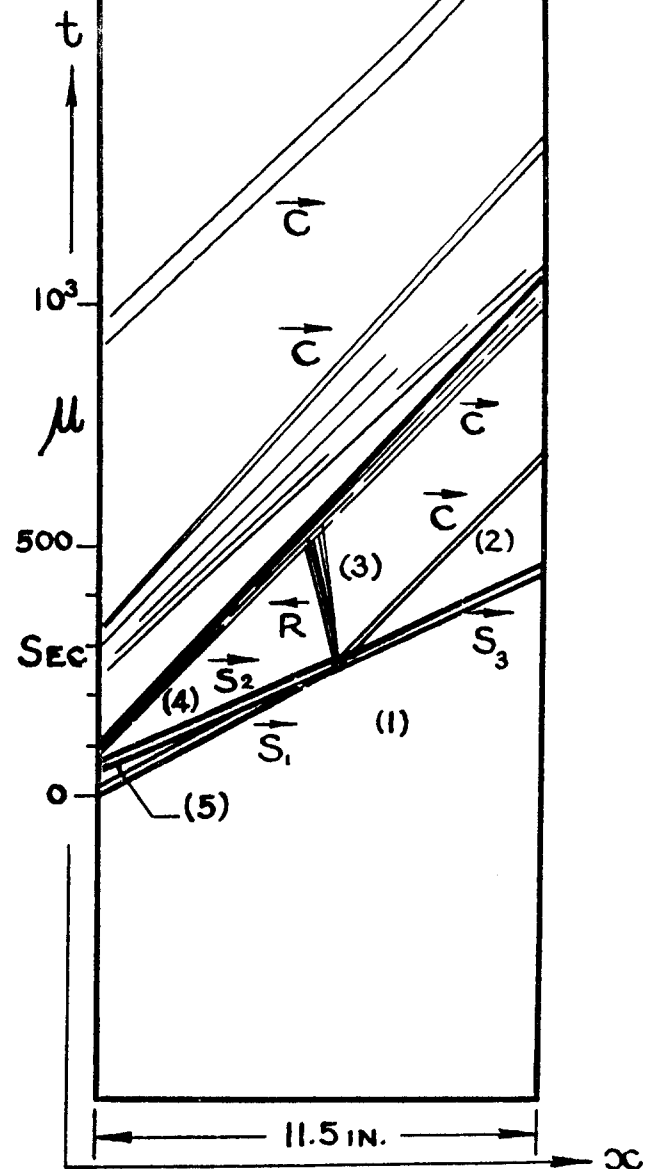


PLATE 37

THE OVERTAKING OF TWO SIMILARLY FACING SHOCK WAVES

VI. CONCLUSIONS.

The theory of the shock tube is developed in section I, from one-dimensional considerations. The modifications that are usually employed for flows with variable specific heats for rarefaction waves and shock waves are outlined. Some of the basic results for wave reflections, refractions and collisions are also included. Where three-dimensional and viscous effects occur, such as in the rupturing of the diaphragm, the transverse shock train which follows the main shock wave, the emergence of a shock or rarefaction wave into the free air, and the head-on collision of a shock wave with a wire screen, a simple analysis based on one-dimensional inviscid considerations is not possible.

The final portion of the report which deals with the experimental work gives an insight into the present status of theory and experiment of the shock tube.

In the study of the origin problem it is shown that the (x, t) -plane has the appearance of a characteristic net, which would result from the motion of a piston. However, it does not lend itself to the analysis by the method of characteristics. Actually, this net is composed of overtaking shock waves which coalesce to form the main shock front.

The shock formation process is more rapid at high diaphragm pressure ratios (P_{41}), but the shock path is curved over a slightly longer distance. Thus uniform speeds are not achieved before 6 to 8 tube widths (18 to 24 inches). Therefore measurements of shock wave velocity should not be made too close to the diaphragm (1 to 2 feet for this tube), since they will be slower. In the low P_{41} range ($P_{41} < 20$), the formation region is extended, but uniform velocity is already achieved one foot from the diaphragm (Fig. 60).

Shock wave attenuation consists of a formation decrement and a distance attenuation. Both of these are absent for weak shock waves when viscous effects are small.

Attempts have been made by several investigators to account for the shock wave attenuation on the basis of non-stationary, viscous, incompressible flow analysis or some adaptation of a stationary flow boundary layer theory. In either case the predicted attenuation is too large (for most shock tubes). The most promising result to have emerged from these treatments is the confirmation of the importance of the time parameter $(\frac{\gamma_2 t}{A})$. It is noted that when this parameter and γ_2 are large, the total shock wave attenuation is correspondingly high, and the converse is also true.

By assuming the existence of a boundary layer displacement thickness at the contact surface (δ^*) and combining this concept with the actual attenuation results, it has been possible to obtain a reasonable order of magnitude and rate of growth of this quantity. It is shown that in the Mach number range 1.3 to 1.5, behind the shock wave, $d\delta^*/dx \approx 0.0004$.

A linear empirical equation (5.09) is given that accounts quite well for the attenuation with the shock distance from the diaphragm (x) in the present tube. Since x was the only variable in $\frac{v_2 t}{A}$ or $\frac{v_2 x}{w_1 A}$ for this series of experiments, it was not possible to extend this relation so that it may be applicable to any shock tube. Nevertheless, it is shown that this equation gives good agreement for tubes of similar area in which $\frac{v_2 t}{A}$ is of the same order of magnitude.

To sum up, it may be stated that no adequate theory exists which will account for the observed total attenuation in shock tubes. Such a theory should take into account the phenomena that occur in real flows. That is, the boundary layer growth is a function of x for a given t , the shock attenuates concurrently with the contact front speed-up, and that viscous dissipation caused by the transverse shock waves is also present. A successful theory should consider at least the contact surface and shock wave phenomena simultaneously and not separately, as has been the case to-date.

Although the question of shock attenuation may appear as not too serious from an experimentalist's point of view, since a calibration curve or the actual wave speed may be used, the problem arises whether this procedure is valid. In other words, is there definite experimental evidence that shows that it is quite permissible to employ the wave speed in order to calculate the physical quantities of the flow in the "uniform" regions separated by the contact surface over a wide range of shock wave Mach numbers. The answer at the present time is in the negative, because most of the available data is based on Mach number measurement by means of wedges, and these can not be accepted as conclusive. A considerable amount of work must be done in order to measure directly the temperature, pressure, density and (velocity) in these two states before a decision can be reached on the relation between the derived and actual values of the physical quantities as a function of a known shock wave velocity.

The available experimental data also points to the fact that the flow regions separated by the contact layer are not uniform, especially for strong shock waves. This will have a very important effect on the use of the shock tube as an intermittent wind tunnel and other applications as well. Therefore the problem of flow uniformity still requires an experimental decision.

In addition, the question of the attainability of high Mach number in the cold state between the contact surface and the rarefaction wave has also to be settled experimentally.

No experimental results are available on the direct measurement of physical quantities in the uniform state behind a reflected rarefaction wave or shock wave over a wide range of diaphragm pressure ratios. The uniform state behind a reflected rarefaction wave offers some interesting work in low temperature physics. The regions behind strong incident and reflected shock waves have opened recently new fields for spectroscopic and magneto-hydrodynamic studies of the flows in a shock tube. It is possible that the shock tube will also be utilized for studies in atomic physics.

One-dimensional wave interactions, such as the collision of two shock waves and shock and rarefaction waves, shock wave refraction at a contact front and at a layer of gas, and preliminary work on the overtaking of two shock waves have been studied, and all have shown good agreement with the simple wave element theory. This is encouraging since it strengthens the assumption that it may be possible to test the theoretical analyses of wave interactions from the measurement of the relevant wave speeds.

Future work in the wave interaction tube on shock wave attenuation, the emergence of shock and rarefaction waves into the free air, the overtaking of two similarly facing shock waves, the interaction of a shock wave and a wire screen, and the study of shock waves produced by spherical diaphragms should prove of interest.

Although emphasis has been given to the one-dimensional work conducted on the wave interaction tube at the Institute of Aerophysics, two and three-dimensional problems have been studied successfully in shock tubes (see, for example, refs. 13, 17, 22, 46, 52 and 57). Yet, it is difficult to state that the shock tube has proven itself as a type of intermittent wind tunnel on the basis of the work that has been done to-date. Here, interferometric investigations certainly offer the best possibilities since the pressure and density fields may be determined over a model and the resultant forces computed. Other reliable rapid response instruments which may be used to measure the transient flow quantities such as pressure, temperature or forces directly have as yet not passed the developmental stage. The application of intermittent flow data to steady flow problems with heat transfer and boundary layers should be done with great caution anyway. Hence, the aerodynamic testing that may be done in a shock tube is rather limited at the present time.

What certainly may be said without qualifications, judging from the wide utilization of the shock tube for numerous basic researches, is that the shock tube has proven to be the "test tube" for the investigation of problems in non-stationary fluid mechanics.

REFERENCES

1. Vieille, P. Sur les discontinuités produites par la détente brusque de gaz comprimés. Comptes Rendus de L'Académie des Sciences 129, 1228 (1899).

2. Payman, W., Proceedings of the Royal Society A120 (1928), A132
Shepherd, W.F.C. (1931), A146 (1935), A158 (1937), A186 (1946).
and others

3. Reynolds, G. R. A Preliminary Study of Plane Shock Waves Formed by Bursting Diaphragms in a Tube.
O. S. R. D. No. 1519 (1943).

4. Smith, L. G. Photographic Investigation of the Reflection of Plane Shock Waves in Air. O.S.R.D. No. 6271 (1945).

5. Fletcher, J.C. Final Report on Shock Tube, Piezoelectric Gauges
Read, W.T., and Recording Apparatus.
Stoner, R. G. & O. S. R. D. No. 6321 (1946).
Weimer, D. K.

6. Geiger, F. W. The Shock Tube as an instrument for the Investigation
and of Transonic and Supersonic Flow Patterns.
Mautz, C. W. Engineering Research Institute, University of
Michigan (1949).

7. Lobb, R. K. A Study of Supersonic Flows in a Shock Tube.
Institute of Aerophysics, University of Toronto,
UTIA Report No. 8 (1950).

8. Glass, I. I. The Design of a Wave Interaction Tube. Institute
of Aerophysics, University of Toronto.
UTIA Report No. 6 (1950).

9. Duff, R. E. The Use of Real Gases in a Shock Tube. Engineering
Research Institute, University of Michigan 53-3 (1951).

10. Laponsky, A. B. Observation of Shock Formation and Growth.
Institute of Research, Lehigh University,
Technical Report No. 1 (1951).

11. Bitondo, D., One Dimensional Theory of Absorption and Amplifi-
Glass, I. I., cation of a Plane Shock Wave by a Gaseous Layer.
and Institute of Aerophysics, University of Toronto,
Patterson, G.N. UTIA Report No. 5 (1950).

12. Bitondo, D. Experiments on the Amplification of a Plane Shock
Wave. Institute of Aerophysics, University of
Toronto, UTIA Report No. 7 (1950).

13. Bull, G. V. Starting Process in an Intermittent Wind Tunnel.
Institute of Aerophysics, University of Toronto,
UTIA Report No. 12 (1951).

14. Glass, I. I. An Experimental Determination of the Speed of Sound in
Gases from the Head of a Rarefaction Wave.
Institute of Aerophysics, University of Toronto,
UTIA Report No. 9 (1951)

15. Nicholl, C. I. H. The Head-On Collision of Shock and Rarefaction
Waves. Institute of Aerophysics, University of
Toronto, UTIA Report No. 10 (1951).

16. Gould, D. G. The Head-On Collision of Two Shock Waves and a
Shock and Rarefaction Wave in One-dimensional
Flow. Institute of Aerophysics, University of
Toronto, UTIA Report No. 17 (1952).

17. Parks, E. K. Supersonic Flow in a Shock Tube of Divergent
Cross-Section. Institute of Aerophysics,
University of Toronto, UTIA Report No. 18 (1952).

18. Emrich, R.J. &
Harrison, F. B.
Emrich R.J. &
Curtis, C. W. Physical Review, Vol. 77, p. 573 (1950).

Physical Review, Vol. 73 (2), p. 1255 (1948).

19. Hertzberg, A.
 &
Kantrowitz, A. Studies with an Aerodynamically Instrumented
Shock Tube, Journal of Applied Physics,
Vol. 21, p. 874 (1950).

20. Huber, P. W.,
Fitton, C. W.
 and
Delpino, F. Experimental Investigation of Moving Pressure
Disturbances and Shock Waves and Correlation
with One-Dimensional Unsteady Flow Theory.
N.A.C.A. T.N. 1903 (1949).

21. Donaldson, C. du P.
 and
Sullivan, R.D. The Effect of Wall Friction on Strength of Shock
Waves in Tubes and Hydraulic Jumps in Channels.
N.A.C.A. T.N. 1942 (1949).

22. Griffith, W.C. Transonic Flow. Princeton University Technical
Report II-7 (1950). (see ref. 52).

23. Cowan, G. R.
 and
Hornig, D. F. The Experimental Determination of the Thickness
of a Shock Flow in a Gas. Jl. Chem. Phys.
Vol. 18, p. 1008 (1950).

24. **Greene, E. F.**
and
Hornig, D. F. The Shape and Thickness of Shock Fronts in Argon, Hydrogen, Nitrogen and Oxygen. JI. Chem. Phys. Vol. 21, p. 617 (1953).
25. **Bleakney, W.,**
White, D.R. &
Griffith, W. C. Measurements of Diffraction of Shock Waves and Resultant Loading of Structures. Journal Applied Mechanics. Vol. 17, p. 493 (1950).
26. **Perry, R.W. &**
Kantrowitz, A. The Production and Stability of Strong Shock Waves. Journal Applied Physics, Vol. 22, p. 878 (1951).
27. **Lundquist, G.A.** The N.O.L. 8 x 8 inch Shock Tube: Instrumentation and Operation. NAVORD Report No. 2449 (1952).
28. **Blondo, D. and**
Lobb, R. K. Design and Construction of a Shock Tube. Institute of Aerophysics, University of Toronto, UTIA Report No. 3 (1950).
29. **Resler, E. L.**
Lin, S. C. and
Kantrowitz, A. The Production of High Temperature Gases in Shock Tubes. Journal Applied Physics, Vol. 23, p. 1390 (1952).
30. **Courant, R. and**
Friedrichs, K.O. Supersonic Flow and Shock Waves. Interscience Publishers (1948).
31. **Kobes, K.** Die Durchschlagsgeschwindigkeit bei den Luftsaug- und Druckluft-bremsen Z. Öst. Ing.-u Arch. Ver. Vol. 62, p. 558 (1910).
32. **Schardin, H.** Bemerkungen zum Druckausgleichsvorgang in einer Rohrleitung. Phy. Zeits. Vol. 33, p. 60. (1932).
33. **Taub, A. H.** Interaction of Progressive Rarefaction Waves Annals of Math. Vol. 47, p. 811 (1946).
34. **Patterson, G.N.** Theory of the Shock Tube, N.O.L.M. 9903 (1948).
35. **Lobb, R. K.** On the Length of a Shock Tube. Institute of Aerophysics, University of Toronto, UTIA Report No. 4 (1950).
36. **Bethe, H. A.**
and
Teller, E. Deviations from Thermal Equilibrium in Shock Waves. Aberdeen Proving Grounds, B.R.L. Report No. X-117 (1945).
37. **Lukasiewicz, J.** Shock Tube Theory and Application. National Aeronautical Establishment Canada, Report No. 15.

38. Steketee, J. A. On the Interaction of Rarefaction Waves in a Shock Tube. Institute of Aerophysics, University of Toronto, UTIA Review No. 4 (1952).
39. Mandl, P. Transition Through a Weak Shock Front, Institute of Aerophysics, University of Toronto, UTIA Report No. 14 (1951).
40. Bull, G. V. The Interaction of Two Similarly Facing Shock Waves. Institute of Aerophysics, University of Toronto, UTIA Report No. 23 (1952).
- Fowell, L.R. and
 Henshaw, D. H.
41. Lampson, C. W. Resume of the Theory of Plane Shock and Adiabatic Waves with Applications to the Theory of the Shock Tube. Ballistic Research Lab. T.N. 139 (1950).
42. Elder, F. K. Experimental Study of the Formation of a
 and Vortex Ring at the Open End of a Cylindrical
 de Hass, N. Shock Tube. Journal Applied Physics, Vol. 23, p. 1065 (1952).
43. Resler, E. L., High Temperature Gases Produced by Strong Shock
 Jr. Waves. Ph.D. Thesis Cornell University (1951).
44. Lin, S. C. Electrical Conductivity of an Ionized Gas Produced by Strong Shock Wave. Ph.D. Thesis Cornell University (1952).
45. Mair, W. A. The Sensitivity and Range Required in a Toepler Schlieren Apparatus for Photography of High-Speed Air Flow. Aero. Quarterly, Vol. 4, p. 19 (1952).
46. Duff, R. E. The Interaction of Plane Shock Waves and Rough Surfaces. Journal Applied Physics, Vol. 23, p. 1373 (1952).
47. Fowler, R. G. Shock Waves in Low Pressure Spark Discharges. Phys. Rev., Vol. 88, p. 137 (1952).
 et al
48. Thibaud, J. Luminosité à la rencontre d'ondes de choc produites
 and par les charges creuses. Il Nuovo Cimento,
 Perrier, D. Vol. 8, p. 705 (1951).
49. Dosanjh, D. S. Study of Transient Hot-Wire Response in a Shock
 Kovasznay, L.S.G. Tube. Johns Hopkins University, Department of
 Clarken, P. C. Aeronautics, Report CM 725 (1952).

50. Pillow, A. F.
and
Levey, H. C. The Formation and Growth of Shock Waves in the
One-dimensional Motion of a Gas, CSIR Report
No. A 47 (Australia) (1947).
51. de Haller, P. On a Graphical Method of Gas Dynamics. *Technique
Rundschau Sulzer* No. 1, p. 6-24 (1945).
RTP Translation No. 2555.
52. Griffith, W. Shock Tube Studies of Transonic Flow Over Wedge
Profiles. *Journal of the Aeronautical Sciences*,
Vol. 19, p. 249 (1952).
53. Uhlenbeck, G.
(submitted by) Diffraction of Shock Waves Around Various Obstacles.
Engineering Research Institute, University of
Michigan, Project M720-4 (1950).
54. Taylor, G. I.
and
Lewis, D. J. The Instability of Liquid Surfaces When Accele-
rated in a Direction Perpendicular to their Planes.
Proceedings of the Royal Society (London)
Part 1, A201 (1950) Part 2, A202 (1950).
55. Pankhurst, R.C.
Holder, D. W. Wind Tunnel Technique,
Pitman and Son, London, (1952).
56. Emrich, R. J. &
Curtis, C. W. Attenuation in the Shock Tube, *Journal Applied
Physics* Vol. 24, p. 360. (1953).
57. Bingham, H.H.,
Weimer, D. K.,
Griffith, W. The Cylinder and Semicylinder in Subsonic Flow.
Princeton University Tech. Report II-13 (1952).
58. Huber, P.W.,
McFarland, D.R.,
Levine, P. Investigation of the Attenuation of Plane Shock
Waves Moving Over Very Rough Surfaces.
N.A.C.A. R.M. SL53D13a (1953).
59. Churchill, R.V. Fourier Series and Boundary Value Problems.
McGraw-Hill, New York (1941).
60. Illingworth, C.R. Unsteady Laminar Flow of a Gas Near an Infinite
Flat Plate. *Cambridge Phil. Soc. Proc.* 46,
p. 603 (1950).
61. Stewartson, K. On the Impulsive Motion of a Flat Plate in a Viscous
Fluid. *Quart. Jl. of Mech. and App. Math.*
Vol. 4, p. 182 (1951).
62. Howarth, L. Some Aspects of Rayleigh's Problem for a Com-
pressible Fluid, *Quart. J. of Mech. and App.
Math.*, Vol. 4, p. 155 (1951).

- 63. Lobb, R. K. Growth of a Laminar Boundary Layer Behind a Shock Wave. Physical Review, Vol. 84, p. 612 (1951).
- 64. Hoover, H. L. Measurement by Timed Spark Shadowgraphs of Shock Velocities in the Shock Tube. Lehigh University, Institute of Research, Tech. Rep. No. 3 (1953).
- 65. Goldstein, S. Modern Developments in Fluid Dynamics. Vol. 1, p. 181-186, Oxford (1938).
- 66. Ruptash, J. Boundary Layer Measurements in the UTIA 5 inch x 7 inch Supersonic Wind Tunnel. Institute of Aerophysics, University of Toronto, UTIA Report No. 16 (1952).
- 67. Goldbaum, G. C. Comparison of Theoretical and Experimental Performance of a Variable Geometry Diffuser at $M = 5.0$. University of Texas, Report DRL-331 (1953).
- 68. Hall, J. G. The Transition Through a Contact Region. Institute of Aerophysics, University of Toronto, UTIA Report No. 26 (1953 - to be published).
- 69. Heybe, W. H. & Condensation Shocks, Weak Detonations and Reed, S. G. Related Phenomena. Navord Report 2779 (1953).
- 70. Keuthe, A. M. & Foundations of Aerodynamics. Schetzer, J. D. John Wiley and Sons (1950).
- 71. Patterson, G. N. An Introduction to the General Equations of Fluid Dynamics. Institute of Aerophysics, University of Toronto, UTIA Review No. 3 (1950).
- 72. Miller, K. S. Partial Differential Equations in Engineering Problems. pp. 130 and 161, Prentice-Hall Inc. (1953).
- 73. Ford, C. A. and An Experimental Study of Shock Wave Refraction Glass, I. I. -- to be published as a UTIA Report.

APPENDIX A

TABLES FOR FIGURES CONTAINED IN
SECTIONS I AND II

The tables in this appendix contain the necessary information to plot certain figures in section I and II. The particular figures involved are indicated on each table. All the values tabulated have been computed to four significant figures.

The following values are of interest and are presented here for reference purposes.

In the case of Air|Air when $M_2 = 1.00$:

$$W_{11} = 2.07 \quad P_{21} = 4.82 \quad P_{41} = 42.0$$

and when $M_3 = 1.00$:

$$W_{11} = 1.63 \quad P_{21} = 2.90 \quad P_{41} = 10.5$$

For the case of He|Air when $M_2 = 1.00$:

$$W_{11} = 2.07 \quad P_{21} = 4.82 \quad P_{41} = 10.1$$

and similarly for $M_3 = 1.00$:

$$W_{11} = 2.97 \quad P_{21} = 10.2 \quad P_{41} = 42.5$$

TABLE 10 (Fig. 17)

$$P_{14} = \frac{1}{P_{21}} \left[1 - (P_{21} - 1) \sqrt{\frac{\beta_4 E_{14}}{\alpha_1 P_{21} + 1}} \right] \frac{1}{\theta_4}$$

Case: Air | Air

1	2	3	4	5	6	7	8	9	10	11
P_{21}	P_{12}	P_{21}	$\alpha_1 P_{21} + 1$	$\beta_4 E_{14} / 4$	$\sqrt{5}$	3×6	$1 - 7$	$8/4$	$P_{14} = 2 \times 9$	P_{41}
1	1.000	0	6.95	.02072	.1439	.0000	1.000	1.000	1.000	1.000
2	.5000	1	12.90	.01116	.1056	.1056	.8944	.4607	.2304	4.340
3	.3333	2	18.85	.007639	.08740	.1748	.8252	.2634	.08779	11.39
4	.2500	3	24.80	.005806	.07620	.2286	.7714	.1648	.04120	24.27
5	.2000	4	30.75	.004682	.06843	.2737	.7263	.1085	.02170	46.08
6	.1667	5	36.70	.003923	.06263	.3132	.6868	.07360	.01227	81.50
7	.1429	6	42.65	.003376	.05810	.3486	.6514	.05097	.007284	137.3
8	.1250	7	48.60	.002962	.05442	.3809	.6191	.03581	.004476	223.4
9	.1111	8	54.55	.002640	.05138	.4110	.5890	.02543	.002825	354.0
10	.1000	9	60.50	.002380	.04879	.4391	.5609	.01804	.001804	554.3
11	.09091	10	66.45	.002167	.04655	.4655	.5345	.01291	.001174	851.8
12	.08333	11	72.40	.001989	.04459	.4905	.5095	.009256	.0007713	1297
13	.07692	12	78.35	.001837	.04286	.5143	.4857	.006640	.0005107	1958
14	.07143	13	84.30	.001708	.04133	.5373	.4627	.004740	.0003386	2953

TABLE 10 (CONTINUED)

1	2	3	4	5	6	7	8	9	10	11
P_{21}	P_{12}	P_{21}^{-1}	$\alpha_1 P_{21} + 1$	$84E_{14}/(4)$	$\sqrt{5}$	$(3) \times (6)$	$1 - (7)$	$(8)^{1/4}$	$P_{14} = (2) \times (9)$	P_{41}
15	.06667	14	90.25	.001595	.03994	.5592	.4408	3.385×10^{-3}	2.257×10^{-4}	4.431×10^3
16	.06250	15	96.20	.001496	.03868	.5802	.4198	2.412×10^{-3}	1.508×10^{-4}	6.631×10^3
17	.05882	16	102.2	.001409	.03754	.6006	.3994	1.707×10^{-3}	1.004×10^{-4}	9.960×10^3
18	.05556	17	108.1	.001332	.03650	.6205	.3795	1.197×10^{-3}	6.645×10^{-5}	1.505×10^4
19	.05263	18	114.1	.001262	.03552	.6394	.3606	8.393×10^{-4}	4.417×10^{-5}	2.264×10^4
20	.05000	19	120.0	.001200	.03464	.6582	.3418	5.787×10^{-4}	2.894×10^{-5}	3.455×10^4
21	.04762	20	126.0	.001143	.03381	.6762	.3238	3.975×10^{-4}	1.893×10^{-5}	5.283×10^4
23	.04347	22	137.9	.001045	.03232	.7110	.2890	1.739×10^{-4}	7.557×10^{-6}	1.323×10^5
25	.04000	24	149.8	.0009616	.03101	.7442	.2558	7.735×10^{-5}	3.094×10^{-6}	3.232×10^5
27	.03703	26	161.7	.0008908	.02953	.7678	.2322	3.938×10^{-5}	1.458×10^{-6}	6.859×10^5
29	.03448	28	173.6	.0008297	.02880	.8064	.1936	1.118×10^{-5}	3.855×10^{-7}	2.594×10^6
31	.03225	30	185.5	.0007765	.02787	.8361	.1639	3.516×10^{-6}	1.134×10^{-7}	3.818×10^6
33	.03030	32	197.4	.0007297	.02701	.8643	.1357	9.475×10^{-7}	2.871×10^{-8}	2.483×10^7
35	.02857	34	209.3	.0006882	.02623	.8918	.1082	1.966×10^{-7}	5.617×10^{-9}	1.780×10^8
37	.02702	36	221.2	.0006511	.02552	.9187	.0813	2.702×10^{-8}	7.301×10^{-10}	1.370×10^9
39	.02564	38	233.1	.0006179	.02486	.9447	.0553	1.860×10^{-9}	4.769×10^{-11}	2.097×10^{10}
41	.02439	40	250.0	.0005879	.02425	.9700	.0300	2.661×10^{-11}	6.490×10^{-13}	1.541×10^{12}
43	.02325	42	256.9	.0005606	.02368	.9946	.0054	1.794×10^{-15}	4.171×10^{-17}	2.398×10^{16}

TABLE 11 (Fig. 18)

$$P_{14} = \frac{1}{P_{21}} \left[1 - (P_{21} - 1) \sqrt{\frac{\beta_4 E_{14}}{\alpha_1 P_{21} + 1}} \right]^{\frac{1}{\beta_4}} \quad \text{Case: He|Air}$$

(1)	(2)	(3)	(4)	(5)	(6)	(7)
P_{21}	$P_{21} - 1$	$\alpha_1 P_{21} + 1$	$\sqrt{(3)}$	$1 - (2) \sqrt{(4) E_{14}} / (5)$	$(6)^{1/4}$	$P_{14} = \frac{(7)}{(6)}$
1	0	6.95	2.639	1	1	1
2	1	12.90	3.596	.9406	.7360	2.717
3	2	18.85	4.347	.9018	.5957	5.036
4	3	24.80	4.986	.8715	.5024	7.962
5	4	30.75	5.552	.8461	.4332	11.54
6	5	36.70	6.065	.8240	.3794	15.82
7	6	42.65	6.538	.8041	.3356	20.86
8	7	48.60	6.979	.7858	.2992	26.74
9	8	54.55	7.394	.7690	.2685	33.52
10	9	60.50	7.787	.7532	.2420	41.32
11	10	66.45	8.161	.7384	.2191	50.21
12	11	72.40	8.519	.7243	.1990	60.31
13	12	78.35	8.862	.7109	.1811	71.77
14	13	84.30	9.192	.6980	.1653	84.67
15	14	90.25	9.511	.6857	.1513	99.15
16	15	96.20	9.820	.6738	.1386	115.4
17	16	102.2	10.12	.6624	.1272	133.7
18	17	108.1	10.41	.6513	.1169	154.0
19	18	114.1	10.69	.6405	.1075	176.7
20	19	120.0	10.97	.6301	.09901	202.0
21	20	126.0	11.24	.6199	.09129	230.0
22	21	132.2	11.50	.6100	.08421	261.3
23	22	138.2	11.75	.6004	.07774	295.8
24	23	144.1	12.01	.5909	.07182	334.2
25	24	150.1	12.25	.5817	.06623	377.4

TABLE 11 (CONTINUED)

(1)	(2)	(3)	(4)	(5)	(6)	(7)
P_{21}	$P_{21}-1$	$\alpha_1 P_{21} + 1$	$\sqrt{(3)}$	$\frac{1 - (2)\sqrt{(3)}(4)}{(4)}$	$(5) k_4$	$P_{41} = \frac{(1)}{(6)}$
26	25	156.1	12.49	.5727	.06139	423.5
27	26	162.0	12.73	.5639	.05680	475.4
28	27	168.0	12.96	.5552	.05255	532.8
29	28	174.0	13.19	.5467	.04865	596.1
30	29	179.9	13.42	.5384	.04504	666.0
31	30	185.9	13.63	.5300	.04166	744.1
32	31	191.4	13.83	.5214	.03853	830.5
33	32	197.8	14.06	.5133	.03563	926.2
35	34	209.3	14.47	.4983	.03059	1144
37	36	221.2	14.87	.4830	.02617	1414
39	38	233.1	15.27	.4686	.02249	1734
41	40	244.0	15.62	.4532	.01902	2156
43	42	256.9	16.03	.4405	.01650	2606
45	44	268.8	16.40	.4271	.01414	3182
47	46	280.7	16.75	.4136	.01204	3904
49	48	292.6	17.11	.4010	.01031	4753
51	50	304.5	17.45	.3882	.008764	5819
53	52	316.4	17.79	.3759	.007459	7105
55	54	328.3	18.12	.3637	.006311	8715
57	56	340.2	18.44	.3515	.005331	10690

TABLE 12 (Fig. 19) Case: Air

$$W_{11} = [\beta_1 (\alpha_1 P_{21} + 1)]^{\frac{1}{2}} \quad U_{21} = \frac{P_{21} - 1}{\chi [\beta_1 (\alpha_1 P_{21} + 1)]^{\frac{1}{2}}} \quad C_{34} = \frac{1}{\beta_4 \chi_4} [1 - (P_{14} P_{21})^{\beta_4}] - [P_{14} P_{21}]^{\beta_4}$$

1	2	3	4	5	6	7	8	9	10	11	12	13
P_{21}	$P_{21} - 1$	$\alpha_1 P_{21} - 1$	β_1 ③	$W_{11} = \sqrt{4}$	χ_1 ⑤	$U_{21} = \frac{P_{21} - 1}{\chi [\beta_1 (\alpha_1 P_{21} + 1)]^{\frac{1}{2}}}$	P_{14}	$P_{14} P_{21}$	$\odot \beta_4$	$1 - \textcircled{10}$	$\frac{1 - \textcircled{11}}{\beta_4 \chi_4}$	$C_{34} = \frac{1}{\beta_4 \chi_4} [1 - (P_{14} P_{21})^{\beta_4}] - [P_{14} P_{21}]^{\beta_4}$
1	0	6.95	1.001	1.000	1.404	.0000	1.000	1.000	1.000	.0000	.0000	-1.000
2	1	12.90	1.858	1.363	1.914	.5225	.2304	.4608	.8945	.1055	.5222	-.3723
3	2	18.85	2.714	1.647	2.312	.8651	.08779	.2634	.8253	.1747	.8648	+.03950
4	3	24.80	3.571	1.890	2.654	1.130	.04120	.1648	.7713	.2287	1.132	.3607
5	4	30.75	4.428	2.104	2.954	1.354	.02170	.1085	.7263	.2737	1.355	.6287
6	5	36.70	5.285	2.299	3.228	1.549	.01227	.07362	.6869	.3131	1.550	.8631
7	6	42.65	6.142	2.478	3.479	1.725	.007284	.05099	.6515	.3485	1.725	1.074
8	7	48.60	6.994	2.645	3.714	1.885	.004476	.03581	.6193	.3807	1.884	1.265
9	8	54.55	7.855	2.803	3.935	2.033	.002825	.02543	.5894	.4106	2.032	1.443
10	9	60.50	8.712	2.952	4.145	2.171	.001804	.01804	.5609	.4391	2.174	1.609
11	10	66.45	9.569	3.093	4.343	2.303	.001174	.01291	.5346	.4654	2.304	1.769
12	11	72.40	10.43	3.230	4.535	2.426	.0007713	.009256	.5095	.4905	2.428	1.919
13	12	78.35	11.28	3.358	4.715	2.545	.0005107	.006640	.4857	.5143	2.546	2.060
14	13	84.30	12.14	3.484	4.892	2.657	.0003386	.004740	.4627	.5373	2.660	2.197

TABLE 12 (CONTINUED)

1	2	3	4	5	6	7	8	9	10	11	12	13
P_{21}	$P_{21}-1$	$\alpha_{1/21}+1$	β_1 ③	$W_{11}=\sqrt{4}$ ④	γ_1 ⑤	$U_{21}=\frac{⑤}{⑥}$	P_{14}	$P_{14} P_{21}$	⑨ β_4	$1-\frac{⑩}{⑪}$	$\frac{1}{\beta_4}$ ⑪	$C_{34}=\frac{⑫}{⑬}-\frac{⑩}{⑪}$
15	14	90.25	13.00	3.606	5.063	2.765	2.257×10^{-4}	3.386×10^{-3}	.4408	.5592	2.768	2.320
16	15	96.20	13.85	3.722	5.226	2.870	1.508×10^{-4}	2.413×10^{-3}	.4199	.5801	2.871	2.451
17	16	102.2	14.72	3.837	5.387	2.970	1.004×10^{-4}	1.707×10^{-3}	.3994	.6006	2.973	2.574
18	17	108.1	15.57	3.946	5.540	3.069	6.645×10^{-5}	1.196×10^{-3}	.3795	.6205	3.071	2.692
19	18	114.1	16.43	4.053	5.690	3.163	4.417×10^{-5}	8.392×10^{-4}	.3606	.6394	3.165	2.804
20	19	120.0	17.28	4.157	5.836	3.256	2.894×10^{-5}	5.788×10^{-4}	.3418	.6582	3.258	2.916
21	20	126.0	18.14	4.259	5.980	3.344	1.893×10^{-5}	3.975×10^{-4}	.3238	.6762	3.347	3.023
22	21	132.0	19.00	4.355	6.125	3.432	1.118×10^{-5}	1.738×10^{-4}	.2875	.7125	3.525	3.237
23	22	137.9	19.85	4.455	6.255	3.517	7.557×10^{-6}	1.735×10^{-5}	.2558	.7442	3.682	3.426
24	23	143.8	20.70	4.550	6.380	3.601	5.094×10^{-6}	7.735×10^{-5}	.2321	.7679	3.799	3.566
25	24	149.7	21.55	4.644	6.500	3.681	3.458×10^{-6}	3.937×10^{-5}	.1936	.8064	3.990	3.796
26	25	155.6	22.40	4.738	6.615	3.761	2.355×10^{-6}	1.118×10^{-5}	.1639	.8361	4.137	3.973
27	26	161.5	23.25	4.832	6.725	3.841	1.534×10^{-7}	3.515×10^{-6}	.1357	.8643	4.276	4.140
28	27	167.4	24.10	4.926	6.830	3.921	1.017×10^{-8}	9.474×10^{-7}	.1082	.8918	4.412	4.304
29	28	173.3	24.95	5.019	6.935	4.001	6.617×10^{-9}	1.966×10^{-7}	.08131	.9187	4.545	4.464
30	29	179.2	25.80	5.113	7.040	4.081	4.301×10^{-10}	2.701×10^{-8}	.05531	.9447	4.674	4.619
31	30	185.1	26.65	5.206	7.145	4.161	2.869×10^{-11}	1.860×10^{-9}	.03001	.9700	4.799	4.769
32	31	191.0	27.50	5.300	7.250	4.241	1.900×10^{-12}	2.661×10^{-11}	.007526	.9925	4.911	4.903
33	32	196.9	28.35	5.394	7.355	4.321	1.271×10^{-13}	1.794×10^{-15}				
34	33	202.8	29.20	5.488	7.460	4.401						
35	34	208.7	30.05	5.582	7.565	4.481						
36	35	214.6	30.90	5.676	7.670	4.561						
37	36	220.5	31.75	5.770	7.775	4.641						
38	37	226.4	32.60	5.864	7.880	4.721						
39	38	232.3	33.45	5.958	7.985	4.801						
40	39	238.2	34.30	6.052	8.090	4.881						
41	40	244.1	35.15	6.146	8.195	4.961						
42	41	250.0	36.00	6.240	8.300	5.041						
43	42	255.9	36.85	6.334	8.405	5.121						

TABLE 13 (Figs. 21 & 22) Case: Air | Air

$$A_{21} = (T_{21})^{\frac{1}{2}} = \left[\frac{P_{21}(\alpha_1 + P_{21})}{1 + \alpha_1 P_{21}} \right]^{\frac{1}{2}}$$

$$\Gamma_{21} = \frac{1 + \alpha_1 P_{21}}{\alpha_1 + P_{21}}$$

$$M_2 = \frac{(P_{21} - 1)}{\alpha_1 [P_{21}(\alpha_1 + P_{21})]^{\frac{1}{2}}}$$

$$A_{34} = (T_{34})^{\frac{1}{2}} = [P_{14} P_{21}]^{\frac{1}{2}} \theta_4$$

$$\Gamma_{34} = [P_{14} P_{21}]^{\frac{1}{2}} \theta_4$$

$$M_3 = \frac{1}{\theta_4} [(P_{14} P_{21})^{-\theta_4} - 1]$$

(1)	(2)	(3)	(4)	(5)	(6)	(7)	(8)	(9)	(10)	(11)
P_{21}	$P_{21} - 1$	P_{14}	P_{41}	$P_{14} P_{21}$	$A_{34} = \textcircled{5}$	$T_{34} = \textcircled{6}$	$1 + \alpha_1 P_{21}$	$\alpha_1 + P_{21}$	$P_{21} \times \textcircled{9}$	$T_{21} = \frac{\textcircled{10}}{\textcircled{8}}$
1	0	1.000	1.000	1.000	1.000	1.000	6.95	6.95	6.95	1.000
2	1	.2304	4.340	.4608	.8945	.8001	12.90	7.95	15.90	1.233
3	2	.08779	11.39	.2634	.8253	.6811	18.85	8.95	26.85	1.424
4	3	.04120	24.27	.1648	.7713	.5949	24.80	9.95	39.90	1.609
5	4	.02170	46.08	.1085	.7263	.5275	30.75	10.95	54.75	1.780
6	5	.01227	81.50	.07362	.6869	.4718	36.70	11.95	71.80	1.956
7	6	.007284	137.3	.05099	.6515	.4245	42.65	12.95	90.65	2.125
8	7	.004476	223.4	.03581	.6193	.3835	48.60	13.95	111.6	2.296
9	8	.002825	354.0	.02543	.5894	.3474	54.55	14.95	134.6	2.467
10	9	.001804	554.3	.01804	.5609	.3146	60.50	15.95	159.5	2.636
11	10	.001174	851.8	.01291	.5346	.2858	66.45	16.95	186.5	2.807
12	11	.0007713	1297	.009256	.5095	.2596	72.40	17.95	215.4	2.975
13	12	.0005107	1958	.006640	.4857	.2359	78.35	18.95	246.4	3.145
14	13	.0003386	2953	.004740	.4627	.2141	84.30	19.95	279.3	3.313

TABLE 13 (CONTINUED)

(1)	(2)	(3)	(4)	(5)	(6)	(7)	(8)	(9)	(10)	(11)
P_{21}	$P_{21}-1$	P_{14}	P_{41}	$P_{14} P_{21}$	$A_{34} = \frac{A_4}{A_3}$	$T_{34} = \frac{T_4}{T_3}$	$1 + \alpha_1 P_{21}$	$\alpha_1 + P_{21}$	$P_{21} \times \frac{A_4}{A_3}$	$T_{21} = \frac{T_2}{T_1}$
15	14	2.257×10^{-4}	4.431×10^3	3.386×10^{-3}	.4408	.1943	90.25	20.95	314.5	3.485
16	15	1.508×10^{-4}	6.631×10^3	2.413×10^{-3}	.4199	.1763	96.20	21.95	351.2	3.651
17	16	1.004×10^{-4}	9.960×10^3	1.707×10^{-3}	.3994	.1595	102.2	22.95	390.2	3.818
18	17	6.645×10^{-5}	1.505×10^4	1.196×10^{-3}	.3795	.1440	108.1	23.95	431.1	3.988
19	18	4.417×10^{-5}	2.264×10^4	8.392×10^{-4}	.3606	.1330	114.1	24.95	474.1	4.155
20	19	2.894×10^{-5}	3.455×10^4	5.788×10^{-4}	.3418	.1168	120.0	25.95	519.0	4.325
21	20	1.893×10^{-5}	5.283×10^4	3.975×10^{-4}	.3238	.1048	126.0	26.95	566.0	4.492
22	22	7.557×10^{-6}	1.323×10^5	1.738×10^{-4}	.2875	.08266	137.9	28.95	665.9	4.831
23	22	7.557×10^{-6}	1.323×10^5	1.738×10^{-4}	.2875	.08266	137.9	28.95	665.9	4.831
24	24	3.094×10^{-6}	3.232×10^5	7.735×10^{-5}	.2558	.06543	149.8	30.95	773.8	5.167
25	24	3.094×10^{-6}	3.232×10^5	7.735×10^{-5}	.2558	.06543	149.8	30.95	773.8	5.167
26	26	1.458×10^{-6}	6.859×10^5	3.937×10^{-5}	.2321	.05387	161.7	32.95	889.7	5.504
27	26	1.458×10^{-6}	6.859×10^5	3.937×10^{-5}	.2321	.05387	161.7	32.95	889.7	5.504
28	28	3.855×10^{-7}	2.594×10^6	1.118×10^{-5}	.1936	.03748	173.6	34.95	1014	5.840
29	28	3.855×10^{-7}	2.594×10^6	1.118×10^{-5}	.1936	.03748	173.6	34.95	1014	5.840
30	30	1.134×10^{-7}	8.818×10^6	3.515×10^{-6}	.1639	.02686	185.5	36.95	1146	6.177
31	30	1.134×10^{-7}	8.818×10^6	3.515×10^{-6}	.1639	.02686	185.5	36.95	1146	6.177
32	32	2.871×10^{-8}	2.483×10^7	9.474×10^{-7}	.1357	.01841	197.4	38.95	1285	6.513
33	32	2.871×10^{-8}	2.483×10^7	9.474×10^{-7}	.1357	.01841	197.4	38.95	1285	6.513
34	34	5.617×10^{-9}	1.780×10^8	1.966×10^{-7}	.1082	.01171	209.3	40.95	1433	6.850
35	34	5.617×10^{-9}	1.780×10^8	1.966×10^{-7}	.1082	.01171	209.3	40.95	1433	6.850
36	36	7.301×10^{-10}	1.370×10^9	2.701×10^{-8}	.08131	.006611	221.2	42.95	1589	7.186
37	36	7.301×10^{-10}	1.370×10^9	2.701×10^{-8}	.08131	.006611	221.2	42.95	1589	7.186
38	38	4.769×10^{-11}	2.097×10^{10}	1.860×10^{-9}	.05531	.003059	233.1	44.95	1753	7.522
39	38	4.769×10^{-11}	2.097×10^{10}	1.860×10^{-9}	.05531	.003059	233.1	44.95	1753	7.522
40	40	6.490×10^{-13}	1.541×10^{12}	2.661×10^{-11}	.03001	.0009006	245.0	46.95	1925	7.859
41	40	6.490×10^{-13}	1.541×10^{12}	2.661×10^{-11}	.03001	.0009006	245.0	46.95	1925	7.859
42	42	4.171×10^{-17}	2.398×10^{16}	1.794×10^{-15}	.007526	.0005664	256.9	48.95	2105	8.195
43	42	4.171×10^{-17}	2.398×10^{16}	1.794×10^{-15}	.007526	.0005664	256.9	48.95	2105	8.195

TABLE 13 (CONTINUED)

(1)	(12)	(13)	(14)	(15)	(16)	(17)	(18)	(19)	(20)	(21)
P_{21}	$A_{21} = \sqrt{(11)}$	$\beta_1 \times (10)$	$\sqrt{(13)}$	$\chi_1 \times (14)$	$M_2 = \frac{(2)}{(5)}$	$\Gamma_{21} = \frac{(8)}{(9)}$	1.6	$(18) - 1$	$M_3 = \frac{(2)}{(4)(5)}$	$\Gamma_{34} = \frac{(5)}{(4)}$
1	1.000	1.000	1.000	1.404	0	1.000	1.000	0	0	1.000
2	1.110	2.290	1.513	2.124	0.4708	1.623	1.118	0.118	0.5831	0.5755
3	1.193	3.887	1.976	2.774	0.7209	2.106	1.212	0.212	1.047	0.3867
4	1.268	5.746	2.397	3.365	0.8915	2.493	1.297	0.297	1.467	0.2769
5	1.334	7.884	2.808	3.942	1.015	2.808	1.377	0.377	1.864	0.2056
6	1.399	10.34	3.215	4.514	1.108	3.071	1.456	0.456	2.254	0.1560
7	1.458	13.05	3.613	5.073	1.183	3.293	1.535	0.535	2.646	0.1201
8	1.515	16.07	4.009	5.628	1.244	3.484	1.615	0.615	3.040	0.09333
9	1.571	19.38	4.403	6.181	1.294	3.649	1.697	0.697	3.445	0.07315
10	1.624	22.97	4.792	6.729	1.338	3.793	1.783	0.783	3.872	0.05728
11	1.675	26.86	5.182	7.276	1.374	3.920	1.871	0.871	4.306	0.04514
12	1.725	31.02	5.569	7.819	1.407	4.033	1.963	0.963	4.762	0.03558
13	1.773	35.48	5.957	8.363	1.435	4.135	2.059	1.059	5.237	0.02811
14	1.820	40.22	6.342	8.904	1.460	4.226	2.161	1.161	5.743	0.02211

TABLE 13 (CONTINUED)

(1)	(12)	(13)	(14)	(15)	(16)	(17)	(18)	(19)	(20)	(21)
P_{21}	$A_{21} = \sqrt{10}$	$\beta_1 \times 10$	$\sqrt{13}$	$\gamma_1 \times 14$	$M_2 = \frac{2}{15}$	$\Gamma_{21} = \frac{8}{9}$	$1/6$	$18 - 1$	$M_3 = \frac{9}{2.24}$	$\Gamma_{34} = 5 \frac{1}{4}$
15	1.867	45.29	6.730	9.448	1.482	4.308	2.269	1.269	6.275	1.740×10^{-2}
16	1.911	50.57	7.112	9.985	1.502	4.383	2.382	1.382	6.833	1.367×10^{-2}
17	1.954	56.19	7.496	10.52	1.520	4.453	2.504	1.504	7.437	1.068×10^{-2}
18	1.997	62.08	7.879	11.06	1.537	4.514	2.635	1.635	8.087	8.291×10^{-3}
19	2.038	68.27	8.263	11.60	1.552	4.573	2.773	1.773	8.770	6.442×10^{-3}
20	2.080	74.74	8.645	12.14	1.566	4.624	2.926	1.926	9.524	4.944×10^{-3}
21	2.119	81.50	9.028	12.68	1.578	4.675	3.088	2.088	10.33	3.783×10^{-3}
23	2.198	95.89	9.792	13.75	1.600	4.762	3.478	2.478	12.26	2.098×10^{-3}
25	2.273	111.4	10.56	14.82	1.619	4.838	3.909	2.909	14.39	1.180×10^{-3}
27	2.346	128.1	11.32	15.89	1.636	4.906	4.308	3.308	16.36	7.291×10^{-4}
29	2.417	146.0	12.08	16.96	1.651	4.966	5.165	4.165	20.60	2.974×10^{-4}
31	2.485	165.0	12.84	18.03	1.664	5.019	6.101	5.101	25.23	1.305×10^{-4}
33	2.552	185.1	13.61	19.10	1.675	5.067	7.369	6.369	31.50	5.126×10^{-5}
35	2.617	206.4	14.37	20.17	1.686	5.110	9.242	8.242	40.77	1.673×10^{-5}
37	2.681	228.8	15.13	21.24	1.695	5.149	12.30	11.30	55.88	4.067×10^{-6}
39	2.743	252.5	15.89	22.31	1.703	5.185	18.08	17.08	84.47	6.049×10^{-7}
41	2.803	277.2	16.65	23.38	1.711	5.217	33.32	32.32	159.9	2.938×10^{-8}
43	2.863	303.1	17.41	24.44	1.718	5.247	132.9	131.9	652.2	3.141×10^{-11}

TABLE 14

(FIGURES 23 & 24)

Case: He|Air

$$M_3 = \frac{1}{\beta_4 \gamma_4} [(P_{14} P_{21})^{-\beta_4} - 1] \quad \Gamma_{34} = [P_{14} P_{21}]^{\frac{1}{\gamma_4}} \quad A_{34} = T_{34} = [P_{14} P_{21}]^{\beta_4}$$

(1)	(2)	(3)	(4)	(5)	(6)	(7)
P_{21}	$P_{14} P_{21}$	$\textcircled{2}^{-\beta_4} - 1$	$\frac{1}{\beta_4 \gamma_4} [\textcircled{3}]$	$\Gamma_{34} = \textcircled{2}^{\frac{1}{\gamma_4}}$	$A_{34} = \textcircled{2}^{\beta_4}$	$T_{34} = \textcircled{6}^2$
1	1	0	0	1	1	1
2	.7360	.05707	.1716	.8320	.9406	.8848
3	.5957	.1090	.3277	.7328	.9018	.8132
4	.5024	.1474	.4434	.6614	.8715	.7595
5	.4332	.1818	.5468	.6052	.8461	.7160
6	.3794	.2136	.6425	.5588	.8240	.6789
7	.3356	.2437	.7329	.5191	.8041	.6465
8	.2992	.2725	.8196	.4846	.7858	.6175
9	.2685	.3004	.9035	.4540	.7690	.5913
10	.2420	.3276	.9854	.4266	.7532	.5673
11	.2191	.3544	1.066	.4018	.7384	.5452
12	.1990	.3807	1.145	.3792	.7243	.5246
13	.1811	.4068	1.223	.3585	.7109	.5053
14	.1653	.4326	1.301	.3394	.6980	.4872
15	.1513	.4584	1.379	.3217	.6857	.4702

TABLE 14 (CONTINUED)

(1)	(2)	(3)	(4)	(5)	(6)	(7)
P_{21}	$P_{14} P_{21}$	$2^{-\theta_4} - 1$	$\frac{1}{\beta_4 \gamma_4} [\textcircled{3}]$	$\sqrt[3]{34} = 2^{\frac{1}{24}}$	$A_{34} = 2^{\theta_4}$	$T_{34} = \textcircled{6}^2$
16	.1386	.4841	1.456	.3058	.6738	.4540
17	.1272	.5098	1.533	.2899	.6624	.4387
18	.1169	.5355	1.610	.2755	.6513	.4242
19	.1075	.5612	1.688	.2621	.6405	.4103
20	.09901	.5871	1.766	.2494	.6301	.3970
21	.09129	.6131	1.844	.2375	.6199	.3843
22	.08421	.6393	1.923	.2263	.6100	.3721
23	.07775	.6657	2.002	.2157	.6004	.3604
24	.07182	.6923	2.082	.2057	.5909	.3492
25	.06623	.7191	2.163	.1962	.5817	.3384
26	.06139	.7462	2.244	.1873	.5727	.3280
27	.05680	.7735	2.326	.1787	.5639	.3179
28	.05255	.8012	2.410	.1705	.5552	.3082
29	.04865	.8292	2.494	.1628	.5467	.2989
30	.04504	.8575	2.579	.1554	.5384	.2898

TABLE 15 (Fig. 36) Case: Air | Air

$$P_{52} = \frac{P_{21}(\alpha_1+2)-1}{\alpha_1+P_{21}} \quad \Gamma_{52} = \frac{1+\alpha_1 P_{32}}{\alpha_1+P_{52}} \quad T_{52} = \left[\frac{P_{52}(\alpha_1+P_{52})}{1+\alpha_1 P_{52}} \right] \quad W_{21} = W_{11} \left[\frac{P_{21}(\gamma_1-1)+1}{\gamma_1 \theta_1 (\alpha_1 P_{21}+1)} \right]$$

(1)	(2)	(3)	(4)	(5)	(6)	(7)	(8)	(9)	(10)	(11)	(12)	(13)
W_{11}	P_{21}	α_1+P_{21}	P_{32}	$P_{21}(\gamma_1-1)+1$	$\alpha_1 P_{21}+1$	$\gamma_1 \theta_1$	$\frac{P_{52}}{1+\alpha_1 P_{52}}$	W_{21}	α_1+P_{32}	$1+\alpha_1 P_{32}$	$\Gamma_{52} = \frac{P_{52}}{1+\alpha_1 P_{52}}$	$T_{52} = \frac{P_{52}(\alpha_1+P_{52})}{1+\alpha_1 P_{52}}$
1.000	1	6.950	1.000	1.404	6.950	1.404	1.000	1.000	6.950	6.950	1.000	1.000
1.647	3	8.950	2.554	2.212	18.85	3.811	.5804	.9559	8.504	16.20	1.905	1.341
2.104	5	10.95	3.541	3.020	30.75	6.218	.4857	1.022	9.491	22.07	2.325	1.523
2.478	7	12.95	4.223	3.828	42.65	8.624	.4439	1.100	10.17	26.13	2.569	1.644
2.803	9	14.95	4.723	4.636	54.55	11.03	.4203	1.178	10.67	29.10	2.727	1.732
3.093	11	16.95	5.105	5.444	66.45	13.44	.4051	1.253	11.06	31.37	2.836	1.800
3.358	13	18.95	5.407	6.252	78.35	15.84	.3947	1.325	11.36	33.17	2.920	1.852
3.606	15	20.95	5.651	7.060	90.25	18.25	.3868	1.395	11.60	34.62	2.984	1.893
3.837	17	22.95	5.852	7.868	102.2	20.66	.3808	1.461	11.80	35.82	3.036	1.928
4.053	19	24.95	6.021	8.676	114.1	23.07	.3761	1.524	11.97	36.82	3.076	1.957
4.259	21	26.95	6.165	9.484	126.0	25.48	.3722	1.585	12.12	37.68	3.109	1.983
4.456	23	28.95	6.290	10.29	137.9	27.88	.3691	1.645	12.24	38.43	3.140	2.003
4.644	25	30.95	6.398	11.10	149.8	30.29	.3665	1.702	12.35	39.07	3.164	2.022
4.825	27	32.95	6.493	11.91	161.7	32.70	.3642	1.757	12.44	39.63	3.186	2.038
5.000	29	34.95	6.577	12.72	173.6	35.10	.3624	1.812	12.53	40.13	3.203	2.054
5.168	31	36.95	6.643	13.52	185.5	37.51	.3604	1.863	12.59	40.53	3.219	2.063
5.332	33	38.95	6.710	14.33	197.4	39.91	.3591	1.915	12.66	40.92	3.232	2.076
5.490	35	40.95	6.770	15.14	209.3	42.32	.3578	1.964	12.72	41.28	3.245	2.086

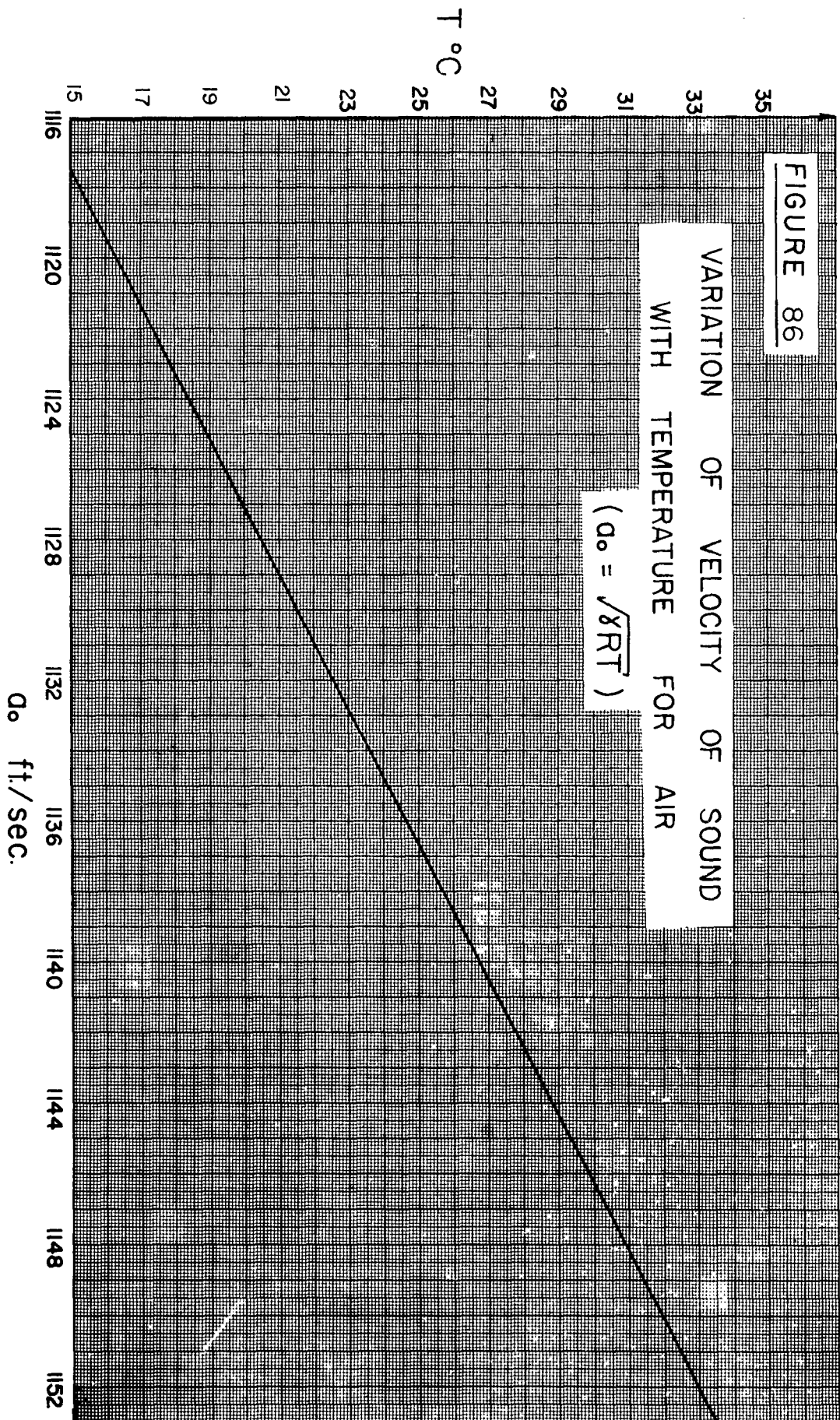
TABLE 15 (CONTINUED) Case: Air|Air

(1)	(2)	(3)	(4)	(5)	(6)
W_{11}	P_{21}^*	P_{52}^*	W_{21}^*	Γ_{52}^*	T_{52}^*
1.523	2.543	2.269	0.935	1.775	1.278
1.984	4.432	3.305	0.969	2.278	1.451
2.377	6.450	4.065	1.019	2.609	1.558
2.725	8.547	4.644	1.071	2.851	1.629
3.041	10.71	5.099	1.120	3.039	1.678
3.331	12.94	5.488	1.169	3.189	1.721
3.611	15.23	5.793	1.218	3.312	1.749
4.235	21.12	6.431	1.334	3.551	1.811
4.797	27.27	6.893	1.434	3.732	1.847

TABLE 16 (Fig.37)

$$T_{64}^{\frac{1}{2}} = \Gamma_{64}^{\beta_4} = P_{64}^{\beta_4} = 2P_{34}^{\beta_4} - 1 \quad \text{Case: Air} | \text{Air}$$

(1)	(2)	(3)	(4)	(5)	(6)
P_{34}	$(P_{34})^{\beta_4}$	$2P_{34}^{\beta_4} - 1$	$T_{64} = \textcircled{3}^2$	$\Gamma_{64} = \textcircled{3}^{\frac{1}{\beta_4}}$	$P_{64} = \textcircled{3}^{\frac{1}{\beta_4}}$
.008121	.5000	0	0	0	0
.009	.5075	.0150	.0002250	.9523x10 ⁻⁸	-
.01	.5153	.0306	.0009364	.3238x10 ⁻⁷	-
.02	.5693	.1386	.01921	.5689x10 ⁻⁴	.1097x10 ⁻⁵
.04	.6291	.2582	.06667	.1234x10 ⁻²	.8254x10 ⁻⁴
.06	.6669	.3338	.1114	.4397x10 ⁻²	.4910x10 ⁻³
.08	.6951	.3902	.1523	.9517x10 ⁻²	.1452x10 ⁻²
.1	.7178	.4356	.1897	.1640x10 ⁻¹	.3118x10 ⁻²
.2	.7942	.5884	.3462	.7257x10 ⁻¹	.2515x10 ⁻¹
.4	.8764	.7528	.5667	.2455	.1392
.6	.9291	.8582	.7365	.4724	.3458
.8	.9684	.9368	.8776	.7241	.6355
.9	.9849	.9698	.9405	.8593	.8082
1.0	1.000	1.000	1.000	1.000	1.000



APPENDIX B

B.1 Empirical Relationship (Eq.5.08)

The empirical relationship shown on figure 84 (Eq.5.09) was found in the following manner. First, the Rankine-Hugoniot curve was approximated by a straight line whose equation is also given on figure 84. Another straight line was drawn through the experimental points for each value of X . The ratio of the experimental slope to the theoretical slope m_x/m_t was then plotted against X to give the curve shown on figure 87. This curve had the form of a power curve and in order to find its equation figure 88 was drawn. On this figure $\ln m_x/m_t$ vs. $\ln X$ is plotted. The relationship on figure 87 was found to be

$$\frac{m_x}{m_t} = 0.996 X^{.0282}$$

Using this relationship equation 5.08 was determined.

It should be noted that although the ratio, m_x/m_t was used to plot figures 87 and 88 the same results can be obtained by plotting m_x against X . This procedure will yield equation 5.08 in fewer steps.

B.2 Theoretical Analysis (Eq.5.13)

For an incompressible fluid with constant viscosity, the generalized Navier-Stokes equation in vector notation takes the form (ref.71)

$$\rho \frac{d\vec{q}}{dt} = \rho \vec{F} - \nabla p + \mu \nabla^2 \vec{q} \quad (1)$$

If body forces are neglected and the pressure is assumed constant everywhere, then

$$\rho \frac{d\vec{q}}{dt} = \mu \nabla^2 \vec{q} \quad (2)$$

For the case of one-dimensional flow in a tube where $v=w=0$ and only u remains then (2) reduces to

$$\frac{\partial u}{\partial t} = \nu \left(\frac{\partial^2 u}{\partial z^2} + \frac{\partial^2 u}{\partial y^2} \right) \quad (3)$$

(The above equation indicates that ν acts everywhere and not in the boundary layer alone. This is the weakness of the present approach. Therefore, the solution is applicable to small tubes (i.e. $\delta \equiv R$) and will give too great an attenuation for larger tubes).

Eq. (3) is a second order linear homogeneous partial differential equation and can be solved by separation of variables.

The boundary conditions are as follows (see also fig. 65)

$$\left. \begin{aligned} (1) \quad u(z, y, 0) &= u_i \quad (0 < z < z_0, 0 < y < y_0) \\ (2) \quad u(0, y, t) &= 0 \\ (3) \quad u(z, 0, t) &= 0 \\ (4) \quad u(z_0, y, t) &= 0 \\ (5) \quad u(z, y_0, t) &= 0 \end{aligned} \right\} \quad (t > 0)$$

A solution can be found of the form

$$u = Z(z) Y(y) T(t)$$

The solution must satisfy the equation

$$\frac{T'}{T} = \nu \left(\frac{Z''}{Z} + \frac{Y''}{Y} \right) = C$$

However, the three terms in this equation must be constant as they are functions of z , y and t separately. Therefore, the following can be written:

$$\frac{Z''}{Z} = -\alpha^2 \quad \frac{Y''}{Y} = -\beta^2 \quad T' = -\nu(\alpha^2 + \beta^2) T$$

The solutions of these three equations for which $u = ZYT$ satisfies all the homogeneous boundary conditions are

$$Z = \sin \alpha z, \quad Y = \sin \beta y$$

$$\text{where} \quad \alpha = \frac{a\pi}{z_0} \quad \beta = \frac{b\pi}{y_0}$$

$$\therefore T = A e^{-\nu \pi^2 \left(\frac{a^2}{z_0^2} + \frac{b^2}{y_0^2} \right) t}$$

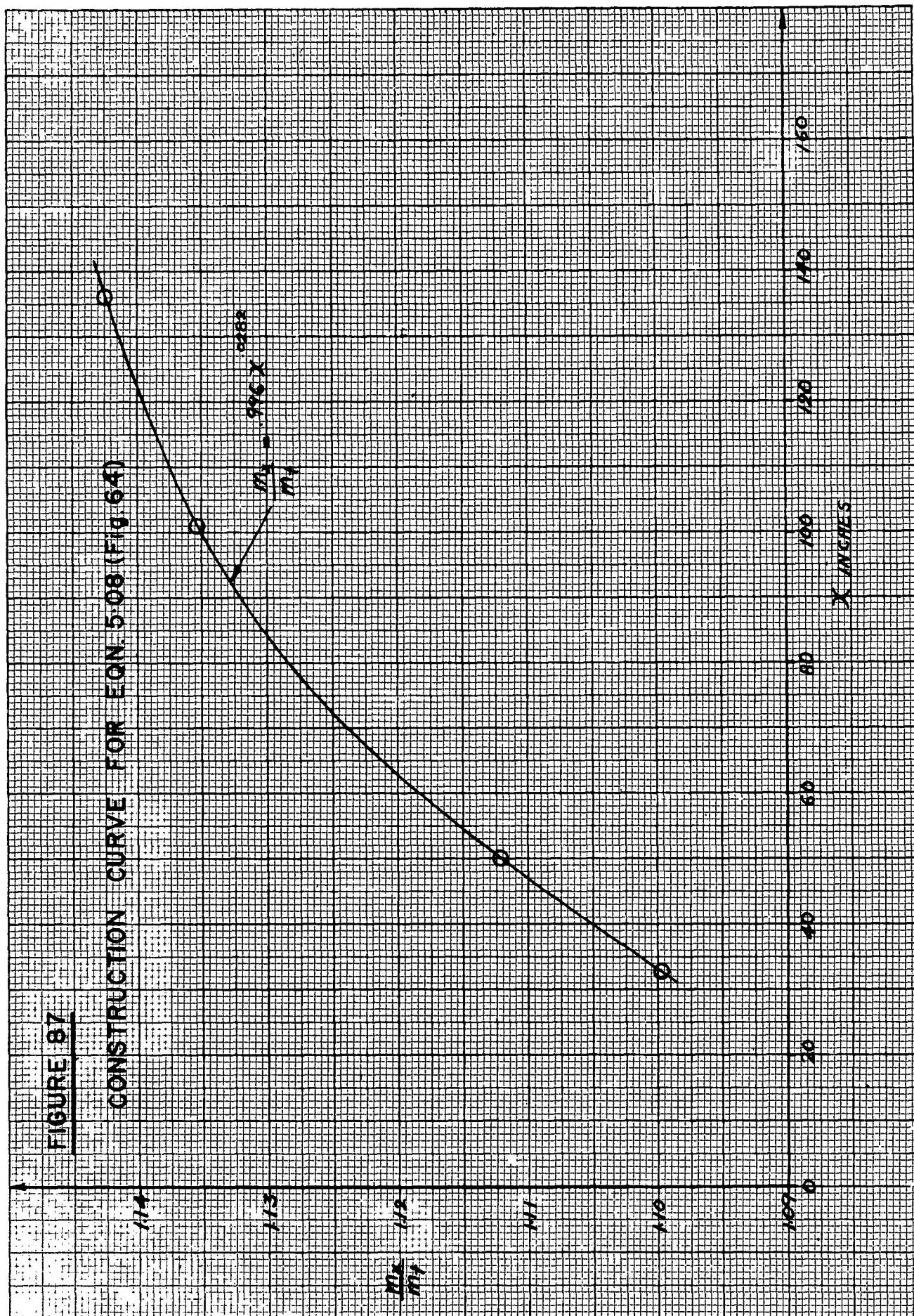
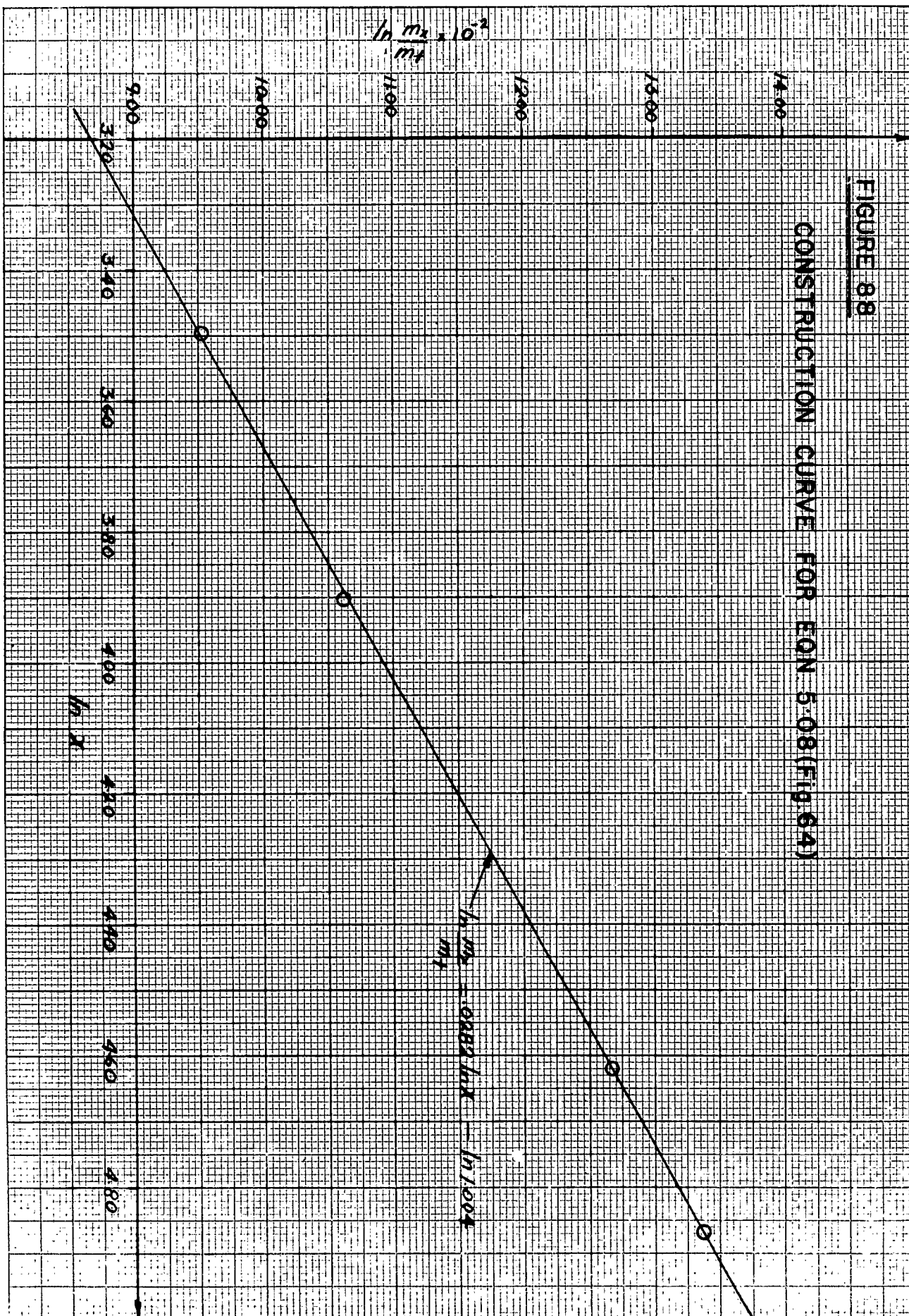


FIGURE 88

CONSTRUCTION CURVE FOR EQN. 5.08 (FIG. 64)



A particular solution is,

$$U_{ab}(z, y, t) = e^{-\nu \pi^2 \left(\frac{a^2}{z_0^2} + \frac{b^2}{y_0^2} \right) t} \sin \frac{a\pi}{z_0} z \sin \frac{b\pi}{y_0} y \quad (4)$$

or the general solution is:

$$U_{ab}(z, y, t) = \sum_{a=1}^{\infty} \sum_{b=1}^{\infty} A_{ab} e^{-\nu \pi^2 \left(\frac{a^2}{z_0^2} + \frac{b^2}{y_0^2} \right) t} \sin \frac{a\pi}{z_0} z \sin \frac{b\pi}{y_0} y \quad (5)$$

Eq. 5 is the solution provided that the coefficients A_{ab} can be found to satisfy B.C. (1) or

$$U(z, y, 0) = \sum_{a=1}^{\infty} \sum_{b=1}^{\infty} A_{ab} \sin \frac{a\pi}{z_0} z \sin \frac{b\pi}{y_0} y = u_i \quad (6)$$

($0 \leq z \leq z_0, 0 \leq y \leq y_0$)

The above is a Fourier sine series in two variables for $U(z, y)$ providing its coefficients have the values

$$A_{ab} = \frac{4}{z_0 y_0} \int_0^{y_0} \sin \frac{b\pi}{y_0} y dy \int_0^{z_0} u_i \sin \frac{a\pi}{z_0} z dz$$

$$\text{or} \quad A_{ab} = \frac{4u_i}{ab\pi^2} [1 - \cos b\pi] [1 - \cos a\pi] \quad (7)$$

Then (5) becomes:

$$U_{ab}(z, y, t) = \sum_{a=1}^{\infty} \sum_{b=1}^{\infty} \frac{4u_i}{ab\pi^2} [1 - \cos a\pi] [1 - \cos b\pi] e^{-\nu \pi^2 \left(\frac{a^2}{z_0^2} + \frac{b^2}{y_0^2} \right) t} \times \sin \frac{a\pi}{z_0} z \sin \frac{b\pi}{y_0} y$$

or

$$\frac{U}{u_i} = \sum_{a=1}^{\infty} \sum_{b=1}^{\infty} \frac{4}{ab\pi^2} [1 - \cos a\pi] [1 - \cos b\pi] e^{-\nu \pi^2 \left(\frac{a^2}{z_0^2} + \frac{b^2}{y_0^2} \right) t} \sin \frac{a\pi}{z_0} z \sin \frac{b\pi}{y_0} y \quad (8)$$

In this case: $z_0^2 = y_0^2 = A$

$$\therefore \frac{U}{u_i} = \sum_{a=1}^{\infty} \sum_{b=1}^{\infty} \frac{4}{ab\pi^2} [1 - \cos a\pi] [1 - \cos b\pi] e^{-\frac{\nu}{4} (a^2 + b^2) \pi^2 t} \sin \frac{a\pi}{z_0} z \sin \frac{b\pi}{y_0} y \quad (9)$$

At $t=0$ the mass flow is given by:

$$m_i = \rho u_i A = \rho u_i z_0 y_0$$

at any other time t

$$m = \int_0^{z_0} \int_0^{y_0} \rho u \, dz \, dy \quad (10)$$

Substituting for u in this equation from (8) yields:

$$m = \sum_{a=1}^{\infty} \sum_{b=1}^{\infty} \frac{4 u_i \rho}{a b \pi^2} [1 - \cos a \pi] [1 - \cos b \pi] e^{-\frac{\nu t}{A} (a^2 + b^2) \pi^2} \int_0^{z_0} \sin \frac{a \pi}{z_0} z \, dz \int_0^{y_0} \sin \frac{b \pi}{y_0} y \, dy \quad (11)$$

Integrating (11) results in

$$m = \sum_{a=1}^{\infty} \sum_{b=1}^{\infty} \frac{4 u_i \rho}{a^2 b^2 \pi^4} [1 - \cos a \pi]^2 [1 - \cos b \pi]^2 e^{-\frac{\nu t}{A} (a^2 + b^2) \pi^2} z_0 y_0$$

or

$$\frac{m}{m_i} = \frac{4}{\pi^4} \sum_{a=1}^{\infty} \sum_{b=1}^{\infty} \frac{[1 - \cos a \pi]^2 [1 - \cos b \pi]^2 e^{-\frac{\nu t}{A} (a^2 + b^2) \pi^2}}{a^2 b^2} \quad (12)$$

This is equation (5.13) in the text and is plotted on figure 66. A typical computation of m/m_i for a relatively large $\frac{\nu t}{A}$ (.01) is given on Table 17. For small values of $\frac{\nu t}{A}$ as many as 81 terms of the series are required.

TABLE 17

$$\frac{m}{m_i} = 4 \sum_{a=1}^{\infty} \sum_{b=1}^{\infty} \frac{[1 - \cos a\pi]^2 [1 - \cos b\pi]^2 e^{-\frac{\nu^+}{\Lambda}(a^2+b^2)\pi^2}}{a^2 b^2 \pi^4}$$

$$\frac{\nu^+}{\Lambda} = .01 \quad e^{-\frac{\nu^+}{\Lambda}(a^2+b^2)\pi^2} = e^{-.09870(a^2+b^2)} \quad \frac{64}{\pi^4} = .6570$$

1	2	3	4	5	2	3	4	5
	$a=1$				$a=3$			
b	$.6570 \times \frac{1}{b^2}$	$.09870 \times (1+b^2)$	$e^{-(3)}$	$(2) \times (4)$	$.6570 \times \frac{1}{9b^2}$	$.09870 \times (9+b^2)$	$e^{-(3)}$	$(2) \times (4)$
1	.6570	.1974	.8209	.5393	.0730	.9870	.3727	.0272
3	.0730	.9870	.3727	.0272	.00811	1.777	.1692	.0014
5	.02628	2.566	.0768	.0020	.00292	3.356	.0349	.0001
7	.01341	4.935	.0072	.0001	.00149	5.724	.0033	-
9	.00811	8.093	.0003	-				
$\Sigma = .5686$					$\Sigma = .0287$			

1	2	3	4	5	2	3	4	5
	$a=5$				$a=7$			
b	$.6570 \times \frac{1}{25b^2}$	$.09870 \times (25+b^2)$	$e^{-(3)}$	$(2) \times (4)$	$.6570 \times \frac{1}{49b^2}$	$.09870 \times (49+b^2)$	$e^{-(3)}$	$(2) \times (4)$
1	.02628	2.566	.0768	.0020	.01341	4.935	.0072	.0001
3	.00292	3.356	.0349	.0001	.00149	5.724	.0033	-
5	.00105	4.935	.0072	-	.00054	7.304	.0007	-
7	.00054	7.304	.0007	-				
$\Sigma = .0021$					$\Sigma = .0001$			

$$\frac{m}{m_i} = .5995$$

UTIA REPORT NO. 2

INSTITUTE OF AEROPHYSICS, UNIVERSITY OF TORONTO



A Theoretical and Experimental Study of the Shock Tube
by I.I. Glass, W. Martin and G.N. Patterson,
Nov. 1953, 281 p., 86 figs., 37 plates, 17 tables

1. Shock Tubes 2. One-dimensional wave interactions
3. Nonstationary Flow 4. Supersonic Flow
I Glass, I.I. II Martin W. III Patterson, G.N.

IV UTIA Report No. 2

Shock tube theory is developed from basic considerations. Comprehensive graphs are presented

Copies obtainable from: Institute of Aerophysics, University of Toronto, Toronto 5, Ontario

UTIA REPORT NO. 2

INSTITUTE OF AEROPHYSICS, UNIVERSITY OF TORONTO



A Theoretical and Experimental Study of the Shock Tube
By I.I. Glass, W. Martin and G.N. Patterson,
Nov. 1953, 281 p., 86 figs., 37 plates, 17 tables

1. Shock Tubes 2. One-dimensional wave interactions
3. Nonstationary Flow 4. Supersonic Flow
I Glass, I.I. II Martin W. III Patterson, G.N.

IV UTIA Report No. 2

Shock tube theory is developed from basic considerations. Comprehensive graphs are presented

Copies obtainable from: Institute of Aerophysics, University of Toronto, Toronto 5, Ontario

UTIA REPORT NO. 2

INSTITUTE OF AEROPHYSICS, UNIVERSITY OF TORONTO



A Theoretical and Experimental Study of the Shock Tube
by I.I. Glass, W. Martin and G.N. Patterson,
Nov. 1953, 281 p., 86 figs., 37 plates, 17 tables

1. Shock Tubes 2. One-dimensional wave interactions
3. Nonstationary Flow 4. Supersonic Flow
I Glass, I.I. II Martin, W. III Patterson, G.N.
IV UTIA Report No. 2

Shock tube theory is developed from basic considerations. Comprehensive graphs are presented

Copies obtainable from: Institute of Aerophysics, University of Toronto, Toronto 5, Ontario

UTIA REPORT NO. 2

INSTITUTE OF AEROPHYSICS, UNIVERSITY OF TORONTO



A Theoretical and Experimental Study of the Shock Tube
by I.I. Glass, W. Martin and G.N. Patterson,
Nov. 1953, 281 p., 86 figs., 37 plates, 17 tables

1. Shock Tubes 2. One-dimensional wave interactions
3. Nonstationary Flow 4. Supersonic Flow
I Glass, I.I. II Martin, W. III Patterson, G.N.
IV UTIA Report No. 2

Shock tube theory is developed from basic considerations. Comprehensive graphs are presented

Copies obtainable from: Institute of Aerophysics, University of Toronto, Toronto 5, Ontario

for determination of wave speeds and physical quantities of uniform states. Effects of variable specific heat on rarefaction and shock waves are considered. Some important one-dimensional wave interactions are discussed.

Experimental and theoretical aspects of origin problem, shock wave attenuation and contact front acceleration are analysed. Experiments on the emergence from shock tube of shock and rarefaction waves, condensation effects, wave refraction, collision of shock waves and wire screens and overtaking of two shock waves are given.

for determination of wave speeds and physical quantities of uniform states. Effects of variable specific heat on rarefaction and shock waves are considered. Some important one-dimensional wave interactions are discussed.

Experimental and theoretical aspects of origin problem, shock wave attenuation and contact front acceleration are analysed. Experiments on the emergence from shock tube of shock and rarefaction waves, condensation effects, wave refraction, collision of shock waves and wire screens and overtaking of two shock waves are given.

for determination of wave speeds and physical quantities of uniform states. Effects of variable specific heat on rarefaction and shock waves are considered. Some important one-dimensional wave interactions are discussed.

Experimental and theoretical aspects of origin problem, shock wave attenuation and contact front acceleration are analysed. Experiments on the emergence from shock tube of shock and rarefaction waves, condensation effects, wave refraction, collision of shock waves and wire screens and overtaking of two shock waves are given.

for determination of wave speeds and physical quantities of uniform states. Effects of variable specific heat on rarefaction and shock waves are considered. Some important one-dimensional wave interactions are discussed.

Experimental and theoretical aspects of origin problem, shock wave attenuation and contact front acceleration are analysed. Experiments on the emergence from shock tube of shock and rarefaction waves, condensation effects, wave refraction, collision of shock waves and wire screens and overtaking of two shock waves are given.